Winter 2009

Sensitive Detection of Novel Effects and Characteristic Signal Structure of Higher Harmonic Detection in Wavelength Modulation Spectroscopy

Mohammad Amir Khan
Old Dominion University

Recommended Citation

Khan, Mohammad A.. "Sensitive Detection of Novel Effects and Characteristic Signal Structure of Higher Harmonic Detection in Wavelength Modulation Spectroscopy" (2009). Doctor of Philosophy (PhD), dissertation, Electrical/Computer Engineering, Old Dominion University, DOI: 10.25777/qnmt-tv66
https://digitalcommons.odu.edu/ece_etds/92

SENSITIVE DETECTION OF NOVEL EFFECTS AND CHARACTERISTIC SIGNAL STRUCTURE OF HIGHER HARMONIC DETECTION IN WAVELENGTH MODULATION SPECTROSCOPY

By

Mohammad Amir Khan
M.E. May 2003, Old Dominion University
M.S. May 2000, Indian Institute of Technology, India

A Dissertation Submitted to the Faculty of Old Dominion University in Partial
Fulfillment of the Requirement for the Degree of

DOCTORATE OF PHILOSOPHY

ELECTRICAL AND COMPUTER ENGINEERING

OLD DOMINION UNIVERSITY
DECEMBER 2009

Approved by:

Amin N. Dharamsi (Director)

Mounir Laroussi (Member)

Vijayan Asari (Member)

Leposava Vuskovic (Member)

ABSTRACT

SENSITIVE DETECTION OF NOVEL EFFECTS AND CHARACTERISTIC SIGNAL STRUCTURE OF HIGHER HARMONIC DETECTION IN WAVELENGTH MODULATION SPECTROSCOPY

Mohammad Amir Khan
Old Dominion University, 2009
Director: Dr. Amin N. Dharamsi

We discuss experimental and theoretical results of absorption features of the oxygen A-band transitions when synchronous detection at higher harmonics using Wavelength Modulation Spectroscopy (WMS) is performed. A key aspect of structure higher harmonic detection is discussed. It is shown that the signal magnitude and spectral locations of turning points and zero crossings of WMS signal demonstrate key signatures of collision dynamics of gaseous specie parameters and lineshape parameters. In addition, it is also shown that these salient features provide sensitive probes for any changes in the gas environment or lineshape parameters. We discuss several advantages and subtle physical effects that can be probed by higher order detection. As an example, we show resolution of several overlapping congested line spectra with highly disparate oscillator-strength. Optically thick regime of oxygen A- band transitions are probed by WMS and shown to exhibit distinctive features that are reflected in higher harmonic signals. These experimental results are the first ones to examine optical pathlength saturation by WMS. These effects greatly depend on the lineshape and gas parameters and experimental variables. The rich structure of WMS signals, especially at higher detection orders, is central to the technique's advantages in resolving these subtle effects. We show greater sensitivity of turning points and zero crossings with lineshape or gas parameters. We also show that in certain situations the sensitivity could be significant especially in the wing

region of the profile where the absorption signal is low.

We discuss two approaches to quantify advantages of higher harmonic detection and structure (number of zero crossings and turning points). The method is based on statistical analysis and principles of Shannon's classical information theory, where the precision in Wavelength Modulation Spectroscopy (WMS) and measurements with molecular species is quantified utilizing information theory.

We show that there is an optimal harmonic detection order that yields the maximum information in presence of distortion and noise. Distortion and noise effects are treated separately. Particular cases of distortion i.e. modulation broadening, pressure broadening, pathlength saturation and Fabry - Perot fringing are discussed, and their relation to information in the measurement of lineshape parameters is outlined. It is shown that the optimal harmonic order can be understood by considerations of complexity in the signal structure rather than those of conventional Signal to Noise ratios. It is also shown that under certain experimental conditions higher detection orders ($N \geq 5$) yield precise and optimal results in estimation of lineshape parameters in a given noise environment. The merit of optimal harmonic detection order is based on maximum information (in bits) that can be extracted at a particular harmonic signal in the presence of noise.

This dissertation is dedicated to all those who made this work possible.

ACKNOWLEDGMENTS

It is with great pleasure that I acknowledge the contributions of those who have assisted in the successful completion of this dissertation. I extend my gratitude to the Faculty and staff in the Department of Electrical and Computer Engineering for their continuing support during the course of my degree. I thank the committee members for their time and guidance. I am particularly grateful to my advisor Dr. Amin N. Dharamsi with whom I worked for the past eight years. I greatly acknowledge his patience, commitment and guidance to his students during their research. His support has not only shaped my research work but also provided me with a perspective that is very important for a successful future in research and academia. I also thank my colleagues James Barrington and Karan Mohan for their invaluable help with the experimental work and productive academic discussions during my research on Wavelength Modulation Spectroscopy. I also express my gratitude to the Director and staff of Student Support Services where I worked occasionally as a teaching instructor. I am also thankful to Dr. Tariq Jawhar for proof reading the dissertation. I am especially indebted to Professor V.K. Tripathi (Indian Institute of Technology, New Delhi) for encouraging me to pursue doctoral research.

Finally, I hold my sincerest appreciation to my family and friends for their continued encouragement, perseverance and understanding that have made it possible for me to succeed in this endeavor. I am deeply indebted to my parents for all the sacrifices they have made to let me pursue higher education. My very special thanks to Hajar Maazia for continued support, encouragement and all the help during the course of my degree.

TABLE OF CONTENTS

Page

LIST OF FIGURES ix

LIST OF TABLES xiii

1. INTRODUCTION 1
    1.1 Experimental observations: Multiple overlapping lines, optical pathlength saturation and sensitivity in wings 2
    1.2 Quantitative metrics of measurement of lineshape parameters 3
    1.3 Structure in WMS signals 4
    1.4 Information theory 5
    1.5 References 7

2. THEORETICAL BACKROUND 10
    2.1 Mathematical expressions for WMS signals 11
    2.2 WMS signals and lineshape profiles 17
    2.3 WMS modeling 24
    2.4 Conclusion 27
    2.5 References 28

3. OXYGEN A-BAND TRANSITIONS AND EXPERIMENTAL RESULTS. 30
    3.1 Structure of Oxygen A-band 30
    3.2 Weak overlapping Oxygen transitions 38
    3.3 Optical pathlength saturation 51
    3.4 Conclusion 65
    3.5 References 66

4. SENSITIVTY TO LINESHPAE PARAMTERS, SIGNAL STRUCTURE AND NOISE COSNIDERATIONS 68
    4.1 Sensitivity at zero crossings and turning points 68
    4.2 Signal structure and measurements 78
    4.3 Loss of precision: distortion and noise 81
    4.4 Signal uncertainty: thermal noise 86
    4.5 Conclusion 89
    4.6 References 89

5. OPTIMAL DETECTION ORDER – I: RESIDUALS AND CHI- SQUARE METRIC 92
    5.1 Quantitative advantages of higher harmonic detection: Chi-Square Metric.... 92
    5.2 Signals with imprecision in measurements 99
    5.3 Metric at higher detection order 102
    5.4 Chi-square measure and information 107

5.5 References......109

6. OPTIMAL DETECTION ORDER – II: INFORMATION THEORY......111
6.1 Information content......112
6.2 Information theory and WMS perspective - precision in measurement of signal at turning points and zero crossings......116
6.3 Information in measurement of a lineshape parameter......123
6.4 Information in experimental signal and model uncertainties......133
6.5 Information and finite precision of instrument......136
6.6 Modulation distortion and resolution of overlapping line transitions......140
6.7 Conclusion......143
6.8 References......146

7. SUMMARY......149

APPENDIXES

A. Mathematical formulation of WMS signals......154
B. Convergence of series expansion of the derivatives of Gaussian, Lorentzian and Voigt function......158
C. Maximum entropy......175
D. Thermal Noise- physics of impedance matching in circuits......177
E. Power distribution and entropy......180
F. Distribution of turning points of overlapping transitions......190
G. MATLAB Codes......192

VITA......200

LIST OF FIGURES

Figure Page

2-1 Conventional absorption signal and its 1st and 4th detection harmonic signal.. 15

2-2 Absorption at the linecenter and the b parameter of the Voigt profile....... 21

2-3 Schematic diagram of various components of WMS experimental setup... 28

3-1 Energy levels of molecular Oxygen A- band. 32

3-2 Oxygen A- band structure. 37

3-3 Block diagram of experimental apparatus. Wavelength of a modulated laser is swept across an absorption region of oxygen......................... 38

3-4 Experimental absorption signal of Oxygen A – band transition............ 40

3-5 Experimental plots and theoretical models of N = 1 to N= 8 detection order of oxygen RR(13,13) , RR*(13, 13) , RQ (12 , 13) and RR(43, 43) transitions.. 41

3-6 Comparison between 'direct' absorption and weaker lines of Oxygen A – band those are resolved at higher detection order............................ 43

3-7 Oxygen transitions with five line transitions in a wavelength scan.......... 44

3-8 Experimental results of 4th order RR(13,13) and three overlapping line transitions.. 48

3-9 Experimental 6th order RR(13,13) and three overlapping weak line transitions (L1, L2 and L3) at different modulation indices................ 49

3-10 Experimental 8th order of RR (13,13) and three overlapping line transitions.. 50

3-11 Schematic of saturation phenomena. An incident white light gets broadened as it traverses within the absorbing media......................... 52

3-12 Experimentally measured direct absorption (no modulation), second, fourth, sixth and eighth harmonic signals of molecular oxygen A-band RR (13, 13) transitions.. 57

3-13 Direct absorption, fourth, sixth and eighth harmonic signals with larger saturation parameter, τ values (τ = 1.3 and m = 1)........................... 58

3-14 Experimental and Theoretical Results. Sixth (a) and eighth (b) - harmonic signals measured with a fixed saturation parameter, τ =1.6 corresponding to L = 210 meters... 61

3-15 Ratio (R_{PS}) of the signal at linecenter and the adjacent turning point of fourth, sixth and eighth-harmonics.. 63

3-16 Ratio of the linecenter magnitude of strong RR (13, 13) transitions vs. weaker RR*(13,13) transition... 64

4-1 Theoretical calculations of direct absorption signal (dashed curve) as well as with modulation with synchronous detection at various harmonics of the modulation frequency... 71

4-2 Theoretical calculations of percentage change in the signal with respect to a reference Doppler linewidth of 2.0 GHz..................................... 72

4-3 Percentage change in the signal at zero crossings and turning points of 5f detection order (N = 5) with the change in the linewidth (from 2 GHz reference linewidth)... 73

4-4 Sensitivity of turning points with the change in b parameter of the Voigt profile.. 74

4-5 Experimental plot of ratios, R_T of the RR (13, 13)) Oxygen (O^{16}) A-band transition.. 77

4-6 WMS signals with respect to the detection order, N (bottom figure). The signal power reduces with the detection order (N), whereas the number of turning points increases with N.. 80

4-7 Wavelength characterization (Fig. (a)) of oxygen A– band spectrum that scans RR (13,13) transitions.. 82

4-8 Representation of uncertainties in wavelength data and lock-in amplifier signal.. 83

4-9 Effects of modulation broadening.. 84

4-10 Pathlength distortion: 4th and 8th harmonic signals with modulation index, m = 1.. 85

4-11 Fabry- perot fringing due to multiple reflections from optical components. 86

5-1 Theoretical signal (solid curve) and Expected signal (dotted curve) of 1st and 5th harmonic WMS signals.. 95

5-2 Mismatch between expected and theoretical harmonic signals. The mismatch is due to difference in the linewidth. Expected Linewidth = 2.0 GHz and Theoretical linewidth= 2.1 GHz.................................... 97

5-3 Graphical representation of photodetector signals with imprecision......... 100

5-4 Deviation of fractional error of harmonic N=1 to N=5 of WMS signals..... 103

5-5 Experimental and modeled plots of 6th (Fig. (a)) and 7th (Fig. (b)) order WMS signals of oxygen RR (13,13) A-band transition.............. 106

6-1 Schematic diagram of a standard communication system.................. 118

6-2 N=1 and N=2 harmonic detection signals with the zero crossings (Zs) and turning points (Ts) as points of interest....................................... 121

6-3 Uncertainty in locations of zero crossings and turning points described by two uniform probability distribution functions. 122

6-4 Schematic of an input absorption lineshape signal with an additive noise... 124

6-5 WMS harmonic signal with additive Gaussian noise at the turning points and zero crossings.. 125

6-6 Full scale sensitivity of individual turning points of N=2 harmonic signal. 128

6-7 Schematic of a lock in amplifier (LIA) [17].................................. 129

6-8 Information extracted vs. the harmonic order, N, for two set of modulation indices and fixed noise power 132

6-9 Cumulative uncertainty in experimental signals and model data is equivalent to the convolution of their individual distribution 134

6-10 Information extracted in linewidth measurements............................ 136

6-11 Detector imprecision modifies the distribution of the turning points to discrete values.. 137

6-12 Information is extracted when the precision is increased. The information extracted at different detection order, N, varies with the available turning points or structure in the signals.. 139

6-13 Information extracted at different detection orders at lower modulation index, m=1 140

6-14 N= 3 and N=7 detection order of two overlapping transitions at modulation indices, m=2, where lines are fully resolved and m=4, when lines are partially resolved 142

6-15 Resolution of weaker lines and direct absorption signal scaled to magnitude of 8th harmonic 144

6-16 WMS setup and its equivalence with a linear system 145

B-1 Convergence of the Gaussian series at the linecenter (x=0). 161

B-2 Convergence of the Gaussian series expansion of two different harmonic orders, N=2 and N=6. 163

B-3 Comparison of the two mathematical methods of N=8 WMS signal. 164

B-4 Ratio of the integral I_N the detection order. 172

B-5 Comparison between Voigt profile computed from Humlicek (1976) algorithm and MATLAB dblquad function. 173

B-6 Comparison between Voigt profile computed from Humlicek (1982) algorithm and MATLAB dblquad function. 174

B-7 Comparison between N=2 Voigt signal computed from Humlicek algorithm and MATLAB dblquad function. 174

D-1 Exchange of thermal power between two resistors 179

D-2 Equivalent circuits for thermal noise 180

LIST OF TABLES

Table Page

5-1 Cumulative measure of error due to mismatch between the expected and theoretical WMS signals at various detection orders........................ 98

6-1 Spectral locations of turning points and zero crossings of N=1 and N=2 signals and linewidth obtained form the combination of these points....... 120

6-2 Number of discernible turning points at different modulation indices (m = 2, 3 and 4) at detection orders N = 1 to 9....................................... 143

CHAPTER 1

INTRODUCTION

Wavelength Modulation Spectroscopy (WMS) [1-10] is a sensitive, convenient, versatile and cost-effective method for monitoring gaseous species and for obtaining quantitative information about molecular collision dynamics through precise measurements of the absorption lineshape function. In nearly every field of technology there is a distinct need for some type of characterization of a gaseous medium. Some examples where such a characteristic is needed include: identifying a particular species within the atmosphere, determining and controlling reactants within a processing environment, and analyzing the velocity and temperature distribution. The technique provides a sensitive probe of molecular species due to its rich structure (derivative like features with turning points and zero crossings) of the harmonic signals. Even slight perturbations in the lineprofile can be measured precisely and, because these perturbations are directly linked to changes in physical conditions of the sampled target, one obtains very precise and non-intrusive measurements of these parameters. Over the last few years, we have extended this technique to the regime of higher harmonic detection [6-10] and demonstrated that, in many cases, one obtains a higher precision by using an optimal harmonic detection order higher than the commonly used second harmonic. Experimental and theoretical results have been presented.

The style model used in this dissertation is *Applied physics B*.

1.1 EXPERIMENTAL OBSERVATIONS: OPTICAL PATHLENGTH SATURATION

The dissertation outlines metric of precision measurements of higher order harmonic detection in Wavelength Modulation Spectroscopy (WMS) experiments. In the first part of the dissertation (Chapters-2 and 3) we show experimental results that demonstrate the advantages of higher detection order and optimal detection based on physical parameters of gas and experimental variables. These results are discussed in Chapters 2 and 3. We show that higher detection order facilitates the probing of subtle features of the direct absorption signal that may not be apparent in direct or conventional aspiration spectroscopy measurements or even at lower detection orders. We further investigate the effects of gas environment, collision dynamics, lineshape function and experimental variables in measurements of these effects. Chapter 2 lays the theoretical foundation of WMS signals and mathematical methods [11, 12] in the literature that have been used to model the signals. We further discuss different types of lineshape functions that are commonly used for modeling the experimental results. In summary, the chapter describes theoretical developments, mathematical theory and modeling of WMS signals. In Chapter 3 we discuss experimental results, particularly the resolution of several overlapping line transitions of Oxygen A-band spectrum and detection [7, 13] order that facilitates accurate modeling and estimation of lineshape parameters e.g. Doppler and collision linewidths. Further, in this chapter we also discuss the experimental results of optical pathlength saturation in WMS and the measurement of saturation parameters. Such measurements in an optically thick environment using WMS are reported here for the first time. In the concluding section of this chapter we discuss a key aspect of experimental results i.e. the growth of weak lines at higher detection order and optical pathlength saturation effects [15, 16] are investigated.

1.2 QUANTITATIVE METRICS OF MEASUREMENT OF LINESHAPE PARAMETERS

The experimental observations indicate an optimal detection order for estimation of lineshape or gas parameters. In the second part of this thesis (Chapters- 4, 5 and 6) we develop a criterion that quantifies structure in WMS signals and advantages of greater structure in estimating lineshape or gas parameters. In chapter 4 we develop the concept of structure and distortion/noise effects that inhibit precise measurements of these parameters. A key idea to the aspects of structure is to first recognize that the WMS technique facilitates investigation of sensitive features of absorption signal by probing variations in the lineshape profile. These variations are exhibited as zero crossings and turning points, which are key markers in the far wing structure of the lineshape profile, thus demonstrating the WMS technique as a sensitive probe to the lineshape parameters [9, 10, 14].

In the following Chapter (5) we discuss practical limitations that lead to imprecision in WMS signals and optimum detection order in presence of noise or distortion. These effects; distortion (systematic aberration in measurements) and noise [17, 18] (a statistical irreversible process that lead to uncertainties in measurements) are considered separately. Consequently, two approaches are developed to quantify the advantage of higher order detection in presence of the distortion and noise in measurements. The first approach is based on deviation of residuals [14, 19, 20] mainly at zero crossings and turning points of WMS signals. The method considers mismatches in theory and experiment that result due to uncertainties in a lineshape parameter. It is shown that mismatches are more prominent at higher orders thus enhancing the precision of measurements when such mismatches are minimized. The second approach is based on Shannon's formulation [21-24] of information theory and its connection to measurement of lineshape parameters using aspects of structure in WMS signals.

1.3 STRUCTURE IN WMS SIGNALS

All measurements probe changes in acquired signals. In spectroscopy the measurements are based on changes in photon intensity with respect to wavelength. It is the signal contrast from a reference that gives information about the parameter being measured. A signal that provides greater contrast from point to point in phase-space is easier to measure, even when it may not exhibit the greatest cumulative signal to noise ratio (SNR). In such cases, conventional SNR is not the most suitable metric for optimizing the measurement. For example, a signal with constant slope reveals less information (about its inherent physical process) compared to a signal with varying slopes or a signal with a number of turning points. This contrast (fractional change in signal magnitude) of a signal with respect to its background enables accuracy in measurements and higher precision in estimation of its distinct parameters. For example, suppose in any experiment one obtains an experimental spectral profile of direct and harmonic signals and matches it with a theoretical model to estimate a lineshape parameter, say the linewidth. Any finite amount of uncertainty in linewidth estimation, due to mismatches in theoretical and experimental results yields greater mismatch at higher harmonics than the lower ones. This result is also shown in Chapter 5 which demonstrates larger deviation (of fractional residuals between the experiment and theory) due to greater structure in WMS signals [19, 20]. To illustrate this point, it is shown that uncertainty in linewidth of 5 percent the difference between the theory and experiment may not be noticeable in direct absorption signals or lower detection orders. However, at higher harmonics e.g. $N \geq 4$, these differences readily appear in greater contrast especially as mismatches at zero crossings and turning points. Therefore, even a small change in the lineshape parameters can cause appreciable effects on higher harmonic signals, which can be detected easily. Therefore, in a harmonic signal the locations of zero crossings and the turning points facilitate a very sensitive probe of lineshape parameters.

1.4 INFORMATION THEORY

The analysis of WMS signals based on information theory [21, 22] regard zero crossings and turning points and their combination as key markers [23, 24]. Any uncertainty in determination of these features in the presence of noise leads to an increase in cumulative uncertainty (in the estimation of lineshape parameters), while removal of these uncertainties extracts information. The Theoretical formulation of entropy in measurements is obtained from probabilistic distribution of zero crossings and turning points. We show that the entropy is directly proportional to signal magnitude to noise power which in certain situations, by increase in modulation index, yields information. Theoretical development [25, 26] of this approach, utilizing combinatoric analysis of zero crossings and turning points, yields the optimal order of detection of WMS signals in presence of a noise.

The combinatoric availability of turning points or zero crossings to estimate lineshape parameters allows one to apply aspects of information theory [21-26]. Therefore, one can primarily extract the information by analyzing spectral locations and signal magnitude of zero crossings and turning points instead of a full WMS spectrum. In any Nth harmonic WMS signal there are N zero crossings and N+1 turning points. Therefore, higher harmonics provide more choices (or combinations of pairs of zero crossing or turning points) to estimate the lineshape parameter. For example, the linewidth of the profile can be obtained using combinations of pairs of zero crossings or turning points. For any Nth detection order there are, ${}^{2N+1}C_1\,, {}^{2N+1}C_2 \ldots {}^{2N+1}C_{2N+1}$ possible combinations to compute the linewidth. Further, if the measurements of zero crossings and turning points are precise, then, in principle, each combination of ${}^{2N+1}C_i$ ($i = 1, 2 \ldots, 2N+1$) pairs will yield the same linewidth values. However, uncertainties in the measurements will lead to a probability distribution of turning points and the linewidth obtained from them. This uncertainty, due to the instrument imprecision is quantified using information theory. The advantage of higher harmonic measurements is demonstrated by showing that more information can be extracted at higher N's, when the precision is changed by a fixed amount. Since the signal magnitude decreases with the increase in harmonic order, this advantage, quantified in *bits*, is not a monotonically increasing function (with respect to N). Instead, it shows an optimal detection harmonic order.

The methods and results obtained in the formulation of this dissertation lay out the future groundwork for a vital advantage (quantified in bits) of weak line resolution of interference from overlapping lines. It is proposed that for particular limitations of the experimental apparatus; there is a finite amount of information that can be transmitted from the probe laser via information source (molecular specie or lineshape) to the detection electronics. This approach is based on Shannon's information-theoretic formulation of a channel with Gaussian noise. The method developed is applied to the experimental results of Oxygen A-band transitions and measurement of subtle features using higher harmonic detection.

In summary, there are two important aspects of WMS signals which are used in development of this theory: Firstly, zero crossings and turnings points of any Nth harmonic provide a sensitive probe, and secondly, the combinatory numbers of the structure provide greater choices to estimate a lineshape parameter. Concepts of information theory combine the two aspects and quantify the advantages of higher harmonic detection.

1.5 REFERENCES

1. G.C. Bjorklund, M.D. Levenson, W. Lenth, and C. Oritz, "Frequency modulation spectroscopy: Theory of lineshapes and Signal-to-Noise analysis," *Appl. Phys. B*, 32, 145 (1983).

2. W. Lenth, C. Ortiz, and G. C. Bjorklund, "Frequency modulation excitation spectroscopy," *Opt.l Commun.* 41, 369–373 (1982).

3. J. Reid and D. Labrie, "Second harmonic detection with tunable diode lasers: comparison of experiment and theory," *Appl. Phys. B*, 26, 203 (1981).

4. Joel A. Silver, "Frequency-modulation spectroscopy for trace species detection: theory and comparison among experimental methods," *Appl. Opt. 31*, 707-717 (1992).

5. J.A. Silver, A.C. Stanton, "Two-tone optical heterodyne spectroscopy using buried double heterostructure lead-salt diode lasers," *Appl. Opt.* 27, 1914 (1988).

6. A.N. Dharamsi, "A theory of modulation spectroscopy with applications of higher harmonic detection," *J. Phys. D* 28, 540 (1996).

7. A. N. Dharamsi and A. M. Bullock, "Applications of wavelength modulation spectroscopy in resolution of pressure and modulation broadened spectra," *Appl. Phys. B,* 63, 283 (1996).

8. A. N. Dharamsi and A. M. Bullock, "Measurements of density fluctuations by modulation spectroscopy," *Appl. Phys. Lett.* 69, 22 (1996).

9. A. N. Dharamsi and Y. Lu, "High-resolution spectroscopy using high-order derivative techniques," *Appl. Phys. Lett.* 65, 2257 (1994).

10. A. N. Dharamsi and Y. Lu, "Sensitive density fluctuation measurements using wavelength modulation spectroscopy with high order harmonic detection," *Appl. Phys. B,* 62, 273 (1996).

11. O. E. Myers and E. J. Putzers, "Measurement broadening in magnetic resonance," *J. Appl. Phys.* 30 (1987).

12. G. V. H. Wilson, "Modulation broadening of NMR and ESR line shapes," *J. Appl. Phys.* 34, 3276 (1963).

13. M.A. Khan, J.M. Barrington and A.N. Dharamsi, "Sensitive Detection of Molecular Species by Modulation Techniques: A Measure of Information Content in Spectroscopy", *Proceedings of SPIE* Vol. 4634, 83–91 (2002).

14. M. A. Khan, Karan D. Mohan and A. N. Dharamsi, "Wavelength Modulation Spectroscopy as a sensitive probe for wing structure of absorption lines," *Manuscript in preparation.*

15. M. A. Khan, Karan D. Mohan and A. N. Dharamsi, " Novel pathlength saturation effects in modulation spectroscopic techniques" *SPIE Symposium on Optics East*, 1-4 6378-47, October (2006).

16. M. A. Khan, Karan D. Mohan and A. N. Dharamsi, "Optical Pathlength Saturation Signatures in Wavelength Modulation Spectroscopy Signals of Atmospheric Molecular Oxygen", *Accepted for publication Appl. Phys. B (2009).*

17. J. Johnson, "Thermal Agitation of Electricity in Conductors," *Physical Review*, 32, 97 (1928).

18. H. Nyquist, "Thermal Agitation of Electric Charge in Conductors," *Physical Review*, 32, 110 (1928).

19. M. A. Khan, J. M. Barrington and A. N. Dharamsi, "Detailed Structure of harmonic Signals in Modulation Spectroscopy and resulting Precision Improvement in Non-Intrusive Laser based Sensors,"

IEEE Lasers and Electro Optic Society Annual Meeting, Conference Proceedings, Vol. I, 25-26 (2003).

20. M.A. Khan and A.N. Dharamsi, "Quantitative metrics of efficacy of higher harmonic detection in wavelength modulation spectroscopy for precision measurements," *Proceedings of SPIE* Vol. 5364, 227–234 (2004).

21. C. E. Shannon, "A Mathematical Theory of Communication- Part 1," *Bell System Technical Journal* 27, 379 (1948).

22. C. E. Shannon, "A Mathematical Theory of Communication- Part 2," Bell *System Technical Journal* 27, 623 (1948).

23. M. A. Khan, Karan D. Mohan, A. N. Dharamsi; "Information Theory of High-Precision Measurements," *Frontiers in Optics: Laser Science-* XXIV (2008).

24. M. A. Khan, Karan D. Mohan and A. N. Dharamsi, "Signal Structure and Precision in Optical Measurements: A new perspective to optimal experimental techniques", *IEEE Lasers and Electro Optic Society Annual Meeting*, Conference Proceedings (2008).

25. M. A. Khan and A.N. Dharamsi, "Information Extraction from Congested Molecular Spectra by Modulation Spectroscopy"– *75th annual southeastern APS meeting* (2008).

26. M. A. Khan and A.N. Dharamsi, "Signal Structure and Sensitive Detection of Molecular Species: Optimal experimental techniques in Wavelength Modulation Spectroscopy" *Proceedings of SPIE*, OPTO (2009).

CHAPTER 2

THEORETICAL BACKGROUND

Modulation spectroscopy is a variant of absorption spectroscopy, where the signals obtained from this technique are a manifestation of variations of the absorption signal obtained from a modulated probe laser. Due to their low cost, tunability range (where many gas molecules have vibrational-rotational transitions.) and compactness, such lasers are currently the best candidate for modulation spectroscopy [1-4], also referred as tunable diode modulation spectroscopy. With the advent of Vertical Cavity Surface Emitting Lasers (VCSEL) and quantum cascade lasers and their tremendous range of tunability from mid infra-red to far infra-red regions of the electromagnetic spectrum, the field of absorption spectroscopy and its variants such as, modulation spectroscopy, cavity enhanced spectroscopy are becoming increasingly popular in research and fundamental science .

There are several experimental techniques currently used to modulate the frequency of a diode laser. Semiconductor lasers can easily be frequency modulated via injection current and laser temperature. In general, depending on the method, the frequency modulation is accompanied with residual amplitude modulation.

In this chapter we study mathematical description of WMS signals. We derive mathematical expressions of wavelength modulation spectroscopy signals utilizing two most common mathematical methods i.e. Myers – Putzers [5] and Wilsons [6] formulation. Myers - Putzers method involves a combination of Taylor's series and

Fourier series expansion, whereas Wilsons approach is direct integral of Fourier components of the absorption signal.

2.1 MATHEMATICAL EXPRESSIONS FOR WMS SIGNALS

In an experiment where the probe - usually a single mode tunable diode laser is frequency modulated and the absorbed signal is demodulated using synchronous detection. The signal thus obtained is given by Fourier harmonics of the modulated probe. The harmonic signals have derivative like features that are characteristics of the transition lineshape profile.

In the absorption experiment, such as the one under consideration one obtains the usual equation describing the attenuation of intensity in an infinitesimal pathlength *dz*, i.e.

$$dI/dz = -n\bar{\sigma}g(v)I \qquad (2\text{-}1)$$

Here n is the density, $\bar{\sigma}$ is the integrated absorption cross-section, L is the length of the absorber. Hence, the absorption signal of a sample normalized with respect to the initial intensity of the probe intensity I_0, (incident laser intensity) is,

$$\frac{\Delta I}{I_0} = 1 - \exp\{-n\bar{\sigma}Lg(v)\} \qquad (2\text{-}2)$$

For weak absorption line, the Beer-Lambert relation yields,

$$I \approx I_0(1 - n\bar{\sigma}g(v)L) \qquad (2\text{-}3)$$

Hence, the signal measured in a phase sensitive apparatus, using harmonic detection originates from,

$$S = I - I_0 \approx -I_0 n\bar{\sigma}g(v)L \qquad (2\text{-}4)$$

In a WMS experiment [2-4] a modulated laser source is used to probe an absorber, typically gaseous specie. The absorbed signal at the photodetector is channeled to a synchronous phase sensitive detection or a Lock-in Amplifier. The reference phase of modulated laser beam is synchronous to the demodulation frequency of the lock-in amplifier. The absorption signal, with imposed modulation on it, is then demodulated at multiples (1f, 2f, 3f….) of the input modulation frequency.

A probe, modulated at frequency, ω_m with amplitude β (in Hz), can be expressed as, $I\,(v + \beta\cos(\omega_m t))$. This is a periodic function of $\omega_m t$ and can be expanded in form of Fourier series.

2.1.1 Fourier components of modulated absorption signal

When, a modulated laser beam is swept slowly across the absorption feature, the effective normalized absorption signal recorded by the detector is therefore:

$$g(v)\delta(v_L + \beta\sin(\omega_m t) = g(v_L + \beta\sin(\omega_m t) = f(\varphi) \qquad (2\text{-}5)$$

Here φ denotes the sinusoidal time variation, modulation signature on the probe laser, and on the absorbed signal.

Any sinusoidal signal, $y = f(v + \beta\cos\phi)$, can be expressed in form of Fourier series expansion given by;

$$y = \frac{a_0}{2} + \sum_{k=1}^{\infty}(a_k\cos k\phi + b_k\sin k\phi) \qquad (2\text{-}6)$$

It has been shown by Meyers and Putzers [5] that *k*th component of the complex Fourier series of *f(φ)* can be written as, (a complete description of the above formulations is given in Appendix A.)

$$a_k = 2\sum_{V=0}^{\infty} \frac{f^{2V+k}}{(2V+k)!} \left(\frac{\beta}{2}\right)^{2V+k} \binom{2V+k}{V} \tag{2-7}$$

Therefore, a pure frequency modulation (ignoring amplitude modulation) Nth harmonic order signal is given by:

$$S^N = -n\bar{\sigma}LI_0(-1)^{[N]/2} \sum_{V=0}^{\infty} \left(\frac{\beta}{2}\right)^{2V+N} \frac{1}{V!(V+N)!} g^{2V+N}(\nu) \tag{2-8}$$

Here, $g(\nu)$ is the lineshape profile and $g^{2V+N}(\nu)$ are the $(2V+N)$th derivative of the lineshape function.

If the lineshape function is a Gaussian, its derivatives [4] can be expressed as series:

$$g_G{}^N(\nu) = \frac{g}{\sqrt{\pi}} \frac{1}{(\Delta\nu_D)^{2N+1}} \sum_{k=0}^{[N]/2} C_{2k,N} \overline{(\Delta\nu_D)}^{2k} (\nu - \nu_0)^{N-2k} \tag{2-9}$$

Here, $\Delta\nu_D$ is the Doppler linewidth (Full width) and ν_0 is the linecenter of the absorption lineshape profile. A complete description of the co-efficients $C_{2k,N}$ is given in Appendix B. In summary the composite absorption signals from Eqns. (2-8) and (2-9) can be expressed as,

$$S^N = -n\bar{\sigma}LI_0(-1)^{[N]/2} \frac{g}{\sqrt{\pi}} \sum_{V=0}^{\infty} \left(\frac{\beta}{2}\right)^{2V+N} \frac{1}{V!(V+N)!} \frac{1}{(\overline{\Delta\nu_D})^{2(2V+N)+1}} \sum_{k=0}^{[2V+N]/2} C_{2k,2V+N} \overline{(\Delta\nu_D)}^{2k} (\nu - \nu_0)^{2V+N-2k}$$

(2-10)

or

$$S^N = -n\bar{\sigma}LI_0(-1)^{[N]/2} \frac{g}{\sqrt{\pi}} \sum_{V=0}^{\infty} \left(\frac{\beta}{2}\right)^{2V+N} \frac{1}{V!(V+N)!} \frac{(\overline{\Delta\nu_D})^{2V+N}}{(\overline{\Delta\nu_D})^{2(2V+N)+1}} \sum_{k=0}^{[2V+N]/2} C_{2k,2V+N} \left(\frac{\nu - \nu_0}{\overline{\Delta\nu_D}}\right)^{2V+N-2k}$$

(2-11)

Further simplifying the above expression,

$$S^N = -n\bar{\sigma} L I_0 (-1)^{[N]/2} \frac{g}{\Delta\nu_D\sqrt{\pi}} \sum_{V=0}^{\infty} (\frac{1}{2})^{2V+N} \frac{1}{V!(V+N)!} \left(\frac{\beta}{(\Delta\nu_D)}\right)^{(2V+N)} \sum_{k=0}^{[2V+N]/2} C_{2k,2V+N} (\frac{\nu-\nu_0}{\Delta\nu_D})^{2V+N-2k} \tag{2-12}$$

Substituting modulation index, $m = \frac{\beta}{(\Delta\nu_D)}$ and the normalized frequency, $x = \frac{\nu-\nu_0}{\Delta\nu_D}$, one obtains,

$$S^N = -n\bar{\sigma} L I_0 (-1)^{[N]/2} \frac{g}{\Delta\nu_D\sqrt{\pi}} \sum_{V=0}^{\infty} (\frac{1}{2})^{2V+N} \frac{1}{V!(V+N)!} (m)^{(2V+N)} \sum_{k=0}^{[2V+N]/2} C_{2k,2V+N} x^{2V+N-2k} \tag{2-13}$$

The above equation is the WMS signal with Gaussian lineshape function. Features of the signals are studied in the following section.

2.1.2 Derivative like features of WMS signal

It can be seen from Eqn. (2-8) that WMS signals have derivative like features of the lineshape function. In a typical Nth order WMS signal there are N+1 zero crossings and N turning points. The odd harmonics have zero crossing at the linecenter whereas the even harmonics have a turning point at the linecenter, see Fig.2.1 below. The Figure shows the conventional absorption signal or the direct signal corresponding to N=0, and first (N=1) and second (N=2) order WMS signals. All the odd harmonics have odd symmetry with zero crossings at line center, ν_0, which can be exploited in measurements of transition line centers. Since each (N+1)th harmonic is effectively a derivative of its previous Nth signal, the locations of turning points and zero crossings of Nth are the zero crossing and turning point of its subsequent (N+1) harmonic order. The WMS signal probes the variations in the lineshape profile; therefore, the sensitivity at the locations of zero crossing and turning point increases with the detection order. The last point to consider is that the signal magnitude decreases as the detection harmonic order increases. This decrease in signal magnitude must be out weighed by the advantages of using wavelength modulation spectroscopy with higher harmonic detection. Although, the signal power decreases with the detection order [4], one can find optimum harmonics for measurement of a lineshape parameter. This also is central to this dissertation, where the aim is to measure lineshape parameters based on the structure (or number of turning points and zero crossings). The signal magnitude and spectral locations of these salient points depend on the experimental controls e.g. the frequency modulation index, the amplitude modulation, and the lineshape or gas parameters such as the linewidth, the lineshape function, absorption cross-section, density etc.

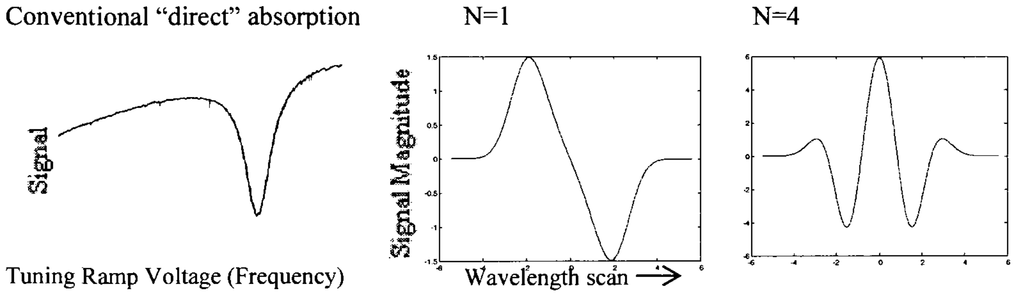

Fig. 2.1. A typical absorption signal and its 1st and 4th detection harmonic signals. N =1 has one zero crossing and two turning points. N=4 has four zero crossings and five turning points.

Semiconductor lasers such as VCSELs can be tuned and modulated by both temperature and injection current. When these lasers are modulated by the injection current, both the wavelength and intensity of the laser beam vary with the current. Therefore, amplitude modulation occurs simultaneously with the wavelength modulation. To account for the wavelength and amplitude modulations, a modification in direct modulation signal is required. As mentioned earlier the frequency modulation is often accompanied with a distortion due to amplitude modulation. A detailed theory and mathematical formulation of the amplitude modulation is discussed in reference [4].

2.1.3 Dependence on modulation index

It can be seen that the factor m^{2V+N} controls the number of terms required for the convergence of the above series. If m << 1, only the first term of the above series is required. This corresponds to derivative spectroscopy. For m >> 1, higher order terms of the series are required which leads to broadening [6] of the signals.

A similar series expression can be obtained for a Lorentzian lineshape [4]. However, there is no analytical series expression to evaluate derivatives of the Voigt function. (Appendix B shows series formulation of the Voigt function.)

In Eqn. (2-13), the ratio $m = \beta / \Delta v$ is the so-called modulation index and is an important parameter in modulation spectroscopy signals. The parameter determines the structure of the electric field that samples the absorption lineshape transition. Generally, in the literature, the modulation index is expressed as $M = \beta / \omega_m$. In frequency modulation spectroscopy, M is generally small because the modulation frequency is large ($\omega_m >> \Delta v$). The sidebands generated by the modulation in this case are spaced far enough apart that only a few sidebands sample the absorption feature. Thus, any changes in β or ω_m affect the shape of the signal. In wavelength modulation spectroscopy, however, M is very large. Consequently, the absorption feature is sampled by a dense spectrum of sidebands, all separated by ω_m. Because the modulation frequency is much less than the transition width ($\omega_m << \Delta\nu$), neighboring side bands probe the transition at roughly the same spectral frequency. When detected with a square-law detector, this results in a signal profile that takes a derivative shape. In wavelength modulation, the spacing of the side bands is dense enough that moderate changes in ω_m do not affect the signal shape. Therefore, it is common in wavelength modulation spectroscopy to redefine the modulation index as the ratio of peak frequency deviation to profile width, $m = \beta / \Delta\nu$, because even slight changes in this parameter affect the shape of the signal. Throughout this study, we have adopted the above definition of modulation index.

2.2 WMS SIGNALS AND LINESHAPE PROFILES

There are several lineshape profiles that have been used to model the transition distribution of absorption lines. The lineshape profiles encode physics of broadening mechanisms of absorbing or emitting transitions. As mentioned in the previous section the shape of WMS signals among other variables depend on the lineshape profile. Throughout our analysis we consider three most commonly used lineshape profiles i.e., Doppler broadened (or a Gaussian function), Collision broadened (or a Lorentzian function) and a Voigt (convolution of Doppler and Collision broadened profiles) [7-11]. For illustration purposes, due to the ease of analytical calculations and faster computational algorithms, we have used the Doppler lineshape at several occasions in this dissertation. However, for experimental models and fitting, we have used the Voigt lineshape profile. The choice of Voigt lineshape profile was also due to the dynamics of the collision processes under investigation, which in most of our experimental conditions was best related to the Voigt profile.

2.2.1 Doppler and Lorentzian Profiles

Doppler broadening is the inhomogeneous broadening of the linewidth of atomic transitions caused by the random movements of atoms. For example, if the atoms have a thermal velocity distribution with temperature T, the linewidth resulting from the Doppler effect is $\Delta v_D = 2\left(\frac{2kT\ln 2}{Mc^2}\right)^{1/2} v_0$; where v_0 is the mean optical frequency and m is the mass of the atoms. The Doppler broadening, e.g. for atoms in a gas cell is typically much larger than the natural linewidth.

Doppler broadening can place severe constraints on precise spectroscopic measurements. However, it can be eliminated in various ways, e.g. by reducing the temperature (e.g. with laser cooling) or by employing a measurement scheme which is intrinsically insensitive to Doppler broadening, such as Doppler-free saturation spectroscopy or the use of two-photon absorption with counter propagating beams.

The mathematical expression of the Doppler broadened profile is given by;

$$g_D(v) = \frac{1}{\sqrt{\pi}\,\Delta v_D}\exp\left(\frac{-(v-v_0)^2}{\Delta v_D^{\;2}}\right) \qquad (2\text{-}14)$$

here the Doppler linewidth is, $\Delta v_D = 2\left(\frac{2kT\ln 2}{Mc^2}\right)^{1/2} v_0$, and, the normalized linewidth is expressed as, $\overline{\Delta v_D} = \frac{\Delta v_D}{\sqrt{4\ln 2}} = \Delta v_D / 1.66$

The Doppler profile assumes that the lifetime of a transition is infinite, i.e., the oscillation is always present. Additionally, the Doppler profile neglects phase changing collisions, i.e., the wave train is continuous without interruption. In a gas at low pressure with few collisions, the Doppler profile is a good approximation of the absorption profile. However, as pressure and collisions increase, phase changing collisions have to be considered. The classical damped electron oscillator given by Siegman [9] provides an excellent model for a wave train with a finite period. Not only does this model give insight to absorption, it also models the phase shift associated with the change of index of reflection.

The Lorentzian lineshape function is given by,

$$g_L(\nu) = \frac{\Delta\nu_{coll}}{2\pi} \frac{1}{(\nu-\nu_0)^2 + (\Delta\nu_{coll}/2)^2} \qquad (2\text{-}15)$$

its collision linewidth is expressed as, $\Delta\nu_{coll} = n\sigma_{coll}V$. Here n is the density, σ_{coll} is the collision cross-section and V is the velocity of atoms.

In situations where experiments are carried out at high atmospheric pressure or density of the molecules, collision broadening is dominant: whereas, at low pressures Doppler broadening plays an important role.

2.2.2 Voigt Profile

If the dephasing collisions and the Doppler effect discussed above are considered statistically independent, then the Lorentzian profile can simply replace the delta function in the Doppler equation before integrating over the velocity resulting in the Voigt line shape,

$$g_V(\nu) = \left(\frac{m}{2\pi kT}\right)^{\frac{1}{2}} \int_{-\infty}^{\infty} \frac{1}{\pi} * \frac{\frac{\Delta\nu_{coll}}{2}}{(\nu_0 - \nu - \frac{\nu_0 V_z}{c})^2 + \left(\frac{\Delta\nu_{coll}}{2}\right)^2} \times \exp\left(-\frac{mV_z^2}{2kT}\right) dV_z \qquad (2\text{-}16)$$

In other words, in most physical situations the gas collision dynamics is not solely Doppler or Collision broadened but the combination of the two. Therefore, the profile is expressed as convolution of the Doppler and Collision lineshape functions. Following from the above equation, a standard Voigt function is given by, (2-17)

$$g_V(x) = \frac{1}{\pi^{3/2}} \frac{b^2}{\delta\nu_0} \int_{-\infty}^{+\infty} \frac{dy e^{-y^2}}{(x+y)^2 + b^2} \qquad (2\text{-}17)$$

Here $\delta\nu_0$ is collision half width ($2\delta\nu_0 = \Delta\nu_{coll}$), and x is the normalized frequency, $x = \frac{\nu - \nu_0}{\Delta\nu_D}$, and the linewidth parameter is, $b = \frac{\Delta\nu_{coll}}{2\Delta\nu_D}$.

2.2.3 The 'b' parameter: Doppler and Collision broadened regimes of Voigt

The range of 'b' parameter of a Voigt profile indicates dominance of collision or Doppler broadened phenomena in the gas dynamics. For example, the absorption at the linecenter, $\nu = \nu_0$ ($x = x_0$) can be expressed as,

$$g_V(x_0) = be^{b^2} erfc(b) / (\pi^{1/2} \Delta\nu_{coll}) \qquad (2\text{-}18)$$

Function $g_V(x_0)$ depends strongly on the ratio of the linewidths for collision and Doppler broadening or parameter 'b' and its complementary error function, Fig. 2.2. When the collision width $\Delta\nu_{coll}$ is much greater than the Doppler width $\Delta\nu_D$, i.e. b >> 1 then

$g_V(x_0) \approx 1/\pi\Delta\nu_{coll}$, which is the case of pure collision broadening. Whereas, in the limit in which the Doppler width is much greater than the collision broadened width, i.e. b << 1 then $g_V(x_0) \approx 1/\pi^{1/2}\overline{\Delta\nu_D}$, which is the case of pure Doppler broadening.

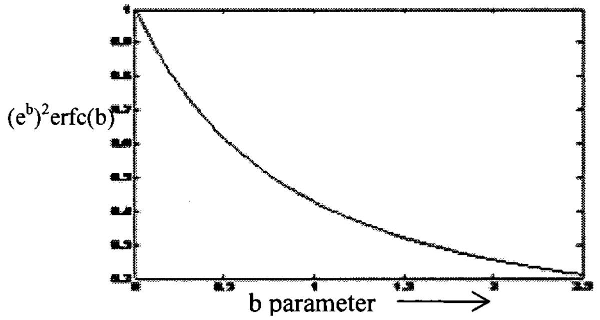

Fig. 2.2. Absorption signal (at the linecenter) and the b parameter of the Voigt profile.

For the general case of arbitrary values of both the parameter b and the normalized frequency *x*, the lineshape function g(x_V) given by Eqn. (2-19) must be evaluated from tabulated values of the more complicated function

$$\int_{-\infty}^{+\infty}\frac{dye^{-y^2}}{(x+y)^2+b^2}=\frac{\pi}{b}\mathrm{Re}\left(\frac{i}{\pi}\int_{-\infty}^{\infty}\frac{dye^{-y^2}}{x+y+ib}\right)=\frac{\pi}{b}\mathrm{Re}\,w(x+ib) \tag{2-19}$$

Here, *w* is the error function of complex argument. Numerical values are tabulated in various mathematical handbooks [12, 13].

2.2.4 Profile Narrowing

Although the Voigt incorporates the basics for the transition line shape in a gas, it lacks the elements to explain the small deviations detected in a precise measurement. For example, Rautian and Sobel'man [14-16] developed a line shape that incorporated a narrowing of the Voigt profile in a dense medium, Dicke [16] narrowing. As discussed in the derivation of the Voigt profile, collisions are not considered to have any affect on molecular velocity; therefore, the contribution of the Gaussian line shape to the Voigt is not altered by collisions. However, the inclusion of velocity-changing collisions, defined as collisions that change the velocity of the molecule but not the phase, can change the measurable velocity distribution.

Physically, it is hard to visualize the Doppler profile narrowing discussed as by Rautian and Sobel'man. For example, their hard collision model considers that after every collision, the memory of the velocity prior to the collision is lost; and its velocity is redistributed in the Maxwellian distribution. Therefore, the instantaneous velocity distribution of the molecules is always Maxwellian. If the energy of the gas in the medium remains the same, it is counter intuitive to expect a narrowing of Doppler profile due to velocity changing collisions. Varghese and Hanson [11, 17] present an extreme case to illustrate this phenomenon qualitatively. Consider a dense medium where a molecule is continuously involved in velocity changing collisions, i.e., the molecule conducts a random walk in velocity space. If the bulk gas is at rest, the mean velocity will approach zero even though the instantaneous velocity distribution is Maxwellian. Therefore, the value of measured velocity will depend on the time it takes to make the measurement. Spectrally, velocity in the line of sight results in a Doppler shift, $\omega_0(1+v_z/c)$; therefore, the velocity is measured over the period of a wave. In this extreme case, if there are enough collisions during one period of the fundamental frequency, i.e., if the path is much less than a wavelength, $2\pi L << \lambda$, where L equals the average velocity times the time between collisions, then the velocity measured will be the mean velocity of the molecule or in the case of a random walk, zero. However, in the other extreme, if collision were such that the path is much longer than the wavelength, $2\pi L >> \lambda$, then velocity changing collision will just interrupt the wave train, broadening the Lorentzian part of the line width. Rautian and Sobel'man [14, 15] derived the following equation to show this effect,

$$I(\omega) = \frac{1}{\pi}\mathrm{Re}\left\{ \frac{\displaystyle\int \frac{W(v)dv}{\upsilon + \frac{\Delta\omega}{2} - i(\omega_0 - \omega - \Delta - \frac{\omega_0 v}{c})}}{1 - \upsilon \displaystyle\int \frac{W_M(v)dv}{\upsilon + \frac{\Delta\omega}{2} - i(\omega_0 - \omega - \Delta - \frac{\omega_0 v}{c})}} \right\} \qquad (2\text{-}20)$$

where *W(v)* is the velocity distribution and υ is the velocity changing collision frequency. The following changes were made to Rautian and Sobel'man's original equation for notation consistency: substituting $\Delta\omega/2 = \Gamma$ and $\omega_0/c = k$, and $\omega_0 - \omega$ was substituted back into the equation for ω. Note, when the velocity distribution is Maxwellian, the real part of the numerator is a Voigt profile with the Lorentzian width equal to $\Delta\omega/2 + \upsilon$. However, the denominator results in narrowing. If the velocity changing collision frequency is small, i.e. much less than the Doppler width, the second term denominator of the equation is negligible, and the line shape is a Voigt. However, in the other extreme, when the velocity changing collision frequency is much larger than the Doppler width, $\upsilon >> \Delta\omega_D$, the second term in the denominator can approach one at line center, i.e., the second term of the denominator is simply an inverted Voigt weighted by the velocity changing collision frequency. When normalized, the center is larger than the Voigt's and narrowed on the sides; however, the wings are larger due to the inclusion of the velocity changing collision frequency in the Lorentzian portion of the Voigt.

Varghese and Hanson [11] replaced these computational difficult integrations of the Voigt with the error function resulting in

$$NG(x',y,\varsigma)=\mathrm{Re}\left[\frac{w(x',y+\zeta)}{1-\sqrt{\pi}\varsigma w(x',y+\zeta)}\right] \qquad (2\text{-}21)$$

where ζ is the dimensionless value of the velocity-changing collision frequency divided by the Doppler width. Note the change of variables in the error function from the definition used in the definition of the Voigt. The deviation from the unperturbed radiation frequency, x', remains the same, but the velocity-changing collision frequency has been added to the collisional broadening frequency, $y + \zeta$.

Numerous other line shapes that are available including speed dependent asymmetries and collision correlation effects. However, such effects are currently not used to model any experimental data.

2.3 WMS MODELING

Myers and Putzers [5] approach discussed in the previous sections requires derivative of the lineshape functions. The method is useful as it allows one to visualize signals as it builds by every additional term in the series expansion. However, series expansion may sometime require a large number of (V) terms for the series to converge and used for modeling purposes. We have seen (Appendix B) that this method works best within a certain range of values of the modulation index (m) and normalized frequencies (x) of the spectrum, Eqn. (2-13). In other regions the method has computational difficulties in terms of convergence of the series (this is discussed in Appendix B). Also, convergence of Gaussian, Lorentzian and Voigt are discussed in the Appendix B.

On the other hand, another approach to compute WMS signals given by Wilsons method [6] has no such convergence problems. The WMS signal from this method is a simple cosine integral of the absorbed signal and is given by,

$$H_N = \frac{1}{\pi} \int_{-\pi}^{\pi} g(v + \beta \cos\phi) \cos N\phi d\phi \qquad (2\text{-}22)$$

Hence, the resultant WMS signal is expressed as,

$$S^N = \frac{-n\bar{\sigma}LI_0}{\pi} \int_{-\pi}^{\pi} g(v + \beta \cos\phi) \cos N\phi d\phi \qquad (2\text{-}23)$$

As noted earlier, Wilsons expression has no such convergence problems and can be used to numerically compute WMS signals. Functional form of Gaussian and Lorentzian functions can be directly used in the formulation. To evaluate the integral of the Voigt function, Humlicek algorithm is commonly used in the literature. Most of the work there was mainly concerned with direct absorption or at the most N = 2 detection: whereas our work required models of higher detection order, upto N=8, where Humlicek algorithm doesn't perform accurately. Therefore, for our computations we have primarily used Matlab dblquad (MATLAB double integration function) to calculate the harmonic signals of Voigt profiles.

Based on the variables involved in the algorithms i.e. the type of lineshape function, range of modulation index and accuracy we have provided a Flowchart of modes of numerical computations. The Flowchart below describes various numerical methods and MATLAB functions that were used to evaluate WMS signals.

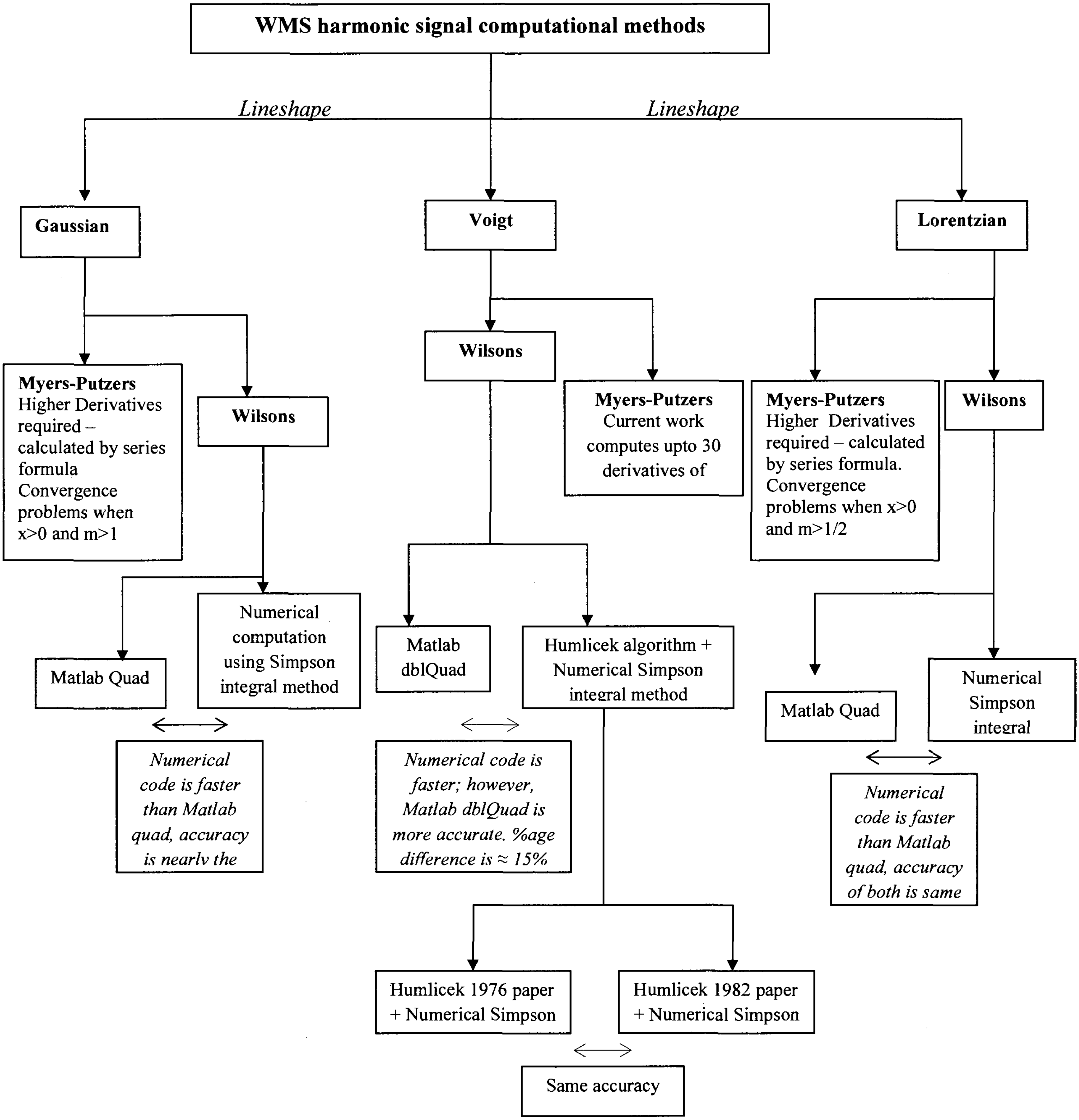
WMS harmonic signal computational methods
Lineshape
Lineshape
Gaussian
Voigt
Lorentzian
Myers-Putzers
Higher Derivatives required – calculated by series formula
Convergence problems when x>0 and m>1
Wilsons
Wilsons
Myers-Putzers
Current work computes upto 30 derivatives of
Myers-Putzers
Higher Derivatives required – calculated by series formula.
Convergence problems when x>0 and m>1/2
Wilsons
Matlab Quad
Numerical computation using Simpson integral method
Matlab dblQuad
Humlicek algorithm + Numerical Simpson integral method
Matlab Quad
Numerical Simpson integral
Numerical code is faster than Matlab quad, accuracy is nearly the
Numerical code is faster; however, Matlab dblQuad is more accurate. %age difference is ≈ 15%
Numerical code is faster than Matlab quad, accuracy of both is same
Humlicek 1976 paper + Numerical Simpson
Humlicek 1982 paper + Numerical Simpson
Same accuracy

Flowchart of WMS mathematical modeling methods

2.4 CONCLUSION

Theoretical formulation and accurate modeling of WMS signals is paramount for an accurate estimation of lineshape and gas parameters. To give an overview of the experimental procedure and theoretical modeling, Fig. 2.3 below shows the schematic of the typical WMS experiment. A probe (diode) laser is modulated and samples across the lineshape profile. In order to achieve that, a sinusoidal modulation (~ 1 kHz) along with a fixed dc bias and a slow ramp (approx. 60 – secs) is input to the probe laser. As mentioned earlier, the (sampled) depth depends on the modulation frequency and modulation amplitude. The absorption signal from the photodetector is processed through a lock-in amplifier (narrow band detection) where the signal is demodulated at various frequencies of the input sinusoidal modulation. In addition, the wavelength of the probe laser is characterized by an interferometer tuned to the laser frequencies. The wavelengths acquired are used for modeling experimental data. In this procedure, the linecenter location and magnitude of both the experiment and theory are matched. Consequently, the parameters of theoretical model that best fits the experimental data give the lineshape parameters of the gaseous specie.

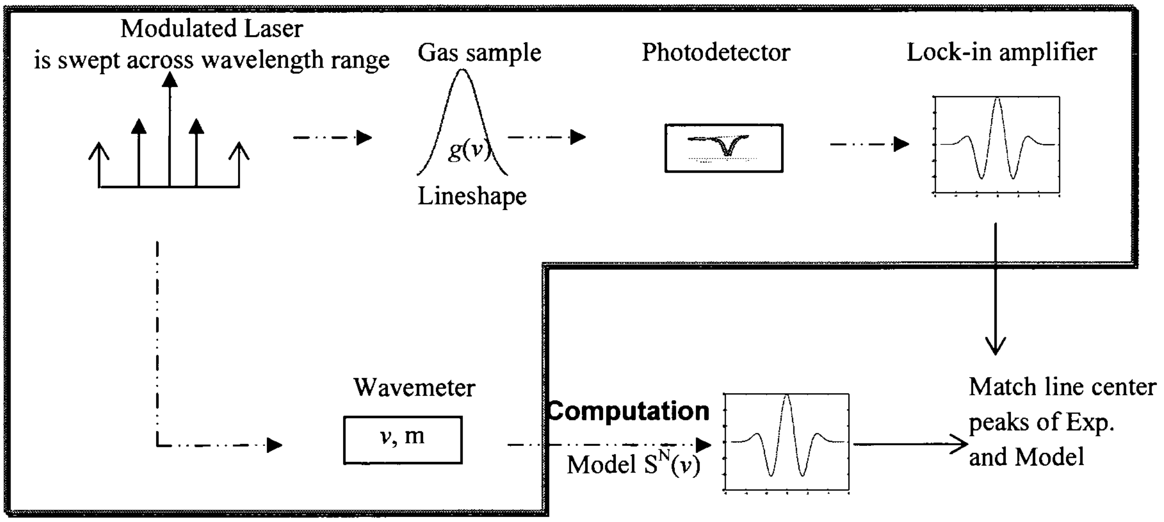

Fig. 2.3. Block diagram of various components of WMS experimental setup. Theoretical models are generally programmed in MATLAB. The experimental data is modeled using theoretical formulation and lineshape (or gas) parameters are estimated from the best fit between experiment and model.

2. 5 REFERENCES

1. J. Reid and D. Labrie, "Second-harmonic detection with tunable diode lasers—comparison of experiment and theory," *Appl. Phys. B*, 26, 203 (1981).

2. G.C. Bjorklund, M.D. Levenson, W. Lenth, and C. Oritz, "Frequency modulation spectroscopy: Theory of lineshapes and Signal-to-Noise analysis," *Appl. Phys. B*, 32, 145 (1983).

3. J.A. Silver, A.C. Stanton, "Two-tone optical heterodyne spectroscopy using buried double heterostructure lead-salt diode lasers," Appl. Opt. 27, 1914 (1988).

4. A.N. Dharamsi, "A theory of modulation spectroscopy with applications of higher harmonic detection," *J. Phys. D* 28, 540 (1996).

5. O. E. Myers and E. J. Putzers, "Measurement broadening in magnetic resonance," *J. Appl. Phys.* 30 (1987).

6. G. V. H. Wilson, "Modulation broadening of NMR and ESR line shapes," *J. Appl. Phys.* 34, 3276 (1963).

7. P.W. Milonni and J.J. Eberly, Lasers, Wiley Interscience, New York (1988).

8. B. H. Armstrong, “Spectrum line profiles: the Voigt function,” *J. Quant. Spectrosc. Radiat. Transfer* 7, 61 (1967).

9. A.E. Siegman, Lasers, University Science Books, Mill Valley (1986).

10. J.T. Verdeyen, Laser Electronics, Prentice Hall, New Jersey (1995).

11. P.L. Varghese and R.K. Hanson, "Collisional narrowing effects on spectral line shapes measured at high resolution," *Appl. Opt*, 23, 2376 (1984).

12. V.N. Faddeyeva and N.M. Terent’ev, Mathematical Tables of the values of complex error function for complex Argument, Pergamon Press, New York (1961).

13. M. Abramowitz and I.E. Stegun, Handbook of Mathematical Functions, Dover Pub., New York (1970).

14. S. G. Rautian and I. I. Sobel'man, “The effects of collisions on the Doppler broadening of spectral lines,” *Soviet Physics Uspekhi* 9 (5), 702-714 (1967).

15. I. I. Sobel'man, L. A. Vainshtein, and E. A. Yukov, Excitation of Atoms and Broadening of Spectral Lines, Second ed. , Springer-Verlag, New York, (1995).

16. R.H. Dicke, “The Effect of Collisions upon the Doppler Width of Spectral Lines,” *Phys. Rev.*, 89, 472 (1953).

17. T. C. Jonathan Liu, J. B. Jeffries, and R. K. Hanson , “Large-Modulation-Depth 2f Spectroscopy with Diode Lasers for Rapid Temperature and Species Measurements in Gases with Blended and Broadened Spectra,” *Appl. Opt.*, 43, 6500 (2004).

CHAPTER 3

OXYGEN A- BAND TRANSITIONS AND EXPERIMENTAL RESULTS

Theoretical formulation of WMS signals in the previous chapter laid the foundation for experimental investigations and analysis of WMS signals. In this chapter we present experimental results of WMS signals that were obtained by probing absorption transitions of the spectrum of atmospheric oxygen [1-7].

It is known that the transitions in molecular oxygen [1-7] are electric dipole forbidden - magnetic dipole driven, that are orders of magnitude smaller than allowed transitions. Higher order WMS signals reveal features that are otherwise subdued in direct absorption or at lower detection e.g. $N \leq 2$. Some of the features discussed in this chapter are: relative growth of weaker transitions in spectra of disparate overlapping lines, optical pathlength saturation and sensitivity of lineshape (or gas) parameters in far wings of the absorption lineshape profile. We show that two transitions with disparate line strengths can be fully resolved only at certain detection order and an appropriate choice of experimental variables. Therefore, under certain experimental conditions, the measurements are considered optimal for precise estimation of lineshape parameters and investigations of subtle features of the absorption lineshape profile.

3.1 STRUCTURE OF OXYGEN A-BAND

The oxygen A-band is one of the four associated bands of molecular oxygen in the visible and near infrared region of the spectrum [1-6]. These bands are denoted by A, B, γ, and δ, correspond to vibrational transitions $A \Rightarrow (0 \leftarrow 0), B \Rightarrow (1 \leftarrow 0), \gamma \Rightarrow (2 \leftarrow 0)$, and

$\delta \Rightarrow (3 \leftarrow 0)$, where the notation is $(v' \leftarrow v'')$, and where v' and v'' are the vibrational levels in upper and lower electron states, respectively. These are formed by a collection of transitions between the triplet ground electronic state, ${}^3\Sigma_g^-$, and the singlet excited electronic state, ${}^1\Sigma_g^+$, i.e., $b^1\Sigma_g^+ \leftarrow X^3\Sigma_g^-$ and the ground state configuration:

$$(\sigma_g 2s)^2 (\sigma_u 2s)^2 (\sigma_g 2p)^2 (\pi_u 2p)^4 (\pi_g 2p)^2 .$$

The two π electrons in the open shell lead to three possible electronic states; ${}^3\Sigma_g^-$, ${}^1\Sigma_g^+$, ${}^1\Delta_g$. By Hund's rule, ${}^3\Sigma_g^-$ has the lowest energy and is therefore the ground state.

3.1.1 Vibrational and Rotational Energy Levels

The potential energy curves for molecular oxygen are shown below in Fig. 3.1. These curves depict the bonding energy of the oxygen atoms as a function of the internuclear separation. The minimum potential energy is seen in the Figure below to occur in the ${}^3\Sigma_g^-$ state at an internuclear separation of approximately 1.1x10^{-8} cm. According to Heisenberg uncertainty principle, though, the internuclear separation can only be defined within a certain range given by the constraint, $\Delta x \Delta p \geq \hbar$. Consequently, the atoms of the molecule must move with a particular velocity, determined in part by their thermal energy, and therefore, the minimum energy must be specified as a quantized level within the potential energy curve.

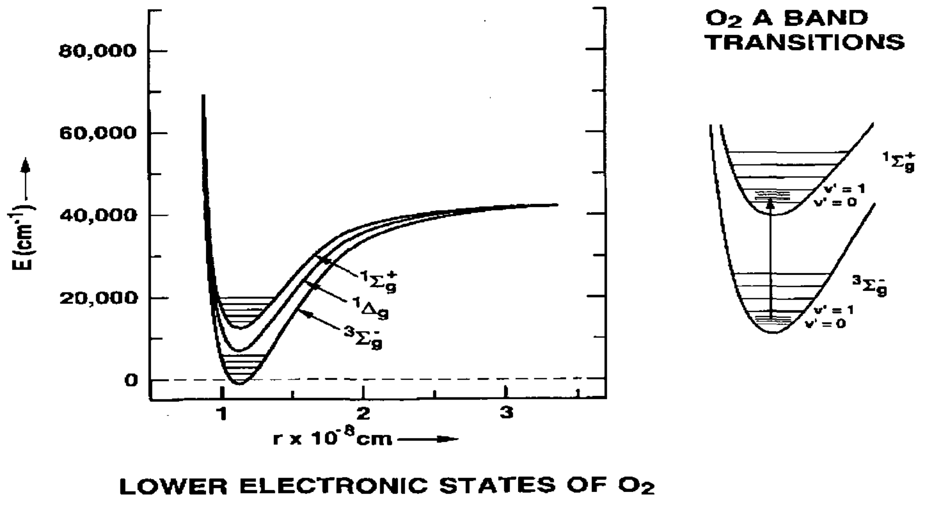

Fig. 3.1. Energy levels of molecular Oxygen A- band. Note that the transitions are from two vibrational levels.

The vibrations of diatomic molecules can be modeled by a mass-spring system, with a spring constant that is derived from the molecular interaction potential. The molecular vibrations take on allowed energy levels within the parabolic portion of the potential well, which to a first approximation can be described by the quantum-mechanical harmonic oscillator, $E_V = \left(v + \frac{1}{2}\right)\hbar\omega$. Here v is the vibrational quantum number and the vibration frequency is $\omega = (\kappa / \mu)^{1/2}$, where $\mu = m_1 m_2 / (m_1 + m_2)$ is the reduced mass and κ is the spring constant. These evenly spaced energy levels are the simplest model of molecular vibrations and only hold for the lower vibrational levels in an electronic state. The energy levels in a physical system deviate from this harmonic oscillator slightly, in that the larger the vibrational quantum the more anharmonic the oscillations. For the anharmonic oscillator the spacing between the levels decreases with increasing vibrational quanta, until the vibrational energy is such that the molecule dissociates. Since the oxygen A-band is formed by transitions between the lowest vibrational levels of the two electronic states, namely $(0 \leftarrow 0) b^1\Sigma_g^+ \leftarrow X^3\Sigma_g^-$, the simple harmonic oscillator model provides a very good approximation for our calculations.

For the lower vibrational energy levels of a diatomic molecule, the distance over which the molecule vibrates is small compared to the equilibrium separation. Hence, to a first approximation the system can also be considered rigid where the radial motion can be decoupled from the angular motion. The quantized rotational levels are described as $E_R = K\left(K+\frac{1}{2}\right)\frac{\hbar^2}{2I} \equiv B_e K\left(K+\frac{1}{2}\right)$. Here, $I = \mu r_o^2$ is the moment of inertia, k is the rotational quantum number, and B_e is called the rotational constant. It is seen that the spacing of the rotational energy levels increases with rotational quanta, which is dependent on the value of the rotational constant. It turns out though, that this approximation is too crude for the calculations of the A-band. The non-rigid rotator must be considered. The energy of a rotating diatomic molecule is mostly kinetic with a small amount of potential energy due to centrifugal force. As the rotational quantum increases, the potential energy gets larger and the molecule behaves less and less like a rigid rotator. In this case the rotational energy levels are better described by the following above expression *of vibrational energy* $E_R = K\left(K+\frac{1}{2}\right)\frac{\hbar^2}{2I} - K^2\left(K+\frac{1}{2}\right)^2\frac{\hbar^4}{2I^2}$ or

$E_R = K\left(K+\frac{1}{2}\right)B_e + K^2\left(K+\frac{1}{2}\right)^2 D_e$, where $B_e = \frac{\hbar^2}{2I}$ and $D_e = -\frac{\hbar^4}{2I^2}$

The values of these parameters, called the rotational constants, determine the spacing of the rotational levels within the vibrational rung. Combining the contributions of all three energies, electronic, vibrational, and rotational gives:

$$E_T(n,v,k) = E_{El} + E_V + E_R = E_{El} + \left(v+\frac{1}{2}\right)\hbar\sqrt{\frac{\kappa}{\mu}} + B_e K\left(K+\frac{1}{2}\right) + D_e K^2\left(K+\frac{1}{2}\right)^2$$

3.1.1 Selection Rules and Line Notation

Detailed analyses of the A-Band were first made by Mulliken and Van Vleck [1-4]. The two electronic states are approximately 1.62 eV apart, making the A-band, which involves the two lowest vibrational rungs, centered near 762 nm. The rotational levels of the oxygen states are designated by the quantum numbers *J* and *N*, where *N* represents the rotational angular momentum, and, *J* the total angular momentum, which is the sum of the rotational and spin angular momenta. The ground state, which has total electron spin of unity, is split into levels corresponding to *J" = N", N"+1, N"-1*, with only odd values of *N"* allowed (double prime and single primes denote lower and upper states respectively). The upper electronic level, which has zero spin, is composed of singlet states with *J'=N'*, where only even values of *N'* are allowed.

Symmetry conditions and selection rules allow only four types of infrared transitions which may be expressed as:

$\Delta N.\ \Delta J(N",J")$, where $\Delta N.\ \Delta J$ = *PP, PQ, RQ,* and *RR*. The *PP(N", J"=N")* and *PQ(N",J"=N"-1)* lines are separated by about 2 cm^{-1}., forming pairs that make up the *P* branch. The *P* branch starts near 13120 cm^{-1} and extends downward in frequency, the spacing between pairs ranging from 6 cm^{-1} between the first two pairs to 10cm^{-1} at *J" =20*. The transitions *RR(N",J"=N")* and *RQ(N",J"=N"+1)* also form 2-cm^{-1} pairs that make up the R branch in the range 13125 (761.905nm) -131170 cm^{-1} (759.301 nm) . The separation between the pairs in the R branch is only about 4.5 cm^{-1} (135 GHz) between the first two pairs and decreases toward higher *J*"; at *J*"=13, the separation between the lines adjacent pairs is less than 2 cm^{-1} (60 GHz), so that the pairs merge, forming a bandhead at about 13165 cm^{-1}.

The transitions involving changes in rotation, vibration, and electronic states are also called *rovibronic* transitions. Due to the differences in symmetry and degeneracy of these two states, the transitions are electric-dipole forbidden and electron spin forbidden, making the bands extremely weak. The transitions are driven by a magnetic dipole coupling of electromagnetic radiation with the electrons in the molecule. Typically, magnetic dipole transitions are approximately four orders of magnitude weaker than the usual allowed transitions; however, these transitions are nearly eight orders of magnitude weaker because in addition to the magnetic coupling, the electron must change its spin during the transition.

These calculations are generally carried out under the Born-Oppenheimer approximation. In this approximation it is assumed that electronic motion occurs on a short time scale compared to the nuclear motion, enabling the molecular wave function to be separated into the product of the wave functions for the individual components. Hence, by treating each component of the rovibronic transitions independently and then summing the individual energies, one can calculate a molecular absorption band. The following section gives an example of this calculation for the oxygen A-band.

The vibration transitions between the two electronic states do not strictly adhere to the same selection rules as they do with in an electronic level. Hence, the change in v can take any value: $\Delta v = 0, \pm 1, \pm 2 \ldots$, however, all values are not equally probable due to the Franck-Condon principle [7]. The A-band is associated with the $\Delta v = 0$ transition.

Selection rules for angular momentum are as follows: the total angular momentum, $J = K + S$, where K is the quantum number for the angular momentum of the revolving nuclei and S is the quantum number for the electronic spin, can change by, $\Delta J = 0, \pm 1$, designated P for -1, Q for 0, and R for +1.

The rotational angular momentum, K, can only change by $\Delta K = \pm 1$, designated P for -1 and R for +1. This leads to two branches in the A-band that begin at $E_{el} + E_V$. The R-branch transitions are higher in energy, while P-branch transitions are of smaller energy. The values of the rotational constants determine the spacing of the rotational levels within the vibrational rung. Herzberg [7] gives the following values for the $v = 0$ levels of the ground and excited states of O_2:

$^3\Sigma_g^-$: $B_e = 1.44\,\mathrm{cm}^{-1}$ and $^1\Sigma_g^+$: $B_e = 1.40\,\mathrm{cm}^{-1}$

$^3\Sigma_g^-$ and $^1\Sigma_g^+$: $D_e = 4.95x10^{-6}\,\mathrm{cm}^{-1}$

The difference in the values of B_e for the two states indicates that the separation of the rotational levels of the ground state are greater than those of the excited state. Consequently, the transitions with $\Delta K = +1$ will increase in energy initially, but reach a maximum energy at some rotational quantum number K''_H, where the branch begins to fold back on itself. This is what is known as the band head (Fig. 3.2) and for the oxygen A-band occurs at approximately 759.57 nm (13165.258 cm^{-1}) in the R-branch.

The spin angular momentum for the ground state is $S = 1$, hence the ground state is triply degenerate, where the degeneracy is given by $(2S+1)$. This results in the following possible values for the total angular momentum:

$$\text{Ground state: } {}^3\Sigma_g^- \quad J'' = \begin{cases} K''+1 \\ K'' \\ K''-1 \end{cases} .$$

The upper state has no degeneracy, since $S = 0$, and J' can take the following values:

Excited state: $^1\Sigma_g^+$ $\quad J' = K'$.

The rotational levels $J'' = K''+1$ and $J'' = K''-1$ are nearly indistinguishable due to the symmetry of the molecule, hence the A-band appears to be composed of doublet line pairs instead of triplet line clusters. Furthermore, due to the individual symmetries of the states, only odd values of K are allowed in the ground state and only even K in the upper state.

The transitions of the band are labeled with the following notation, where prime indicates the upper state and double primes indicate the lower state:

$$\Delta K \cdot \Delta J(K'', J'') \qquad \Delta K = \begin{cases} -1 & P \\ +1 & R \end{cases} \qquad \Delta J = \begin{cases} -1 & P \\ 0 & Q \\ +1 & R \end{cases}$$

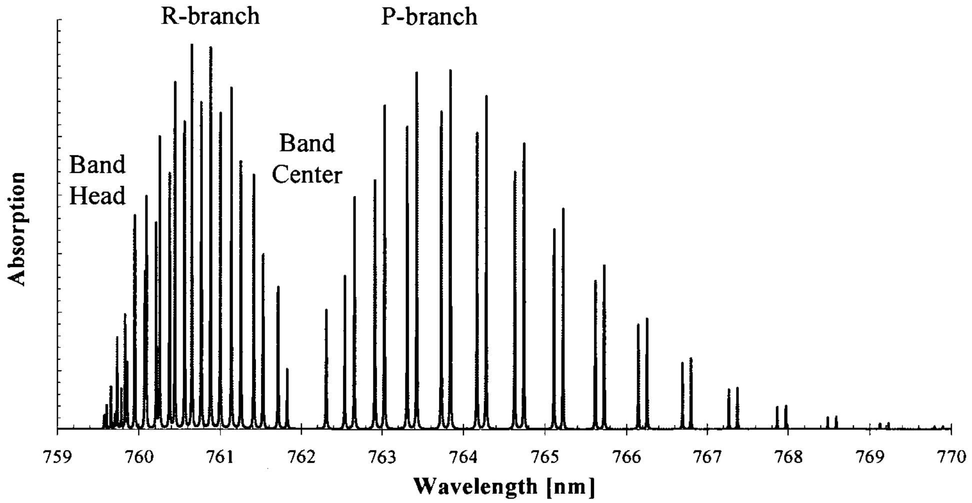

Fig. 3.2. Oxygen A- band structure. The experimental work was carried out in wavelength range of 760.30 – 760.42 nm

3.2 WEAK OVERLAPPING OXYGEN TRANSITIONS

The apparatus used to perform wavelength modulation spectroscopy experiments is shown in Fig. 3.3 below. The key components of the experimental setup are a tunable single mode diode laser, temperature controller, current controller with ramp, external oscillator, photodiode detector, and a lock-in amplifier. There are several advantages of the apparatus used in this research. First, it is compact and the device can be fabricated as a single unit with a manual or automatic control system or, the individual components can be connected and controlled by a computer. The lasers we used for experimentation primarily include Fabry-Perot type, VCSELs, and an external-cavity laser all centered around 762nm for oxygen a-band measurements which was tuned and modulated by varying the cavity length. This method of tuning allows for large continuous tuning ranges and pure wavelength modulation. Most common edge emitting diode lasers are tunable with temperature and injection current for over at least several hundred wavenumbers, which is sufficient to measure a large number of lines in the A-band.

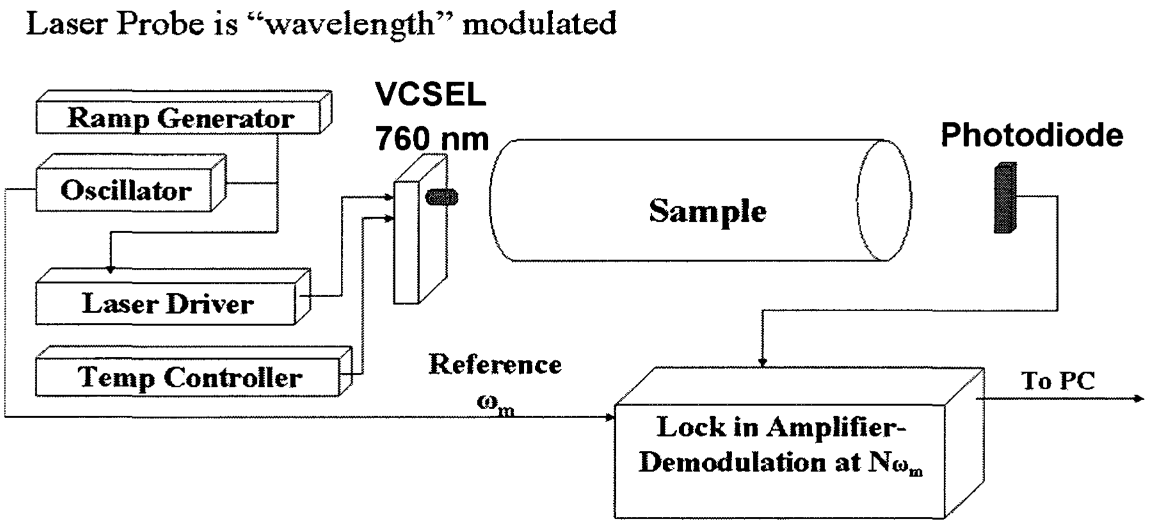

Fig. 3.3. Block diagram of the experimental apparatus. Wavelength of a modulated laser is swept across the absorption region of interest of Oxygen A-band. The signal from a photodetector is processed by a (narrow band) lock-in amplifier and demodulated at the integral frequencies of the reference oscillator.

In measuring the weak lines of the oxygen A-band, for example those with absorption cross sections on the order of 10^{-24} and 10^{-27} cm^2 cm^{-1} mol^{-1}. To increase the sensitivity and the magnitude of the signal for probing weaker transitions, we found that it is beneficial to lengthen the absorption path by beam folding with a multipass cell. With the 10cm spherically concave mirrors that were used, we were able to achieve as many as 135 passes at about 1.36 meters, giving a total path length of approximately 210m.

A qualitative way to look at wavelength modulation spectroscopy (WMS) is to recognize that this method leads to derivative like signals that contain detailed structure associated with the turning points or variations in the absorption lineshape signal. The locations of these turning points with respect to the linecenter carry information about the linewidths and the lineshape profile. The relative magnitudes of the turning points give information about the absorption cross-section and any perturbations to the lineshape profile. In this section we discuss the experimental observations of variations or subtle physical effects of the absorption features that can be resolved using higher detection order. To illustrate this point we consider a probe region (of Oxygen A-band transitions) where four or five overlapping transitions that are fairly close to each other that are not discernible in direct ($N = 0$) measurements. We show that when lines of disparate strength overlap it can be advantageous to use higher harmonic detection to resolve the lines.

One example of such a result is shown in the figure below. Fig. 3.4 shows the signal obtained in a direct ($N = 0$) absorption scheme, where a tunable VCSEL is used to probe a particular region of the molecular oxygen A-band where there are several overlapping lines with greatly disparate absorption cross sections. It is clear that one cannot discern these lines [8].

However, it is seen from Fig. 3.5 that as one uses WMS one begins to see the individual lines. In particular, the higher the harmonic detection used in this case (we went up to the 8th, i.e.8 f detection) the better the resolution becomes. In this case the mechanism by which this relative growth of the weaker lines occurs is because of *distortion* due to optical pathlength saturation. It turns out that for the pathlengths used, the stronger lines saturate before the weaker lines and consequently the stronger lines result in signals that are broadened more than the weaker lines. Now, it is known that the magnitude of a signal obtained in WMS depends on the modulation index which is defined as the modulation amplitude divided by the width of the line ($m = \beta/\Delta\nu$). Since the effective widths of the stronger lines are larger because of the aforementioned saturation, the effective modulation index for a stronger line is smaller than that for a weaker line and consequently one obtains the result in Figs. 3.5 (a)-(h). The magnitude of a WMS signal scales as $\sim m^N$, where m is the effective modulation index and N is the detection harmonic. Hence the signals due to the weaker lines begin to grow with respect to the stronger ones as the harmonic detection order increases.

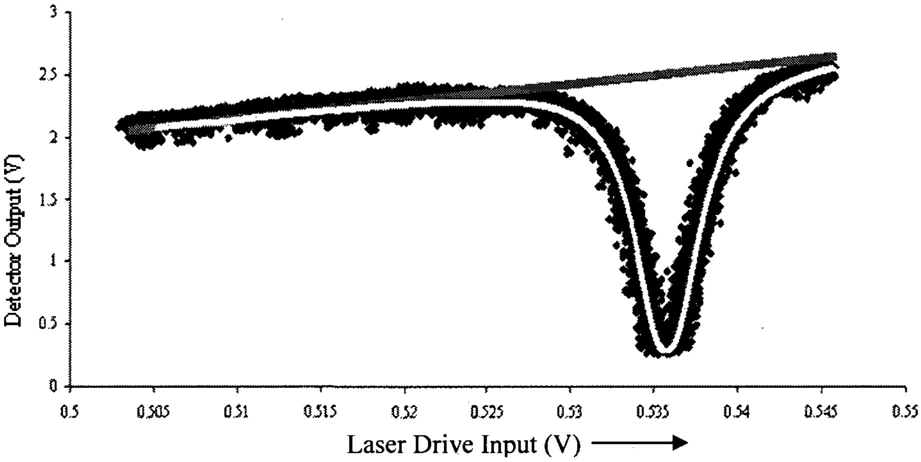

Fig. 3.4. Experimental Absorption signal of Oxygen A – Band transition. Strong absorption from RR (13,13) is shown in the figure. Weak overlapping lines are not visible. The laser wavelength is scanned from 760.30 – 760.40 nm. This range covers five oxygen transitions of disparate strength. The linear line is the input to the laser ramp voltage.

The following figures show WMS signals of the above "direct" absorption signal. The above experiments show the advantage of higher harmonic detection in resolution of overlapping lines. The experiments show four overlapping lines [8] which are not discernible at direct absorption and lower harmonics. These lines become apparent in higher order detection (Fig. 3.5). A peculiar feature of the optical pathlength saturation effect which is directly connected to relative growth of weaker transitions is also seen in Fig. 3.5(h) where center lobes, which are peak values, are relatively depressed. This is due to pathlength saturation [9, 10]. An extensive discussion of this effect is in the following sections.

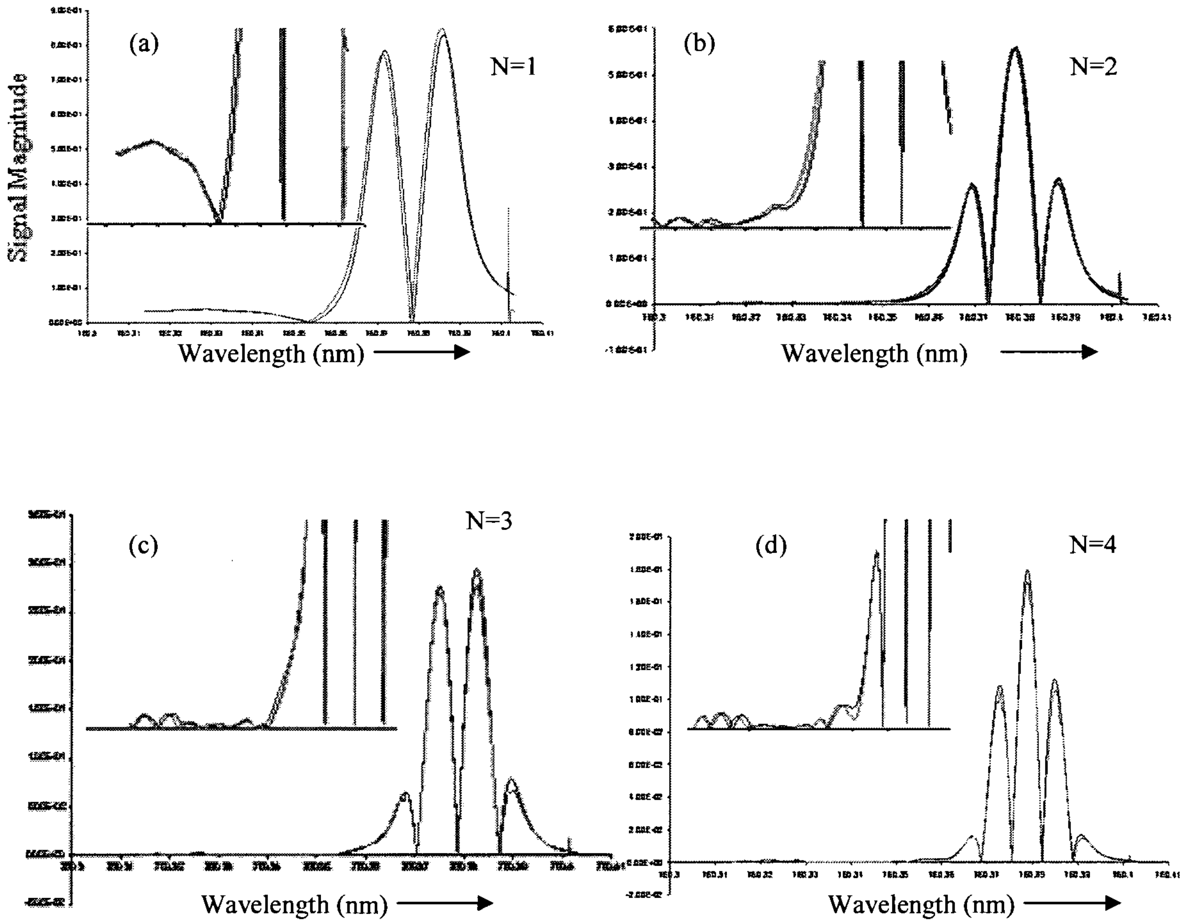

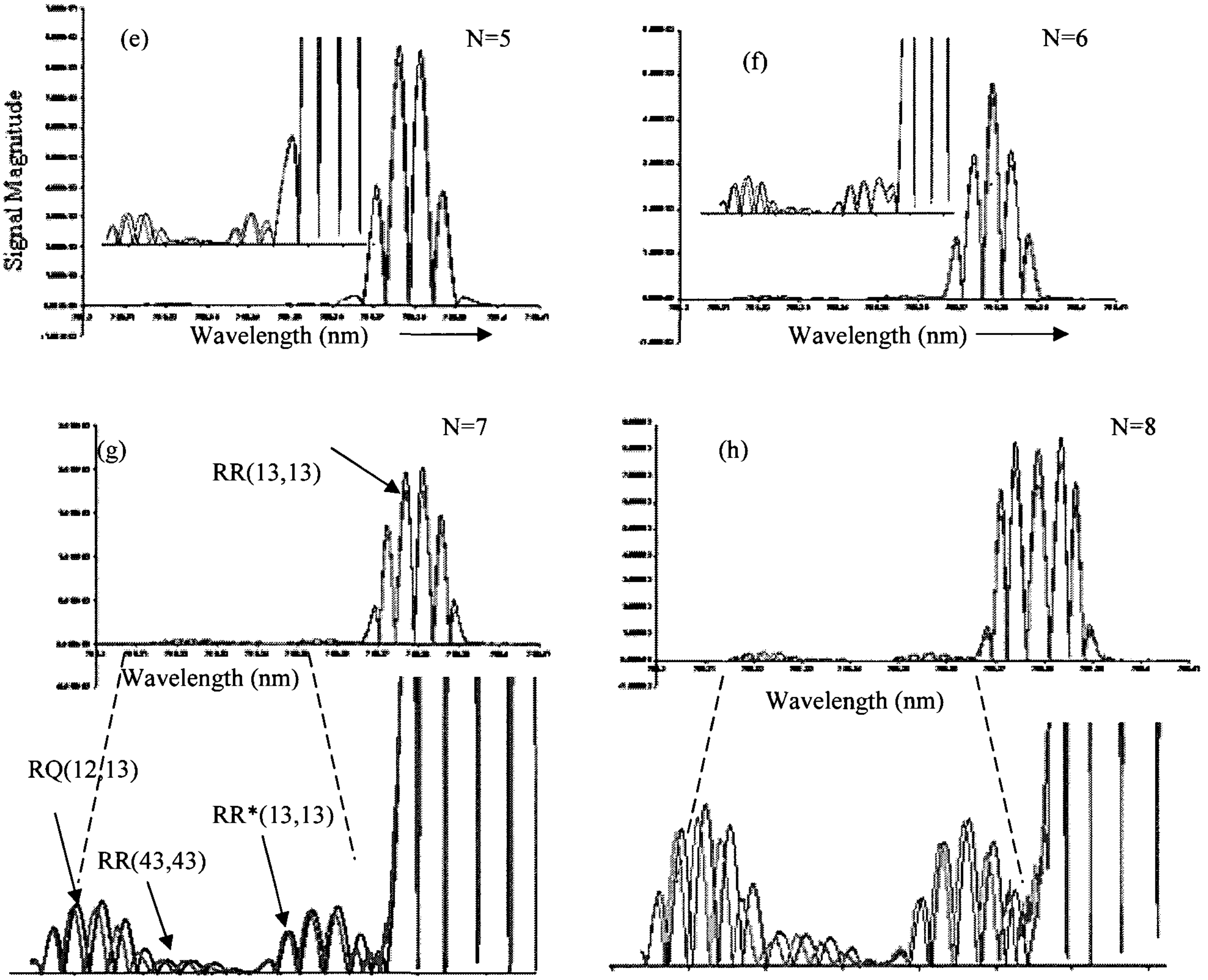

Fig. 3.5. Experimental plots and theoretical models of N = 1 to N= 8 detection order of oxygen RR(13,13), RR*(13, 13), RQ (12, 13) and RR(43, 43) transitions. The weaker line begins to appear at N= 2 but the lines are not fully resolved until at N=7 or 8. The experiment was performed at 180 meters of pathlength. The modulation index was, m=4.

A comparison between (see Fig. 3.6) the direct absorption signal and the 8th detection order, specifically focusing in the spectral region of the weaker transitions, shows the strength of the technique. This resolution critically depends on the experimental controls which are discussed in the following section.

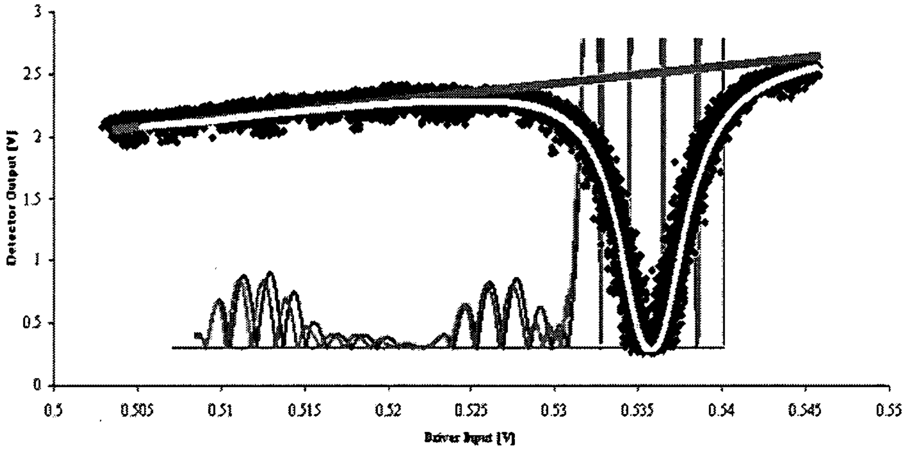

Fig. 3.6. Comparison between 'direct' absorption and weaker lines of Oxygen A – band those are resolved at higher detection order. The figure shows three overlapping transitions in vicinity of a strong absorption transition. In the scale above the strong absorption line is not shown completely.

3.2.1 Modulation index and line resolution

The experimental results presented in the previous section show an optimal detection order that resolves distinctive features of the absorption lineshape profile. This is important because ultimately for accurate modeling one needs to fully identify these features in the signal. A range of values of modulation voltage (or modulation amplitude β) were used to obtain the best resolution and practically useable Nth harmonic signal. Ideally, a very small modulation would be sufficient to resolve all the features of the lineshape profile. This in practical situations results in signals that are considerably smaller in magnitude at higher detection order (to overcome the impediment noise and distortion). On the other hand, although a large modulation index gives a strong signal, the signal tends to broaden and cause significant overlap with the neighboring transitions. It is seen that if the modulation index was increased up until m = 4, four overlapping transitions, were resolved Figs. 3.5(a)-(f). However, by employing smaller values of m (i.e. m=2) an additional weaker transition was resolved, see Fig. 3.7. The transition is referred to as RQ (11,12) (centered at 13150.7471 cm $^{-1}$ and line strength of 1.52 x 10^{-26} cm^2 molecule^{-1}cm^{-1} (according to the HITRAN data base [11])) on the long wavelength region of strong RR (13,13). Although the signal at higher detection orders was considerably small, RQ (11,12) was evident and partially resolved. This tradeoff between the choice of modulation index and resolution of lines comes at the cost of accuracy of estimation of lineshape parameters.

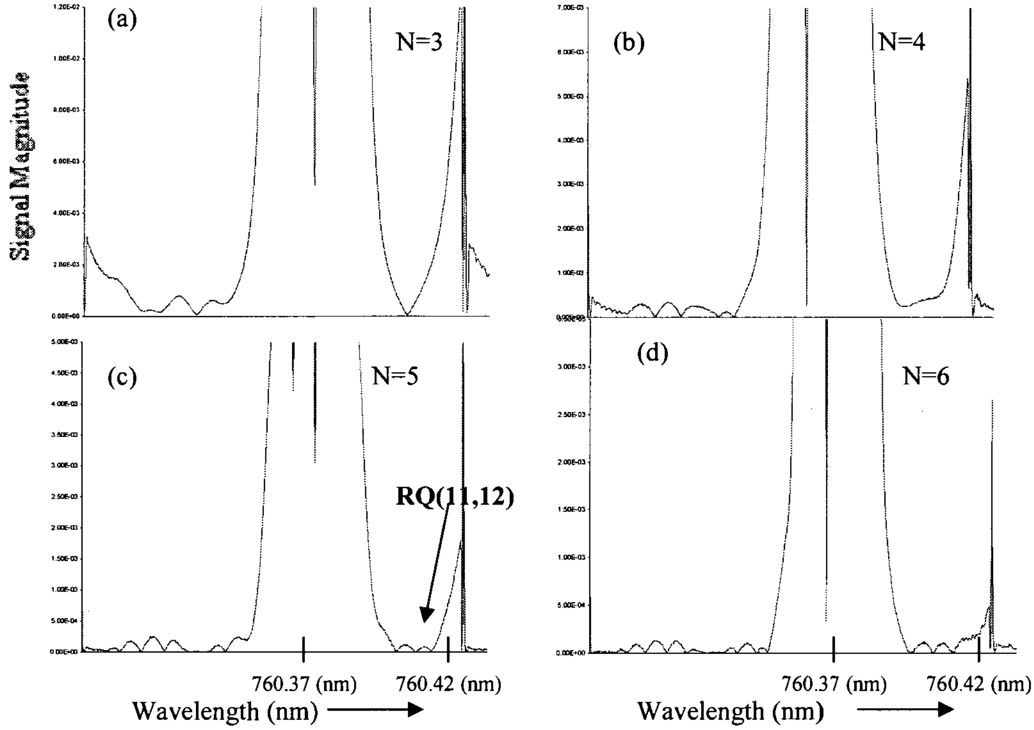

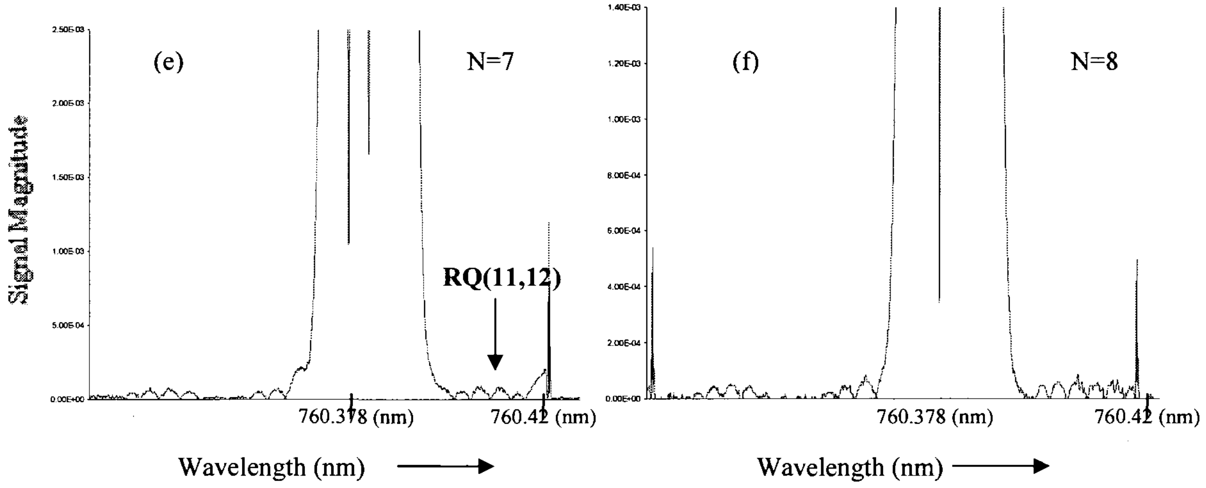

Fig. 3.7. Oxygen transitions with five line transitions in a wavelength scan. The set of experiments were performed under similar conditions except with lower modulation index. RQ(11,12) transition begin to appear at N = 6. The signal here is relatively weaker compared to the results discussed in the previous section. The modulation index was, m=2.

3.2.2 Mechanism of modulation index and probe of WMS signals

WMS probes the variation in the absorption signal; these variations could result from the inherent physical processes of the gas or distortion from the probe. Therefore, the absorption signal mainly depends on the lineshape function, lineshape and gas parameters e.g. linewidths, density, absorption cross-section etc. Detection at Nth harmonics can be regarded as Nth order (derivative) variation of the absorption signal. The frequency modulation index (*m*) determines the spectral range that the laser probes the profile at any point in the spectrum. For example, a smaller value of m ($= \beta/\Delta\nu$) indicates that at a fixed wavelength, the probe samples two points are close to each other. In other words, if for instance the probe laser is tuned to the linecenter of the absorption line and m<<1 (i.e. modulation amplitude is smaller than the linewidth, $\beta \ll \Delta\nu$), the WMS signal obtained resembles feature of the absorption signal within range of half-width around the linecenter. Whereas, if m is large (m>>1), the probe samples a much larger region of the spectrum and the contribution from the region in the wing of the absorption profile is significant. This is the basis of the magnitude and broadening of signals at higher index values. As an example, it will be shown that one can discern optical pathlength saturation effects only for a specific set of values of modulation index and at a particular detection order. This is because, strong absorption predominantly occurs "at" and "around" the line center, which leads to broadening around linecenter. The distortion due to this is extrememy small and only index (and higher N) that samples the absorption signal in that equivalent region (of saturation) exhibits this effect in WMS signals. To illustrate this point, consider, Δs to be the span of the spectral region of the absorption signal where broadening due to saturation occurs. It should be noted here that the so-called broadening is quite different to broadening of the signals due to large modulation depth, where m is large. In addition, the effects of broadening will significantly depend on the sensitivity of the photodetector.

The ratio of Δs to the linewidth (Δv) is a measure of the saturation index, i.e. $\Delta s/ \Delta v$. The effective modulation index required to discern saturation effect should be less than or equal to the saturation index. Hence, if $m \leq \Delta s/\Delta v$, these effects begin to appear as abrupt depression in the center lobes of even harmonic signals. If $m > \Delta s/ \Delta v$, then these effects are masked by the modulation broadening (as the probe samples a larger region of the absorption profile) of the signal and are not discernible.

With the same token one can also correlate resolution of overlapping lines and the modulation index. In this case if we consider the separation between two transitions to be $\Delta v_{0,}$, the lines will appear resolved only if $m \leq \Delta v_0/\Delta v$.

3.2.3 Experiments at large optical pathlengths

The figures below show experimental results of N = 4, 6 and 8th detection orders, Figs. 3.8, 3.9 and 3.10, obtained at varying modulation amplitudes. The experiment were performed at a fixed pathlength of 180 meters (or $\tau = 1.4$). It can be seen from the figures below that each harmonic shows distinct features of saturation and modulation broadening at various index values. At smaller values of m, a clear suppression of center lobes shows saturation whereas a similar suppression in linecenter magnitudes occurs at large m values due to modulation broadening. N = 4 detection does not show suppression in linecenter for any set of m values that were used in the experiment. In the same context, smaller values of m give a weak signal of N = 8, which is practically not useable for analysis. We found that N = 6 was the optimum detection order for most measurements, since it shows features of saturation and growth of overlapping lines for lagers set of values of m. In the figures below, four transitions are shown, the strong RR (13,13) transition and weak RR (13,13)* (isotopic transition of O^{18}), RR(43,43) and RQ (12,13). The line strength of strong RR (13,13) is of the order of 10^{-24} (HITRAN units) where as RR (13,13)* , RR(43,43) and RQ(12,13) have line strength of 10^{-26}, 10^{-28} and 10^{-26} (all in HITRAN units) respectively. These weaker transitions are labeled as L1 (RR(13,13)*), L2 (RR(43,43)) and L3 (RQ (12,13)) in figures below. Fig. 3.8 is the 4th harmonic signal of the absorption features of four lines. Figs. 3.9 and 3.10 are 6th and 8th order signals of same absorption scan. The experimental control parameters were kept same in all the set of experiments in Fig. 3.8, 3.9 and 3.10 below.

N=4 detection order at various modulation indices

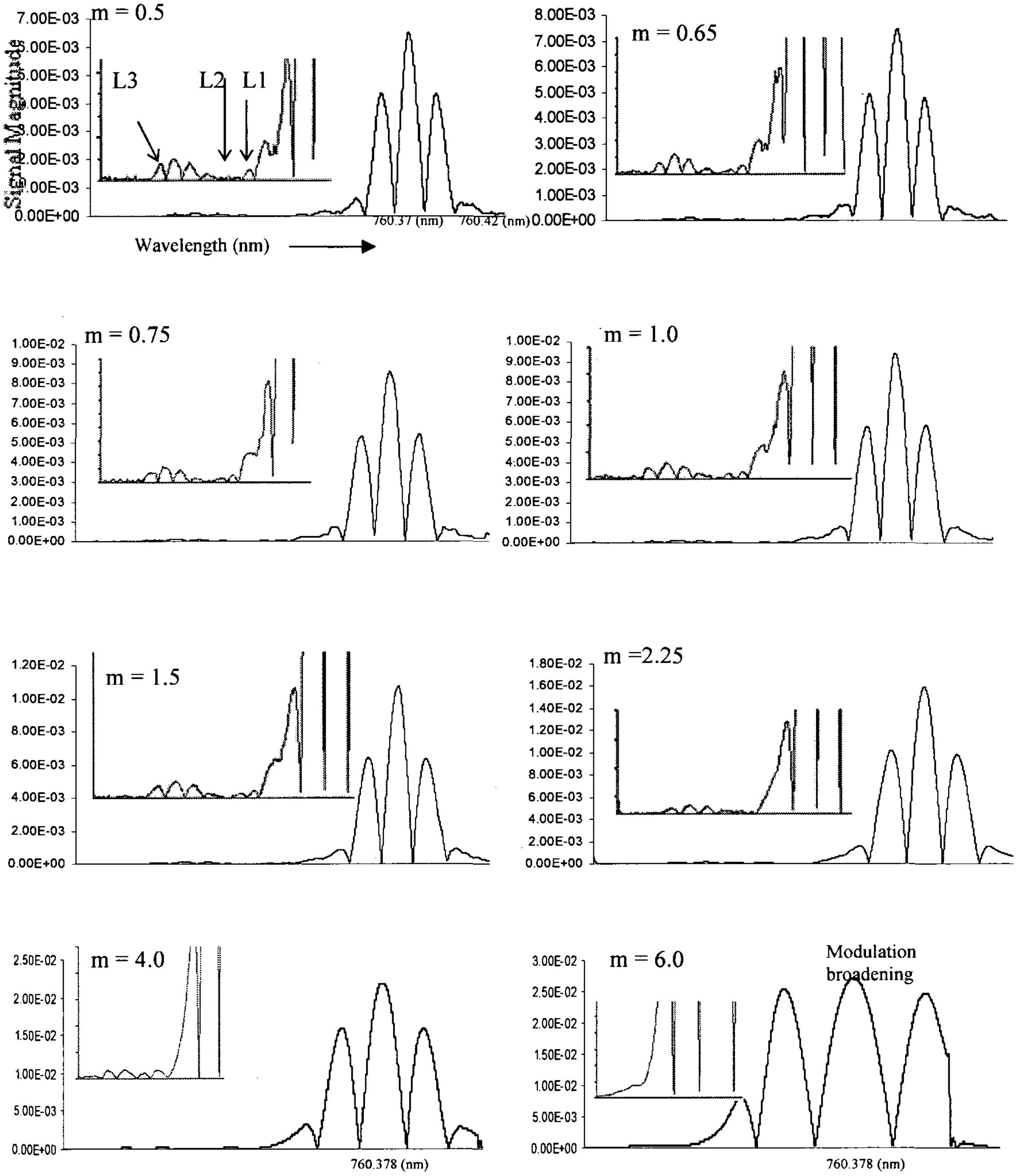

Fig. 3.8. Experimental results of 4th order RR(13,13) and three overlapping weak line transitions (L1, L2 and L3). The experiments were performed at pathlengths of 210 meters and modulation index was varied from m = 0.5 to m = 6.0. At m=0.5 weak RR(13,13)* transition (L1) begin to appear and RQ(12,13) transition (L2) is discernible completely. The weakest RR(43,43) transition (L3) is not discernible at any m values. This is because either its signal is extremely weak or it is masked by the neighboring lines. Large values of m begin to cause significant overlap of weaker transitions from stronger transition.

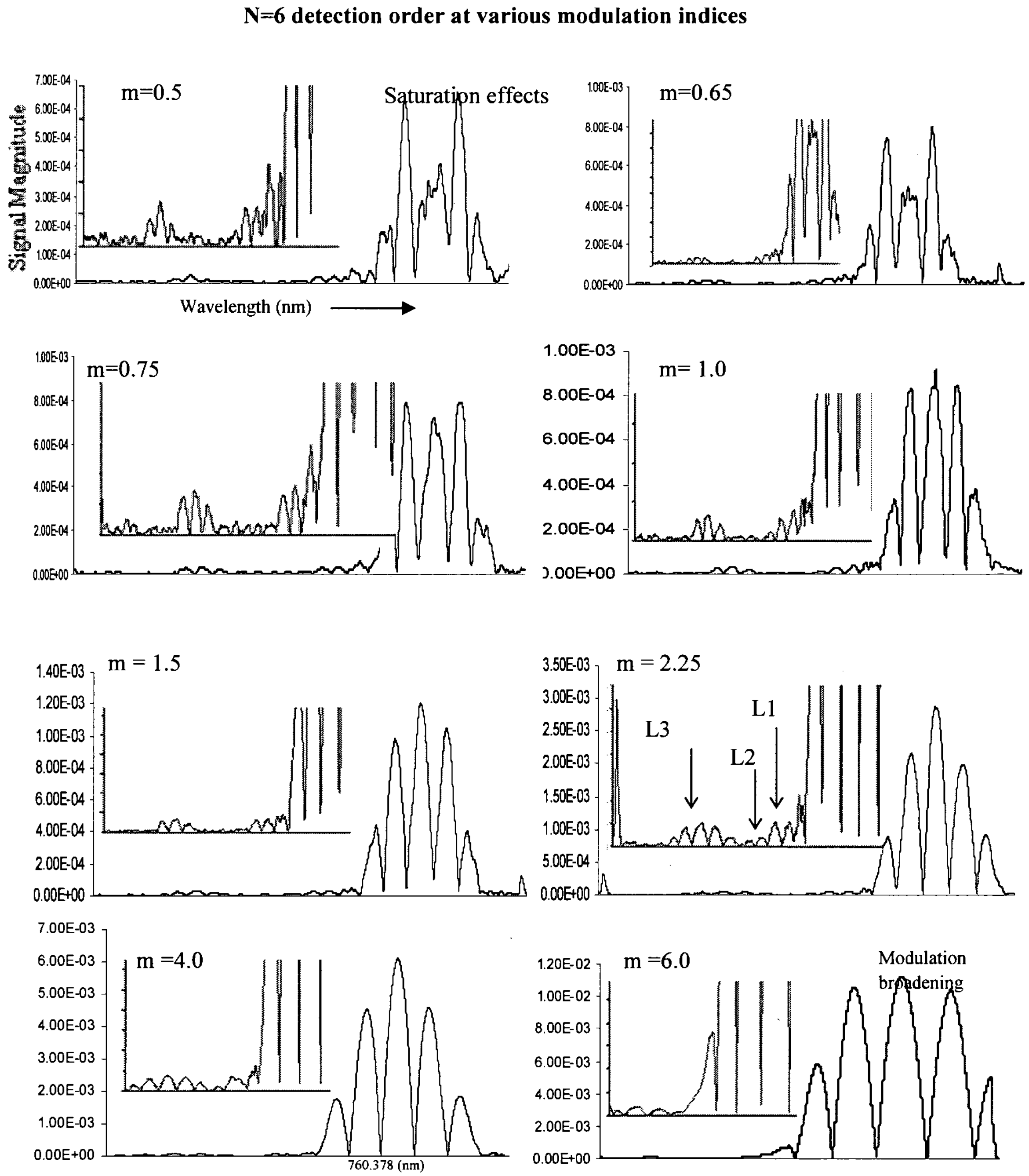

Fig. 3.9. Experimental 6th order RR(13,13) and three overlapping line transitions (L1, L2 and L3) at different modulation index. Small m values (. m = 0.5 to m=1) show clear signs of saturation. However, at those index values the weak lines are not strong in signal. The index value of m = 2.25 seems to be optimum for resolution of overlapping lines, but does not show visible effects of saturation.

N=8 detection order at various modulation indices

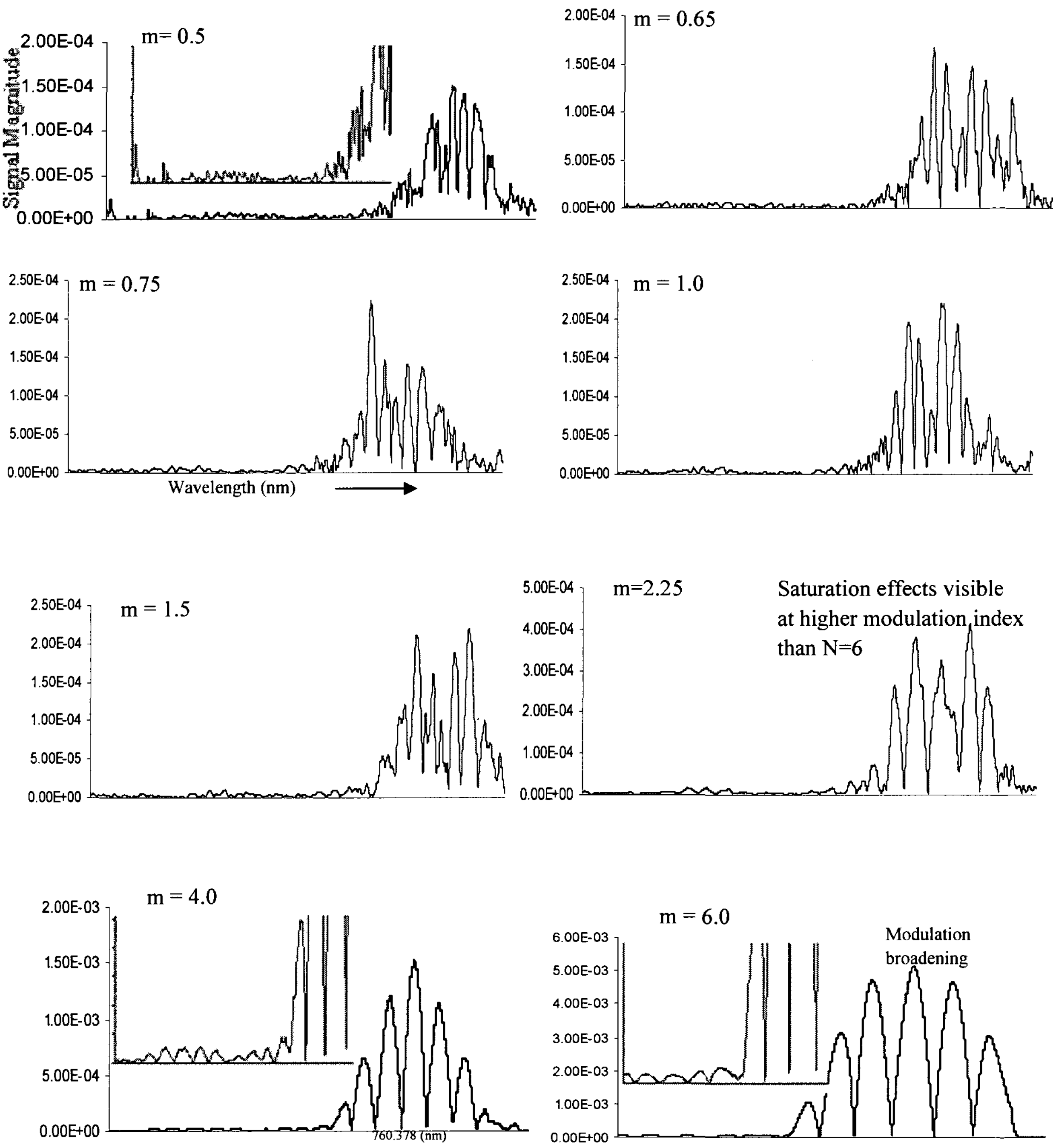

Fig. 3.10. Experimental results of 8th order RR (13,13) and three overlapping line transitions (L1, L2 and L3) . The signals at small index value are weak and not useable for estimation of parameters. Although at those values the signal show signs of depression of center lobe. This effect is sustained for relatively longer range of index values. The weaker lines begin to grow with m, where m = 4 resolves two of the three transitions.

3.3 OPTICAL PATHLENGTH SATURATION

In the above section, we have demonstrated the experimental results of measurement at large pathlengths. In this section we discuss these results [9, 10] of absorption features of the oxygen A- band transitions in the optically thick regime when synchronous detection at higher harmonics ($N \geq 2$), using wavelength modulation spectroscopy (WMS), is performed. We have shown that the absorption saturation effects demonstrate a distinctive feature which results in suppression of the linecenter lobes of the harmonic signals. These effects depend on the optical pathlength as well as on the modulation index.

Detection at higher harmonics reveals effects that are subdued in direct absorption measurements or in lower order detection. One such effect is absorption saturation, resulting from large optical depth or strong absorption of the incident light. This effect can play an important role in measurements of absorption in planetary (including that of the earth) and stellar atmospheres [12]. An absorption signal propagating over long distances exhibits characteristic effects that result from the fact that, because lineshape profiles vary rapidly with wavelength, each successive small (infinitesimal) absorbing path reacts to an incoming optical beam whose spectral profile is highly dependent on the cumulative path that beam has traversed prior to reaching this infinitesimal section.

Pathlength saturation in any absorption experiment is the effect that appears because of non-uniform absorption across the transition lineshape frequency profile, with increasing penetration into the medium being probed, Fig. 3.11. Effectively, any element of the medium sees an input probe whose profile is different from that seen by a preceding section because of the stronger absorption at, and around, the line center. The result is that the probe signal detected appears broadened.

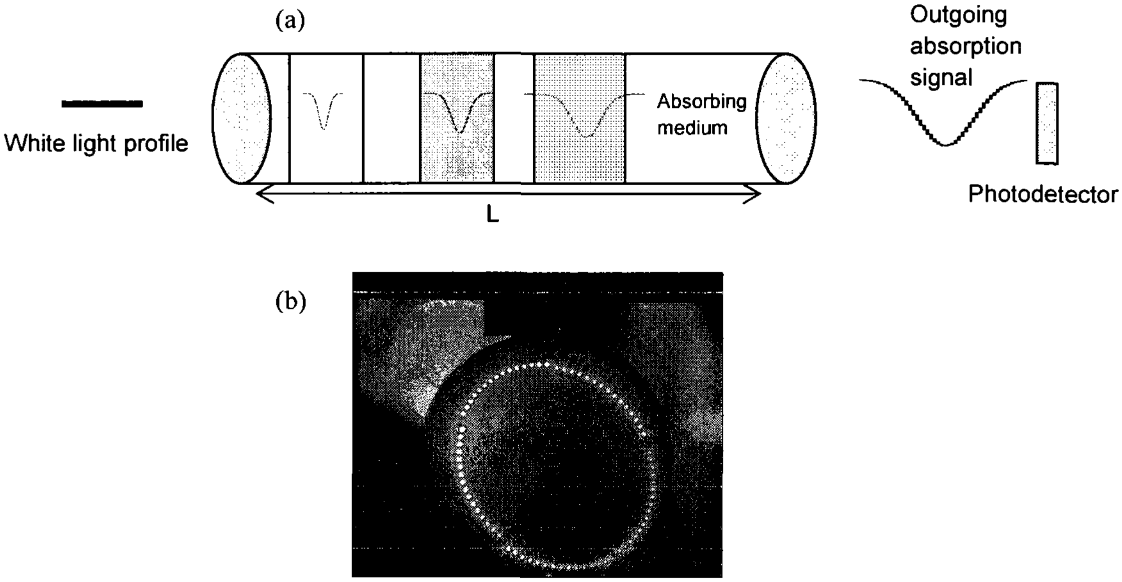

Fig. 3.11. Schematic of saturation phenomena in an absorption experiment. An incident white light gets broadened as it traverses within the absorbing media. As a result, the outgoing beam at the detector appears broadened. Fig. (b) shows the spot pattern on one of the mirrors of the multipass cell.

The basic equation of absorption (or emission) by a two level atom or molecule is;

$$dI/dz = \frac{A_{21}\lambda^2}{8\pi^2}\{n_2 - (g_2/g_1)n_1\}g(\nu)I \equiv I\gamma(\nu) \tag{3-1}$$

Here, $\gamma(\nu)$ is the gain co-efficient (m^{-1}), A_{21} is Einstein's spontaneous emission coefficient, n_2 and n_1 are the population densities in levels 1 and 2 with degeneracy factors of g_1 and g_2 and $g(\nu)$ is the lineshape profile.

In an absorption experiment, such as the one under consideration $n_2 << (g_2/g_1)n_1$ and one obtains the usual equation describing the attenuation of intensity in an infinitesimal pathlength dz, i.e.

$$dI/dz = -n\bar{\sigma}g(\nu)I \tag{3-2}$$

Hence, the absorption signal of a sample of length L, normalized with respect to the initial intensity of the probe I_0, is

$$\frac{\Delta I}{I_0} = 1 - \exp\{-n\bar{\sigma}Lg(\nu)\} \tag{3-4}$$

Where, $n=(g_2/g_1)n_1$ and $\bar{\sigma} = \int_0^{\infty}\sigma(\nu)d\nu$ is the integrated absorption cross-section. Then, it follows from Eqn. (3-4) that the signal at the linecenter, $\nu = \nu_0$ is

$$\frac{\Delta I(\nu_0)}{I_0} = 1 - \exp\{-n\bar{\sigma}Lg(\nu_0)\} = 1 - \exp(-\tau) \tag{3-5}$$

Here, $g(\nu_0)$ is the magnitude at linecenter of the lineshape profile and the dimensionless saturation parameter, $\tau = n\bar{\sigma}Lg(\nu_0)$ is a measure of optical depth: a small value of τ signifies little or no saturation.

In this work we assume the Voigt lineshape profile, which can be written as:

$$g_{\text{v}}(x) = \frac{1}{\pi^{3/2}}\frac{1}{\delta\nu_{coll}}\int_{-\infty}^{+\infty}\frac{dye^{-y^2}}{(x+y/b)^2+1} \tag{3-6}$$

Let the frequency in normalized difference between ν and ν_0 be given by, $x_{\text{v}} = (\nu-\nu_0)/2\delta\nu_{coll}$. Let b be the ratio of collision and Doppler linewidths given by, $2\delta\nu_{coll}/\overline{\Delta\nu_D}$ $(\overline{\Delta\nu_D}=\Delta\nu_D/\sqrt{4\ln 2})$, then g_{v} $(x_{\text{v}} = 0)$ = $be^{b2}erfc(b)$ $(\pi)^{1/2}$ $\delta\nu_{coll}$ and saturation parameter τ is $\tau = n\bar{\sigma}Lg_{\text{v}}(x_{\text{v}} = 0)$. The linecenter magnitude, $g_{\text{v}}(x_{\text{v}}= 0)$ depends strongly on the ratio of the linewidths for collision and Doppler broadening i.e. on the parameter 'b'. When the collision broadening dominates $\delta\nu_{coll}$ is much greater than the Doppler width $\Delta\nu_D$ (b>>1) and $g_{\text{v}}(x_{\text{v}} = 0) \approx 1/\ \pi\delta\nu_{coll}$. On the other hand in the Doppler broadened region, (b<<1), $g_{\text{v}}(x_{\text{v}} = 0) \approx 1/\sqrt{\pi\Delta\nu_D}$. The saturation parameter in these two cases will be

$\tau_{coll} = \bar{n}\sigma L/\pi\delta\nu_{coll}$ and $\tau_{Dop} = \bar{n}\sigma L/\sqrt{\pi}\Delta\nu_D$ respectively. A detailed theoretical description of the lineshape profiles and their effects on saturation is discussed in the reference [9].

A probe, modulated at modulation frequency, ω_m with modulation amplitude (β – in Hz), can be expressed as, $I\,(\nu + \beta\cos[\omega_m t])$. In the experimental procedure whose results are described below the modulated beam is swept slowly across the absorption feature. The effective normalized absorption signal recorded by the detector is therefore:

$$\frac{\Delta I(\nu+\beta\cos\theta)}{I_0} = 1 - \exp\left\{-K\int_{-\infty}^{+\infty}\frac{dy e^{-y^2}}{(x_\nu + m\cos\theta + y/b)^2 + 1^2}\right\} \qquad (3\text{-}7)$$

Here, $K = \bar{n}\sigma L/\pi^{3/2}\delta\nu_{coll}$, $\theta = \omega_m t$ is the angular modulation frequency, and $m = \beta/2\delta\nu_{coll}$ is the modulation index normalized to the collision linewidth.

Expanding the above signal in terms of Fourier series to express Nth harmonic signal [9, 13] one obtains,

$$S_N = \frac{I_0}{\pi}\int_{-\pi}^{\pi}\Delta I(\nu+\beta\cos\theta)\cos N\theta d\theta \qquad (3\text{-}8)$$

In all the previous literature in wavelength modulation spectroscopy measurements [13], the absorption signal was weak due to small optical pathlengths ($\tau \ll 1$). Therefore, Beer- Lambert law ($\Delta I/I_0 \approx -\bar{n}\sigma L g(\nu)$) was applicable in the analysis. However, in the current work large pathlengths were used (i.e. $\tau \geq 1$). Hence, we use the exact expression of absorption signal on the photodetector given by Eqns. (3-6), (3-7) and (3-8) to model the experimental results.

3.3.1 Experimental Results

Experimental measurements of the oxygen A-band (the rotational lines in the $0 \leftarrow 0$ vibrational rung of the $b^1\Sigma_g^+ \leftarrow X^3\Sigma_g^-$ low lying electronic transition) were made using an experimental set up whose main components have been described in the beginning of this chapter. Briefly, it consists of a tunable diode laser (VCSEL 760 nm) which is tuned to near an absorption line by controlling its temperature and the injected DC current. A modulation current is introduced along with a very slow (compared to the inverse of the modulation frequency) current ramp which sweeps the probe wavelength across the absorption feature. Detection is performed using a photodiode, whose signal is processed by a lock-in amplifier in which synchronous demodulation is performed at the modulation frequency, f, and its harmonics, Nf. The measurements were made in a multipass open-air cell, based on the design by Altman, [13-14], in which the path length could be varied. Fig. 3.11 (b) shows the spot pattern on one of the mirrors of the multipass cell in such an experiment. Measurements were made on the RR (13, 13) line, which is centered at 13151.34015 cm^{-1} (760.378 nm) and has a line strength of 5.67 x 10^{-24} cm^2 $molecule^{-1}cm^{-1}$ (according to the HITRAN data base [11], Note: The 2008 HITRAN Database lists a value of 13151.34866 cm-1 for the RR (13, 13) line. The results obtained in this dissertation (using the value of 13151.34015 cm^{-1} using HITRAN 2000 version) are not affected since the wavelength scales in the figures in this paper are with respect to the center of this line itself.)

As mentioned earlier, measurements were performed by scanning across the line feature without modulation (i.e. in “direct absorption”: effectively with $N = 0$) as well as with synchronous detection at the modulation frequency and other harmonics. In the notation of the following section, these measurements correspond to N=0, 1, 2, 3...8). A typical span of wavelength to probe RR (13,13) transition ranges from 760.32 nm to 760.40 nm and was obtained by slowly varying laser current on a fixed DC bias. In addition a 1 kHz modulation frequency was imposed on the laser driving current. The experiments were performed at room temperature in open air with pathlengths ranging from approximately 55m (τ = 0.43) to 210m (τ = 1.6). For this paper we present results obtained for direct absorption and for the even harmonic detection orders (N = 2, 4, 6 and 8).

The results presented below show second, fourth, sixth and eighth-harmonic at various modulation indices and τ values of 0.43 (Fig. 3.12) and 1.6 (Fig. 3.13) respectively.

Figs. 3.12(a)-(e) show experiments performed at smaller pathlengths or τ = 0.43, for which pathlength saturation is small and the given modulation index of m=1 the signals show conventional WMS features. They have N+1 turning points and N zero crossings (which is also true for lower detection orders when experiments were performed at relatively higher pathlengths i.e. 210 m or τ = 1.6 in Fig. 3.13.)

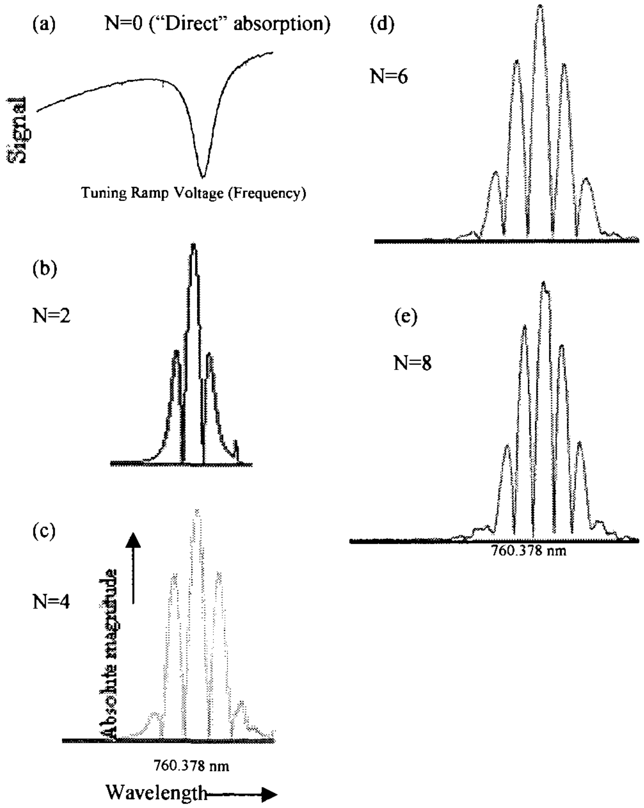

Fig. 3.12. Experimentally measured direct absorption (no modulation), second, fourth, sixth and eighth harmonic signals of molecular oxygen A-band RR (13, 13) transitions. τ is a measure of saturation effects, which in this case , are small (see Eqn. (2)).The direct absorption curve in (a) rides on a ramp that is the result of the slow current ramp in the laser driver current that results in a corresponding change in the laser intensity. (For all $N > 0$ signal magnitudes are plotted). Here, $m=1$ and $\tau = 0.43$. For clarity the signals shown in (b)-(d) are normalized to the same height (Higher harmonic signal power decreases with increasing N [13]). The absolute R – signal of the lock-in amplifier is shown in all the figures (b) - (e).

In Fig. 3.13 the experiment was repeated- the only change being that the pathlength was increased now to 210 m corresponding to $\tau = 1.6$. Particular care was taken to maintain the same modulation index so that modulation broadening did not interfere with optical pathlength saturation effects.

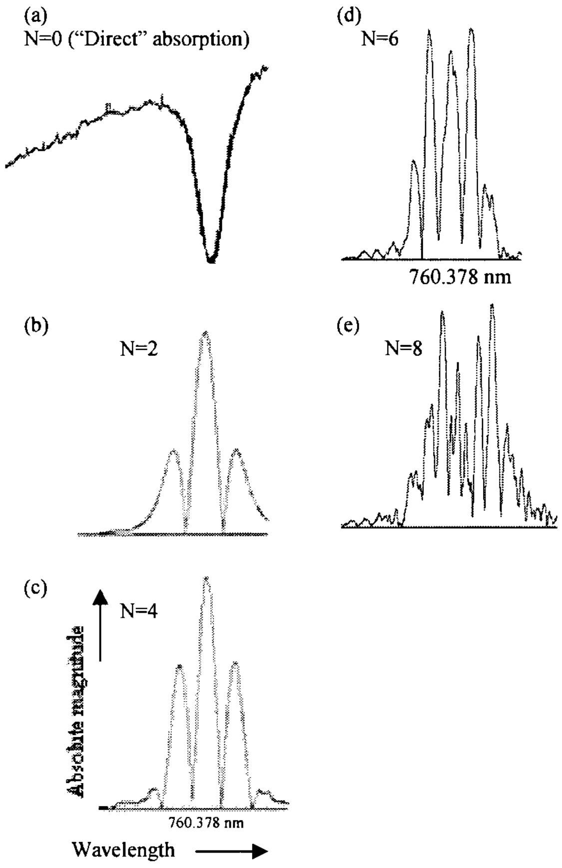

Fig 2.13. Direct absorption, fourth, sixth and eighth harmonic signals with larger saturation parameter, τ values ($\tau = 1.3$ and $m = 1$). Higher order detection, sixth harmonic clearly shows effects of saturation, where the center is suppressed with respect to the side lobes. The eighth harmonic is extremely weak. The turning points are not clear and predominantly distorted; nonetheless the signal shows the characteristic depression of the center lobe indicating optical pathlength saturation. Ratio, R_{PS} of the harmonic signals is the ratio of linecenter magnitude to the adjacent turning point.

Due to strong absorption (i.e. $\tau >>1$) around the linecenter, the absorption signal tends to broaden. The experimental results show the effects of perturbation due to such saturation which is clearly visible in sixth and eighth harmonic detection. These effects are more pronounced at higher detection orders because the Nth harmonic order probes higher order variations (corresponding qualitatively, and approximately, to Nth derivative) of the lineshape function). This Nth order variation of the broadened linecenter appears as a deep depression at the higher harmonics. This allows us to obtain another measure of optical pathlength saturation, namely the ratio (R_{PS}) of the signal magnitude at the linecenter to that at an adjacent turning point.

Therefore, for a combination of m and τ, if the ratio tends to zero, the saturation effects are significant. On the other hand modulation broadening tends to increase this ratio. The ratio grows with the increase in modulation index until the signal appears modulation broadened. Therefore, for WMS experiments R_{PS} provides a more convenient measure of pathlength saturation than τ. From a practical point of view, one may say that the region for which $0 < R_{PS} \leq 1$ for a given set of modulation indices, optical pathlength saturation is pronounced.

In Figs. 3.14(d) & (e) the center lobes show significant depression in magnitude in sixth and eighth harmonic signals, demonstrating the saturation phenomenon clearly. While, of course, saturation is present at all detection orders and even in direct absorption signal (i.e. in Fig. 3.12 and Figs 2.13(a)-(c)) they are not obvious. If one were to perform extremely precise measurements, in principle, these effects can be observed at any detection orders and τ values with an appropriate set of modulation indices. But, given ever-present practical limitations, the suppression of center lobes of WMS signals are a much clearer and obvious and definite indication of this saturation effect.

3.3.2 Dependence on modulation index and detection order

As is well known, Wavelength modulation spectroscopy signals depend strongly on the modulation index, m. A larger modulation index increases the signal magnitudes but also results in a broadening ("modulation broadening"). We have found previously [13] that there is an optimum modulation index (together with an optimum N) that needs to be used to extract overlapping lines. Similarly there is an optimal range of modulation indices in which one should operate for which the pathlength saturation effect is most pronounced i.e. $R_{PS} << 1$. Too small a value does not result in useable signals (e.g. Fig. 3.13(e)), while too large a modulation index masks any saturation effects. This is seen in Figs. 3.14(a)-(c) where, with N = 6, the suppression of the center lobes seen in Fig. 3.14(a) completely disappears on increasing the modulation index, when m is increased from 0.5 in Fig. 3.14(a) to 2.25 in Fig. 3.14(c). However, the center lobe suppression, a signature of optical pathlength saturation, is displayed again at m = 2.25 but that requires detection at N = 8.

3.3.3 Modeling the Experimental Results

The experimental results were modeled (see Fig. 3.14) assuming a Voigt profile, substituting Eqn. (3-7) in Eqn. (3-8). Theoretical values of Doppler and collision linewidth of RR (13,13) transitions that best match the experiments were found to be 2.5

GHz and 3.1 GHz respectively. These values compare to the HITRAN [11] database values of 3.0 GHz and 3.1 GHz of the relevant oxygen transitions.

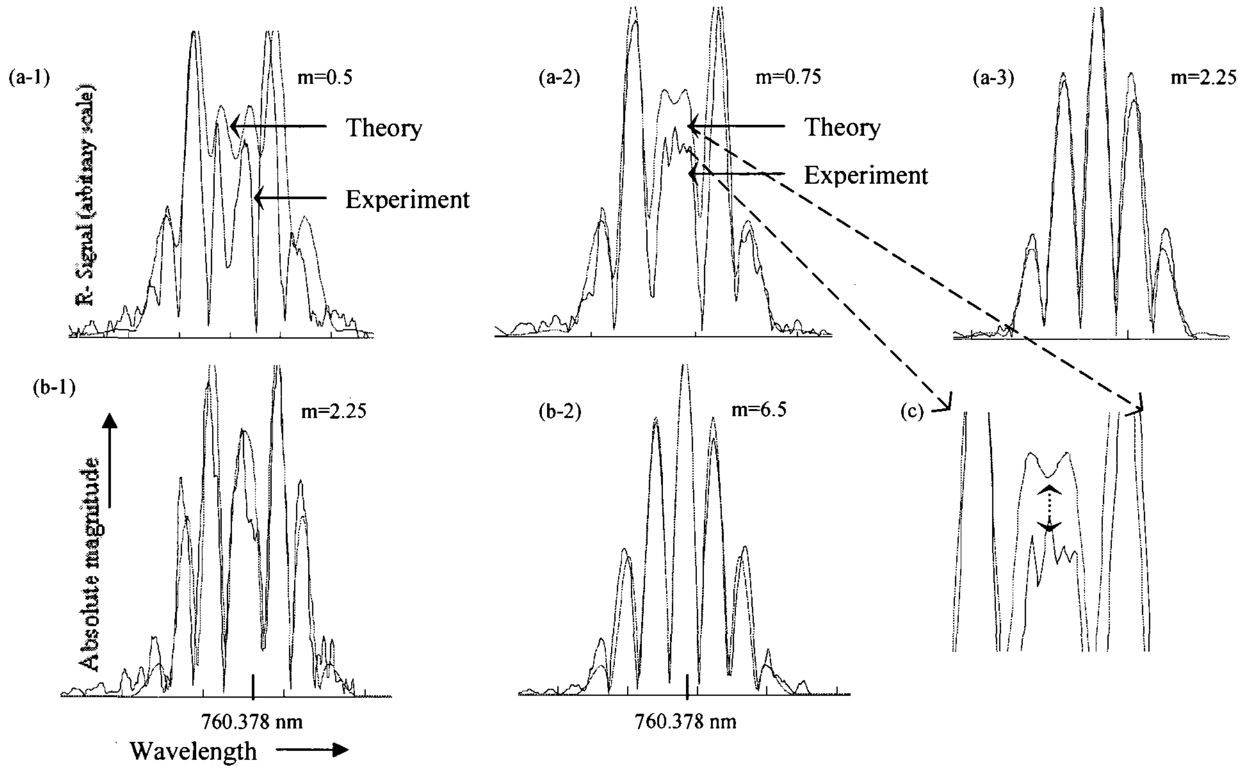

Fig. 3.14. Experimental and Theoretical Results. Sixth (a) and eighth (b) - harmonic signals measured with a fixed saturation parameter, τ =1.6 corresponding to L = 210 meters. The suppression of the center lobe, a characteristic of optical path length saturation in WMS with even harmonic detection, is masked as the modulation index is increases (a-1)–(a-3). The suppression is recovered at a higher detection order (N=8) (Fig. (b-1)) only to be masked at even larger values of m (Fig. (b-2)). Note that the two curves around linecenter in Figs. (a-1) and (a-2) are the experimental and modeled plots, shown on a magnified scale in Fig 13(c).

It is emphasized that our modeled values were obtained by the very stringent constraints that a set of WMS measurements imposes: For a given pathlength and modulation index a match between theoretical and experimental values was sought for the highest N, usually N = 8 in our experiment. This often required a match between the theoretical and experimental values of N+1 (= 9) turning points and N (= 8) zeros. Since, the experiment did not measure absolute optical power, the experimental and theoretical values of the peak of the center lobe at this highest N were set equal. The constraint placed was that all the other experimental measurements obtained would have to match to the model, with no other adjustment. Hence a set of measurements with say N = 2, 4, 6 and 8 required that (5 + 9 + 13 + 17 = 44) values of turning points and zeros to match. In such a procedure, there are therefore 43 (removing the one value for the normalization of the center lobe of N = 8) independent measurements that are an automatic check for self consistency. This illustrates how the detailed structure of WMS signals allows one to have a high degree of confidence in any conclusion drawn.

3.3.4 Quantitative study of ratio of turning point and linecenter

The discussions above can also be illustrated by the results plotted in Fig. 3.15. The values of R_{PS} vs. m shown in Fig. 3.15, for each of the fourth, sixth and eighth harmonic orders show two main regions each where either saturation or modulation broadening is dominant. The ratio is less than unity when the center is suppressed relative to the adjacent turning point, indicating substantial optical pathlength saturation. For a particular detection order, saturation effects are more prominent in the range of smaller index values whereas at higher index values modulation broadening masks these effects. In addition, each detection harmonic has a characteristic span of these saturation or modulation dominant regions.

The results in Fig. 3.15 illustrate the utility of WMS measurements from another perspective: Such measurements have many salient points that allow relevant experimental conditions to be ascertained and checked for self consistency without having to measure the full spectral profile. In the case of Fig. 3.15, conclusions can be drawn by monitoring the ratio R_{PS} obtained by measurement of the signal at the center and turning points.

As mentioned earlier, the saturation parameter, τ and hence the ratio R_{PS}, strongly depends on the lineshape parameter e.g. collision and Doppler linewidth (b parameter of Voigt) or gas parameters e.g. density, absorption cross-section etc. Therefore, accurately modeling these effects enhances accuracy in measurements of lineshape and gas parameters. In addition, the models are more precise if a small variation in any experimental parameters causes larger change in signal magnitudes. For example, from Fig. 3.15 it is seen that the change in the ratio R_{PS} is much greater at for N=8 than that of N= 4 or 6 which demonstrates sensitivity of higher harmonic detection.

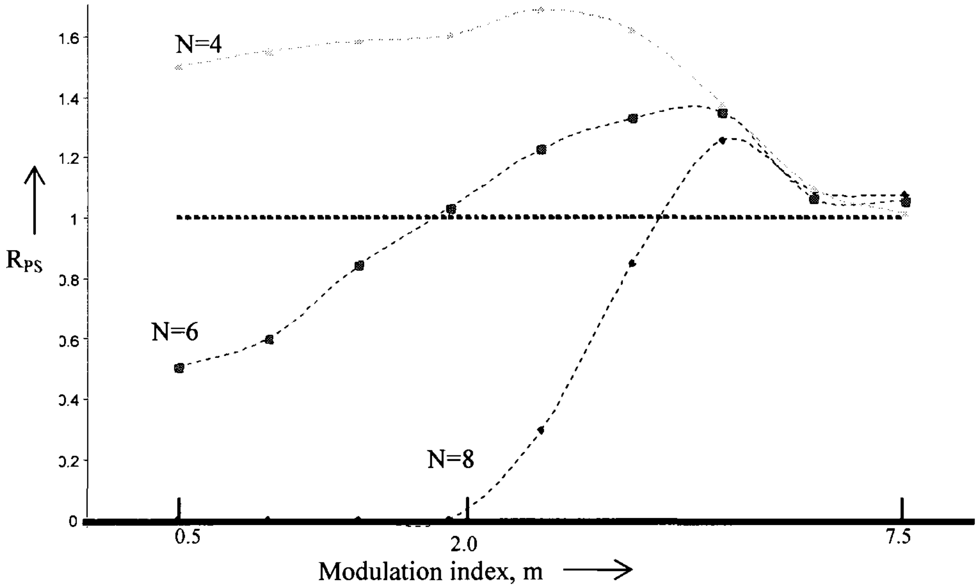

Fig. 3.15. Ratio (R_{PS}) of the signal at linecenter and the adjacent turning point of fourth, sixth and eighth-harmonics. The dotted line refers to the point where the linecenter lobe and adjacent turning point are of equal heights (R_{PS} =1). In the saturation dominant region ($0 < R_{PS} \leq 1$), the ratio increases with the modulation index as the center lobe begins to grow. In modulation broadening dominant regions ($1 < R_{PS} < (R_{PS})max$) the ratio reduces from its peak value to a minimum resulting in depression of center lobe, which is a common effect of broadening. Note that the rate at which the ratio for fourth, sixth and eighth harmonic changes is significant and demonstrates the sensitivity of higher order detection to optical pathlength saturation. Measurements are made at the detection at the points represented by the integers N.

3.3.5 Growth of overlapping lines and optical pathlength saturation

The growth of overlapping lines (discussed in section 3.1) is directly connected to optical pathlength saturation discussed in the previous section. The figures below show the ratio of linecenter magnitude of weak isotopic O^{18}, RR (13, 13) transition to O^{16} RR (13, 13) and weaker of N = 1 to N = 8 detection order and pathlengths values of 88 (τ=0.8), 150mts (τ=1.1), 170 (τ=1.2) and 210 (τ=1.6) meters. It can be seen from Figs. 3.16 (a) and (b) a considerable growth in a weaker line occurs at higher detection order (N=8) and at relatively large pathlength. This is because at 210 meters the (direct) absorption signal is significantly broadened and therefore the linecenter of 8f detection is significantly depressed than other turning points of the WMS signal.

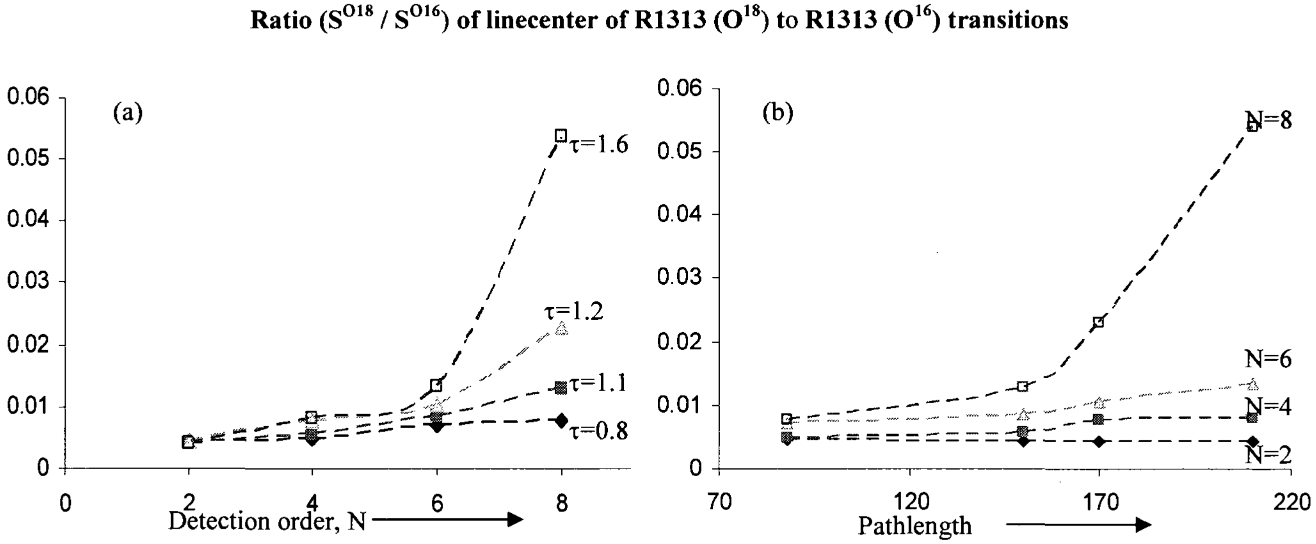
Ratio (S^{O18} / S^{O16}) of linecenter of R1313 (O^{18}) to R1313 (O^{16}) transitions

Fig. 3.16. Ratios of the linecenter magnitude of strong RR (13, 13) transitions vs. weaker RR*(13,13) transition. The ratio grows almost exponentially at higher detection order, indicating significant growth of weaker lines with the detection order. This growth is also reflected at various higher optical depths. For a fixed pathlength, the ratio is greater for larger detection order.

3.4 CONCLUSION

Wavelength modulation spectroscopy (WMS) was utilized for the first time to probe effects of saturation of an absorption signal as it traverses a long path length. Among other effects it was seen that this very phenomena was also key to the growth of overlapping lines in a congested line spectra. The detailed structure of WMS signals which, in general, show N+1 turning points and N zero crossings when Nf detection is used allows the effects of such saturation to be probed conveniently throughout the spectral profile. The method discussed allows one to probe lineshape profiles by observing how the signal profile varies with the absorption pathlength. In particular, the signal around linecenter displays the effects of saturation that are characteristic of the lineshape. And, since different lineshape profiles exhibit different saturation behavior, detection of the latter by higher harmonic detection provides a new method to perform sensitive measurements. While in the above discussion we have focused mainly on the effects of saturation on the central lobes, there are definite relationships between the variation of the individual side lobes as well as their relative magnitudes that yield further information about saturation as well as about the lineshape function itself. This aspect of variation of the signal in the wing region and its sensitivity to line parameters is addressed in the following chapters.

All other factors being equal, the investigation of relative heights of zero crossings and turning points in WMS signals allows one to quantify results with a tighter precision and greater sensitivity than in a direct absorption measurement. The results of the present work, however, show that one could use the VCSEL diode laser sensor employed with modulation spectroscopic technique to measure such absorption saturation effects in wide areas of applications.

3.5 REFERENCES

1. R. S. Mulliken, "Interpretation of the atmospheric absorption bands of oxygen," *Physical Review* 32, 880-887 (1928).

2. R. S. Mulliken, "The interpretation of band spectra: Parts I, IIa, and IIb," *Review of Modern Physics* 2, 60-115 (1930).

3. R. S. Mulliken, "The interpretation of band spectra Part IIc," *Review of Modern Physics* 3, 90-155 (1931).

4. R. S. Mulliken, "The investigation of band spectra: Part III. Electron Quantum numbers and states of molecular and their atoms," *Review of Modern Physics* 4 (1), 1-85 (1932).

5. K. J. Ritter and T. D. Wilkerson, "High resolution spectroscopy of the oxygen A band," *Journal of Molecular Spectroscopy* 121, 1-19 (1987).

6. K. J. Ritter, "A high resolution spectroscopic study of absorption line profiles in the A-band of molecular oxygen," Ph. D., University of Maryland, (1986).

7. G. Herzberg, D. Van, Spectra of Diatomic Molecules, Norstrand Co., New York, (1959).

8. M.A. Khan, J.M. Barrington and A.N. Dharamsi, "Sensitive Detection of Molecular Species by Modulation Techniques: A Measure of Information Content in Spectroscopy", *Proceedings of SPIE* Vol. 4634, 83–91 (2002).

9. M. A. Khan, Karan D. Mohan and A. N. Dharamsi, " Novel pathlength saturation effects in modulation spectroscopic techniques" *SPIE Symposium on Optics East*, 1-4 6378-47, October (2006).

10. M. A. Khan, Karan D. Mohan and A. N. Dharamsi, "Optical Pathlength Saturation Signatures in Wavelength Modulation Spectroscopy Signals of Atmospheric Molecular Oxygen", *Accepted for publication, Appl. Phys. B (2009).*

11. Rothman et al "The HITRAN molecular spectroscopic database: edition of 2000 including updates of 2001," J. *Quant. Spectrosc. Radiat. Transfer* 82, 5–44 (2003).

12. L. H. Aller, Atoms, Stars, and Nebulae, Cambridge University Press; 3rd ed. Aug. 30, (1991).

13. A.N. Dharamsi, "A theory of modulation spectroscopy with applications of higher harmonic detection," *J. Phys. D* 28, 540 (1996).

14. J. Altmann, R. Baumgart, and C. Weitkamp, "Two mirror multipass absorption cell," *Appl. Optics* 20, 995 (1981).

CHAPTER 4

SENSITIVTY TO LINESHPAE PARAMTERS, SIGNAL STRUCTURE AND NOISE COSNIDERATIONS

In this chapter we analyze WMS signals from another perspective i.e. structure or zero crossings and turning points in the signal. It is known that Nf detection has N+1 turning points and N zero crossings. Under practical conditions not all of these turning points are discernible and precisely measured. This depends on various factors such as the detection order, frequency modulation index, signal-to-noise power, distortion and interference from the neighboring transitions. We discuss aspects of structure and sensitivity of turning points to the changes in lineshape parameters or perturbations in absorption lineshape profile. In the concluding part of this chapter we address characteristics of distortion and noise that are common to WMS measurements [1-4] and their effects on measurements of lineshape or gas parameters.

4.1 SENSITIVITY TO LINESHPAE PARAMTERS AND STRUCTURE: ZERO CROSSINGS AND TURNING POINTS

In this section we discuss a quantitative measure of sensitivity of lineshape and gas parameters utilizing signal magnitudes of turning points and spectral locations of zero crossings in wavelength modulation spectroscopic (WMS) signals. The ratios of the signal magnitude at the linecenter and turning points depend on the lineshape profile and modulation probe, which itself carries information about molecular collisional dynamics. The structure of WMS signals, characterized by combinations of the ratios of signal magnitude at turning points, provides a unique scale that quantifies lineshape parameters. It is also shown that under certain experimental conditions higher detection orders give more sensitive measurements, especially if the frequency modulation index is such that the turning points and zero crossings occur in the wings of the absorption lineshape profile. Wing structure of absorption lines and its relation to molecular collision dynamics, as revealed by WMS techniques, is discussed.

The synchronous phase sensitive WMS technique provides a probe that mines variations of the lineshape profile. These variations correspond to the derivatives (of detection order) of the profile. WMS signals with synchronous detection at the Nth harmonic of the modulation frequency (Nf detection) yield N+1 turning points and N zero crossings. These 2N+1 salient features (and their combinations) contain a large fraction of information about the lineshape characteristics and, hence, of the molecular collision dynamics. In this paper we study the dependence of the signal magnitude at turning points on lineshape parameters. (A turning point in the Nth harmonic detection generally corresponds to a zero crossing in the (N+1)f signal since an Nf WMS signal resembles the Nth frequency derivative of the lineshape function.) The signal magnitude and spectral locations of these features depend on the experimental parameters such as frequency modulation index (ratio of modulation amplitude and the linewidth, $m = \beta/\Delta\nu$), amplitude modulation, sample length, as well as on the lineshape function and the oscillator-strength of transition being probed. The span of zero crossings and turning points provide key markers (Fig. 4.1) at various locations throughout the spectrum. Furthermore, detection at higher harmonics provides a greater number of such markers. The spacing between zero crossings, the signal magnitude at turning points and their span (from the linecenter into the wings) all depend strongly on the frequency modulation index. In addition, the modulation index also plays a key role in determining the sensitivity of the signal to any variations in lineshape profile. For example, in order to resolve overlapping lines a frequency modulation index of the order of the line separation is optimal. This is because the probe laser effectively samples the spectral region of the direct absorption signal in the range of the frequency swing of the modulation. (By "direct" absorption we mean the absorption signal such as that obtained by conventional spectroscopy using no probe modulation). Such direct absorption signals may be viewed as a subset, with N = 0, of WMS signals.) Similarly, in optical pathlength saturation effects [5], where the signal broadens due to strong absorption around the linecenter, the effects are most easily discernible when the frequency modulation index is comparable to the spectral span of such broadening in the direct absorption signal.

Any perturbation or deviation in the lineshape profile is strongly manifested in the wing region (because the absorption in those regions is smaller compared to that around the linecenter) and a small change in the gas dynamics can therefore produce significant change in the wings. Since the WMS signals effectively probe the Nth derivative of the absorption signal, the presence of such features in the wings provide sensitive locations to probe such perturbations or deviations in any assumed lineshape profile. In the following sections we will investigate the importance of zero crossings and turning points, especially those in the wings of the absorption profile, in determination of lineshape parameters, e.g. collision and Doppler linewidth of a profile.

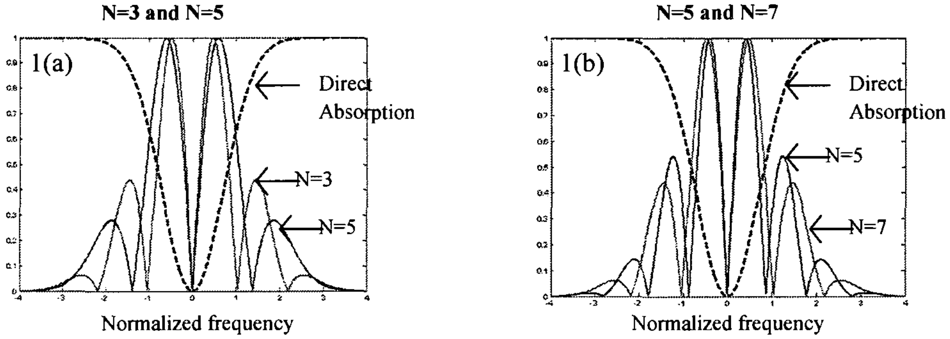

Fig. 4.1. Theoretical calculations of direct absorption signal (dashed curve) as well as with modulation with synchronous detection at various harmonics of the modulation frequency. The modulation index used is m = 1 for which, the first turning point or zero crossing occurs at spectral range of approximately half-width from the linecenter. The remaining turning points and zero crossings are distributed in the rest of the spectrum. Higher detection orders provide more such markers. Note that the signal magnitude decreases with the detection order [1] but, for illustration purposes, N = 3, 5 and 7 signals have been scaled to the magnitude of direct absorption signal at line center.

4. 1.1 Sensitivity in Far-Wing

It can be summarized from the above that zero crossings and turning points are sensitive locations in WMS signals. In addition, a higher detection order has a greater number of such features available in the wing region of the absorption profile. This aspect will be discussed in detail in the following chapter. The increasing sensitivity to deviations in the wing structure with increasing N is illustrated further in the calculations shown in Fig. 4.2. Here we have used a Doppler lineshape function in order to reduce computation time. However, the discussion in this section applies, in general, to all lineshape profiles.

Figs. 4.2(a) and (b) show calculations of percentage changes in the WMS signal at various locations of (2N+1) turning points and zero crossings when the linewidth of a Doppler broadened profile is changed. The figure shows results for 5f detection (i.e. N = 5) with a modulation index, m = 1, and a reference linewidth of 2 GHz. Computations of the change in signals at the turning points and zero crossings when the assumed linewidth is varied by ± 0.2 GHz are plotted. It is seen that the signal at turning points (or zero crossings) in the wings are more sensitive than those closer to linecenter. For example in Figs. 4.2(a) or 4.2(b), the signal at turning points T_2 and T_3 or zero crossings Z_1 and Z_2 is more sensitive to changes in the linewidth than at the points T_1 or Z_1, which are closer to line center (see the locations of these points with respect to line center which are shown in Fig. 4.2(c)).

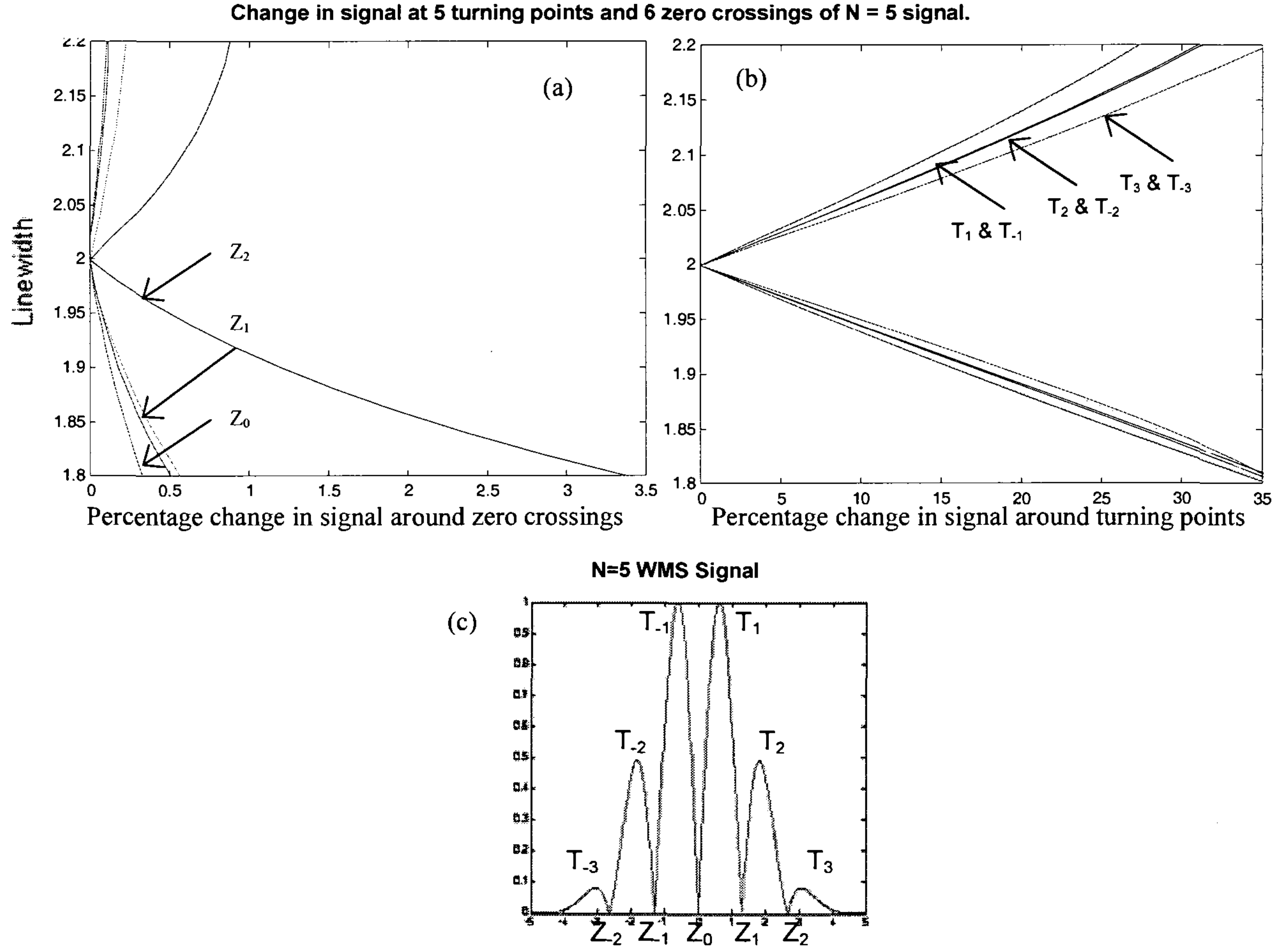

Fig. 4.2. Theoretical calculations of percentage change in the signal with respect to a reference Doppler linewidth of 2.0 GHz. The nomenclature of the turning points and zero crossings is shown in Fig. 3(c). T_2, T_3 and Z_1, Z_2 are the turning points and zero crossing in the wings. Z_0 is the linecenter and T_1 is approximately half-width from the linecenter.

Furthermore, the sensitivity of the signal at turning points and zero crossings is reduced at higher modulation index values (Fig. 4.3(a) and 4.3(b)). This is a result of modulation broadening of the signal [1, 2].

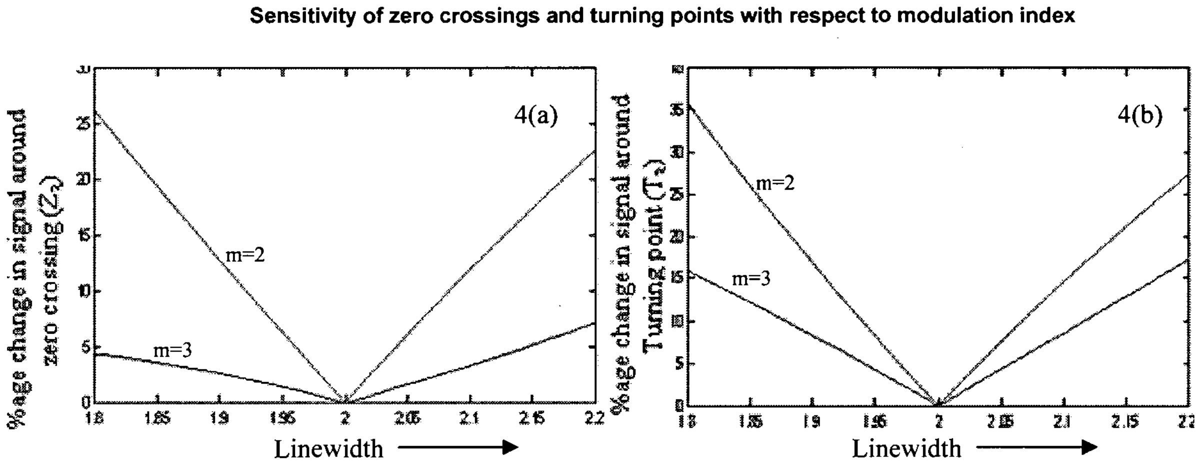

Fig. 4.3. Percentage change in the signal at zero crossings and turning points of 5f detection order (N = 5) with the change in the linewidth (from 2 GHz reference linewidth). Modulation broadening of the WMS signal decreases the sensitivity of variations in the linewidth.

The locations of the zero crossings and turning points and their sensitivity considerably depend on the lineshape function and the probe modulation index (m). For example, if m≥1 the turning points (in wings) are less sensitive to the changes in the line width. This is because, for m ≥1, (the modulation amplitude is of the order of or greater than the linewidth) the first turning point occurs in spectral range of halfwidth, while the remaining turning points (and zero crossings) appear in the wings. Since, the Doppler broadened lineshape function falls off rapidly in the wings, the corresponding WMS signals manifest this feature on the wing structure in their locations and in their sensitivity of the turning points. In contrast, if the profile is collision broadened i.e.

sharper peak and falls off much more slowly in pedestals, the turning points are relatively more sensitive for values of m ≥ 1.

4.1.2 Sensitivity of b parameter of Voigt profile

In this section we discuss a more general case of lineshape profiles i.e. the Voigt profile and the effect of ratios of turning points with changes in the 'b' (the ratio of collision and doppler linewidths, $\delta v_{coll} / 2\overline{\Delta v_D}$) parameter of the Voigt profile, Fig. 4.4. The range of b parameter signifies whether the profile is Doppler or collisional broadened dominant, i.e. if b>>1 the profile is collision broadened, and if b<<1, the profile is Doppler broadened. The variation in the ratios of turning points gives a characteristic signature of the b parameter. As discussed earlier, for b >1, the pedestal of the lineshape falls slowly and there is no significant change in the ratios of turning points compared to when b<1, which is indicated in the ratios of turning point of WMS signals. In other words, if m$\geq$1, and b<1, the turning points in far wings show no significant variations (when the b parameter is slightly changed), as opposed to the case when b>1.

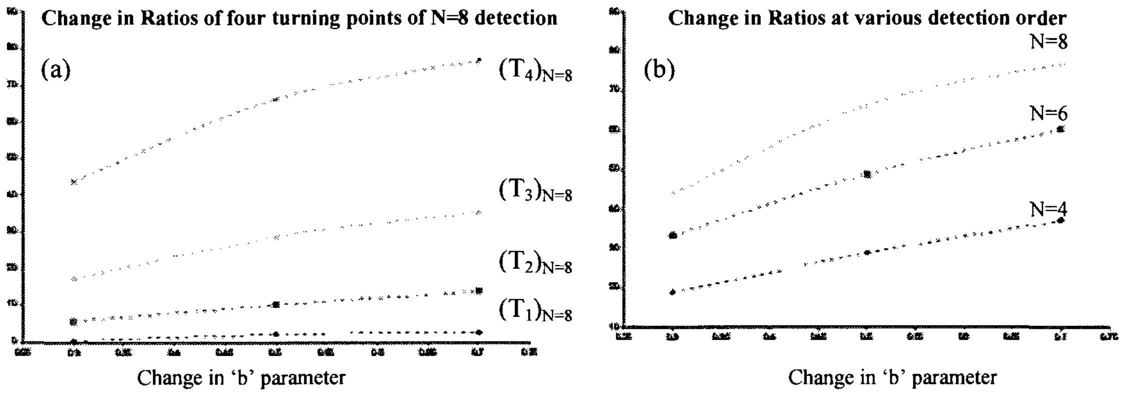

Fig. 4.4. Sensitivity of turning points with the change in b parameter of Voigt profile. Fig. (a) shows turning points of 8th detection order in far wings. The turning point farthest in the wing region shows greatest sensitivity. Also, higher detection orders have turning points with greater sensitivity.

4.1.3 Sensitivity to Optical Pathlength

As mentioned earlier, the turning points and zero crossings are sensitive to changes in the wing structure of WMS signals. For instance, there are situations when variations in the signal in the wing region may be prominent even though the total signal power may not show appreciable change, or in some cases may even decrease. Therefore, the turning points in these regions are quite important as they readily reflect such changes. This is illustrated by an example below, where the aspect of structure and effective growth of signal in the wing region is shown.

Experimental measurements of variation in the signal amplitude (or linecenter magnitude of even harmonics) in WMS has been discussed previously [6, 8, 10]. However, analyzing the signal at the turning points with respect to the linecenter provides a new perspective of investigating wing structure of the lineshape profile. This normalized ratio, R_T (= T_i/S_0, where, S_0 is the signal magnitude at the linecenter of Nf signal; for odd harmonics, $S_0 = 0$)) is a quantitative scale that shows characteristic features of variations in the signal in the wing region. We discuss characteristic behavior of the ratio, R_T with respect to an experimental parameter namely the optical pathlength ($\tau = n\bar{\sigma}Lg(v_0)$), which is a measure of the optical depth (here, n is the density, $\bar{\sigma}$ is the absorption cross-section and $g(v)$ is the lineshape profile). In a measurement where n, $\bar{\sigma}$ and $g(v)$ are fixed, τ can be varied by the pathlength (L) that laser beam traverses in the absorbing medium. In situations when optical depth is large, i.e. $\tau >> 1$, results in absorption saturation or strong absorption of the incident light. It has been shown [10] that WMS is a sensitive probe of pathlength saturation effects, especially when the detection is performed at higher harmonics. The signal at higher detection order readily reveals peculiar features of saturation.

Fig. 4.5(a) shows the ratio R_T of the turning points of 8th detection order of absorption signal of optically saturated Oxygen A- band transition (RR (13,13) O^{16} transition centered at 13151.3486 cm^{-1} and has a line strength of 5.67 x 10 $^{-24}$ cm^2 $molecule^{-1}$ cm^{-1}). The ratios are measured as the optical pathlength parameter (or τ) is increased from a value of 0.5 to 2.5. As the optical pathlength is increased, there are certain regions in the wing where there is a net effective growth in the signal. This can be seen from increase in the ratio as the pathlength is increased. The knee region in Fig. 4.5(a) shows onset of strong saturation. This region is more exaggerated in the turning points (e.g. T_1 and T_2) closest to the linecenter. Whereas, the turning point (T_3), which is farthest from the linecenter, is least affected by saturation effects. Furthermore, it can be seen from Fig. 4.5(b) that turning point T_3 is most sensitive to changes in the pathlength. Therefore, it can be postulated that this region (T_3), which is relatively unperturbed, can be useful in investigating subtle lineshape deviations e.g. profile narrowing effects or asymmetries in the lineshape profile. The above mentioned increase in the signal in the wing region is also true for detection at higher harmonics. Here, even though the total signal power decreases with the increase in detection order the wing region of 8th detection still seems be most sensitive the pathlength parameter, Fig. 4.5(c).

The neighboring weak lines especially the RR (13,13) O^{18} isotopic transition (centered at 13151.72491 cm^{-1} and has a line strength of 1.15 x 10 $^{-26}$ cm^2 $molecule^{-1}cm^{-1}$) begins to grow as the pathlength is increased and cause significant overlap with turning points in farthest wing of the stronger RR (13,13) line. Therefore, the fourth turning point of 8f detection is indiscernible and hence not shown in the figure below.

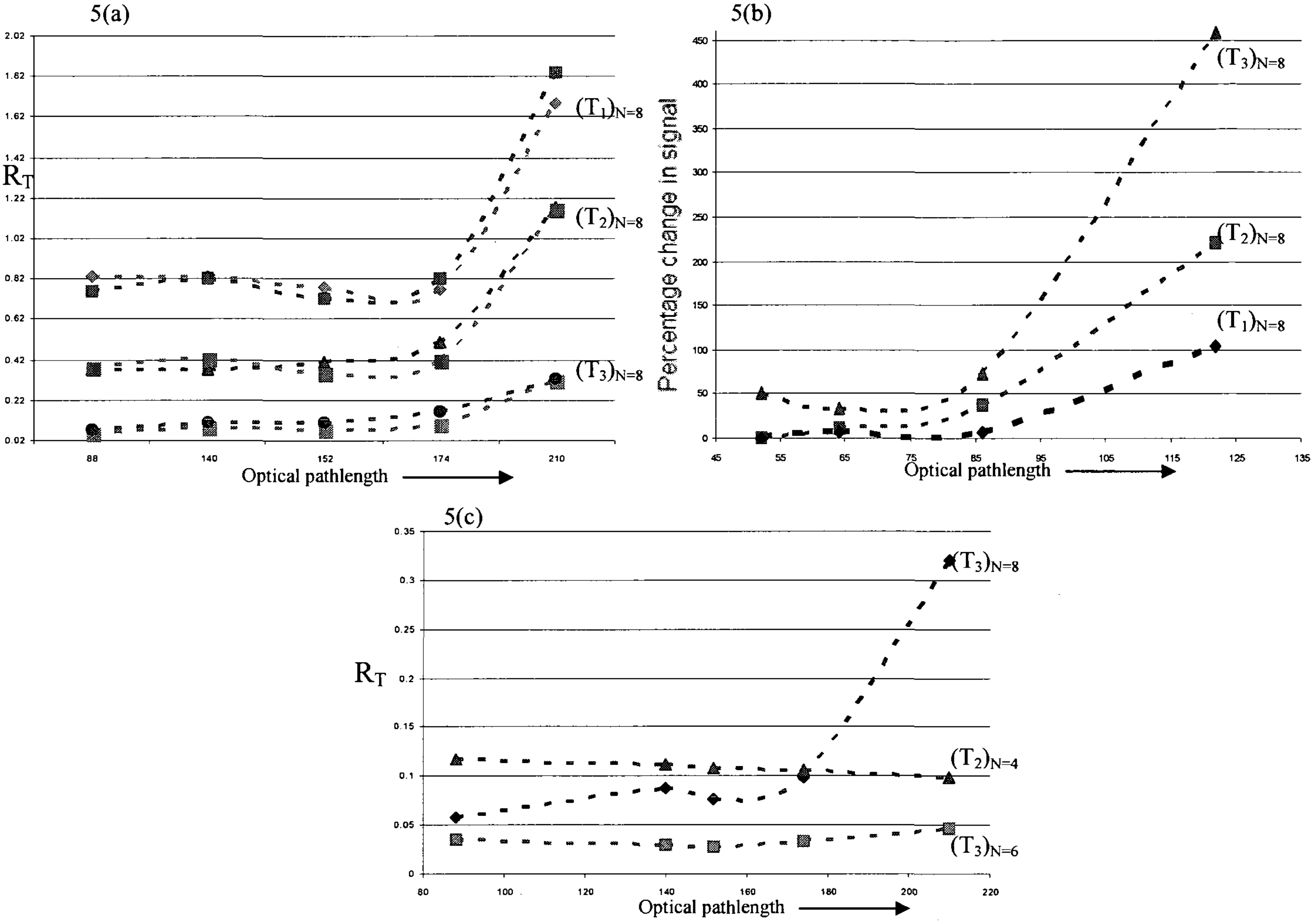

Fig. 4.5. Experimental plot of ratios, R_T of RR (13, 13)) Oxygen (O^{16}) A-band transition. In Fig. 5(a), T_3 is the turning point farthest in the wing region of the absorption lineshape profile. The paired lines shows variation of the two identical turning points that are on long and short wavelength side of the linecenter. The difference in the two pairs could be result of any experimental nonlinearities or effects of intensity modulation. Fig. 5(b) shows values of R_T at 4th, 6th and 8th detection order. 8f detection shows greatest sensitivity to the optical pathlength. It is seen that although the total signal power reduces with the detection order, the region around T_3 still shows relative growth.

4.2 SIGNAL STRUCTURE AND MEASUREMENTS

All measurements probe changes in acquired signals. In spectroscopy measurements are based on changes in intensity with wavelengths. The signal contrast from a reference then gives the quantity being measured. Similarly, scattering experiments query changes in the number of particles (including photons) in a spatial region. It is the signal contrast from a reference that gives information about the parameter being measured. The most common approach taken to increase sensitivity and precision (something always sought) is to maximize the SNR. A signal that provides greater contrast from point to point in phase-space is easier to measure, even when it may not exhibit the greatest *cumulative* signal to noise ratio (SNR). Conventionally, measurements are considered optimal when the signal to noise (SNR) ratio is maximum. That approach has been very successful and in most cases is quite adequate. However, there are situations where the overall signal power does not tell the whole story. An example is the resolution of overlapping lines [1,3] in which the overall signal power is important but the variation of the signal resulting from line interferences can be even more critical: We have demonstrated, experimentally, that the *highest resolution* of the interfering lines is often *obtained for values of conventional SNR that are not the maximum* [7-12]. We develop an approach to deal with such situations and in the process bring out essential features that classical information theory reveals We provide a new perspective for quantifying optimal measurements: a signal with greater structure is more suitable, even when it may not exhibit the greatest SNR since the latter is a measure of the *cumulative* signal and noise powers. For example, a signal with constant slope reveals few details of the physical process generating it compared to a signal with turning points. In such cases, conventional SNR is not the most suitable metric for optimizing the measurement. For example, a signal with a constant slope may reveal few details of the physical process generating it as compared to a signal with a number of turning points. This section examines the signal structure in a precision measurement. We show how concepts of information theory can be used to determine the extraction of the maximum amount of information from any metrological signal.

4.2.1 Signal Structure and SNR

In any given signal the locations where fractional changes are large facilitate more precise measurements. For example, a signal with a constant slope will reveal less information (about its inherent physical process) than a signal with varying slopes. This contrast (fractional change in magnitude) of a signal with respect to its background can provide measurements of high precision. The derivative like structure of a modulation spectroscopy signal provides such contrast and accounts for the higher sensitivity as compared to "direct" absorption techniques.

It has been shown [7] that zero crossings and turning points of WMS signals are very sensitive to changes in the parameters being measured. Moreover, a fixed change in a lineshape parameter induces greater changes at turning points and zero crossings when the detection harmonic order is increased. This is because a higher order signal is a higher derivative, and the signal variations become sharper- up to some optimum value of the detection harmonic order, N.

Although, the total signal power in the Nf signal reduces (see Fig. 4.6) with increasing detection order, N, higher order signals provide increased structure, in the form of additional turning points and zero crossings. These can more than compensate for the decreased conventional SNR at higher N. The various combinations of these salient points facilitate independent measurement of lineshape parameters [9-12]. A combinatorial analysis allows one to introduce aspects of information theory to demonstrate the advantages mentioned. Such an approach is outlined in the following chapters.

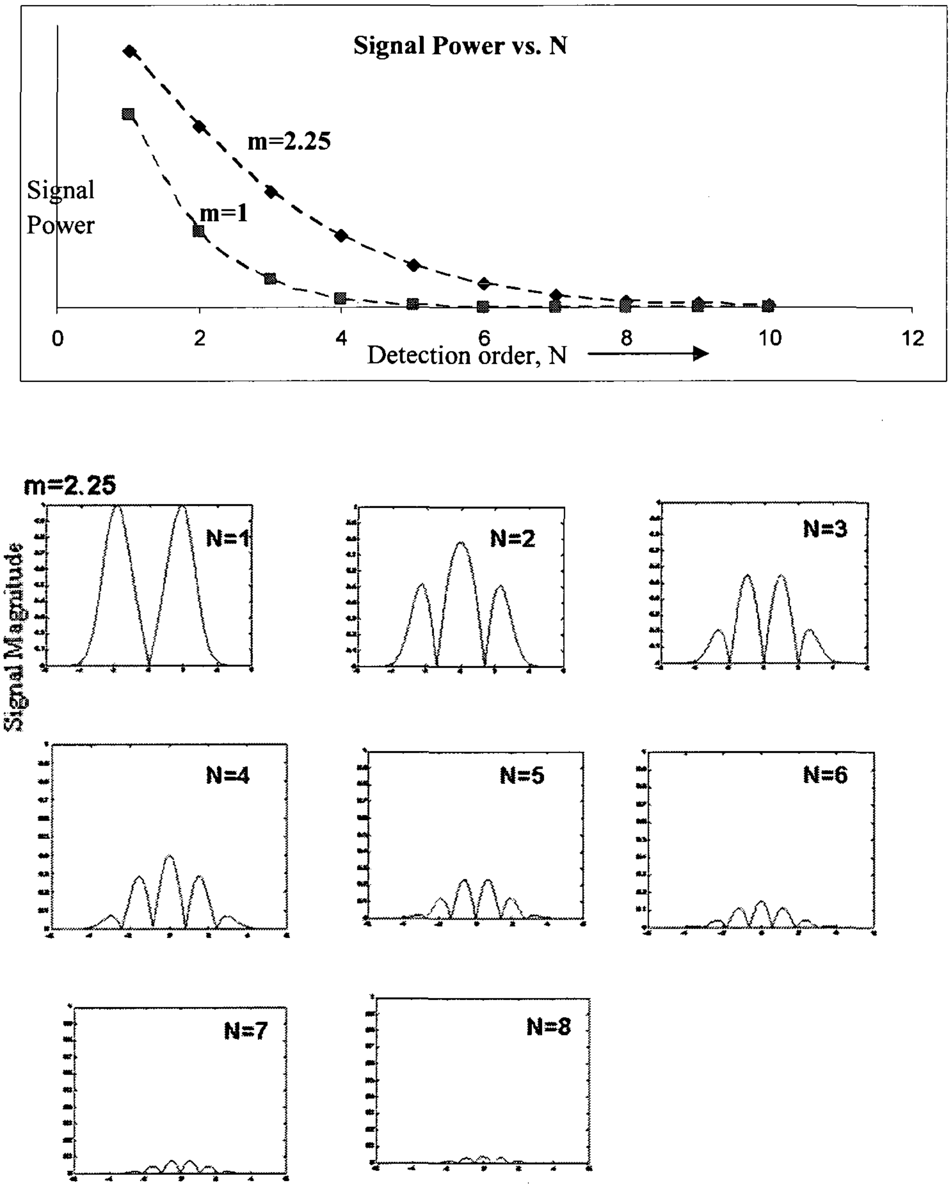

Fig. 4.6. WMS signals with respect to the detection order, N (bottom figure). The signal power reduces with the detection order: whereas, the number of turning points increases with N. Modulation index, m also plays important role in the cumulative SNR.

4.3 LOSS OF PRECISION: DISTORTION AND NOISE

The turning points and zero crossings provide a sensitive probe for any measurement due to significant changes in the signal at these locations. In general, estimation of any lineshape parameter will depend on the precision with which one can determine spectral location and signal magnitudes of these salient features.

In a typical experiment there are several sources that can cause imprecision in measurements. For example uncertainties associated with (1) instrumentation: diode laser, laser current drivers, temperature controllers, acquisition electronics, wavemeter, photodetector, lock in amplifier etc. (2) measurement of experimental variables, such as frequency modulation index (m), amplitude modulation index (r), pathlength (L), (3) probe distortion: optical pathlength saturation [5], interference of overlapping lines, modulation or pressure broadening [1,2], Fabry - Perot fringing [4] etc. We classify the uncertainties in an experiment in two categories. A systematic uncertainty, also referred to as distortion, is mainly due to instrumentation or experimental parameters that cause systematic aberration in measurements. Up to some extent, these effects can be measured and adequately modeled. For example, a distortion like modulation broadening, amplitude modulation, pressure broadening and pathlength saturation can be accounted for theoretical models of WMS signals [1, 2, 4, 5]. We have shown accurate modeling of such distortion effects previously [1, 4, 5] and also in the previous chapters.

On the other hand, uncertainty due to noise is fundamental in nature that originates from thermodynamic properties of the matter. This type of randomness is probabilistic (statistical) in nature where the phase space of constituent particles of the material tends to occupy maximum possible configurations to attain a state of maximum disorder in thermodynamic equilibrium. In electronics this noise originates from "resistive" nature (or "random collisions") of the circuits. The two most common types of noise are thermal and shot noise which has been dealt with extensively in several places in the literature [13, 14]. Due to their inherent statistical nature, these noise uncertainties cannot be fully accounted; only their average behavior is quantified and considered in experimentation

It is important to recognize how these uncertainties translate into error in measurements and mismatch in experiments and models. Fig.4.8 illustrates this point, where uncertainty in wavelength acquisition is considered. The figure shows a simplified schematic of wavelength characterization and signal acquisition. Uncertainty in the wavemeter translates into uncertainty in the values of the model computed from the wavelength data, Figs. 4.7 and 4.8. Similarly, uncertainty in the lock-in amplifier data corresponds to the uncertainty in experimental signals. Both combined together will give imprecise values of the desired parameter, e.g. the linewidth or the absorption cross-section.

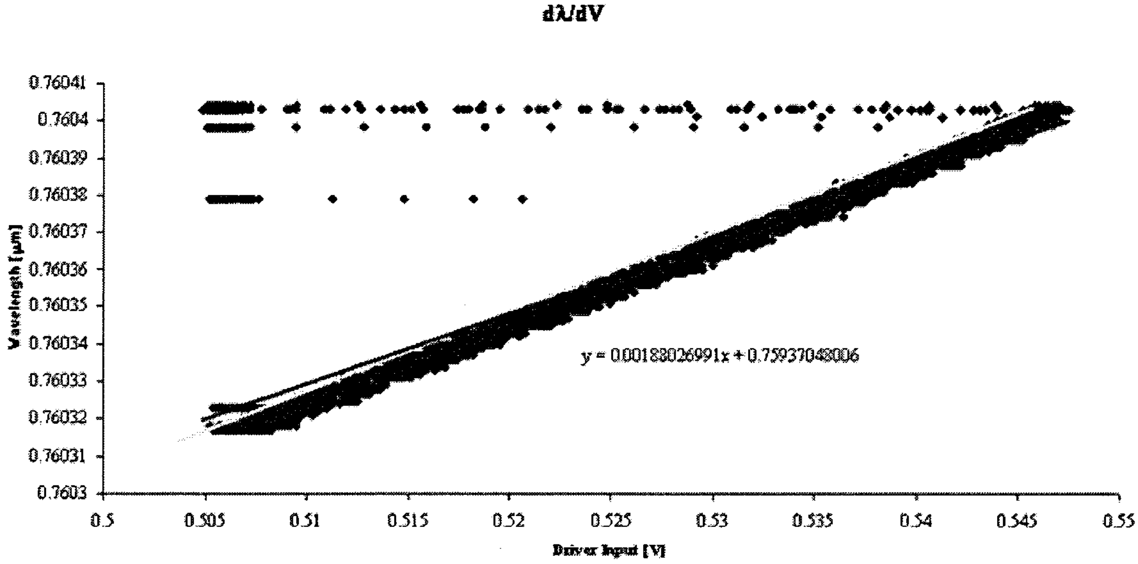

Fig. 4.7. Wavelength characterization (Fig. (a)) of oxygen A– band spectrum that scans RR(13,13) transitions. The wavelength range is 760.30 nm – 760.41 nm . The figure shows 6 scans within this range.

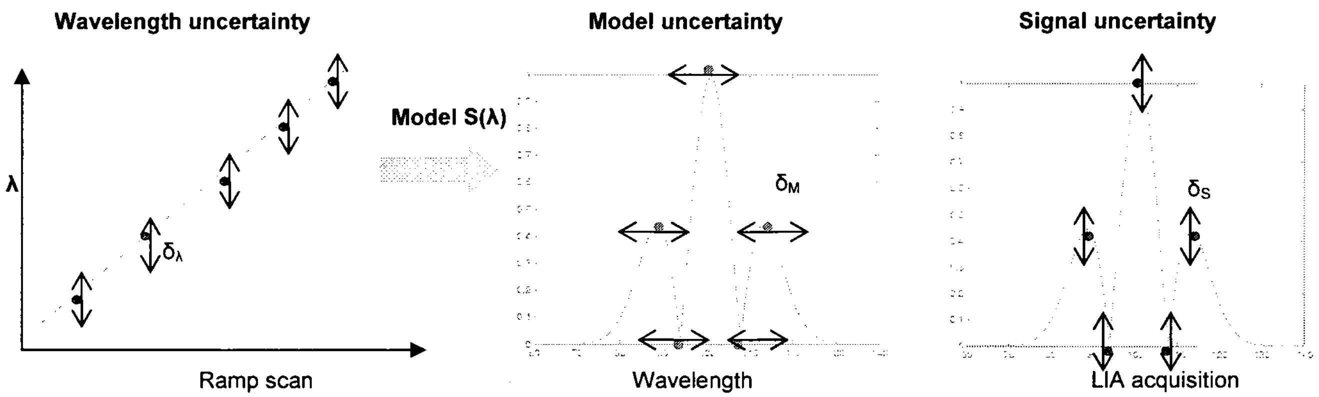

Fig. 4.8. Representation of uncertainties in wavelength data and lock in amplifier signal. Wavelength imprecision results in error in the model. Uncertainty in the lock in amplifier signal is mainly due to distortion or noise in the detection electronics, experimental apparatus or fluctuations in gas environment. The total mismatch in experiment and model (and error in estimation of parameters) is due to cumulative uncertainties in estimation of spectral locations and signal magnitude.

4.3.1 Signal Uncertainty – Distortion Effects

In WMS measurements there are distortion effects that inhibit accurate estimation of turning points or zero crossings. For example, if the signal is broadened, the spectral location and magnitude of the turning points is imprecisely measured: and therefore, estimation of the parameters is inaccurate. We now give a brief description of these effects:

Modulation Broadening: This broadening [1, 2] occurs due to higher values of modulation indices. The cumulative signal strength grows with the modulation index ($\sim m^N$) , but also results in broadening of the resultant signal. This is because, for large modulation amplitudes (β) the probe laser samples a greater spectral region of direct absorption signal. Typically for lower modulation indices the center lobe of the harmonic signal is the highest in signal magnitude while the side lobes decrease with their respective distance from the linecenter. In case of higher modulation indices the signal broadens and center lobes begin to depress and the side lobes grow in magnitude, see Fig. 4.9.

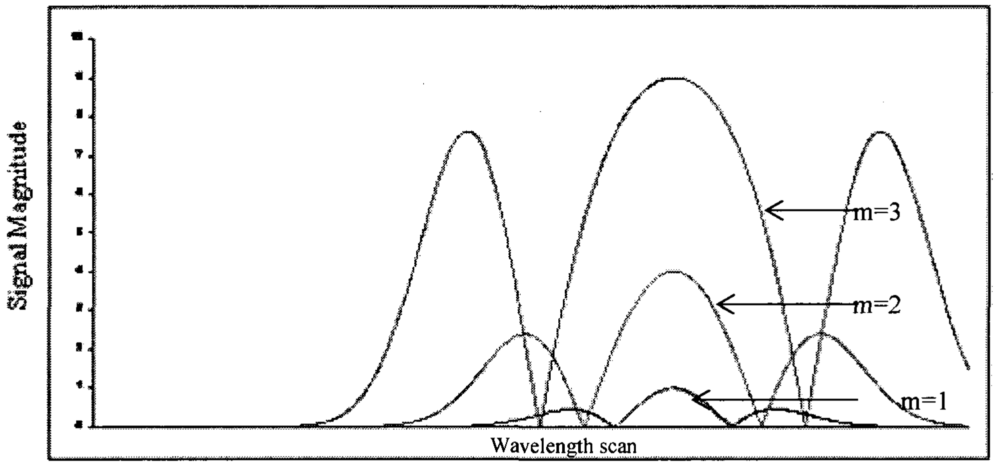

Fig. 4.9. Modulation distortion broadens WMS signals. The signal broadens around linecenter resulting in lowering of the linecenter peak magnitude. The cumulative signal power increase as ~ m^N

Pressure (Collision) Broadening: The effects of pressure broadening are the same as that of modulation broadening. In this case also, the signal broadens at higher pressures (>250 Torr) as the effects of the collisions between the gas molecules becomes prominent. In this range of pressures, collision broadened transitions are more dominant than Doppler broadened transitions.

It has been show that effects of modulation or pressure broadening leads to flattening of the signal and hence, less precision in estimation of zero crossings or turning points. In addition, overlapping lines appear to be resolved at lower modulation indices. Therefore, any broadening effect inhibits the structure in signal and measurement precision.

Optical Pathlength Saturation: As discussed in the previous chapter, this effect [5] appears because of non-uniform absorption across the transition lineshape frequency profile, with increasing penetration into the medium being probed. Effectively, any element of the medium sees an input probe whose profile is different from that seen by a preceding section because of the stronger absorption at, and around, the line center. The result is that the probe signal detected appears broadened, see Fig. 4.10. Consequently, with the choice of suitable modulation index higher order (even) harmonics show this effect as suppression of their linecenter lobes.

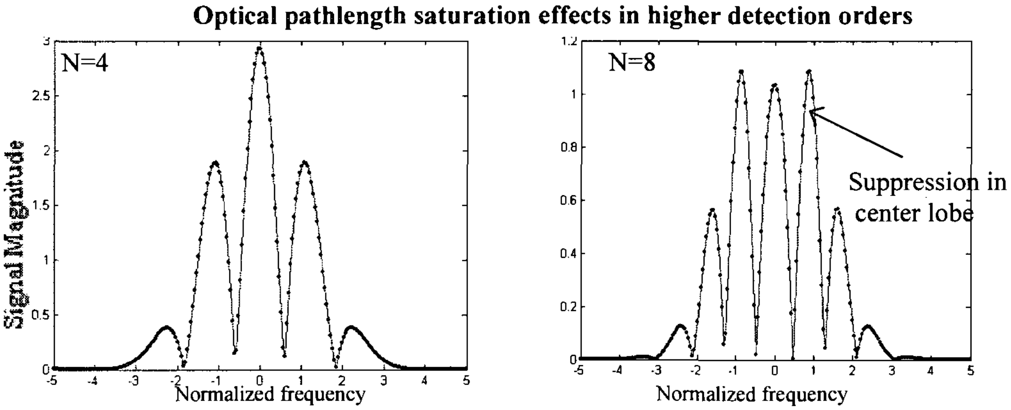
Optical pathlength saturation effects in higher detection orders

Figs. 4.10. Pathlength distortion: 4th and 8th harmonic signals with modulation index, m = 1. The saturation parameter, τ = 1.0. Note that in N=8, the center peak is depressed due to pathlength saturation. Also, for the same τ values lower order harmonic (N=4) do not show saturation effects.

Fabry-Perot Fringing: This type of distortion effect occurs due to the multiple reflections of the probe beam inside the optical components of the experimental apparatus (Fig. 4.11). This is an oscillatory signal which limits the signal to noise ratio of the WMS signals. A detailed description of this effect is given reference [4].

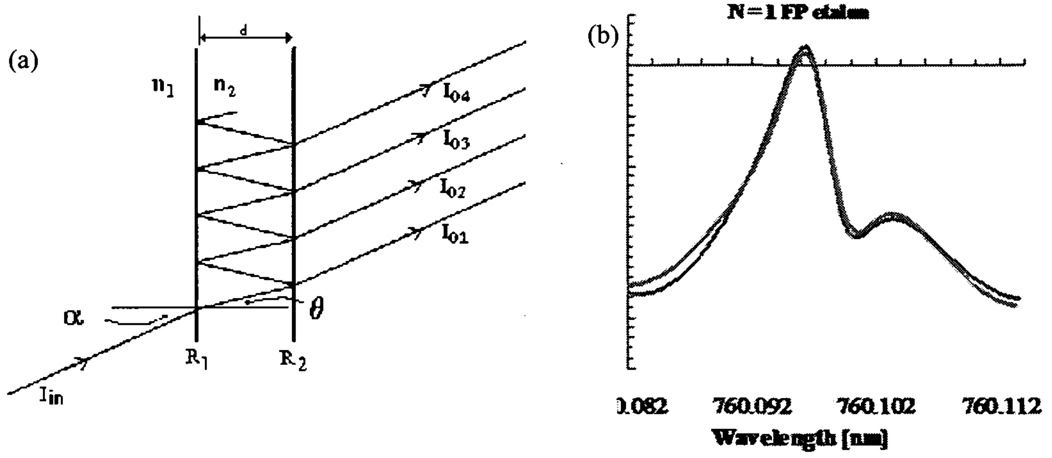

Fig. 4.11. Fabry- Perot fringing due to multiple reflections from optical components. Fig. (b) shows N=1 signal with Fabry-Perot etalon. Due to etaloning effect the harmonic signal is distorted. The experimental signal and modeled plots [4] are shown together (Fig. (b)).

4.4 SIGNAL UNCERTAINTY: THERMAL OR GAUSSIAN NOISE

Thermal noise is a result of the discrete nature of photons (Bosons) and their thermal equilibrium between particles i.e. atoms or the lattice. This results in a distribution that maximizes their configuration in phase space also known as state of maximum entropy (or maximum disorder). The distribution is given by Planck's formula [15] of the blackbody radiation. The equivalent distribution in semiconductors is the cause of noise effects. The particles involved in this case are free electrons that are in thermal equilibrium with local e-fields (phonons or lattice vibrations). The distribution of these particles in thermal equilibrium is such that it describes maximum entropy in the phase (define by their energy and momentum). Although, at a finite temperature, a typical blackbody spectrum ranges from far infra red to gamma wavelengths, noise spectrum of a semiconductor electronic material is (band) limited to radio frequencies. This is due to the collision mean free path or the response time of the electronic devices. It can be shown that the voltage distribution of this uniform spectrum of noise is a Gaussian distribution (Appendix E).

Thermal noise [13, 14] (or Nyquist noise, see Appendix D for detailed physics of the topic) is one of the most common types of noise that appears in electronic circuits. This type of noise originates from resistive elements in the circuits. The noise occurs due to thermal collisions of electrons with atoms. As mentioned earlier, thermal noise has its roots in blackbody radiation; therefore, the noise distribution is the same as that of blackbody distribution (see Appendix D). However, this distribution is approximated to kT, due to the range of frequencies that are common to electronic circuit design. Therefore, a standard power distribution has a width of, $kT\Delta f$ (Δf is the bandwidth of the device, due to capacitive effects of the circuits). In engineering terminology, this approximate version of thermal noise is also known as white noise. As the name suggests, white noise has a uniform distribution in frequency (this should not be interpreted as infinite power in infinite range of frequencies because the white noise energy expression, kT, is an approximation of $hv/(e^{hv/kT}-1)$, which has a finite power over an infinite range of frequencies.)

Since, white noise has a uniform power distribution, each noise pulse, independent of the other pulse, has a fixed variance. As a consequence of the central limit theorem, this distribution is a Gaussian with an average power, $kT\Delta f$, as its variance (see also Appendix E). During the collisions of individual electrons with atoms, each collision radiates a tiny pulse of electromagnetic waves, whose sum is the observed noise. A circuit element of resistance R ohms, develops, across its terminals in a small frequency band, Δf, a fluctuating mean square open circuit voltage, $V^2 = R\ kT\Delta f$. Therefore, it can deliver to another circuit element the maximum power $P = kT\Delta f$ watts.

At room temperature, $T = 300\text{K}$, and since, $k = 1.38*10^{-23}$ Joules/K, the maximum power is about, $P = 4*10^{-15}$ watts/megahertz bandwidth. Any signal of lower intensity than this will be lost in the thermal noise and cannot be recovered, ordinarily, by any amount of amplification. However, prior information about the kind of signal to be expected may enable signal-processing techniques to extract weaker signals. For example, in a synchronous detection using Lock in Amplifier, a weak modulated signal can be extracted by performing demodulation at higher frequencies.

4.4.1 Thermal Collisions and Bandwidth in a detector

It can be seen from both Feynman's and Nyquist's treatment [13, 14] that the thermal fluctuations or noise occurs due to collisions of electrons with atoms in a conductor. Since, the "resistor" by itself is not resonant or has a bandwidth, the bandwidth limitation comes from the channel that conveys the information about these collisions in the form of current of voltage variation, which is measured. Similarly, in a semiconductor, the collision occurs between the electron and the lattice. The resistive action of the semiconductor arises due to these collisions which are random in nature. These thermal collisions are transferred from one location to another in the lattice by the collision times of the carries. Therefore, bandwidth limitations of such collision arise due to semiconductor properties e.g. collision time, capacitance, diffusion length or response time of the semiconductor material.

4.5 CONCLUSION

The analysis presented above allows distinctive features in the wings of an absorption line to be probed by using modulation spectroscopy with detection at harmonics that are relatively high (certainly greater than $N = 2$). The technique can be employed to study fluctuations in the lineshape parameters due to any changes in the gas environment and collision dynamics. Also since the method effectively probes (approximately) derivatives of the lineshape function, higher harmonic detection can pick up variations in the wings that are not discernible at lower values of N. This could, among other things, allow subtle features of narrowing effects on the spectral lineshapes such as Dicke narrowing to be studied more accurately.

Sources of noise and distortion and their implication in measurements of WMS signal were discussed in this chapter. In the following analysis, we consider these aberrations on the signal magnitude and spectral locations of turning points and zero crossings and their impact on precision in measurements of lineshape parameters.

4.6 REFERENCES

1. A.N. Dharamsi, “A theory of modulation spectroscopy with applications of higher harmonic detection,” *J. Phys. D* 28, 540 (1996).

2. G. V. H. Wilson, “Modulation broadening of NMR and ESR line shapes,” *J. Appl. Phys.* 34, 3276 (1963).

3. A. N. Dharamsi and A. M. Bullock, “Measurements of density fluctuations by modulation spectroscopy,” *Appl. Phys. Lett.* 69, 22 (1996).

4. A. N. Dharamsi, P. C. Shea, and A. M. Bullock, “Reduction of effects of Fabry-Perot fringing in wavelength modulation experiments,” *Appl. Phys. Lett.* 72 (24), 3118-3120 (1998).

5. M. A. Khan, Karan D. Mohan and A. N. Dharamsi, “Optical Pathlength Saturation Signatures in Wavelength Modulation Spectroscopy Signals of Atmospheric Molecular Oxygen,” *Appl. Phys. B* (2009)

6. Rothman et al “The HITRAN molecular spectroscopic database: edition of 2000 including updates of 2001,” *J. Quant. Spectrosc. Radiat. Transfer* 82, 5–44 (2003).

7. M. A. Khan, J. M. Barrington and A. N. Dharamsi, “Detailed Structure of harmonic Signals in Modulation Spectroscopy and resulting Precision Improvement in Non-Intrusive Laser based Sensors,” *IEEE Lasers and Electro Optic Society Annual Meeting*, Conference Proceedings, Vol. I 25-26 (2003).

8. M.A. Khan and A.N. Dharamsi, “Quantitative metrics of efficacy of higher harmonic detection in wavelength modulation spectroscopy for precision measurements,” *Proceedings of SPIE* Vol. 5364, 227–234 (2004).

9. M. A. Khan, Karan D. Mohan, A. N. Dharamsi, “Information Theory of High-Precision Measurements,” *Frontiers in Optics: Laser Science*- XXIV (2008).

10. M. A. Khan, Karan D. Mohan and A. N. Dharamsi, “Signal Structure and Precision in Optical Measurements: A new perspective to optimal experimental techniques,” *IEEE Lasers and Electro Optic Society Annual Meeting*, Conference Proceedings (2008).

11. M. A. Khan and A.N. Dharamsi, “Information Extraction from Congested Molecular Spectra by Modulation Spectroscopy,”– *75th annual southeastern APS meeting* (2008).

12. M. A. Khan and A.N. Dharamsi, “Signal Structure and Sensitive Detection of Molecular Species: Optimal experimental techniques in Wavelength Modulation Spectroscopy,” *Proceedings of SPIE, OPTO* (2009).

13. J. Johnson, “Thermal Agitation of Electricity in Conductors,” *Physical Review*, 32, 97 (1928).

14. H. Nyquist, “Thermal Agitation of Electric Charge in Conductors,” *Physical Review*, 32, 110 (1928).

15. Planck, Max “On the Law of Distribution of Energy in the Normal Spectrum,” *Annalen der Physik* 4, 553 (1901).

CHAPTER 5

OPTIMAL DETECTION ORDER -I: RESIDUALS AND CHI SQUARE METRIC

In the following chapter, we discuss quantitative aspects of optimal detection order in WMS signals. In the previous chapters, we have seen that higher detection orders reveal subtle effects that are not apparent in conventional direct measurements or lower detection orders. This is quite important for an accurate estimation of lineshape parameters. In this chapter, we address the fact that greater structure (or number of turning points and zero crossings) is quite advantageous as it imposes tighter constraints on fitting the experiments and hence enhances accuracy of the obtained parameters. Therefore, we study a criterion that provides a quantitative metric of efficacy in measurements, utility of structure and the corresponding detection order.

5.1 QUANTITATIVE ADVANTAGES OF HIGHER HARMONIC DETECTION: CHI-SQUARE METRIC

The distortion and noise effects discussed in the previous chapter lead to imprecision in the measurement of the signal and hence an uncertainty in lineshape parameters. This ultimately will reflect in mismatches between the experiments and theoretical models. In the following section, we quantify the mismatches and investigate regions where these errors can be minimized. Therefore, we investigate higher harmonic detection and their sensitive locations that can be potentially used to identify such errors with greater precision and facilitate accurate estimation of lineshape parameters. To proceed we discuss a statistical analysis approach that quantifies criteria of fitting experiment and theory. The method is based on the least mean square of residuals [1,2] or chi-square measure, which computes the mismatch of experimental and theoretical WMS signals that occur due to uncertainties in lineshape parameter e.g. the linewidth. The analysis shows that the figure of merit (of residuals) is higher at higher harmonics and hence allows a better fit between experiment and model. In summary, we show that one identifies the errors with greater accuracy at an optimal detection order using aspects of structure.

5.1.1 Quality of fit between experiment and model

In this section, a quantitative analysis of Wavelength Modulation Spectroscopy (WMS) signals at various harmonic detection orders for use in precision, non-intrusive measurements is performed utilizing statistical analysis of fractional error (mismatches between theory and experiment) distribution and structure of WMS signals. Here we define the error metric as variance of fractional error throughout the spectrum. A theoretical analysis of the fitting of WMS detailed structures at various harmonic detection orders is studied [1, 2] and analyzed, using statistical measures. It is shown that the error metric increases with mismatches in linewidth in a particular (Nth order) harmonic signal. However, this rate of increase in variance is characteristic of the harmonic detection order used, thereby demonstrating the advantage in measurements at different harmonics. It is shown that for a constant error in estimation of linewidth of a profile, the error can be higher for higher detection orders. Therefore, mismatches in fits are more prominent at certain optimal detection orders.

Experiments with WMS at various detection orders have been done to measure quantities like absorption cross-section, temperature, pressure and concentration of gaseous species. These small perturbations of a lineshape profile reveal details of the molecular collision kinetics, and hence yield precise measurements that are difficult to achieve by other techniques. These sensitive measurements not only require an accurate fitting of the experimental data with the theoretical model but also require a measure of the quality of the fit. Therefore, it becomes imperative to analyze the statistical behavior of these fits and their dependence on quantities like linewidth, modulation index etc. For these purposes we demonstrate a criterion, based on the variance of errors, which is used to quantify the quality of a fit.

A model, which for reference we call the "theoretical signal" using a precisely known linewidth, ($\Delta\nu_D$) is given by Eqn. (5-1) below.

$$S^N = -I_0 n\bar{\sigma}L(-1)^{[N]/2}\frac{g}{\sqrt{\pi}}\frac{1}{\Delta\nu_D}\sum_{\nu=0}^{\infty}\frac{1}{\nu!(\nu+N)!}\{\left(\frac{m}{(2)}\right)^{2\nu+N}\left(\frac{(\nu-\nu_0)}{\Delta\nu_D}\right)^{2\nu+N}\sum_{k=0}^{[2\nu+N]/2}C_{2k,2\nu+N}\left((\frac{\Delta\nu_D}{(\nu-\nu_0)})\right)^{2k}\} \qquad (5\text{-}1)$$

Here m is the frequency modulation index, $m = \beta/\Delta\nu_D$.

The features of such a model also depend on the modulation index, m. In addition, another signal, which we call the calculated "expected signal" is generated with an induced error (ε) in the linewidth, $\Delta\nu_D$. Hence the theoretical signal has linewidth, $\Delta\nu_D$ while the expected signal has linewidth ($\Delta\nu_D \pm \varepsilon$). The resultant errors induced in this way vary across the signal spectrum because of the detailed structure of these signals. The statistical behavior of such errors is investigated by examining the induced variance of error for different harmonic detection orders.

In Figs. 5.1 (a) and (b) the solid curve denotes the theoretical signal (Gaussian lineshape with linewidth $\Delta\nu_D$= 2GHz) of 1st and 5th harmonic WMS signals. The dotted curves represent the expected signal. For these purposes we have included an assumed 5% error (i.e. ε = 0.1 GHz) in the linewidth. The modulation index used was m=1. Convergence of the series in Eqn. (5-1) required a total of five terms (v = 4) for both 1st and 5th harmonics. The range of wavelengths selected for the signals are those that are typical for absorption lines in the Oxygen A band [3].

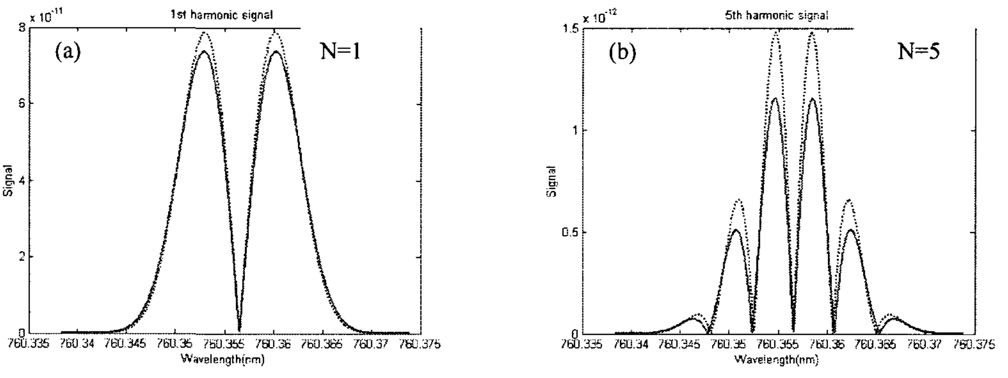

Fig. 5.1. Theoretical signal (solid curve) and Expected signal (dotted curve) of 1st and 5th harmonic WMS signals. Linewidth of theoretical signal = 2GHz. Linewidth of expected signal=2.1GHz.

It is obvious that mismatch between the theoretical and expected signals is due to the difference in their linewidths. An important point to note is that the mismatch in the 5th harmonic detection order signal is greater than in the 1st harmonic detection order signal. This difference of mismatch between the harmonics is reflected in the variance of errors analysis, discussed below, and is central to the advantage that accrues when one uses higher harmonic detection orders.

5.1.2 Fractional residuals

Figs. 5.1(a) and (b) show the mismatch between theoretical and expected signals because of the induced error in linewidth. In order to define the criteria of mismatch we first note that magnitude of a particular harmonic signal varies significantly throughout the spectrum, because of the large amount of structure in these signals. Also, magnitude of the harmonic signal depends on the detection order, N. For example, the residuals (difference between theoretical and expected signal) of 1st harmonic will be greater than that of 5th harmonic, simply because the magnitude of 1st harmonic signal is 100 times the magnitude of 5th harmonic signal. Therefore any useful measure of mismatch for WMS signals should be independent of location of the residues in the spectrum as well as their harmonic order. Hence, we use the fractional error (at each wavelength in the spectrum) as a criterion of mismatch. The fractional errors are residues between the theoretical and expected signals at each wavelength, normalized to the magnitude of the theoretical signal at that particular wavelength. This yields a scatter of fractional errors throughout the spectrum. The variance of these fractional errors can then be used as a measure of the quality of the fit of harmonic signals. The fractional error for any Nth harmonic WMS signal is therefore defined as;

$$f_e^N(\nu) = \left| \frac{S^N{}_{theoretica\ l}(\nu)}{S^N{}_{\exp eriment}(\nu)} - 1 \right| \tag{5-2}$$

Note that here it is more meaningful to consider the absolute magnitudes of the mismatches.

The variance of fractional error is given by the usual definition:

$$\sigma^N = \frac{1}{n}\sum_{i=1}^{n}(f^N{}_e(\nu) - \overline{f_e})^2 \tag{5-3}$$

Here n is total number of data points (or wavelengths) and $\overline{f_e}$ is the average fractional error.

Obviously, for a perfect match the variance of fractional error is zero, and generally speaking a smaller magnitude of variance of error indicates a better quality of the fit. It has been shown earlier that if mismatches occur only due to error in estimation of linewidths (ε), the variance of error increases with the increase in error (ε), as is expected.

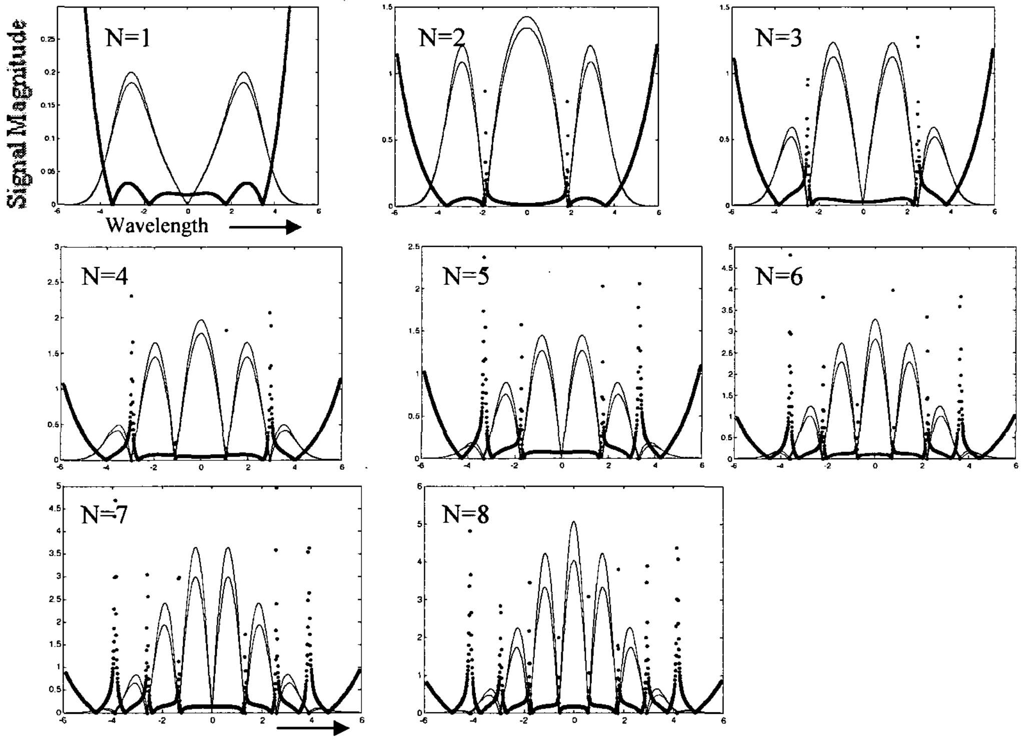

Fig. 5.2. Mismatch between expected and theoretical harmonic signals. The mismatch is due to difference in the linewidth. Expected Linewidth = 2.0 GHz and Theoretical linewidth= 2.1 GHz and. Mismatches are significant at higher order specially at, N = 6 to N = 8, at the locations of zero crossings and turning points. In addition, higher order harmonic provide more visibility of these mismatches than lower ones. The scatters show the magnitude of fractional error along the spectrum.

Fig. 5.2 shows an assumed model and observed data with a finite difference in the linewidth. The scatter plot imposing on the two plots indicate a mismatch due to a fractional difference from the observed data. It can be seen that zero crossings and turning points are the most sensitive locations where the scatter (in error) is the greatest. Therefore, one can conclusively show that most of the errors between the signals occur at these locations. To reinforce this argument, we calculated errors around these turning points and zero crossings and compared it with the total error throughout the spectrum. The table below shows a concentration of errors at the location of zero crossings and turning points. It can be seen that a greater percentage of error (of total error in spectrum) is concentrated around zero crossings and turning points. This could provide faster algorithms that are adaptive and compute values around these salient points instead of the full WMS spectrum.

Table 5.1. Cumulative measure of error due to mismatch between the expected and theoretical WMS signals at various detection orders. First column shows percentage error in the vicinity of zero crossings and turning points of WMS spectrum. Third column is the deviation of the error, higher detection order show greater deviation. This is due to mismatch at several of these salient features.

Detection Order	Average fractional error around Ts and Zs	Average fractional error of spectrum excluding Ts and Zs	Deviation of fractional Error (full spectrum)
N=1	0.03(15%)	0.17	0.08
N=2	0.12(40%)	0.18	0.08
N=3	0.19(50%)	0.19	0.09
N=4	0.3(58%)	0.21	0.11
N=5	0.37(62%)	0.23	0.12
N=6	0.46(63%)	0.26	0.16
N=7	0.52(64%)	0.29	0.20
N=8	0.57(64%)	0.32	0.22

Figs. 5.1(a) and (b) showed a situation for theoretical and expected signals and the mismatch between them. In practical applications, a theoretical model (for example Eqn.

(5-1)) will be used to fit the real experimental data. An additional consideration that must be brought to bear in any experimental situation is the fact that in practical situations the experimental data will be subjected to imprecision of the measuring instruments. Such imprecision can result from many factors, including noise as well as the ever-present finite resolution of any instrument. Two such important effects, namely the variation of the photodetector signal due to noise and the finite resolution of the interferometeric measurement used to identify the wavelength at which a given measurement is done are now addressed.

5.2 SIGNALS WITH IMPRECISION IN MEASUREMENTS

In a typical WMS experiment a modulated laser beam is shined on the sample and the signal from the absorber is collected by a photodetector. The signal from the photodetector is then processed through a Lock in Amplifier (demodulated at different harmonics) to obtain the harmonic detection signal. In such experiments, the wavelength of the laser is usually measured by a "wavemeter" which is essentially an interferometer. In the analysis below it is assumed that both the photodetector and wavemeter have certain imprecision (or uncertainties) in measurements.

Fig. 5.3 shows a graphical representation of any WMS data acquisition scheme with such imprecision. We analyze the situation when the reading obtained by the wavemeter is known to have a finite uncertainty. The rectangles represent possible signals on the photodetector at three different frequencies (or wavelengths), $\nu-\Delta$, ν and $\nu+\Delta$. It is assumed that these three values are equally likely to be true. In addition, the vertical dotted arrow represents the range of imprecision of the photodetector, due to any noise.

Therefore, at any one possible frequency for example ν-Δ, any of the signals S_{E01}, S_{E21} or S_{E11} is likely to be registered at the photodetector. It is assumed that all these are equally likely.

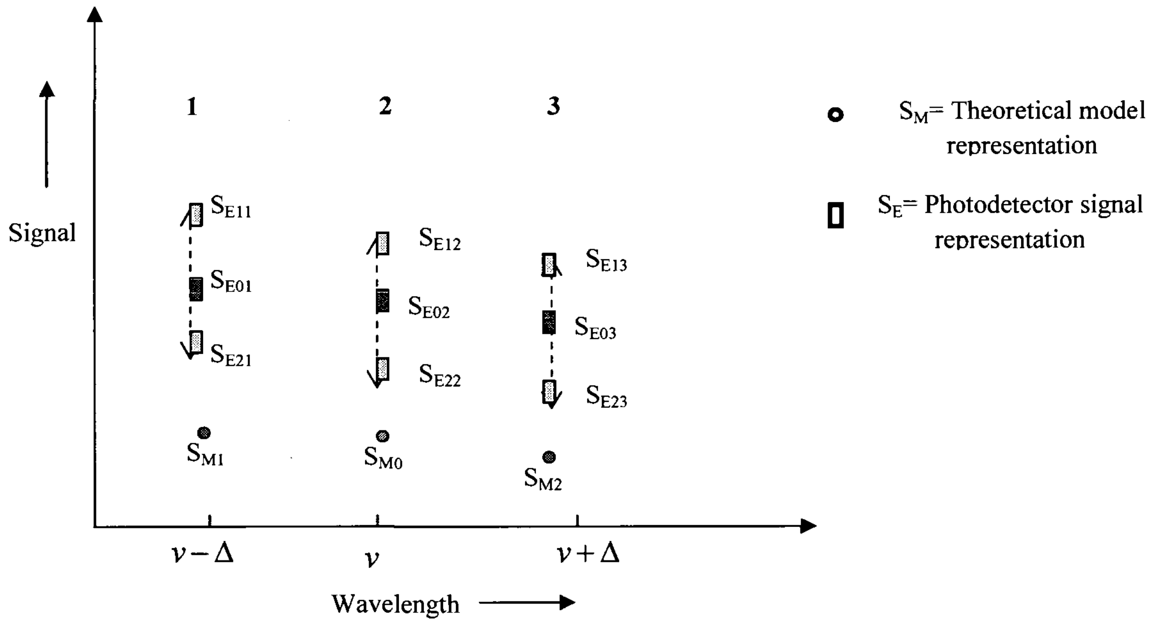

Fig. 5.3. Graphical representation of photodetector signals (in rectangles) with imprecision (vertical dotted arrows). Circles denote the theoretical model computed at three frequencies. The fractional error is a measure of expanse of theoretical model data point from any one of the photodetector signal data point on signal scale.

All of the nine photodetector signals and three theoretical model data points (at ν-Δ, ν and ν+Δ) form 27 possible, equally likely combinations that will enter ino a computation of the fractional error. Here, the fractional error is mismatch of any one of the photodetector signals (S_{Eij} , i = 0,1,2 and j = 1, 2, 3) from any one of the theoretical model data points (S_{Mk} , k =0,1,2). For example, the fractional error S_{E11} and S_{M1} is written as;

$$f_{e1} = p(1) * p(S_{M1}) * p(S_{E11}) * [\frac{S_{E11} - S_{M1}}{S_{E11}}] \qquad (5\text{-}4)$$

Here p(1) is the probability of occurence of photodector signal-1, $p(S_{M1})$ is the probability of occurence of frequnecy ν-Δ (or model S_{M1}) and $p(S_{E11})$ is the probability of occurence of S_{E11} of photodetector signal-1.

Computing all possible combinations of the photodetctor signal and theoretical model data, the general form of average fractional error weighted over all combinations, is:

$$f_e = \sum_{j=1}^{3} \sum_{i=0}^{2} \sum_{k=0}^{2} p(j) * p(S_{Mk}) * p(S_{Eij}) * [\frac{S_{Eij} - S_{Mk}}{S_{Eij}}] \qquad (5\text{-}5)$$

It can be seen from the above equation that fractional errors depend on the probability of occurence of photodetector signals and wavemeter data (or theoretical model data points) lying in the region of imprecision of the instruments. Hence it follows that the fractional errors depend on the statistical distribution of the signals and the noise characterstics of the instruments.

To generate the theoretical signals that represent a photodetector signal we used Eqn. (5-1) gaussian lineshape and fixed linewidth of $\Delta\nu_D$ = 2GHz) and introduced a 10% error (as imprecision of the photodetector) in each of the data points representing photodetector signals. A finite error (of Δ to represent imprecision of the wavemeter) was also introduced in the frequency data (wavelength scan of R13R13 line of oxygen). The expected signals were generated at these frequencies also using Eqn. (5-1)

(gaussian lineshape and linewidth of $(\Delta\nu_D + \varepsilon) = (2 + \varepsilon)$ GHz, range of ε was taken from 0.02 GHz to 0.1 GHz). The fractional errors were computed assuming uniform distribution of the imprecision of the photodetector and the wavemeter. The results in the following section show variance of errors not only due to error in estimation of linewidths but also due to finite imprecision in the measuring instruments.

5.3 METRIC AT HIGHER DETECTION ORDER

The variance of error of different harmonics (N = 1 to N = 5) was calculated incorporating imprecision in wavelength and signal measurements. All the computations were done with a modulation index, m=1. It was estimated that for this modulation index, four terms (v = 4) in the series expansion in Eqn. (5-1) were sufficient to represent the full WMS signal. A four percent criterion for convergence was used- namely that computations were stopped when consecutive values differed by less than this amount. The calculations were carried to include higher terms in the series and the computations were terminated after verification that the next several terms gave a tighter convergence. For fixed modulation index m, it was found that the number of terms required to express full WMS signal remain same for all the harmonics. In other words, detection orders N=1 to N=5 required four terms to represent the full WMS signal. However, the number of terms (needed to satisfy the 4% convergence criterion) increases with the modulation index m. For example for a fixed linewidth of 2 GHz, m = 1 requires a total of four terms (v =3), m=2 and m=3 requires 15 and 35 terms respectively. This is because of the effects of "modulation broadening" in the expected signals.

Fig. 5.4 shows the trend of deviation of fractional error (Eqn. (5-3)) with error (ε) in estimation of linewidth for N=1 and N=5 detection orders. For these computations, the error (ε) in the linewidth was varied from 0.02 GHz to 0.1 GHz.

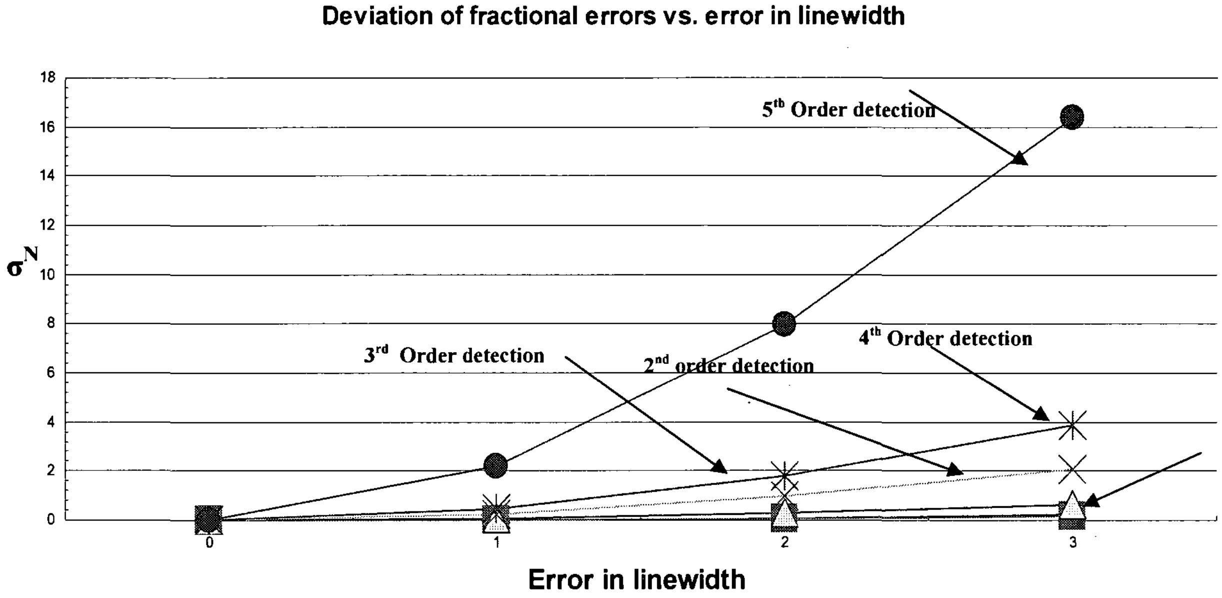

Fig. 5.4. Deviation of fractional error of harmonic N=1 to N=5 of WMS signals. Higher order harmonic show greater deviation of errors and steeper slopes. Note: The harmonics N=1, 2 and 3 are scaled 10 times.

The above figure shows comparison of deviation of fractional error for N=1 to N=5 harmonic order WMS signals. The plot shows that higher order detection signals have higher as well as steeper slopes under the assumptions of these computations (Gaussian lineshape and uniform distribution of errors in photodetector and wavemeter measurements). Also, the mismatches between theoretical and expected signals increase with increasing error (ε) in the linewidth, as expected, of course. This is reflected in a higher magnitude of the variance of error. Better fits are characterized by smaller variance of errors. The quantification of the quality of the fit between experiment and the theory facilitates precise estimates of quantities like absorption cross section, $\bar{\sigma}$.

The theoretical analysis developed above can be extended to other lineshape profiles such as Lorentzian, Voigt etc. While the exact values of variance of errors must, of course, depend on the exact characteristics of the lineshapes, the types of noise and the distribution of the imprecision of the instruments, the general trends should remain intact. One other way to look at the results obtained above is from the perspective of information content [4-7] due to the effects of noise and other signal "blurring" that results from the practical environment during any measurement. We will discuss this in some detail in the following chapter.

5.3.1 Experimental Results and deviation of residuals

It has been shown [1, 8] that the locations of zero crossings and turning points are sensitive to any changes in a lineshape parameter such as the linewidth. Figs. 5.5(a) and 5.5(b) show experimental and computed 5th and 7th order WMS signals of oxygen A-Band RR(13,13) rotation-vibrational transitions. The modeling was done assuming a Voigt lineshape function. The model that best fit the experiment was obtained whose residuals were least from a set of b (the ratio of collision and Doppler linewidths in a Voigt profile). The scatter plots imposed on these figures show the fractional errors (at each spectral location) between theory and experiment. It can be seen that the mismatch (shown as an inset in Fig. 5.5(c)) is large at the locations of zero crossings and turning points. In addition, a higher detection order has a greater number of such locations with higher mismatches. This aspect is brought out in Fig. 5.5(d) which is a Chi-square (a measure of standard deviation of fractional errors between experiment and theory) plot that shows what could be regarded as cumulative figures of merit for a particular detection order. Note that the chi square was estimated for three different values of the collision broadening parameter, b ($b = \Delta\nu_{Coll.} / 2\overline{\Delta\nu_D}$) one of which gives the minimum chi-square value, and was the best fit to the experimental results. Also note that in Fig. 5.2(d) the difference between the values of chi-square metric is very small at lower detection orders and begins to grow with the detection order. Recall that mismatches of this type between an experimental measurement and a model, with a particular parameter such as the linewidth, ultimately improve the measurement's precision: the greater the mismatch that occurs as a result of a fixed change in an assumed value, the more precise the measurement will be when the mismatch is minimized. Hence, all other factors being the same, Fig. 5.5 (d) shows that 7f detection would provide the most precise results for a linewidth measurement.

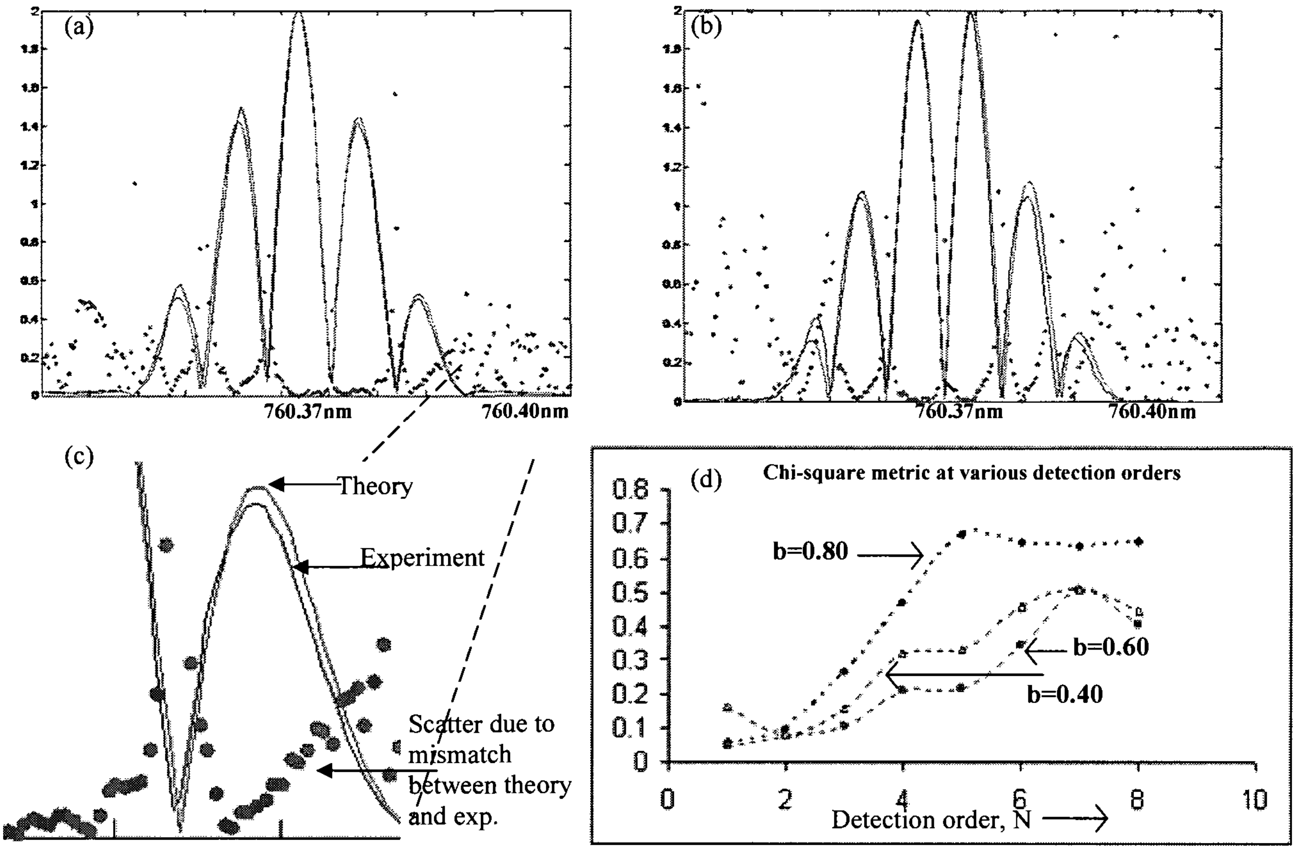

Fig. 5.5. Experimental and modeled plots of 6th (Fig. (a)) and 7th (Fig. (b)) order WMS signals of oxygen RR (13,13) A-band transition. The scatter shows the magnitude of mismatch between theory and experiment at each spectral location. Note the greater scatter is in the wings. Fractional error around the locations of (2N+1) zero crossings and turning points is 57% (N = 6) and 61% (N = 7) of the total cumulative error throughout the spectrum, showing the importance of these salient points. The linewidth parameter of a Voigt profile that gives the best fit, corresponds to b=0.60 (Doppler width = 3 GHz and collision broadened width = 2 GHz. Fig. (d) is the chi-square curve for the best fit (i.e. where cumulative error between theory and experiment is the least i.e. b = 0.60) as well as for two other values (b = 0.40 and b = 0.80). b = 0. 60 shows the least error for all detection orders. Note that at lower harmonics the three chi-square curves are relatively close to each other and gradually spread apart showing greater mismatch at higher detection order. This shows that higher harmonic detection can be advantageous. Since the signal power decreases with increasing N, after a certain N the advantage of higher harmonic detection is lost in the noise- the WMS signals' turning points and zero crossings becoming indiscernible from noise.

5.4 CHI-SQUARE MEASURE AND INFORMATION

The idea of Information [4-6] and information loss owing to indistinguishability or distortion of events has been discussed previously [6]. It was shown that such a blurring of events whatever the cause, results in a loss of information. In the analysis developed above, the variance of error is a result of two factors: namely an error in estimation of linewidth and an imprecision of the instruments. In a practical situation these two factors will be coupled together. However, for convenience we examine them separately.

First, consider an ideal (hypothetical) situation where experiments are done with perfect instruments and with 100% accuracy, i.e. we assume, initially, that the instruments are ideal. Then, in Fig. 5.3, instead of nine data points (rectangles) representing the photodetector signal and three data points of the Wavemeter (that gives theoretical data points denoted by circles), one would register only one data point. Therefore we would compute only one value of a fractional error.

In this idealized scenario the variance of error will be due only to errors in the linewidth assumed in the theoretical model. If the exact lineprofile and linewidth were known then there would be a perfect match between the theoretical and expected models. Hence the fractional errors and the variance of error would be zero.

Now consider the second factor, namely the more realistic scenario where we recognize that the measuring instruments are not precise. This effect will also contribute to the variance of error. Again referring to Fig. 5.3, if the imprecision in the instruments is such that each of the nine photodetector signals (rectangles) and Wavemeter data points are equally probable, then each of the photodetector signals occurs with a probability $p(S_{Eij}) = 1/9$ and each data point of the Wavemeter occurs with probability $p(S_{Mk}) = 1/3$. Hence for one theoretical data point there will be nine possibilities of the photodetector expected signals from which to compute an average fractional error. This gives 27 equally probable fractional error data points. It should be noted that a variance of error in the presence of imprecision in measurements will never be zero even if the exact lineshape profile and line parameters like linewidth are known. Clearly, imprecision in the instruments limits the minimum possible variance of error that one can achieve and therefore limits the best possible fit between the experimental and theoretical data.

In order to extract the most information from an experiment, by changing the harmonic detection order in a WMS experiment, one needs to set up conditions so that initially one has a *large* variance of errors. In that case then, *after the model is fit to the experimental data,* one will have extracted the largest amount of information. This is consistent with the basic result of information theory of Shannon in which the greater the decrease in entropy (or uncertainty) the greater the amount of information that is extracted.

Measurements done by modulation experiments will have certain optimal harmonic detection orders that yield the most precise results. This will intimately be dependent on the given set of experimental apparatus and the particular noise environment.

For instance, the method discussed in this chapter allows features in the wings of an absorption line to be probed by using modulation spectroscopy with detection at harmonics that are relatively high (certainly greater than $N = 2$). The technique can be employed to study fluctuations in the lineshape parameters due to any change in gas environment and collision dynamics. Also since the method effectively probes (approximately) derivatives of the lineshape function, higher harmonic detection can pick up variations in the wings that are not discernible at lower values of N. This could, among other things, allow subtle features of narrowing effects on the spectral lineshapes such as Dicke narrowing to be studied more accurately.

There are many instances where measurements at higher harmonic detection orders and at certain spectral locations of the signal will yield a higher precision in-spite of the fact that with every increase in the detection order the signal decreases. It should also be emphasized that this increase in precision in measurement is *quite separate* from the well-recognized increase in signal to noise ratio that is obtained by synchronous detection at frequencies at which the noise spectral intensity is low. The inherent advantage of higher harmonic detection demonstrated here is due to the richer structure and sensitivity to variation in lineshape profile. The result has been demonstrated by a statistical analysis in this chapter, where we see that the sensitivity of a lineshape parameter can be optimum in region in the far wing structure of the lineshape profile. As we will see in the following chapter, this notion is closely related to the idea of information content in terms of the entropy expression developed by Claude Shannon [4, 5] in the mid part of the last century.

5.5 REFERENCES

1. M. A. Khan, J. M. Barrington and A. N. Dharamsi, "Detailed Structure of harmonic Signals in Modulation Spectroscopy and resulting Precision Improvement in Non-Intrusive Laser based Sensors", *IEEE Lasers and Electro Optic Society Annual Meeting, Conference Proceedings*, Vol. I 25-26(2003).

2. M.A. Khan and A.N. Dharamsi, "Quantitative metrics of efficacy of higher harmonic detection in wavelength modulation spectroscopy for precision measurements," *Proceedings of SPIE* Vol. 5364, 227–234 (2004).

3. A.N. Dharamsi, "A theory of modulation spectroscopy with applications of higher harmonic detection," *J. Phys. D* 28, 540 (1996).

4. C. E. Shannon, "A Mathematical Theory of Communication- Part 1," *Bell System Technical Journal* 27, 379 (1948).

5. C. E. Shannon, "A Mathematical Theory of Communication- Part 2," *Bell System Technical Journal* 27, 623 (1948).

6. M.A. Khan, J.M. Barrington and A.N. Dharamsi, "Sensitive Detection of Molecular Species by Modulation Techniques: A Measure of Information Content in Spectroscopy", *Proceedings of SPIE* Vol. 4634, 83–91 (2002).

7. M. A. Khan, Karan D. Mohan and A. N. Dharamsi, "Signal Structure and Precision in Optical Measurements: A new perspective to optimal experimental techniques", *IEEE Lasers and Electro Optic Society Annual Meeting, Conference Proceedings* (2008).

8. M. Amir Khan, Karan D. Mohan and A. N. Dharamsi, "Wavelength Modulation Spectroscopy as a sensitive probe for wing structure of absorption lines," *Manuscript in preparation.*

CHAPTER 6

OPTIMAL DETECTION ORDER –II: INFORMATION THEORY

In this chapter we apply concepts of Shannon's information theory [1-2] to Wavelength Modulation Spectroscopy (WMS) to obtain quantitative figures of merit such as the measurement precision and a prediction of the optimal detection harmonic order [3-6]. The amount of information, in bits, that can be extracted in any WMS measurement is calculated. The theory is applied to experimental results we have obtained in WMS experiments in congested spectra with overlapping lines that have highly disparate absorption cross-sections. A key result is that the complexity of signal structure can play a much more important role than the conventional signal to noise ratio. We show that there are some parts (where it exhibits turning points and zero crossings) of the structurally-rich WMS signal that play a larger role in conveying information about the measurement than other parts of the signal. We also show that, for a particular noise limitation of the apparatus, there is a finite amount of information that can be transmitted (to the detection equipment) by the probe laser as it samples the probed species. The apparatus is analogous to a Shannon's information channel. Application of the theory developed to our experimental absorption measurements in the Oxygen A-band shows why high detection harmonic orders (up to the 6th or 8th) yield the highest resolution. This is in contrast to statements in the literature, based on conventional signal to noise ratio considerations, that the best results are to be expected with second harmonic detection.

This chapter complements the quantitative analysis of optimal detection order in the previous chapter. It is seen that the absorption features, and therefore the WMS signal, depend mainly on the gas environment, lineshape parameter and experimental controls, signal magnitudes, and noise environment. In addition, we have seen that locations of zero crossings and turning points are most sensitive, and in some situations sufficient for signal analysis instead of the full WMS spectrum. Therefore, an optimal detection order for estimation of any lineshape or gas parameter depends on the measurement of these salient features in a given noise environment.

6.1 INFORMATION CONTENT

There has been a great deal of interest currently in the field of information theory and its connections with other fields of science e.g. statistical mechanics, quantum mechanics, optics, etc. According to Bennett [7-11] every physical process can be considered as an information processing experiment, which requires the generation, transmission and measurement of a bit. The process also involves a computation in that mathematical operations occur on the bit. In spectroscopy, the generation of the bit is inherent to the physical transition being probed. Ultimately, the total amount of information in such an experiment is described quantitatively by the lineshape profile, which is a probability density function in the frequency (or wavelength) domain. The lineshape profile therefore gives the maximal information content (of the source) that can be measured in an ideal, noise free, environment. However, this maximum amount of information cannot be extracted fully because the processes of transmission, computation and measurement are inevitably subject to the practical limitations of the apparatus.

These ideas are applied to a general spectroscopic measurement to provide quantitative measures of how much information is lost as a result of practical limitations on the apparatus. The approach taken is to note that in most spectroscopic techniques (whether they involve absorption, emission or scattering phenomena) the precision and sensitivity of the results depend mainly on the accurate measurement of a wavelength and intensity. The measurement of the wavelength serves to identify the species being probed and the intensity of signal (absorbed, emitted or scattered) allows one to quantify the density of the species. In this chapter we quantify information loss in WMS measurement by recognizing that any measurement on a lock-in-amplifier, photodetector or a spectrometer- interferometer will have a finite precision which is associated with the uncertainty in this measurement of intensity, voltage, wavelengths etc. The loss of information in a measurement of intensity in general depends on many factors such as noise, nonlinearities and saturation in the detector [10-13].

Shannon's mathematical theory of communication [1, 2] laid the foundation of modern information theory. The theory generally groups the major components of a communication system into the source, the channel, a receiver and a destination (where an observer accesses the transmitted information). The information content is associated with the entropy H of the source. This entropy depends on the probabilistic distribution of the source's messages. In general, of course, this set of messages can be any collection of suitable signals. Shannon's measure of entropy is closely related to that in statistical mechanics and thermodynamics. According to Shannon, entropy is uncertainty in a source that has a probabilistic distribution of messages. In statistical mechanics, uncertainty is number of distinguishable arrangements that can be drawn from a group of particles. Entropy in a communication set up is the number of distinguishable messages that can be sent from an information source.

The entropy of a system of N particles can be obtained by combinatorial analysis of all possible arrangements of these particles. In standard statistical mechanical arguments [14] N would be the number of distinguishable particles and each arrangement of particles may be regarded as a message. In a collection of N particles in which m groups of particles n_1, n_2 … n_m are of same kind (i.e. they are indistinguishable from one another) the logarithm of average of possible number of distinguishable arrangements is the entropy of source (H_S) . This is given by [14]:

$$H_S = LogG_S = L\log\left(N!/n_1!n_2!.......n_m!\right)^{1/N} = -\sum_{i=1}^{m} p_i \log p_i \qquad (6\text{-}1)$$

where, $p_i = n_i/N$. Hence, the logarithm of the average number of arrangements, where each one of the latter can be considered to code a message, allows one to identify Eqn. (6-1) with the information content of the set of messages.

For continuous signals, with a probability density function *p(x)* Shannon has shown that the corresponding expression is,

$$H_S = -\int_{-\infty}^{\infty} p(x)\log p(x)dx \qquad (6\text{-}2)$$

This measure depends on the base unit of the variable x (whose information is sought) and has to be interpreted in the context of differences in entropy.

6.1.1 Information loss

In an ideal environment, where one group of objects (particles or messages) is distinguishable from another, the information content is given by Eqn. (6-2). Information loss occurs whenever two or more originally distinct particles can no longer be distinguished. For example, if for some reason n_1 of these particles appear the same as n_2

$(n_1, n_2 \rightarrow n_1 + n_2)$ at the detector then the entropy at the destination (H_D) with such a distortion will be:

$$H_D = LogG_D = Log\left(N!/(n_1 + n_2)!.......n_m!\right)^{1/N} = -(p_1 + p_2)\log(p_1 + p_2) - \sum_{i=1}^{3} p_i \log p_i \quad (6\text{-}3)$$

The resulting loss of information (ΔH) is given by, $\Delta H = |H_S - H_D|$

Information loss, ΔH , could be the result of distortion, noise or imprecision in a device or any combination of these, anywhere between the source and the detector. ΔH is a quantitative measure of metric of any measurement. $\Delta H \rightarrow 0$ implies that measurements are ideal; whereas, a large value of ΔH signifies amount of imprecision in the measurements.

It should be noted here that ΔH is the loss of information about the source due to imprecision in measurement. Two cases arise depending on the nature of distortion, where $\mathrm{H_D} \leq H_S$. In a situation where $\mathrm{H_D} \leq H_S$, the nature of distortion is such that there is no additional uncertainty imposed by the measuring apparatus. For example, in intensity measurements with a photodiode, photomultiplier or a phototransistor, the device generates a response proportional to the light received by the component (which is usually a transistor or a diode) up to a certain intensity level. When the amount of light surpasses that level, the detector becomes saturated and output (current) does not increase even as the light intensity increases In this scenario, the two distinct current values (or messages) become identical due to saturation and results in a loss of information.

Loss of information can also occur at the cost of heat dissipation [7-9] (or noise) at the location (i.e. imprecise receiver in the experimental apparatus) of information loss, resulting in the increase of entropy of the system.

Eqn. (6-3) applies for discrete signals (in which one would use Eqn. (6-2) for discrete signals) as well as for continuous signals that is relevant for absorption spectroscopy. For this latter case one would use Eqn. (6-2) in Eqn. (6-3).

In any spectroscopy experiment e.g. absorption, scattering (Raman), photoelectron, Fluorescence, X ray spectroscopy etc., it requires measurements of wavelength (of the probe) and intensity from the spectrum (of the sample under investigation). Due to practical limitations of the measurement apparatus e.g. interferometer, photodetector, filters etc. these suffer from inevitable distortion and noise, resulting in loss of information about the source (or sample). This loss of information (measured as change in entropy) is characteristic of the type of distortion or imprecision of the measuring apparatus. These imprecision occur due to commonly known effects e.g. responsivity, saturation, rise time (bandwidth or averaging), nonlinear response of detector, noise sources such as thermal noise, shot noise etc. In the following section we discuss information in perspective of WMS signals and the amount of structure i.e. zero-crossings and turning point that each harmonic provides for a measurement.

6.2 INFORMATION THEORY AND WMS PERSPECTIVE- PRECISION IN MEASUREMENTS OF SIGNAL AT TURNING POINTS AND ZERO CROSSINGS

The connection of information theory to the general concepts in physics is a strength that can lead to progress in many other areas of current research. In fact, an argument can be made that whenever any measurement is made, information is being extracted from the system of interest. It is not very difficult to identify any measurement scheme in terms of

Shannon's original five-part communication system [1, 2] comprising of the message source, the coding block, the channel, the receiver and the destination. And, of course, every real measurement will contain some source of noise, and this also is an integral part of Shannon's formulation. Of interest to us here are aspects of information theory as they relate to spectroscopic measurements in general and to modulation spectroscopy in particular. It should come as no surprise that spectroscopic measurements could be discussed in the light of communication theory, if for no reason than the fact that a central aspect of such measurements involves the probing of a feature that can be described by probability density functions (the lineshape profiles). Information theory, statistical mechanics and thermodynamics all concern themselves with random processes, and the very nature of any transition that would be probed in a spectroscopic method involves such processes.

In the WMS experiments discussed previously, the source messages may be regarded as having been generated when the probe interacts with the sample under investigation. The messages are then transmitted along the rest of the optical path (which may be regarded as the channel) and measured at the receiver (which is often just a photodetector). Any spectroscopic measurement can be represented as a model of a communication system consisting of a source, a transmitter, a channel, a receiver and a destination. A spectroscopy experiment may be considered equivalent to a standard communication system as shown in Fig. 6.1 below.

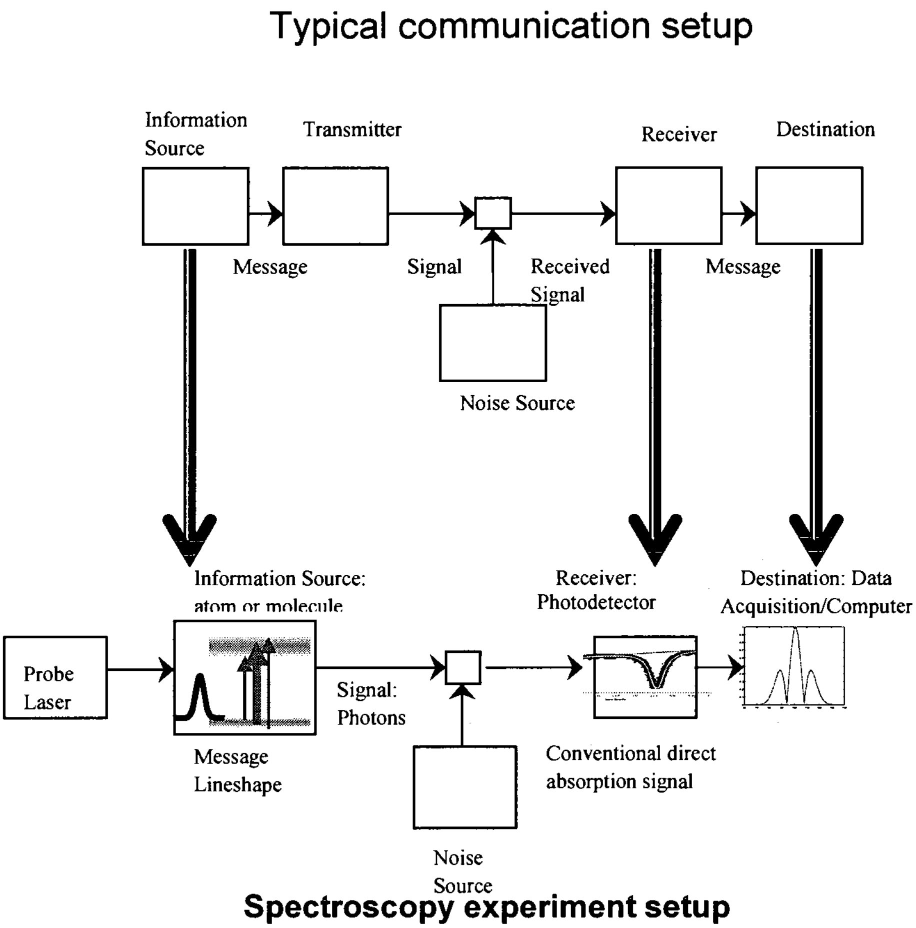

Fig. 6.1. Schematic diagram of a standard communication system. An absorption spectroscopy apparatus modeled as a communication system.

In these sections below, we introduce concepts of information theory and its connection to the structures of WMS [5-7], signals to illustrate the theory developed. As mentioned earlier in WMS, a probe is modulated and synchronous detection performed at one of the harmonics of the modulation frequency. WMS signals show variations of the lineshape in the form of structure that have features associated with frequency derivatives of the lineshape profile probed. In general, Nth harmonic detection (where N is an integer) yields signals with N+1 turning points and N zero crossings. We have shown in the previous chapters that the zero crossings and turning points provide the most sensitive [15, 16] measurements in an experiment. We define the salient structure parameter M = Z+T = 2N+1, where Z is the number of zero crossings and T is the number of Turning Points (both maxima and minima). A combinatorial analysis of the arrangements of spectral locations and signal magnitudes of the turning points and zero crossings is used to find the amount of information that is extracted when one uses WMS signals to measure a lineshape parameter, for example, the linewidth: (see Table 6.1 and Fig. 6.2). The turning points and zero crossings allow one to *quantify* the signal information content, *in bits*. If, say, the linewidth is being measured it can be estimated from combinations of pairs Ts and Zs. Each harmonic detection order, N, yields $^{2N+1}C_2$ (= (2N+1)!/{(2!) (2N-1)!}) independent measurements and higher harmonic (larger N) detection provides greater precision. In general there $^{2N+1}C_1$, $^{2N+1}C_1$, ...$^{2N+1}C_{2N+1}$ such combinations of Ts and Zs that can be used to estimate the parameter,

Without any loss of generality, we assume that the lineshape profile of the absorption signal is a Gaussian, and that the modulation index is small so that the derivative approximation is valid. We can then restrict ourselves to the V= 0 terms in Eqn. (6-4).

$$S^N = -n\bar{\sigma}LI_0(-1)^{[N]/2}(\frac{\beta}{2})^N g^N(v) \qquad (6\text{-}4)$$

Here, *n* is the density, $\bar{\sigma}$ is the integrated absorption cross-section, *L* the length of the absorber, *I* is the incident laser intensity and *g* the lineshape profile. g^N is Nth derivative (in v) of the profile.

Table 6.1 shows theoretical locations (in frequency space) of the turning points (Ts) and zero crossings (Zs) of the first and second order harmonic calculated from Eqn. (6-4).

The linewidth of the profile is computed from linear combinations of pairs of these Ts and Zs. Therefore, each experimental harmonic detection order, N, gives ${}^{2N+1}C_2$ number of ways to compute the linewidth, the parameter being measured. The nomenclature of the turning points is shown in Fig. 6.2 below.

Table 6.1. Spectral locations of turning points and zero crossings of N=1 and N=2 signals and linewidth obtained form the combination of these points.

N=1	**Location (freq.)**	**Linewidth** ($\Delta\nu_D$)	**N=2**	**Location (freq.)**	**Linewidth** ($\Delta\nu_D$)
Z_0	ν_0	$Z_0 - T_{-1}$ $T_1 - Z_0$ $T_1 - T_{-1}$	Z_{-1}	$\nu_0 - \Delta\nu_D$	$T_1 - T_{-1}$, $Z_1 - T_0$; $Z_1 - Z_{-1}$, $T_0 - Z_{-1}$ $\sqrt{(1/3)}(T_0 - T_{-1})$, $\sqrt{(1/3)}(T_1 - T_0)$ $a_1(Z_{-1} - T_{-1})$, $a_1(Z_1 - T_1)$ $a_2(Z_1 - T_{-1})$, $a_2(T_1 - Z_{-1})$ *{here : $a_1 = \sqrt{3} + 1$, $a_2 = \sqrt{3} - 1$}*
T_{-1}	$\nu_0 - \Delta\nu_D$		Z_1	$\nu_0 + \Delta\nu_D$	
T_1	$\nu_0 + \Delta\nu_D$		T_0	ν_0	
			T_{-1}	$\nu_0 - \sqrt{3}\Delta\nu_D$	
			T_1	$\nu_0 + \sqrt{3}\Delta\nu_D$	

In the following section, we show that the rich structure afforded by the 2N + 1 salient points (turning points plus zero crossings) allows one to calculate the *quantitative* amount of information, in bits, that can be extracted. Considerations of the usual precision limits of, and the noise in, the apparatus are included.

Information in the Structure of Signals: The Turning Points (Ts) and Zero Crossings (Zs) of the signal encode information about the linewidth. The question now posed is *"Given the conditions of the experiment, what is the maximum amount of information, in bits, about the linewidth that can be extracted, and at what harmonic detection order, N, will this be achieved?"* An experiment using this N would therefore be the optimal one. In a practical environment infinitely precise measurements are not possible due to the limitations of the apparatus, noise, interference with other overlapping lines, etc. But, it is just this limitation of finite precision that allows us to exploit Claude Shannon's information theory [1, 2] to answer the question posed. The central point is that it is the removal of uncertainty in measurements that leads to information acquisition.

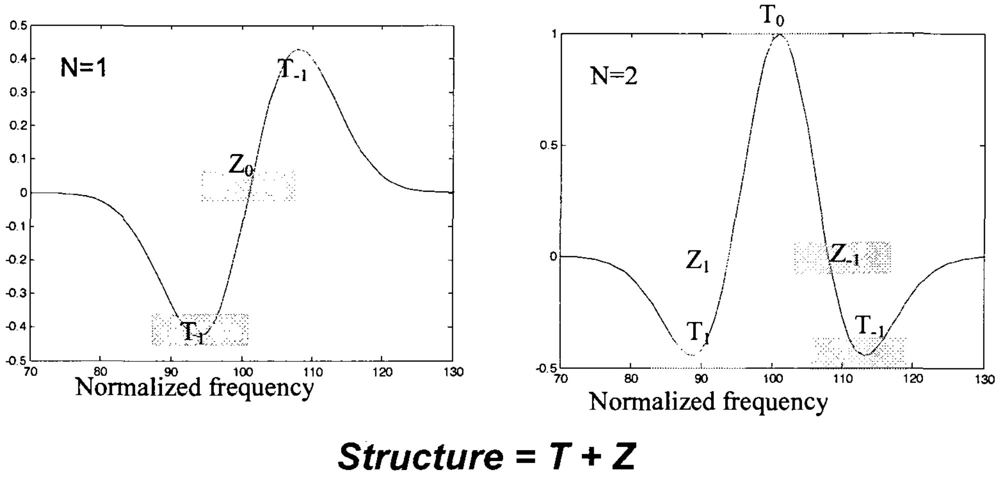

Fig. 6.2. N=1 and N=2 harmonic detection signals with the zero crossings (Zs) and turning points (Ts) as points of interest.

In any practical measurement the locations of the Ts and Zs will not be precisely known. Consider first an uncertainty in these locations that can be described by a uniform discrete probability function:

$Z^N_j \rightarrow Z^N_{j1}, Z^N_{j2}, Z^N_{j3}$

And, $T^N_j \rightarrow T^N_{j1}, T^N_{j2}, T^N_{j3}$.

This implies that Z^N_j could be (with equal probability) at any one of the three locations Z^N_{j1}, Z^N_{j2}, Z^N_{j3}, and similarly the turning point T^N_j could be at any one of the three locations T^N_{j1}, T^N_{j2}, T^N_{j3}. Therefore, the linewidth which is being measured could be anywhere in a range of values determined by the uncertainties in Z^N_j and T^N_j.

The amount of information related to linewidth that can be extracted increases when the precision of the instruments is increased. In this case, an increased precision means smaller ranges for the sets $\{Z^N_{j1}, Z^N_{j2}, Z^N_{j3}\}$ and $\{T^N_{j1}, T^N_{j2}, T^N_{j3}\}$ (see Fig. 6.3).

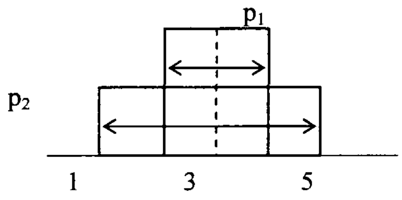

Fig. 6.3. Uncertainty in locations of zero crossings and turning points described by two uniform probability distribution functions.

There are ${}^{2N+1}C_2$ ways of picking a pair of values from the 2N+1 values of Zs and Ts. So the number of combinations for first and second harmonic (N = 1, 2) detection are ${}^{3}C_2$, and ${}^{5}C_2$. If the uncertainties are described by a uniform probability distribution function, p_i, then the information gained by increasing the precision (from p_1 to p_2) for first order detection, N=1 is,

$\Delta H^1 = H^1_{p1} - H^1_{p2} = 3[\log(4) - \log(2)] = 3 bits.$

The corresponding gain for N=2 (second harmonic detection) is;

$\Delta H^2 = H^2_{p1} - H^2_{p2} = 10[\log(4) - \log(2)] = 10 bits.$

Hence, $\Delta H^2 = (10/3)\,\Delta H^1$.

In general, $\Delta H^M / \Delta H^N = {}^{2M+1}C_2 \,/\, {}^{2N+1}C_2$ showing that more information is extracted from higher harmonic detection, where there is more structure ($H^M > \Delta H^N$ with $M > N$). Note carefully signal power does not enter into these considerations. This result *quantifies* the qualitative and intuitively obvious statement that *more information is extracted from a practical apparatus when it can be configured to yield a signal with a larger amount of structure regardless of the signal magnitude.* This is the central result that, as far as we know, has not been discussed in the literature so far. A generalization of the method to situations where the imprecision is described by any probability distribution function is straightforward. For instance, for a Gaussian noise in the apparatus, one obtains:

For N =1

$H^{1}(\Delta v) = \sum^{3}_{k=1} H(\sigma^{1}_{k})$

for N = 2;

$H^{2}(\Delta v) = \sum^{10}_{k=1} H(\sigma^{2}_{k})$,

here, σ_k is the variance obtained from of the distribution of each of the Zs and Ts of N=1 and N = 2 harmonic order. It will be seen in the following sections that σ_k relates to signal and noise power and hence depends on signal magnitudes and bandwidth of detection of detection order. In summary, there are two aspects of WMS measurements that are critical for information extraction, namely, the amount of imprecision (due to noise, distortions etc.) in the experiment and number of discernible turning points and zero crossings available to estimate a parameter. A generalized analysis with Gaussian noise is discussed in the following section.

6.3 INFORMATION IN MEASUREMENT OF A LINESHAPE PARAMETER

Using the theory described above, if one was to determine a lineshape or gas parameter with combinations of all possible pairs of Ts and Zs ($T^{N}_{i}T^{N}_{j}$, $T^{N}_{i}Z^{N}_{j}$, $Z^{N}_{i}Z^{N}_{j}$) there are ${}^{2N+1}C_{2}$ pairs for computation. In an ideal (noiseless channel) measurement, each of the pairs yield exactly the same magnitude of the parameter being measured irrespective of the choice of pairs or the harmonic order. However, due to imprecision in measurement, the values of Ts or Zs is a probability distribution with an equivalent to the nature of uncertainty induced by the imprecision. Therefore, the resultant values of lineshape parameter will depend on the functional form of the distribution and a number of pairs used for computation (since each order has ${}^{2N+1}C_2$ modes of measurements). For instance, in case of a Gaussian noise (or thermal noise) in an apparatus, Ts and Zs will have a normal distribution with finite variance equivalent to the noise power.

The figure below shows a schematic where noise is introduced at the location where T/Z are being measured.

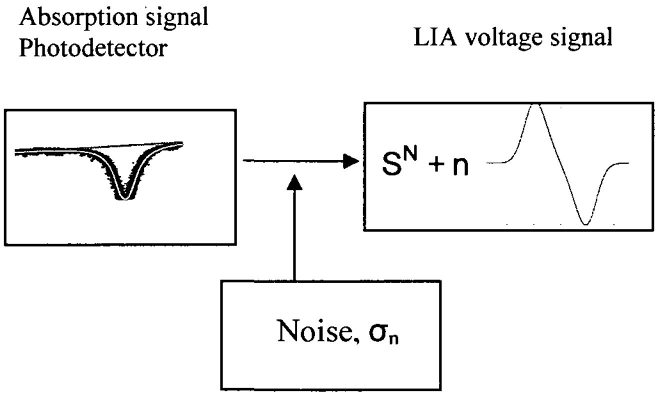

Fig. 6.4. Schematic of an input absorption lineshape signal with an additive noise. The resultant signal with imposed noise is accessed at the destination.

To illustrate the above point, consider a WMS experimental setup described in Fig. 6.2, further assume that the additive Gaussian noise (denoted by discrete n_i values in Figs. 6.4 and 6.5) centered at n_0 and variance, σ_n. Therefore, the distribution of the Ts and Zs is centered at $(T_i^N + n_0)$ with variance, σ_n (here, T_i^N is the ith turning point of Nth detection order) . Since Ts and Zs are used to estimate a lineshape parameter any uncertainty in their magnitudes will translate into an equivalent uncertainty in the parameter being estimated.

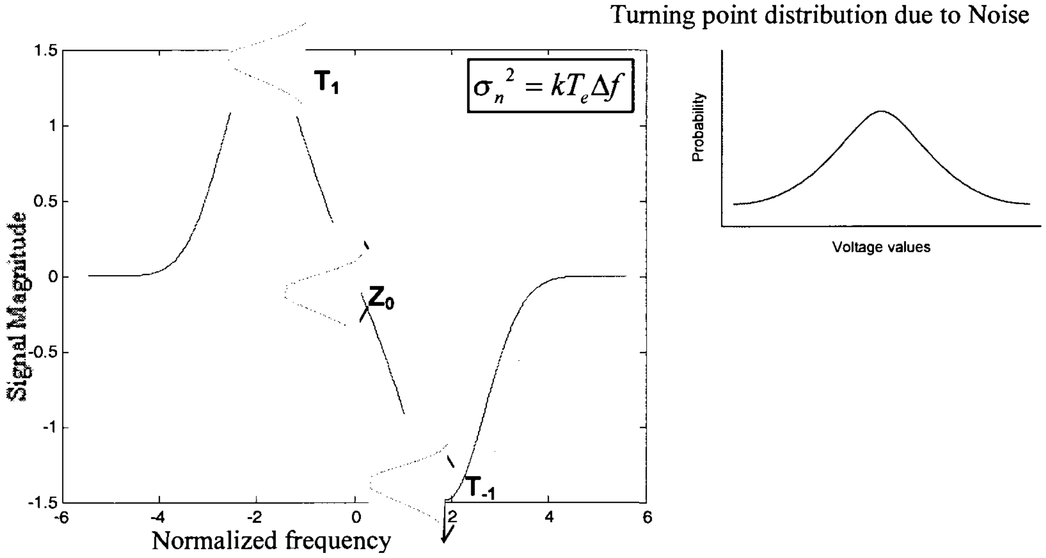

Fig. 6.5. WMS harmonic signal with additive Gaussian noise at the turning points and zero crossings. The noise distribution results in uncertainties in both spectral location and signal magnitudes

Consequently, the lineshape parameter will be a random variable. For example, the linewidth of the profile in this case will be a random variable with a distribution given by the convolution (because the linewidth can be expressed as linear combination of T/Zs) of distributions of T/Z. Once the distribution function of the parameter is obtained using Shannon's formulation, the entropy of the parameter is obtained. The following steps outline the necessary mathematical formulation.

Consider, Gaussian probability distribution of noise center at n_0 and variance, σ. Therefore,

$$p(n) = \frac{1}{\sqrt{2\pi}\,\sigma} e^{-(n-n_0)^2/2\sigma^2} \qquad (6\text{-}5)$$

This additive noise distorts each of the turning points and zero crossings which now have a distribution,

$$p(S) = \frac{1}{\sqrt{2\pi}\,\sigma} e^{-\left(S-(T_i^N+n_0)\right)^2/2\sigma^2} \qquad (6\text{-}6)$$

Here, S is the random variable associated with the values of T/Zs . T_i^N is the ith turning point (or zero crossing) of Nth detection order

For simplicity, we assume, $n_0 = 0$ (or zero mean Gaussian noise). Therefore,

$$p(S) = \frac{1}{\sqrt{2\pi}\,\sigma} e^{-\left(S-T_i^N\right)^2/2\sigma^2} \qquad (6\text{-}7)$$

since pairs of turning points are used to compute a lineshape parameter let σ_i *and* σ_j be the noise corresponding to each ith and jth turning point. The resultant distribution obtained form two turning points, T_i and T_j is

$$p(\Delta S) = p(S-S') = p(S) * p(S') = \frac{1}{\sqrt{2\pi\sigma_i}} \exp-\left(\frac{\left(S-T_i^N\right)^2}{2\left(\sigma_i\right)^2}\right) * \frac{1}{\sqrt{2\pi\sigma_j}} \exp-\left(\frac{\left(S'-T_j^N\right)^2}{2\left(\sigma_j\right)^2}\right) \qquad (6\text{-}8)$$

or

$$p(\Delta S) = \frac{1}{\sqrt{2\pi}\,\{\sigma_i+\sigma_j\}} \exp-\left(\frac{\left(\Delta S - \{T_i^N - T_j^N\}/2\right)^2}{2\{\sigma_i+\sigma_j\}^2}\right) \qquad (6\text{-}9)$$

The resultant distribution is also a Gaussian with mean and variance given by $\Delta S_{average} = \{T_i^N - T_j^N\}/2$ and, $\sigma = \sigma_i + \sigma_j$

If in case, the noise distribution is the same throughout the scan of signal acquisition, then, $\sigma_i = \sigma_j = \sigma_N$, therefore, $\sigma = 2\sigma_N$

A quick calculation of entropy (*H*) of the distribution from the combinations of T/Z of N= 1 harmonic order gives,

$$H_{N=1} = H(T_1 Z_0) + H(T_{-1} Z_0) + H(T_{-1} T_1)$$

It can be shown (Appendix E) that entropy of a Gaussian is given by, $H = \log(\sqrt{2\pi e \sigma})$, therefore,

$$H_{N=1} = \log\left(\sqrt{2\pi e}\left\{\sigma(T_1 Z_0).\sigma(T_{-1} Z_0).\sigma(T_{-1} T_1)\right\}\right)$$

And, since each of Ti and Tj have same variance , σ

$H_{N=1} = 3 * \log\left\{\sigma_N\right\} + D$

here $D = \log\sqrt{2\pi e}$

The entropy of Nth detection order can be generalized as,

$$H_N = {}^{2N+1}C_2 * \log\left\{\sigma_N\right\} + D \qquad (6\text{-}11)$$

Information *(ΔH)* is extracted by change of precision in measurements, change in temperature (*Te*) or detection bandwidth (*Δf*), since, thermal noise power have dependence given by, $\sigma_n{}^2 = kT_e \Delta f$

$$\Delta H_N = \sum_{k=1}^{M} \log\left\{\frac{\left\{\sigma_{N,k}\right\}_{T_{e1}}}{\left\{\sigma_{N,k}\right\}_{T_{e2}}}\right\} \qquad (6\text{-}12)$$

Here, $M = {}^{2N+1}C_2 = N(2N+1)$

Bits extracted in this case depends on number of pairs of combinations or detection order, N, and noise power σ^N.

6.3.1 Full scale sensitivity of lock in amplifier and information

The signal magnitudes of turning points vary with their location from the linecenter, i.e. the linecenter (of even harmonic) is a peak value: whereas, distant turning points (in wing region) decrease in magnitude with the distance from the linecenter. Exact relation between the spectral location and magnitude is not known, but it depends mainly on experimental variables such as modulation index, linewidths, pathlength etc. A physical argument to clarify this point is as follows:

A lineshape parameter can be estimated accurately using a combination of turning points e.g. for N = 2; combinations (T_2T_{-2}) and (T_1T_{-2}) can be used to compute the parameter. Since, T_2 is smaller in magnitude than T_1 the precision it is measured will be much smaller than that of T_1. Therefore, (T_1T_{-2}) is more likely to give a more precise value than (T_2T_{-2}). To account for this disparity, each turning point is weighted equally according to its magnitude, or, in other words, each is measured at full scale of 1V. Fig. 6.6, below illustrates this point.

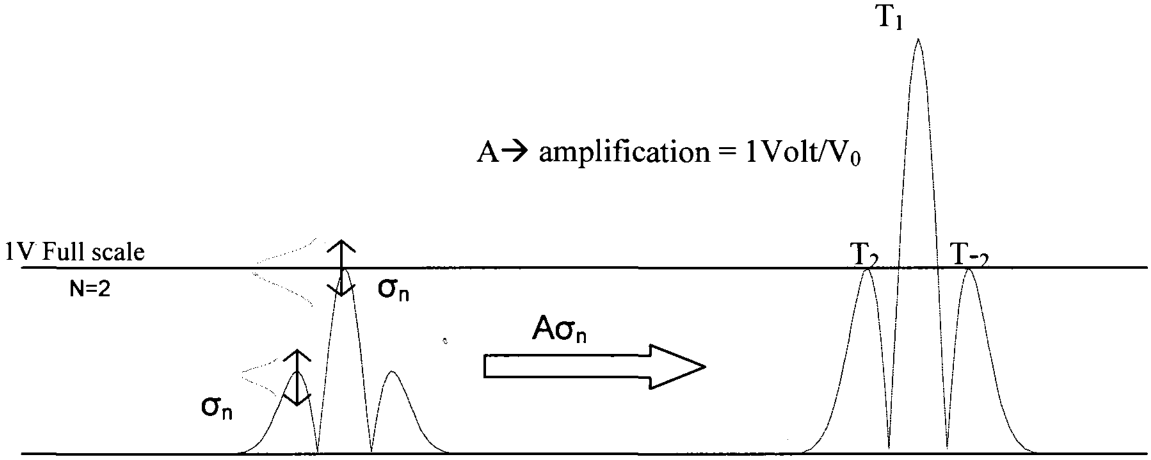

Fig. 6.6. Full scale sensitivity of individual turning points of N=2 harmonic signal. Each turning point is weighted equally with equivalent amplification of the signal to 1V.

Consider a turning point, whose voltage (distribution) on the lock in amplifier is,

$$p(V)dV = \frac{1}{\sqrt{2\pi}\sigma} e^{-(V-V_0)^2/2\sigma^2} dV \qquad (6\text{-}13)$$

Here V_0 is the average voltage. Accordingly, the signal magnitude (distribution) of each turning point weighed that is due to this amplification (A) to full scale will be,

$$p(AV)d(AV) = \frac{1}{\sqrt{2\pi}\sigma / V_0} e^{-(V/V_0-1)^2/2(\sigma/V_0)^2} dV \qquad (6\text{-}14)$$

With amplification, A = V/V_0, the normalized distribution is,

$$p(\overline{V}) = \frac{1}{\sqrt{2\pi}\,\overline{\sigma}} e^{-(\overline{V}-1)^2/2(\overline{\sigma})^2} \qquad (6\text{-}15)$$

Here, $\overline{\sigma} = \frac{\sigma}{V_0}$ is the normalized variance.

Typical values of gain sensitivity of the lock in amplifier at each detection order is given below.

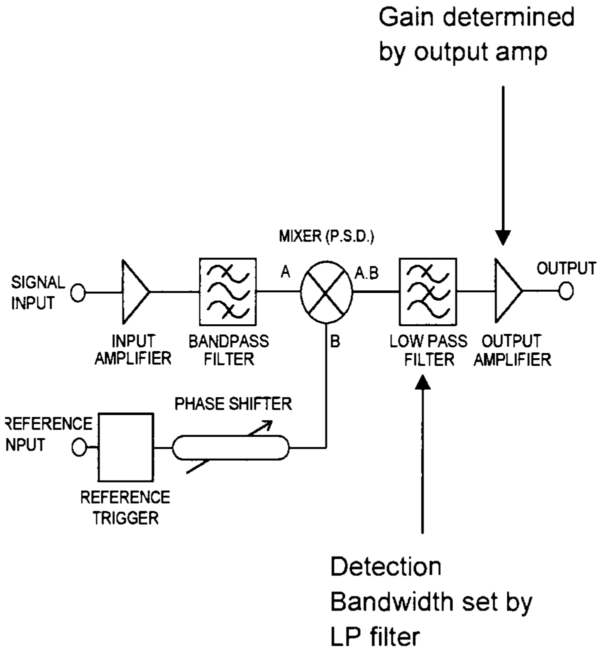

Harmonic Order, N	**FS sensitivity (mV)**	**Gain (dB)**
1	1000	20
2	500	26
3	200	34
4	200	34
5	100	40
6	100	40
7	50	46
8	50	46

Fig. 6.7. Schematic of a lock in amplifier (LIA) [17]. Typical values of LIA full scale sensitivity and gain in a WMS experiment are shown in the figure.

6.3.2 Entropy and detection order

It has been mentioned previously that there are three possible pairs of turning points and/or zero crossings ($T^1_1T^1_{-1}$, $T^1_1Z^1_0$, $T^1_{-1}Z^1_0$) for N=1 detection order to obtain lineshape parameter. Now following from the analysis in the previous section to obtain the expression for the entropy, their respective distributions can be expressed as,

$$p(\overline{\Delta S}) = p(\overline{S_i - S_j}) = \frac{1}{\sqrt{2\pi}\,\overline{\sigma}_{ij}} \exp - \left(\frac{\left(\overline{\Delta S} - 1\right)^2}{2\left(\overline{\sigma}_{ij}\right)^2} \right) \qquad (6\text{-}15)$$

The above equation is a cumulative distribution of the ith and jth turning point. Here, $\overline{\sigma}_{ij}$ is the variance of normalized magnitude of turning points T_i and T_j whose individual distribution is described (in a previous section) as $p(S_i)$ and $p(S_j)$. Therefore,

$$\overline{\sigma}_{ij} = \frac{\sigma_i + \sigma_j}{T_i - T_j}, \text{ since } \sigma_i = \sigma_j = \sigma_N$$

$$\overline{\sigma}_{ij} = \sigma_N \left(\frac{2}{T_i - T_j} \right)$$

Following from this, the entropy (for N = 1) of a parameter from the pair of three independent distributions [3-6] can be expressed as,

$$H_{N=1} = H(\overline{T}_1\overline{Z}_0) + H(\overline{T}_{-1}\overline{Z}_0) + H(\overline{T}_{-1}\overline{T}_1) \qquad (6\text{-}16)$$

Since, the individual distributions are Gaussian; the total entropy is then given by;

$$H_{N=1} = \log\sqrt{2\pi e}\left\{\overline{\sigma}(T_1Z_0).\overline{\sigma}(T_{-1}T_0).\overline{\sigma}(T_{-1}T_1)\right\} \qquad (6\text{-}17)$$

Substituting from above,

$$H_{N=1} = \log\sqrt{2\pi e}\left\{\sigma_N\left(\frac{2}{T_1 - Z_0}\right).\sigma_N\left(\frac{2}{T_{-1} - Z_0}\right).\sigma_N\left(\frac{2}{T_1 - T_{-1}}\right)\right\} \qquad (6\text{-}18)$$

$$H_{N=1} = -\log\left\{((T_1 - Z_0)/\sigma_N).)(T_{-1} - Z_0)/\sigma_N).((T_1 - T_{-1})/\sigma_N)\right\} + D' \quad (6\text{-}19)$$

where constant, $D' = \log 2^3\sqrt{2\pi e}$

or,

$$H_{N=1} = -\sum\nolimits_{i,j=-1}^{1} \log\left\{\Delta S_{ij}/\sigma_N\right\} + D' \qquad (6\text{-}20)$$

In general, the entropy of Nth harmonic:

$$H_N = -\sum\nolimits_{i,j=-k}^{k} \log\left\{\Delta S_{ij}/\sigma_N\right\} + D' \qquad (6\text{-}21)$$

$k = {\left({}^{2N+1}C_2\right)-1}\big/{2}$; $Nodd$ and $k = {\left({}^{2N+1}C_2\right)}\big/{2}$; $Neven$

6.3.3 Information and optimal detection order

In any measurement information is gained from the reduction of uncertainty, mainly due to change in measurement precision. The question we address is: "*How much information is gained in any Nth harmonic when instrument precision is increase by a finite amoun?*" Assuming that the measurements are performed for two sets of experiments with a variable, e.g. modulation index, changed from m_1 to m_2. Therefore, information extracted (or change in entropy), using Eqn. (6-21),

$$\Delta H_N = \sum\nolimits_{i,j=-k}^{k} \log\left\{\frac{\left\{\Delta S_{ij}/\sigma\right\}_{p_2}}{\left\{\Delta S_{ij}/\sigma\right\}_{p_1}}\right\} \qquad (6\text{-}22)$$

Here, p_1 and p_2 is denotation for precision in the two sets of experiments. It should be noted from above, information that is extracted depends on the total number of *discernible* turning points that are available and the signal to noise power. Although signal magnitude increase with index values, in certain experiments small index values are required. This choice of index is imperative for probing sensitive effects such as, pathlength saturation or resolution of overlapping lines. The disadvantage of small modulation index is weaker signal magnitude, where the turning points in wings may not appear discernible.

The figure below shows information extracted with respect to detection order for two set of experiments where modulation index is varied by a certain amount.

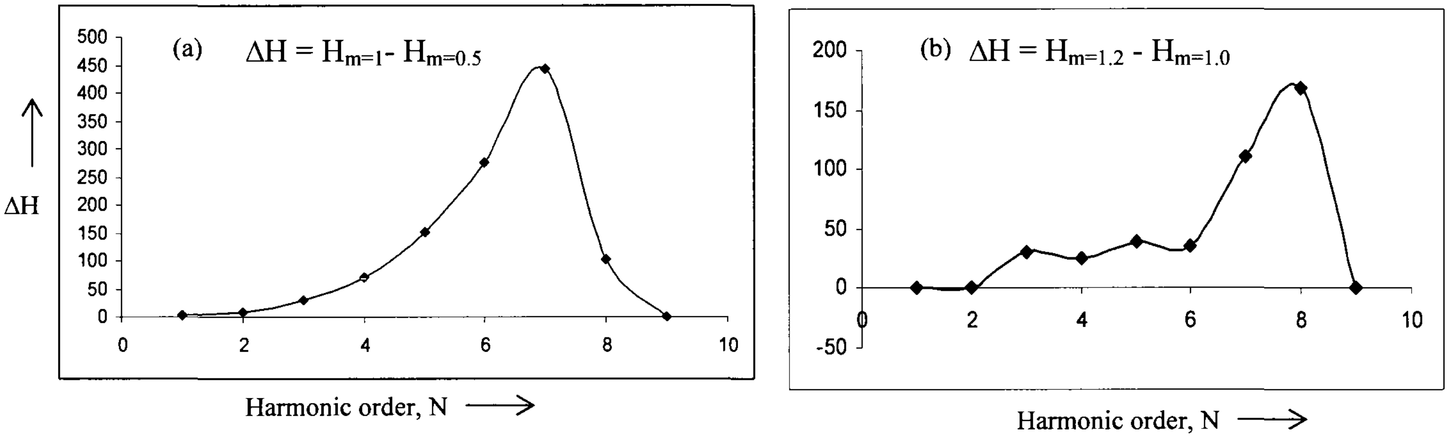

Fig. 6.8. Information extracted vs. the harmonic order, N, for two set of modulation indices and fixed noise power (σ_n). Maximum information is extracted at N=7 and N=8. The available turning points (or structure) that are discernible are maximum at N=7 and N=8.

In other words, the measurement precision increases with the modulation indices, but may result in loss (of information) of subtle effects (complete overlap of weaker transitions or saturation effects) as a result of modulation broadening. The plots in Fig. 6.8 (a) and (b) above indicate two important aspects of information and structure. The information extracted peaks at the values (N =7) where maximum turning points are discernible and begins to fall since the turning points cannot be mined even if the modulation index is increased. This is also demonstrated when the peak in the next figure moved to higher detection order (N = 8) where a higher index was employed.

6.4 INFORMATION IN LINEWIDTH MEASURMENTS

As mentioned in chapter 4, a lineshape parameter e.g. linewidth or absorption cross-section is estimated from the best fit between theory and experiment. This is one of the reasons that turning points and zero crossings are considered key markers because the mismatches due to deviations in an absorption profile are significant. The uncertainty in experiment is due to imprecision in measurement of signal magnitude of turning points. Similarly, the uncertainties in models are the result of imprecise measurements of wavelength, modulation index and also in lineshape function, but for simplicity we assume the functional form, g(*v*) is precisely known. Both these uncertainties in experiment and model, which are independent of each other, result in a cumulative uncertainty in estimation of a lineshape parameter.

Consider the error or difference between the theoretical model and experimental expressed as,

$E = |S^N{}_{exp} - S^N{}_{model}|$.

Therefore, the error distribution is the mismatch between experiment and theory, or the error, is,

$$p(E) = \frac{1}{\sqrt{2\pi}\,\sigma_E} e^{-(E-E_0)^2/2\sigma_E^2} \qquad (6\text{-}23)$$

From the above Eqn. (6-22), the mean of the error distribution given by,

$E_0 = |S^N_{exp} - S_{model}|_{average.}$

Note that this error is similar to the analysis in chapter 5.

The deviation or the error distribution, E, is given by the sum of the individual uncertainties (see schematic, Fig. 6.9 below).

$\sigma_E = \sigma_{exp} + \sigma_\lambda$

Assuming that both the experimental lock-in amplifier signal and the model have the same uncertainty i.e. $\sigma_{exp} = \sigma_\lambda = \sigma_N$. The normalized uncertainty that is due to disparate signal magnitudes across the WMS spectrum is:

$$\overline{\sigma}_N = \frac{\sigma_{exp} + \sigma_\lambda}{\left|S^N_{model} - S^N_{exp}\right|_{av}} = \frac{2\sigma_N}{E_0} \qquad (6\text{-}24)$$

Note: σ_λ is the wavelength or model uncertainty. Here, we assume that the transformation from wavelength to a model data is a linear one i.e. $S_{model} = k\lambda$, therefore, $\sigma_{model} = \sigma_\lambda$

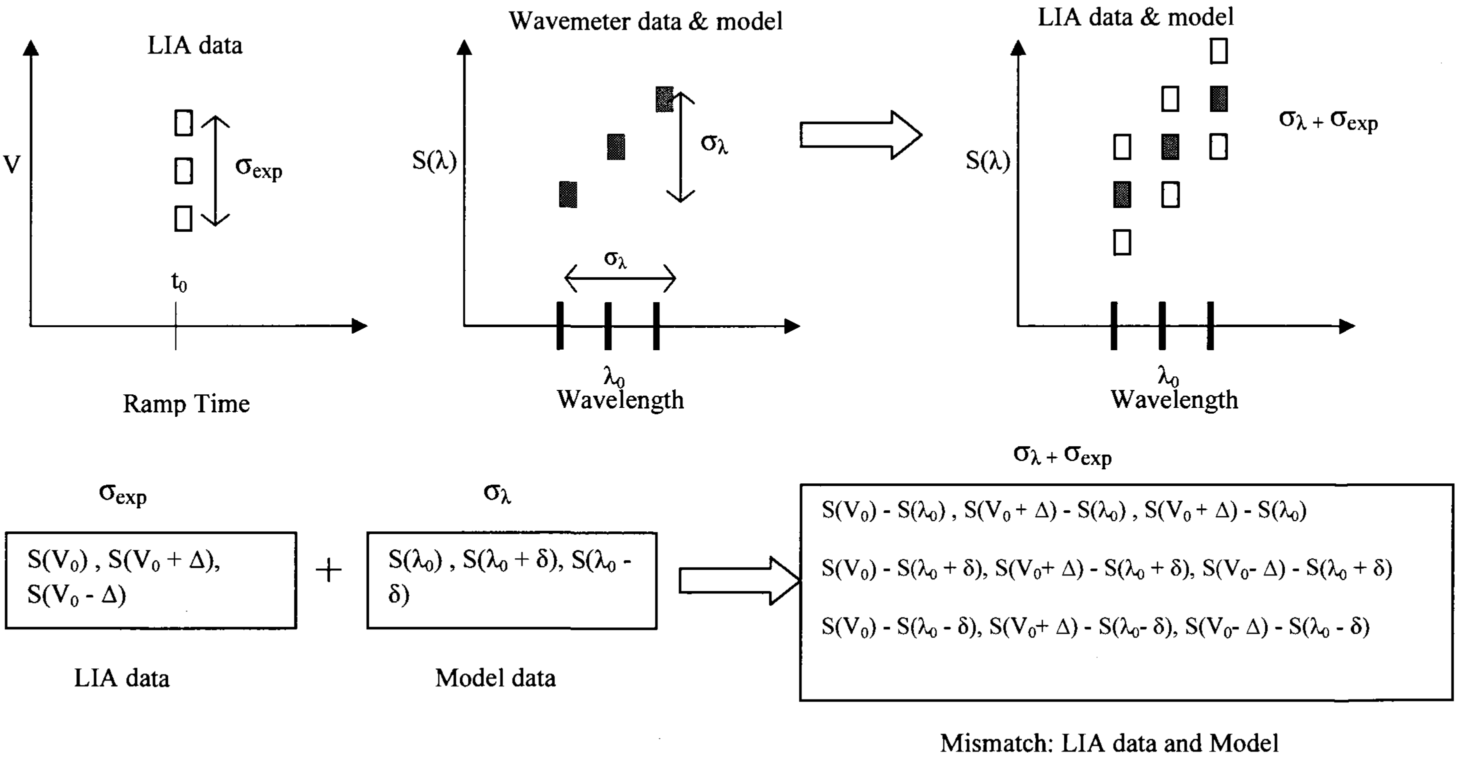

Fig. 6.9. Cumulative uncertainty in experimental signals and model data is equivalent to the convolution of the individual distribution.

From the above distribution, the entropy is given by,

$$H_{\Delta\nu}^{N} = -\sum_{i}^{k} \log\left\{E_i^N / \sigma\right\} + D \tag{6-25}$$

Here, k = 2N+1 or number of discernible turning points.

The information extracted by a finite change in the precision is:

$$\Delta H_{\Delta\nu}^{N} = \sum_{i}^{k} \log\left\{E_i^N / \sigma\right\}_{m_2} / \sum_{i}^{k} \log\left\{E_i^N / \sigma\right\}_{m_1} \tag{6-26}$$

The figure below shows information as a change in harmonic order. The information is extracted when the error between model and experiment is optimized. The error in the analysis is considered due to mismatch in the linewidth or absorption cross-sections. At higher harmonic, the mismatch is higher or ΔS/σ is greater. The curve below peaks at the detection where the maximum number of turning points are discernible and cumulative mismatch is the largest. And ultimately the curve reduces to a finite value because the signal deteriorates at that noise power to the extent that it completely blurs turning points. Therefore, additional turning points do not show and structure is reduced. The above analysis can also be extended to deviation in a lineshape profile and their corresponding WMS signals are due to density or pressure variations. There are aspects that are closely related to the variance of error analysis discussed in the previous chapter.

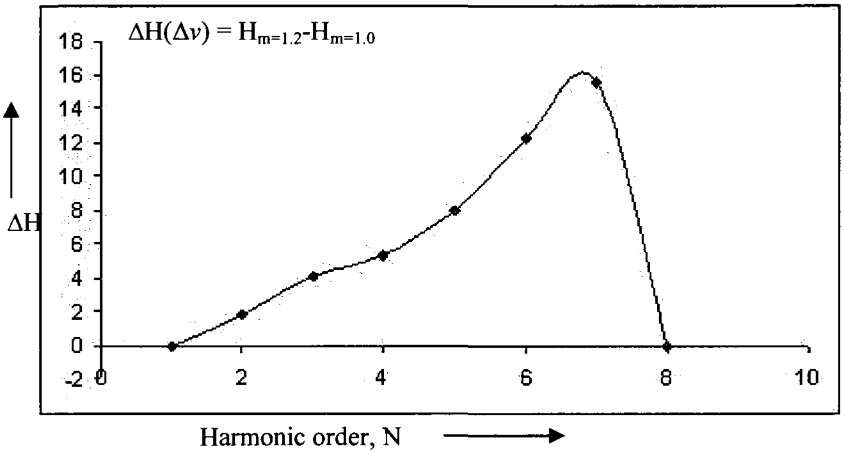

Fig. 6.10. Information extracted in linewidth measurements. Given the set of experimental conditions and noise environment, N=7 is found to be the optimal detection order.

6.5 INFORMATION AND FINITE PRECISON OF INSTRUMENT

Apart from the noise uncertainty discussed in the previous section, the measuring instruments have a certain precision in measurements that result in loss of information. To illustrate the above point, consider a schematic of WMS detection electronics as shown in Fig. 6.4. We assume that the additive noise is Gaussian in nature and it adds to the Lock-in-amplifier (LIA) data. The final output is such that its mean is shifted by the signal magnitude of the LIA. Also, the variance of the signal magnitude of turning points or zero crossings is the same as σ. Now if the measuring apparatus has a finite precision (Fig. 6.11) the noise (or turning points) distribution will modify to a discrete (a step function) function. The analysis below accounts for this additional uncertainty.

The distribution of measured voltage values of turning points of WMS signals in the presence of Gaussian noise is given by Eqn. (6-26) below. Any Nth order harmonic will have N+1 such distributions of turning points and N distributions of zero crossings.

$$p(V)dV = \frac{1}{\sqrt{2\pi}\sigma} e^{-(V-V_0)^2/2\sigma^2} dV \qquad (6\text{-}27)$$

In addition to noise, the precision of the instruments being used also needs to be considered. Fig. 6.11 shows this in the form of an imprecision of 2Δ in the measurement of the voltage representing the signal. A finite precision of the detector blurs any voltage (V →V ± Δ) in a certain range of values, Δ, initially distinct, to appear indistinguishable. The relevant probability distribution of a measurement in which such an uncertainty is introduced is,

$$p_i = \int_0^{V_i+\Delta} p(V)dV - \int_0^{V_i-\Delta} p(V)dV \qquad (6\text{-}28)$$

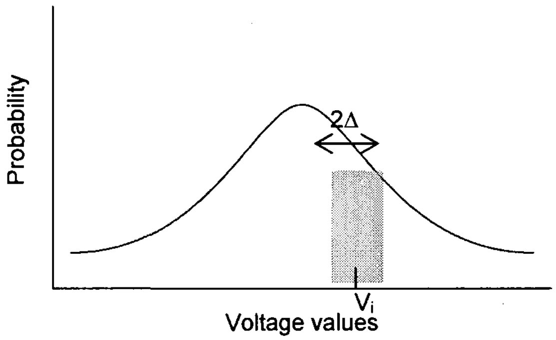

Fig. 6. 11. Detector imprecision modifies the distribution of the turning points to discrete values.

Therefore,

$$p_i = \frac{2}{\pi}\{erf(x_i + \overline{\Delta}) - erf(x_i - \overline{\Delta})\} \qquad (6\text{-}29)$$

where, $x = (V - V_0)/\sqrt{2}\sigma$ and $\overline{\Delta} = \Delta/\sqrt{2}\sigma$

The entropy, $H = -\sum_i \{p_i\}\log\{p_i\}$ in the above case depends on the noise distribution, σ_n, and the detector precision, Δ. If the measurements were infinitely precise (something obviously not possible in practice), then one would extract a maximal amount of information. It should be noted that an infinitesimal value of Δ recovers the original distribution of the turning points. In this case one extracts maximal information, since each p_i is absolutely distinct.

Figs. 6.12 and 6.13, show information extracted at various detection orders, N, when the precision size, Δ (= ηV; η is %age uncertainty in the magnitude, V, of a given turning point) is changed, and, there is a fixed amount of Gaussian noise, σ_n, for all detection orders. In addition, in the calculations peak value of N=1 harmonic is normalized to unity, and all the other harmonics (N>2) are factored with the peak value of N=1 harmonic signal. It is also assumed that the total number of turning points (or structure in the signal) available at a particular detection order, N, depend on the ratio of their magnitudes to the noise. In other words, one registers a turning point only if it is above a certain noise tolerance (taken, in this case, $V/\sqrt{2}\sigma_n \geq 5$); all other turning points are assumed obscured by noise and not considered for computational purposes. For example, in N=9 detection order for a given modulation index the turning points that are farther in the wings, are very small compared to the noise variance. Hence, eventually a further increase in detection order, N, brings about diminishing returns and we begin to lose turning points (or structure) as their magnitude reduces significantly compared to noise. Therefore, the amount of information extracted does not increase continuously with the detection order, and shows a maximum at a particular detection order. In the specific case shown in Fig. 6.12 the optimum harmonic detection order is N = 7.

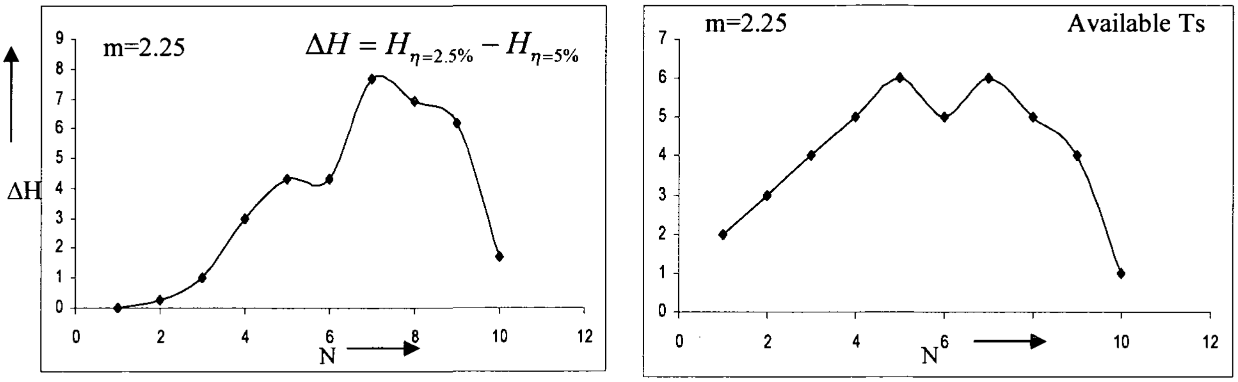

Fig. 6.12. Information is extracted when the precision is increased. The information extracted at different detection order, N, varies with the available turning points or structure in the signals. The total number of turning points (Ts) discernible (above a certain noise tolerance) in any detection order show the same trend as that of ΔH.

6.5.1 Dependence of information extracted on the frequency modulation index

A WMS signal grows with the modulation index, m. In comparison the noise power does not change significantly. Therefore, the conventional SNR increases with m, and the total number of turning points discernable at higher detection increases. For smaller m values, the number of available turning points is greatly reduced at higher values of N.

Fig. 6.13 shows results of computations performed at lower index values, m=1, than in the previous set of m = 2.25 (in Fig. 6.12 above). The plots with lower modulation values, m=1, yield maximal information at a lower order, N=4, compared to the plots with relatively higher m = 2.25, (maximum information at N=7) for the same instrument precision. It should be noted that for m=1 the maximum number of available turning points are at N= 3: whereas, for m= 2.25 the maximum number is at N= 5 and 7.

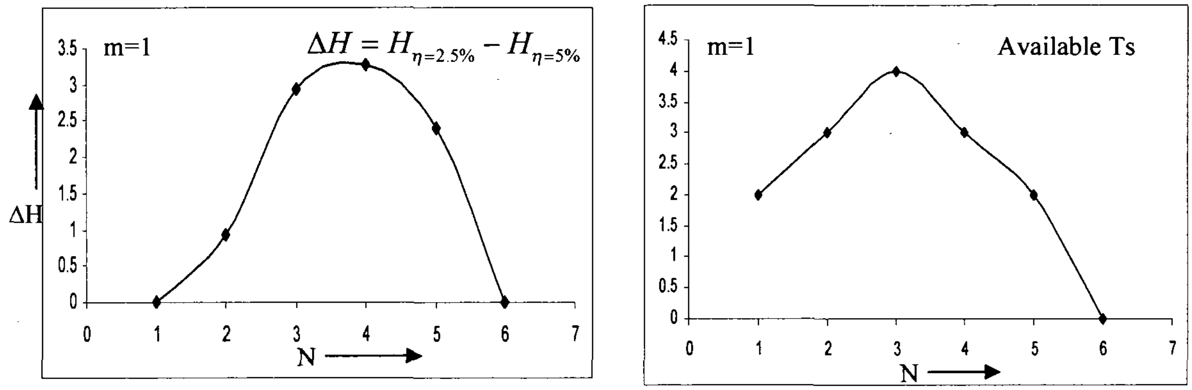

Fig. 6. 13 Information extracted at different detection orders at lower modulation index, m=1. Compared to m=2.25 the maximal information occurs at lower harmonic order. Due to smaller SNR the total number of available turning points (Ts) reduces significantly.

6.6 MODULATION DISTORTION AND RESOLUTION OF OVERLAPPING LINE TRANSITIONS

Higher modulation indices improve signal power and therefore the conventional SNR. In this respect an increased modulation index results in a larger amount of information extracted (as can be seen by comparing Fig. 6.12 with Fig. 6.13). On the other hand, an increased modulation index also results in signal broadening [18] and this can be detrimental in resolution of overlapping lines. This imposes limitations, and the choice of an optimal modulation index becomes quite complicated when the aim is to resolve interfering lines.

The presence of an interfering line increases the turning points ($2N_{(LINE1 + LINE2)} + 2$) and zero crossing ($2N_{(LINE1 + LINE2)}$). To illustrate this point consider an example where the spectrum of interest contains two absorption features with exactly the same lineshape parameters, except the linecenter. If the absorption lines are relatively far apart then one can fully resolve the transitions at lower harmonics with relatively small modulation indices. However, if the line separation is significantly small, then one might resort to higher detection orders. This generally requires a set of higher modulation values. The resolution of lines becomes more challenging if the two have disparate lineshape parameters, especially if the absorption cross-section of one line is orders of magnitude smaller than the other. Therefore, there exist a range of modulation indices (depending on the noise figures of the detection electronics) for a set of lineshape parameters that allows resolution of these interfering transitions. This *range of modulation index determines the total number of turning points of the two overlapping transitions that are distinct.* In other words, there is a finite amount of information that can be extracted in each detection order when the modulation index is varied within a finite range of values. For example, the calculation below shows information extracted in, N=3 and N=7 detection orders obtained at two modulation indices, when two overlapping lines appear fully resolved, (i.e. all 2N+2 turning points due to the two lines are completely distinct) and when they are partially resolved.

For, N=3

$\delta H_{N=3} = \sum_i \log\{\sigma_n (V_{i,m=2, N=3})\} - \sum_i \log\{\sigma_n (V_{i,m=4, N=3})\}$

$= 8\log\{ \sigma_n \}-6\log\{ \sigma_n \} = \mathbf{2\log\{ \sigma_n \}}$

Also, the information extracted for N=7;

$\delta H_{N=7} = \sum_i \log\{\sigma_n (V_{i,m=2, N=7})\} - \sum_i \log\{\sigma_n (V_{i,m=4, N=7})\}$

$= 16\log\{ \sigma_n \}-11\log\{ \sigma_n \} = \mathbf{5\log\{ \sigma_n \}}$

Fig. 6.14 shows 3rd and 7th order WMS signals of two overlapping lines (same linewidth) with different absorption cross-sections, σ_{abs} ($\sigma_{abs\text{-}LINE1} = 10\ \sigma_{abs\text{-}LINE2}$). The plots show that the lines are fully resolved lines when m = 2: whereas, the increased modulation broadening at m = 4 results in only a partial resolution of the interfering lines. It can be seen that the amount of information extracted (Appendix F) is different for the two detection orders by the same changes in modulation indices from, m = 4 to m = 2. It should be noted, that the total number of turning points, or the structure in the signal, is the sum of turning points (of individual transition), that are not masked due to overlap or obscured due to noise or distortion.

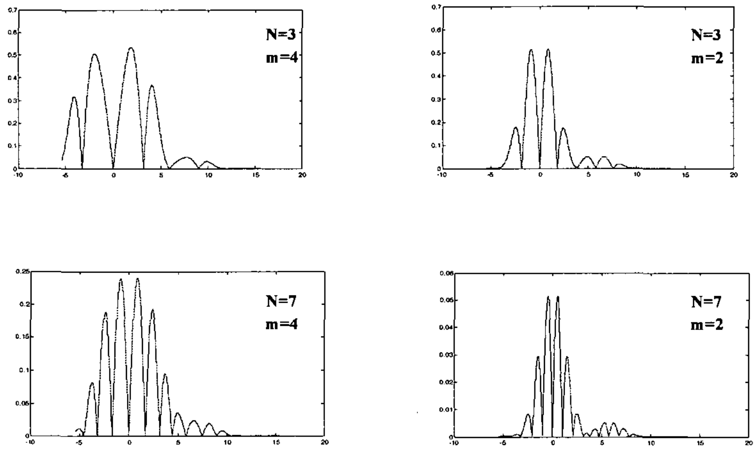

Fig. 6.14. N= 3 and N=7 detection order of two overlapping transitions at modulation indices, m=2, where lines are fully resolved and m=4, when lines are partially resolved. For N=3, the total number of turning points in fully resolved lines (at m=2) is 8 and for N=7 it is 16. At higher modulation indices (m=4) some of these turning points are masked due to overlap, i.e. for N=3, the total number of available turning points are 6, where as for N=7 it is 11. Therefore, the information extracted when modulation index is changed from fully resolved (m=2) to partially resolved (m=4) lines is $2log\{\sigma_n\}$ for N=3 and $5log\{\sigma_n\}$ for N=7.

The table below shows the amount of information extracted (at various detection orders) when two overlapping lines are fully resolved at smaller values of modulation index (m = 2) compared to the case when these lines are partially resolved at relatively higher m values, m = 3 and m = 4. The calculations for the table are carried out with a Gaussian uncertainty in the turning points due to noise: however, there is no imprecision considered (as in the previous section) in this case.

Table. 6.2 Number of discernible turning points at different modulation indices (m = 2, 3 and 4) at detection orders N = 1 to 9. Information extracted for fixed noise power is directly proportional to number of additional turning points discernible by change in index values.

N	**TPs at m=2** *(fully resolved)*	**TPs at m=3** *(partially resolved)*	**TPs at m=4** *(partially resolved)*	**Information extracted,** $\delta H(m=2 \rightarrow m=3)$	**Information extracted,** $\delta H(m=2 \rightarrow m=4)$
1	4	4	3	$log\{\sigma_n\}$	$log\{\sigma_n\}$
2	6	5	5	$log\{\sigma_n\}$	$log\{\sigma_n\}$
3	8	6	6	$2log\{\sigma_n\}$	$2log\{\sigma_n\}$
4	10	8	7	$2log\{\sigma_n\}$	$3log\{\sigma_n\}$
5	12	10	9	$2log\{\sigma_n\}$	$3log\{\sigma_n\}$
6	14	11	11	$3log\{\sigma_n\}$	$3log\{\sigma_n\}$
7	16	11	11	$5log\{\sigma_n\}$	$5log\{\sigma_n\}$
8	18	13	11	$5log\{\sigma_n\}$	$7log\{\sigma_n\}$
9	20	16	14	$4log\{\sigma_n\}$	$6log\{\sigma_n\}$

In the given set of computations given above, maximal information is extracted when the lines are fully resolved. This occurs at N = 7 and N = 8. The results presented in the previous sections and in the table that for a set of experimental parameters there exists an optimal detection order where maximal information can be mined about an experiment based on structure rather than its SNR.

6.7 CONCLUSION

An aspect of Shannon's formulation of information and entropy is introduced in the analysis of information content in modulation spectroscopic signals. It is seen that the amount of relevant information (quantified in bits) depends on the structure of WMS signals, noise and imprecision in the measuring apparatus. A key aspect of distortion in WMS is modulation broadening. Its connection to information extracted in overlapping lines was investigated. It is observed that in certain situations higher detection orders ($N \geq 2$) enable one to extract more information and the signals are fully resolved. This is in agreement with trends that we have verified experimentally previously. The analysis presented in this chapter can be extended to the situations where the spectrum contains absorption features of more than two overlapping transitions. In addition several subtle effects such as optical pathlength saturation, distortion effects like Fabry-perot fringing can also be quantified in terms of information theory. In addition, practical limitations such as noise in the detection electronics, finite bandwidth, photodetector sensitivity when combined with the distortion effects in the experiment; the information theory developed in this chapter reproduces features of WMS experiments and optimal detection order.

A comprehensive theory of information in estimation of lineshape or gas parameters in a WMS would require accounting for all possible distortion and noise sources in the experiment. These are categorized in two possible classifications, as shown below.

Uncertainties in the Detection Electronics

- Photodetector Noise
- Finite Precision
- Full scale sensitivity
- LIA bandwidth

⊕

Probe distortion/Physical effects

- Modulation and Pressure Broadening (m)
- Pathlength Saturation (τ)
- Fabry-Perot Fringing (Q)
- Interference from overlapping transitions ($\Delta \nu_0$)

⇩

Amount of information extracted in an experiment

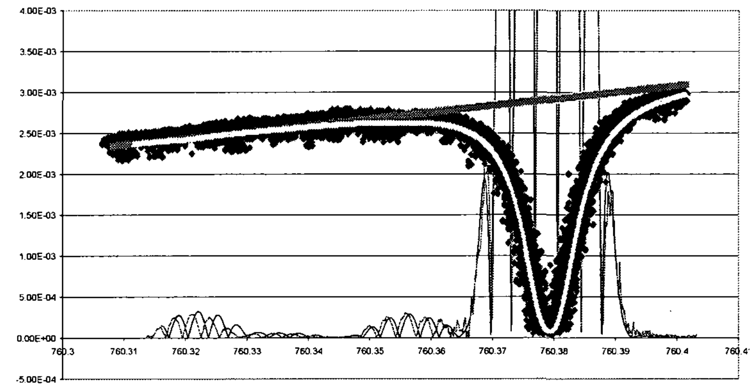

Fig. 15. Resolution of weaker lines and direct absorption signal scaled to magnitude of 8th harmonic. The WMS signal, which is variation of the lineshape profile shows considerable structure and hence an aid to resolution.

On a final note of consideration, an absorption spectrum in a given scan can be viewed as a linear system. The input is an absorption lineshape profile, which is processed by a narrow band amplifier, whose effective response function (A) is a function of experimental and detection parameters. The output is a signal with structure that encodes the information about the input convolved with the response function of the (narrow band) amplifier.

$$A = m_{eff} = f(\beta, \Delta\nu_{eff}, \bar{\sigma}, g, n, L, k) \qquad (6\text{-}30)$$

Here, β is the modulation amplitude and $\Delta\nu_{eff}$ is the effective linewidth of the profile that the laser samples. This is due to the fact that broadening effects like saturation modify the linewidth and hence the modulation index for that particular transition, i.e. $m_{eff} = \beta / \Delta\nu_{eff}$

Also, in the above expression, $\bar{\sigma}$ is the absorption cross-section, g is the lineshape function, n is the density of the absorber, L is the sample length and k is the detection order. Therefore, the effective amplification of the signal depends on the characteristics of the detection electronics and collision dynamics of the physical process under investigation.

Information in Resolution of Overlapping Lines- Amplification (A) of Weak lines

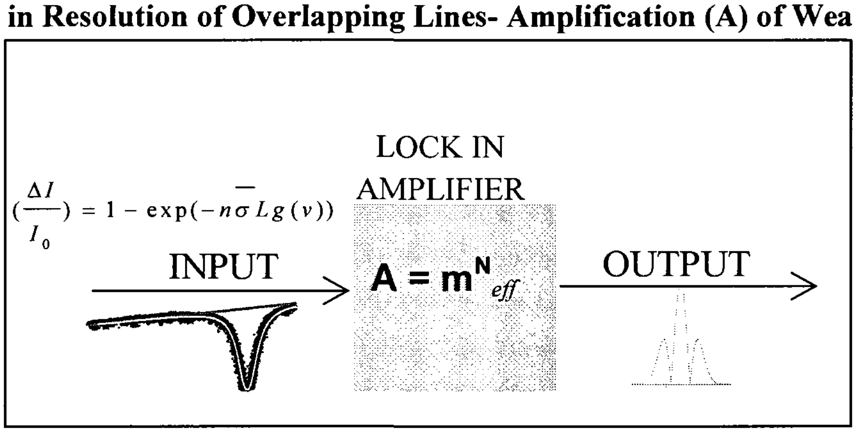

Fig. 16. WMS setup and its equivalence with a linear system.

Aspects of information theory developed in this chapter are also closely related to the chi-square measure discussed in the previous chapter. It is shown that there is a connection [19, 20] between chi-square measure and principles of maximum likelihood or maximum entropy. While the analysis deals with WMS signals it can also be extended to other measurement techniques where signals have a significant contrast with respect to a reference- for example, such applications include scattering measurement and those that are done with phased antenna arrays [21, 22].

6.8 REFERENCES

1. C. E. Shannon, "A Mathematical Theory of Communication- Part 1," *Bell System Technical Journal* 27, 379 (1948).

2. C. E. Shannon, "A Mathematical Theory of Communication- Part 2," *Bell System Technical Journal* 27, 623 (1948).

3. M. A. Khan, K. D. Mohan, A. N. Dharamsi, "Information Theory of High-Precision Measurements" *Frontiers in Optics: Laser Science-* XXIV (2008).

4. M. A. Khan, Karan D. Mohan and A. N. Dharamsi, "Signal Structure and Precision in Optical Measurements: A new perspective to optimal experimental techniques," *IEEE Lasers and Electro Optic Society Annual Meeting, Conference Proceedings* (2008).

5. M. A. Khan and A.N. Dharamsi, "Information Extraction from Congested Molecular Spectra by Modulation Spectroscopy,"– *75th annual southeastern APS meeting* (2008).

6. M. A. Khan and A.N. Dharamsi, "Signal Structure and Sensitive Detection of Molecular Species: Optimal experimental techniques in Wavelength Modulation Spectroscopy" *Proceedings of SPIE, OPTO* (2009).

7. C.H. Bennett, "Thermodynamics of Computation-A review," *Intl. Journal of Theoretical Physics*, 21, 12 (1982).

8. C.H. Bennett and R. Landauer, "The Fundamental Physical Limits of Computation," *Scientific American*, 253, 48-56 (1985).

9. R. Landauer, "Computation, Measurement, Communication and Energy Dissipation," Selected Topics in Signal Processing, 18-47, Wiley Press (1998).

10. M. A. Khan, Karan D. Mohan, A. N. Dharamsi, "Thermodynamic Efficiency of Information Processing in Photonic Devices" Frontiers in Optics: *Laser Science*- XXI (2005).

11. M.A. Khan, J.M. Barrington and A.N. Dharamsi, "Sensitive Detection of Molecular Species by Modulation Techniques: A Measure of Information Content in Spectroscopy", *Proceedings of SPIE* Vol. 4634, 83–91 (2002).

12. K. D. Mohan, M. A. Khan and A. N. Dharamsi, "Optimization of Nano photonic sensors and detectors by information theoretic principles," *Proceeding of SPIE* Vol: 6008 Nanosensing Materials and Devices II, p318, (2005).

13. K. D. Mohan, M. A. Khan and A. N. Dharamsi, "Thermodynamics of information loss in spectroscopic measurements," *SPIE Symposium on Optics East*, 6377-27 (2006).

14. R.C. Tolman, The Principles of Statistical Mechanics, Dover Pub. , New York, (1980).

15. M.A. Khan and A.N. Dharamsi, "Quantitative metrics of efficacy of higher harmonic detection in wavelength modulation spectroscopy for precision measurements," *Proceedings of SPIE* Vol. 5364, 227–234 (2004).

16. M. A. Khan, Karan D. Mohan and A. N. Dharamsi, "Wavelength Modulation Spectroscopy as a sensitive probe for wing structure of absorption lines," *Manuscript in preparation.*

17. Stanford Research Lock-in Amplifier - SRS 830 data manual, www.thinksrs.com.

18. G. V. H. Wilson, "Modulation broadening of NMR and ESR line shapes," *J. Appl. Phys.* 34, 3276 (1963).

19. J.N. Kapur, Maximum-Entropy Models in Science and Engineering, John Wiley, New York (1989).

20. Karmeshu (Editor), Entropy Measures, Maximum Entropy Principle and Emerging Applications, Springer, (2003).

21. K. D. Mohan, M. A. Khan and A. N. Dharamsi, "Information Content in Antenna Radiation Patterns"- *75th Annual Meeting of the Southeastern Section of APS meeting* (2008).

22. K. D. Mohan, M. A. Khan and A. N. Dharamsi, "A quantitative measure for information content in antenna array radiation patterns" *SPIE Symposium on Defense and Security*, April (2009).

CHAPTER 7

SUMMARY

Shannon's information theory is applied to Wavelength Modulation Spectroscopy (WMS) providing quantitative figures of merit such as the measurement precision and a prediction of the optimal detection harmonic order to be used. The analysis was based on complexity in the structure of WMS signals and uncertainty in these salient points. The removal of this uncertainty ultimately leads to information, in bits, that can be extracted in any WMS measurement.

The central result of this dissertation can now be stated: Measurements done by modulation experiments will have certain optimal harmonic detection orders that yield the most precise results, given a certain set of experimental apparatus and a particular noise environment. There are many instances where measurements at higher harmonic detection orders will yield a higher precision in-spite of the fact that with every increase in the detection order the signal decreases [Chapters 4 and 5]. It should also be emphasized that this increase in precision in measurement is quite separate from the well-recognized increase in signal to noise ratio that is obtained by synchronous detection at frequencies at which the noise spectral intensity is low. The inherent advantage of higher harmonic detection demonstrated here is due to the richer structure of the signals [Chapter 6].

The theory is applied to experimental results we have obtained in WMS experiments in congested spectra with overlapping lines that have highly disparate absorption cross-sections [Chapter 3]. We have shown that there are some parts (where it exhibits turning points and zero crossings) of the WMS signal that play a larger role in conveying information about the measurement than other parts of the signal. All other factors being equal, the investigation of relative heights of zero crossings and turning points in WMS signals allows one to quantify results with a tighter precision and greater sensitivity than in a direct absorption measurement.

The experimental methods discussed in the dissertation allow one to probe lineshape profiles by observing how the signal profile varies with various parameters e.g. the modulation index, lineshape parameters, gas environment or absorption pathlength. This is particularly evident in the signal around line center displays effects of saturation that are characteristic of the lineshape. This method is powerful because, ultimately, all the information about any measurement is contained in the lineshape profile. And, since different lineshape profiles exhibit different saturation behavior the higher harmonic signals then display characteristic features of the functional form of the lineshape. In our discussion we have addressed the features of subtle effects on the central lobes as well as turning points in wings. There are definite relationships between the variation of the individual side lobes as well as their relative magnitudes that yield further information about these effects as well as about the lineshape function itself. Although the dissertation mainly concentrated on the analysis with Voigt lineshape profile, the method can be extended to other profiles like Rautian and Sobelman or Galatary profiles. Each of these profiles shows characteristic behaviors of collision dynamics, perturbation or narrowing effects and its signatures on them. In summary, the results of the present work, however, show that one could use the diode laser sensor employed with modulation spectroscopic technique to measure such absorption saturation effects in wide areas of applications.

Although the emphasis was mainly on WMS measurements, the analysis can be extended to any measurements of signals with structure with any spectroscopy measurements in general. Practical applications follow immediately. For instance, the technique, which is non intrusive and a sensitive probe can be used for a variety of applications including atmospheric remote sensing, areas in astronomy (study of stellar phenomena and atmospheres), characterization of (diode) lasers etc. The aspect of structure and information can be extended for a generalized theory that optimizes measurements.

The aspect of information discussed in the dissertation is not a new notion. There have been several theories that have been proposed to address problems in science and engineering in the framework of information theory [1-6]. Key ideas like maximum likelihood or maximum entropy are general and applicable to any scenario where one seeks an optimal solution to a problem which is statistically dependent on a number of parameters and their probability distribution. In addition, there have been several places in study of spectroscopy where signals (concentration of signature peaks in spectra) and their properties were analyzed in light of information theory. Some of these works have been reported in Nuclear Magnetic Resonance spectroscopy (NMR), Optical information and spectroscopic imaging techniques.

Future work can address inherent physical effects i.e. perturbations in molecular (or gas) dynamics and its connection to information theory. For example, effects that leads to deviation in lineshape profiles e.g. narrowing effects (Dicke Narrowing) and the amount of information extracted when such effects are probed at different set of experimental precision. Their dependence on the environment and experimental variables can be quantified and ultimately a combination of optimal set of parameters can be obtained that give maximal information about narrowing parameters. One could in this case give a range of sets of these parameters and conditions, when these subtle effects can be accurately measured. In the dissertation, we have shown that measurements in certain regions of far wing structures of the lineshape profile, where the sensitivity to a lineshape parameter (or narrowing parameter) could be maximum precise and give more accurate measurements of the profile. For instance, we have shown that there are regions in far-wing where turning points show significant growth when cumulative signal power reduces with the detection order. Therefore, one can postulate subtle effects like narrowing could possibly be measured accurately in certain wing regions of the harmonic signals.

On a final note, it has been established by the works of Bennett, Launderer and Feynman [7-11] that there is a close connection between information, erasure (information loss) and heat generated in that process. This ultimately gives a fundamental limit on thermodynamics of computation, thus connecting a computational (or algorithmic) notion of information to a physical entity. This kind of explicit accounting of entropy as well as energy is not done now but will become necessary as the measurements approach their fundamental physical limits. Therefore, the connection can be utilized in obtaining the fundamental limit of efficiency of components e.g. photonic devices that are used in measurements. This ultimately will encompass all aspects of physical dynamics of an experiment where the required elements of measuring, modeling, and predicting the information in a system will be much more broadly applicable throughout the optimization of information processing systems.

REFERENCES

1. Sibusiso et al, "Maximum entropy signal processing in practical NMR spectroscopy", *Nature*, 311, 446, (1984).

2. K.M. Wright and P.S. Belton, "A new definition of the information content of N.M.R. spectra suitable for use in maximum entropy signal processing," *Molecular Physics*, 58, 485, (1986).

3. J.G. Powles and B. Carazza, "A 'non classical' information theory of spectral lineshape," *J.Phys. A:Gen. Phys.*, 3, (1970).

4. G. Margatitondo, "The information content of Photoemmison spectroscopy and spectromicroscopy", *Surface Review Letters*, 2, 305, (1995).

5. G.Z. Czajkowski, "An information-theoretical lineshape: general case", *J. Phys: amth., Nucl. Gen.*, 6, 906, (1973).

6. B. Carazza, "On the Lorentzian shape and the information provided by an experimental plot," *J.Phys. A: Math. Gen.*, 9, (1976).

7. C.H. Bennett "Thermodynamics of Computation-A review," *Intl. Journal of Theoretical Physics*, 21, 12 (1982).

8. C.H. Bennett and R. Landauer, "The Fundamental Physical Limits of Computation," *Scientific American*, 253, 48-56 (1985).

9. R. Landauer, "Computation, Measurement, Communication and Energy Dissipation," *Selected Topics in signal Processing*, 18-47, Wiley Press (1998).

10. N. Gershenfeld, "Signal entropy and the thermodynamics of computation" *IBM Systems Journal*, 35, (1996).

11. R.P. Feynman, "Simulating Physics with Computers", *International Journal of Theoretical Physics*, 21, 467, (1982).

APPENDIXES

A. MATHEMATICAL FORMULATION OF WMS SIGNALS

Myers and Putzers approach:

Consider a function *y*, on which phase sensitive detection is employed,

$y = f(v + \beta\cos\phi)$; Here *f* can be any function e.g. in our case Gaussian, Lorentzian or a Voigt function.

Expressing function y as a Fourier series

$$y = \frac{a_0}{2} + \sum_{k=1}^{\infty}(a_k \cos k\phi + b_k \sin k\phi) \qquad \text{(A-1)}$$

Fourier coefficients are given by

$$a_k = \frac{1}{\pi}\int_{-\pi}^{\pi} f \cos k\phi d\phi \qquad \text{(A-2)}$$

$$b_k = \frac{1}{\pi}\int_{-\pi}^{\pi} f \sin k\phi d\phi \qquad \text{(A-3)}$$

$$c_k \equiv a_k + ib_k = \frac{1}{\pi}\int_{-\pi}^{\pi} f e^{ik\phi} d\phi \qquad \text{(A-4)}$$

Here, *k* is the harmonic order, for any function *f*(*v*) analytic in region $|v - v_1| < \rho$ about $v = v_1$ we have Taylor series expansion, given by,

$$f(v) = \sum_{n=0}^{\infty} \beta^n \cos^n \phi \frac{f^n(v)}{n!} \qquad \text{(A-5)}$$

The above equation is only valid for $|\beta \cos \phi| < \rho$

$$c_k = \frac{1}{\pi}\int_{-\pi}^{\pi} e^{ik\phi} d\phi \sum_{n=0}^{\infty} \frac{f^n}{n!}[\frac{\beta}{2}(e^{i\phi} + e^{-i\phi})]^n \qquad \text{(A-6)}$$

$$c_k = 2\sum_{n=0}^{\infty} \frac{f^n}{n!}\{\frac{1}{2\pi i}\oint_{|z|=1} z^{k-1-n}[\frac{\beta}{2}(z^2+1)]^n\} = 2\sum_{n=0}^{\infty} \frac{f^n}{n!}(\frac{\beta}{2})^n B_{n,n-k} \qquad \text{(A-7)}$$

$$(z^2+1)^n = \sum_{p=0}^{n} \binom{n}{p} z^{2p}$$

Since, $(x+a)^n = \sum_{k=0}^{n} \binom{n}{k} x^k a^{n-k}$

Coefficients of z^{n-k} in the expansion of $(z^2+1)^n$

In Eqn. (A-7) $n - V = 2k$ i.e. if n is even k = even and if n is odd k = odd

Hence $n = 2k + V$ (k is the harmonic order)

$$c_k = 2\sum_{n=0}^{\infty} \frac{f^n}{n!}(\frac{\beta}{2})^n B_{n,n-k} = 2\sum_{n=0}^{\infty} \frac{f^n}{n!}(\frac{\beta}{2})^n B_{2V+k,2v} \qquad \text{(A-8)}$$

and

$$a_{2k} = 2\sum_{V=0}^{\infty} \frac{f^{2V+2k}}{(2n+2k)!}(\frac{\beta}{2})^{2n+2k} B_{2V+2k,2V}$$

$$a_{2k+1} = 2\sum_{v=0}^{\infty} \frac{f^{2V+2k+1}}{(2V+2k+1)!}(\frac{\beta}{2})^{2V+2k+1+1} B_{2V+2k+1,2V}$$

Coefficients of z^{2v} in expansion of $(z^2+1)^V$

$$B_{2V+k,2V} = \begin{pmatrix} 2v+k \\ V \end{pmatrix}$$

Therefore,

$$a_{2k} = 2\sum_{V=0}^{\infty} \frac{f^{2V+2k}}{(2V+2k)!}(\frac{\beta}{2})^{2V+2k} \begin{pmatrix} 2V+2k \\ V \end{pmatrix} \qquad \text{(A-9)}$$

$$a_{2k+1} = 2\sum_{n=0}^{\infty} \frac{f^{2V+2k+1}}{(2V+2k+1)!}(\frac{\beta}{2})^{2V+2k+1} \begin{pmatrix} 2V+2k+1 \\ V \end{pmatrix}$$

or in general,

$$a_k = 2\sum_{v=0}^{\infty} \frac{f^{2V+k}}{(2V+k)!}(\frac{\beta}{2})^{2V+k} \begin{pmatrix} 2V+k \\ V \end{pmatrix} \qquad \text{(A-10)}$$

Alternative method to obtain series expression for harmonics

From Eqn. (A-5) $f(v+\beta\cos\phi) = \sum_{n=0}^{\infty} \beta^n \cos^n \phi \frac{f^n}{n!}$ (A-11)

Fourier series expansion of $\cos^n \phi$ gives,

$$\cos^n \phi = c_{n,0} + c_{n,1}\cos\phi + c_{n,2}\cos 2\phi + -- + c_{n,m}\cos m\phi + ---- = \sum_{n=0}^{m} c_{n,m}\cos m\phi \qquad \text{(A-12)}$$

Substituting above in Eqn. (A-11)

$$f(v+\beta\cos\phi) = \sum_{n=0}^{\infty} \beta^n \cos^n \phi \frac{f^n(v)}{n!} = \sum_{n=0}^{\infty} \beta^n \frac{f^n(v)}{n!} \{\sum_{m=0}^{n} c_{n,m}\cos m\phi\} \qquad \text{(A-13)}$$

Here,

$$c_{n,m} = \frac{m!}{2^{m-1}[\frac{m+n}{2}!\frac{m-n}{2}!]}$$

Also, Fourier series of f gives;

$$f(v+\beta\cos\phi) = \sum_{k=0}^{\infty} H_k \cos k\phi \tag{A-14}$$

Also, comparing coefficients of $\cos k\phi$ gives;

$$H_k = \sum_{m=0}^{\infty} \frac{f^{2m+k}\beta^{2m+k}}{(2m+k)!} c_{k,2m+k} \tag{A-15}$$

Compare the above Eqn. (A-15) with Eqn. (A-10)

$$a_k = 2\sum_{V=0}^{\infty} \frac{f^{2V+k}}{(2V+k)!}(\frac{\beta}{2})^{2V+k}\begin{pmatrix} 2V+k \\ V \end{pmatrix} \tag{A-16}$$

Wilsons method:

Since f is even function of ϕ, from Eqn. (A-14)

$$H_k = \frac{1}{\pi}\int_{-\pi}^{\pi} f(v+\beta\cos\phi)\cos k\phi d\phi \tag{A-17}$$

B. CONVERGENCE OF SERIES EXPANSION OF THE DERIVATIVES OF GAUSSIAN AND LORENTZIAN FUNCTIONS

Derivatives of lineshape functions are required to compute WMS signals using Myers and Putzers method. The number of terms in the series expansion is determined by its region of convergence. This critically depends on the values of modulation index and spectral location with respect to the linecenter or the normalized frequency. In this appendix we study this region of convergence of different lineshape functions.

A complete series version of WMS harmonic signal is given by;

$$S_N = -n\bar{\sigma}LI_0(-1)^{[2N]/2}\sum_{V=0}^{\infty}\left(\frac{\beta}{2}\right)^{2V+N}\frac{1}{V!(V+N)!}g^{2V+N} \tag{B-1}$$

To test the convergence we evaluate the ratio of two consecutive terms (*V*) in the above expansion at any normalized frequency value, *x*,

$$\frac{T_{V+1}}{T_V} = \left(\frac{m}{2}\right)^2 \frac{1}{(V+1)(V+1+N)} \frac{g^{2(V+1)+N}}{g^{2V+N}} \tag{B-2}$$

1. Convergence of Gaussian Function

Nth derivative of a Gaussian function can be expressed as;

$$g_G^N(\nu) = \frac{g(\nu)}{\sqrt{\pi}} \frac{1}{(\Delta\nu_D)^{2N+1}} \sum_{k=0}^{[N]/2} C_{2k,N}(\Delta\nu_D)^{2k}(\nu-\nu_0)^{N-2k} \tag{B-3}$$

or

$$g_G^N(v) = \frac{g(x)}{\sqrt{\pi}} \frac{1}{(\Delta v_D)^{N+1}} \sum_{k=0}^{[N]/2} C_{2k,N} x^{N-2k} \tag{B-4}$$

where $x = \dfrac{v - v_0}{\Delta v_D}$, $C_{2k,N} = (-1)^k \dfrac{N!}{(N-2k)!} \dfrac{(-2)^{N-2k}}{k!}$ and $g(x) = \exp(-x^2)$

[N] = *N-1* ; *N* is odd

= *N* ; *N* is even

The ratio now becomes,

$$\frac{T_{V+1}}{T_V} = \left(\frac{m}{2}\right)^2 \frac{1}{(V+1)(V+1+N)} \frac{\sum\limits_{k=0}^{[2v+N+2]/2} C_{2k,2V+N+2} x^{2V+N-2k+2}}{\sum\limits_{k=0}^{[2v+N]/2} C_{2k,2V+N} x^{2V+N-2k}} \tag{B-5}$$

a. Convergence at x = 0

From the Eqn. (B-2) above, the ratio of terms at the linecenter is

$$\frac{T_{V+1}}{T_V} = \left(\frac{\beta}{2}\right)^2 \frac{1}{(V+1)(V+N+1)} \frac{g^{2(V+1)+N}}{g^{2V+N}}$$

Since, $$\frac{g^{2V+N+2}}{g^{2V+N}} = \frac{\dfrac{g(v)}{\sqrt{\pi}} \dfrac{1}{(\Delta v_D)^{2(2V+N+2)+1}} C_{2V+N+2,2V+N+2} (\Delta v_D)^{(2V+N+2)}}{\dfrac{g(v)}{\sqrt{\pi}} \dfrac{1}{(\Delta v_D)^{2(2V+N)+1}} C_{2V+N,2V+N} (\Delta v_D)^{(2V+N)}} = \frac{C_{2V+N+2,2V+N+2}}{(\Delta v_D)^2 C_{2V+N,2V+N}} \tag{B-6}$$

or

$$\frac{C_{2V+N+2,2V+N+2}}{C_{2V+N,2V+N}}=\frac{\dfrac{(-1)^{(2V+N+2)/2}(2V+N+2)!}{(\frac{2V+N+2}{2})!}}{\dfrac{(-1)^{(2V+N)/2}(2V+N)!}{(\frac{2V+N}{2})!}}$$

$$\frac{C_{2V+N+2,2V+N+2}}{C_{2V+N,2V+N}}=(-1)(2V+N+2)(2V+N+1)\frac{(\frac{2V+N}{2})!}{(\frac{2V+N+2}{2})(\frac{2V+N}{2})!}$$

$$\frac{C_{2V+N+2,2V+N+2}}{C_{2V+N,2V+N}}=\frac{(-1)(2V+N+2)(2V+N+1)}{(\Delta v_D)^2(\frac{2V+N+2}{2})}=\frac{(-2)(2V+N+1)}{(\Delta v_D)^2}=\frac{g^{2V+N+2}}{g^{2V+N}} \qquad \text{(B-7)}$$

Substituting, g^{2v+N+2} / g^{2v+N}, Eqn. (B-6) in the ratio, Eqn. (B-7). The ratio now becomes,

$$\frac{T_{V+1}}{T_V}=\left(\frac{\beta}{2\Delta v_D}\right)^2\frac{-2(2V+N+1)}{(V+1)(V+N+1)}$$

Dividing the above by V

$$\frac{T_{V+1}}{T_V}=\left(\frac{m}{2}\right)^2\frac{-2(2+\frac{N}{V}+\frac{1}{V})}{(1+\frac{1}{V})(1+\frac{N}{V}+\frac{1}{V})} \qquad \text{B-8}$$

for large V → ∞

$$\left|\frac{T_{v+1}}{T_v}\right|\Rightarrow m^2$$

Therefore, convergence test $\left|\frac{T_{v+1}}{T_v}\right|<1$ requires, m<1.

The numerical plot shows the ratio $\left|\frac{T_{v+1}}{T_v}\right|$ for m=3, N=6, the series converges at about V = 10.

Note that the above ratio is not sufficient condition for the series to converge. In other words, even though the series show ratio of less than unity for large V terms, it does not mean that series converges; it may still require large number of terms which makes this method computationally cumbersome.

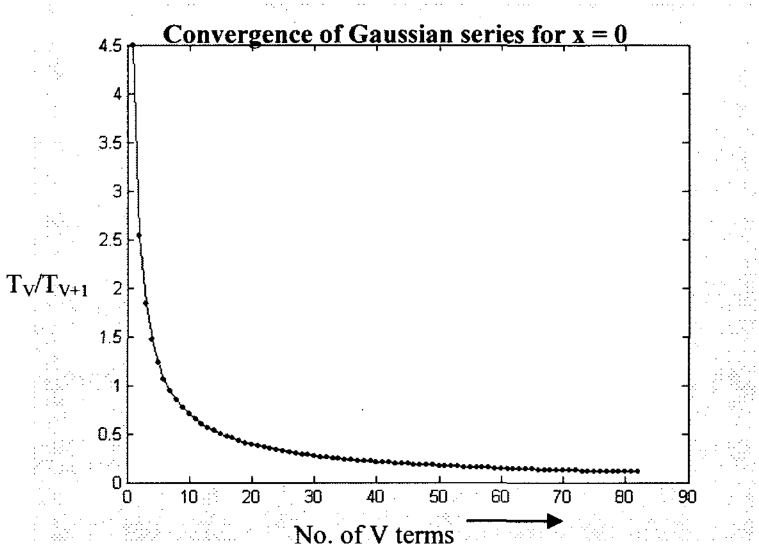

Fig. B-1. Convergence of the Gaussian series at the linecenter (x=0). Here, modulation index is m=3 and harmonic order is, N=6. The series begin to converge as the larger number of terms is added in the series. The convergence range strongly depends on the m and N.

b. Series Convergence at x > 0

The WMS signal with a Gaussian lineshape function obtained by substituting Eqn. (B-3) in Eqn. (B-1), is given by,

$$S_N = \frac{-n\overline{\sigma} L I_0 (-1)^{[N]/2}}{\sqrt{\pi}\,\Delta v_D} g(x) \sum_{V=0}^{\infty} \left(\frac{m}{2}\right)^{2V+N} \frac{1}{V!(V+N)!} \sum_{k=0}^{[2V+N]/2} C_{2k,2V+N} x^{2v+N-2k} \qquad (\text{B-9})$$

Again, we find the ratio of subsequent V terms to test for convergence,

$$\frac{T_{V+1}}{T_V}=\left(\frac{m}{2}\right)^2\frac{1}{(V+1)(V+1+N)}\frac{\sum_{k=0}^{[2V+N+2]/2}C_{2k,2V+N+2}x^{2V+N-2k+2}}{\sum_{k=0}^{[2V+N]/2}C_{2k,2V+N}x^{2V+N-2k}} \tag{B-10}$$

or

$$\frac{T_{V+1}}{T_V}=\left(\frac{m}{2}\right)^2\frac{1}{(V+1)(V+N+1)}\frac{x^2\sum_{k=0}^{[2V+N+2]/2}C_{2k,2V+N+2}x^{2V+N-2k}}{\sum_{k=0}^{[2V+N]/2}C_{2k,2V+N}x^{2V+N-2k}} \tag{B-11}$$

Also, since,

$$C_{2k,N+2}=\frac{4(N+2)(N+1)}{(N+2-2k)(N+1-2k)}\frac{N!(-2)^{N-2k}}{k!(N-2k)!} \tag{B-12}$$

Therefore, expressing above as a recursive relation,

$$C_{2k,N+2}=\frac{4(N+2)(N+1)}{(N+2-2k)(N+1-2k)}C_{2k,N} \tag{B-13}$$

Substituting Eqn. (B-13) in Eqn. (B-11) one obtains,

$$\frac{T_{V+1}}{T_V}=(mx)^2\frac{(2V+N+2)(2V+N+1)}{(V+1)(V+N+1)}\frac{\sum_{k=0}^{[2V+N+2]/2}\frac{1}{(2V+N-2k+2)(2V+N-2k+1)}C_{2k,2V+N}x^{2V+N-2k}}{\sum_{k=0}^{[2V+N]/2}C_{2k,2V+N}x^{2V+N-2k}} \tag{B-14}$$

In the limit, V→ ∞

$$\frac{T_{V+1}}{T_V} \Rightarrow (mx)^2$$

For $x = 0$ this reduces to the expression in part (a). Among other factors, the convergence of the series depends on the values of spectral location from the linecenter or 'x.' The numerical plot of the ratio when x>0 shows oscillatory behavior.

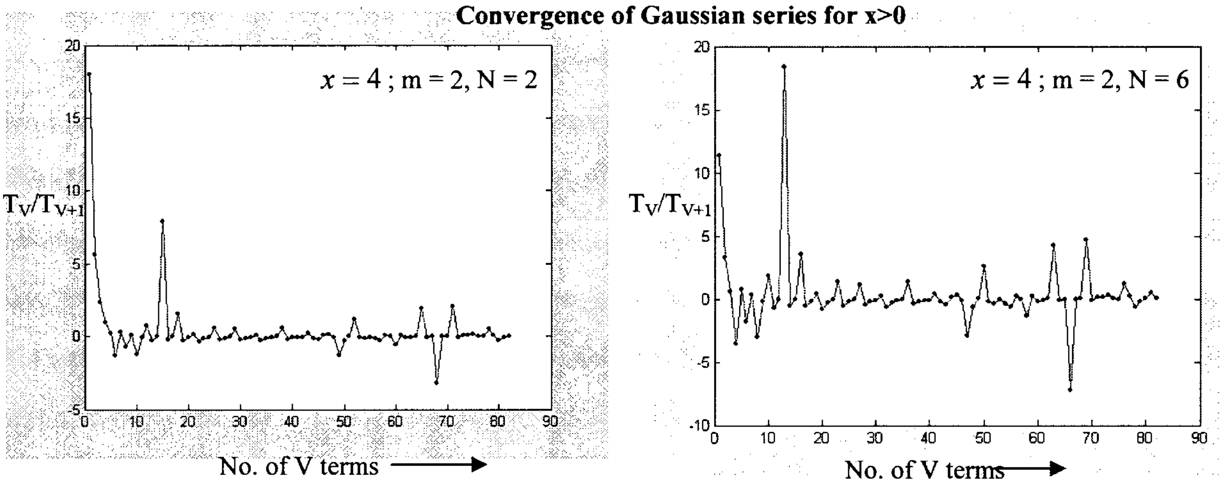

Fig. B-2. Convergence of the Gaussian series expansion of two different harmonic orders, N=2 and N=6. Here the normalized frequency is $x = 4$ and modulation index is, m=2 The ratios show oscillatory behavior which makes it difficult to predict the range of convergence and the terms required to accurately calculate the WMS

To test the validity of convergence range obtained in the above analysis we computed the WMS signal using Myers and Putzers (or series) formulation and Wilsons method. Wilson method has no such known issues with convergence, probably because of the (integral) nature of the function. It is seen, the disparity in WMS signal from the two methods is more prominent in wing region (x>> 0) of the lineshape profile (see figure below). This could be due to convergence of Gaussian series, requiring larger number of terms in that region. In addition, higher detection orders, N, show even greater difference, since they require even more number of terms in order for the series to converge. The figure below shows N = 8 signal computed using Myers and Putzers method and Wilsons method. The lineshape function is a Gaussian. The signals obtained from the two methods match within 5% around the linecenter but tend to deviate significantly (> 10%) in the wing region of the lineshape profile.

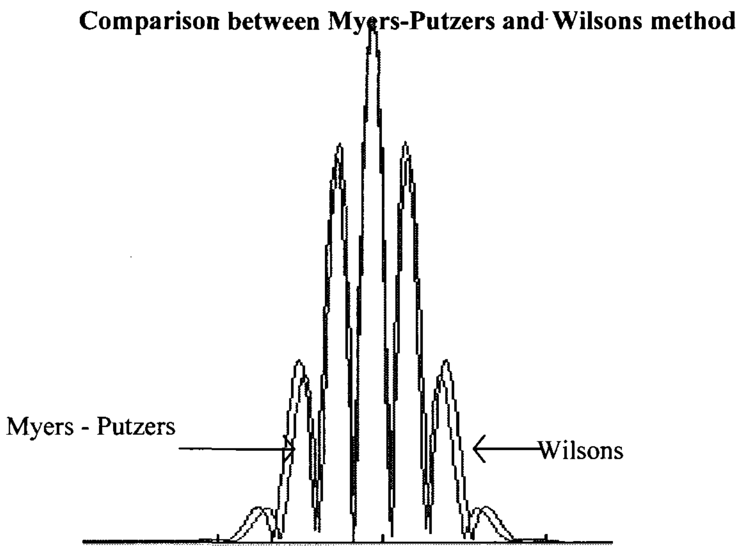

Comparison between Myers-Putzers and Wilsons method

Fig. B-3. Comparison of the two mathematical methods of N=8 WMS signal. Myers and Putzers (or the series expansion of the lineshape function) and the Wilsons method (Fourier integral of the lineshape function). The slight discrepancy is due to convergence of Myers Putzers method at large values of the normalized frequency, x .

2. Convergence of Lorentzian derivatives

We repeat the same steps as in the previous section to obtain region of convergence of a series expansion of a Lorentzian function. Nth derivative of a lorentzian function given by,

$$g_L^N(\nu) = \frac{\Delta\nu}{2\pi}\frac{(-1)^N}{y^{N+1}}\sum_{k=0}^{[N]/2} C_{2k,N}\left(\frac{\Delta\nu}{2}\right)^{2k}(\nu-\nu_0)^{N-2k} \qquad \text{(B-15)}$$

Where, $y = (v - v_0)^2 + (\frac{\Delta v}{2})^2$

$$C_{2k,N} = (-1)^k \frac{(N+1)!}{(2k+1)} \binom{N}{2k}$$

$$\binom{N}{2k} = \frac{N!}{(N-2k)!(2k)!}$$

[N] = N-1 ; N is odd

= *N ; N* is even

From the equation above, the ratio of consecutive terms is,

$$\frac{T_{V+1}}{T_V} = \left(\frac{\beta}{2}\right)^2 \frac{1}{(V+1)(V+N+1)} \frac{g^{2(V+1)+N}}{g^{2V+N}} \tag{B-16}$$

At the line center $y \to y_0 = (\frac{\Delta v}{2})^2$

Therefore,

$$\frac{g^{2(V+1)+N}}{g^{2V+N}} = \frac{\frac{\Delta v}{\pi} \frac{(-1)^{2(V+1)+N}}{y_0^{2(V+1)+1}} (\frac{\Delta v}{2})^{2(V+1)+N} C_{2(V+1)+N,2(V+1)+N}}{\frac{\Delta v}{\pi} \frac{(-1)^{2V+N}}{y_0^{2V+1}} (\frac{\Delta v}{2})^{2V+N} C_{2V+N,2V+N}}$$

$$\frac{g^{2(V+1)+N}}{g^{2V+N}} = \frac{1}{y_0^2} (\frac{\Delta v}{2})^2 \frac{C_{2(V+1)+N,2(V+1)+N}}{C_{2V+N,2V+N}} \tag{B-17}$$

Also the recursive relation of C_k's can be obtained,

$$\frac{C_{2(V+1)+N,2(V+1)+N}}{C_{2V+N,2V+N}} = \frac{(-1)^{(\frac{2V+N+2}{2})}\dfrac{(2V+N+3)!}{(2V+N+3)}\begin{pmatrix}2V+N+2\\2V+N+2\end{pmatrix}}{(-1)^{(\frac{2V+N}{2})}\dfrac{(2V+N+1)!}{(2V+N+1)}\begin{pmatrix}2V+N\\2V+N\end{pmatrix}}$$

$$\frac{C_{2(V+1)+N,2(V+1)+N}}{C_{2V+N,2V+N}} = (-1)\frac{(2V+N+3)(2V+N+2)(2V+N+1)}{(2V+N+3)}$$

$$\frac{C_{2(V+1)+N,2(V+1)+N}}{C_{2V+N,2V+N}} = (-1)(2V+N+2)(2V+N+1) \tag{B-18}$$

Therefore from Eqns. (B-17) and (B-18),

$$\frac{g^{2(V+1)+N}}{g^{2V+N}} = \frac{1}{{y_0}^2}(\frac{\Delta v}{2})^2(-1)(2V+N+2)(2V+N+1) \tag{B-19}$$

From Eqn. (B-16) the ratio now becomes,

$$\frac{T_{V+1}}{T_V} = \left(\frac{\beta}{2}\right)^2 \frac{1}{(V+1)(V+N+1)}\frac{1}{{y_0}^2}(\frac{\Delta v}{2})^2(-1)(2V+N+2)(2V+N+1) \tag{B-20}$$

Dividing numerator and denominator by V,

$$\frac{T_{V+1}}{T_V} = \left(\frac{\beta}{2}\right)^2 \frac{1}{(1+\frac{1}{V})(1+\frac{1}{V}+\frac{N}{V})}\frac{1}{{y_0}^2}(\frac{\Delta v}{2})^2(-1)(2+\frac{N}{V}+\frac{2}{V})(2+\frac{N}{V}+\frac{1}{V})$$

In the limit V→∞

$$\frac{T_{V+1}}{T_V} = \left(\frac{\beta}{2}\right)^2 4\frac{1}{\left(\frac{\Delta v}{2}\right)^2}(-1) = \left(\frac{\beta}{\Delta v}\right)^2 4(-1) \qquad \text{(B-21)}$$

or

$$\left|\frac{T_{V+1}}{T_V}\right| \to 4m^2$$

Here m is the modulation index. For the series to converge $\left|\frac{T_{V+1}}{T_V}\right| < 1$ i.e. $4m^2 < 1$ or $m < \frac{1}{2}$

If x>0 and V→∞

$$\left|\frac{T_{V+1}}{T_V}\right| = \left(\frac{\beta}{2}\right)^2 \frac{4}{(x+1)^2} = (m)^2 \frac{4\Delta v^2}{x^2+1} \qquad \text{(B-22)}$$

Convergence of Gaussian vs. *Lorentzian:* The difference between the Gaussian and Lorentzian lineshapes is in their variation around linecenter and in the wing. The Gaussian is broader at the linecenter whereas Lorentzian is steeper and therefore higher in the linecenter value. In the wing region the Lorentzian falls off slowly than a Gaussian which falls of steeply. This behavior is also reflected in their convergence, and region of convergence at different index values. For example for large m values the magnitude of turning points in the wing region for a Lorentzian will be higher than that for a Gaussian. This is because the turning points are a measure of the slope of the function. Therefore, Lorentzian has a smaller region of convergence than a Gaussian. On the other hand it is postulated that the region of convergence of a Voigt, which is a combination of Gaussian and Lorentzian function will depend on its b parameter (ratio of the Lorentzian to Gaussian linewidths). This is studied in the following section.

3. Convergence of series expansion of the derivatives of Voigt Function

A complex error probability function is given by,

$$w(z) = \exp(-z^2)[1 + \frac{2i}{\sqrt{\pi}} \int_0^z \exp(-t^2)dt] = u(x,y) + iv(x,y) \tag{B-23}$$

In another representation, the integral representation of complex probability function can be expressed as,

$$w(z) = \frac{i}{\pi} \int_{-\infty}^{\infty} \frac{\exp(-t^2)}{z-t} dt = u(x,y) + iv(x,y) \tag{B-24}$$

The real part of the above equation is the Voigt function. It can be shown that the real part of the derivatives of the above equation also represents the derivative of the Voigt function

the Nth derivative of *w*(z) can be written as,

$$w^N(z) = (-1)^N (N!) \frac{i}{\pi} \int_{-\infty}^{\infty} \frac{\exp(-t^2)}{(z-t)^{N+1}} dt \tag{B-25}$$

Expressing, $z - t = (x-t) + iy = R(\cos\theta + i\sin\theta)$

$$\frac{1}{(z-t)^{N+1}} = \frac{1}{R^{N+1}[\cos\{(N+1)\theta\} + i\sin\{(N+1)\theta\}]} \tag{B-26}$$

Separating real and imaginary parts one obtains,

$$\frac{1}{R^{N+1}[\cos\{(N+1)\theta\} + i\sin\{(N+1)\theta\}]} = \frac{\cos\{(N+1)\theta\} - i\sin\{(N+1)\theta\}}{R^{N+1}}$$

$$R = \{(x-t)^2 + y^2\}^{1/2}$$

$$\theta = \tan^{-1}\{\frac{y}{x-t}\}$$

Substituting R and θ in equation 1

$$w^N(x,y) = (-1)^N (N!)\frac{i}{\pi}\int_{-\infty}^{\infty}\exp(-t^2)\{\frac{\cos\{(N+1)(\tan^{-1}[\frac{y}{x-t}])\}}{\{(x-t)^2+y^2\}^{(N+1)/2}}\}dt$$
$$+(-1)^N (N!)\frac{1}{\pi}\int_{-\infty}^{\infty}\exp(-t^2)\{\frac{\sin\{(N+1)(\tan^{-1}[\frac{y}{x-t}])\}}{\{(x-t)^2+y^2\}^{(N+1)/2}}\}dt \qquad \text{(B-27)}$$

The real part (2nd term) of the above equation the Nth derivative of the Voigt function

$$u^N(x,y) = (-1)^N (N!)\frac{1}{\pi}\int_{-\infty}^{\infty}\exp(-t^2)\{\frac{\sin\{(N+1)(\tan^{-1}[\frac{y}{x-t}])\}}{\{(x-t)^2+y^2\}^{(N+1)/2}}\}dt \qquad \text{(B-28)}$$

In above equations;

$x = (\ln 2)^{1/2}\frac{\nu_0-\nu}{\delta\nu_D}$, where δνD is Doppler half-width

$$y = (\ln 2)^{1/2}\frac{\delta\nu_L}{\delta\nu_D}$$

Also, since, $\frac{dw(z)}{d\nu} = \frac{dw}{dz}\frac{dz}{dx}\frac{dx}{d\nu}$ and $\frac{dz}{dx} = 1; \frac{dx}{d\nu} = \frac{\sqrt{\log 2}}{\delta\nu_D} = K$

One can write, $\frac{dw(z)}{d\nu} = K\frac{dw}{dz}$ and subsequently, $\frac{d^2w(z)}{d\nu^2} = \frac{d}{d\nu}\{\frac{dw}{d\nu}\} = \frac{d}{d\nu}\{K\frac{dw}{dz}\}$

Let, $\frac{dw}{dz} = A(z) \Rightarrow \frac{d^2w}{d\nu^2} = K\frac{dA}{d\nu} = K\frac{dA}{dz}\frac{dz}{dx}\frac{dx}{d\nu} = K^2\frac{dA}{dz} = K^2\frac{d^2w}{dz^2}$

Therefore, in general; $\frac{d^Nw}{d\nu^N} = K^N\frac{d^Nw}{dz^N}$

From Eqn. (B-28) Nth derivative of a Voigt function can be expressed as,

$$u^N(x,y) = (-1)^N (N!)\frac{1}{\pi}\int_{-\infty}^{\infty}\exp(-t^2)\{\frac{\sin\{(N+1)(\tan^{-1}[\frac{y}{x-t}])\}}{\{(x-t)^2+y^2\}^{(N+1)/2}}\}dt$$

At linecenter, $x = 0$

$$u^N(0,y) = K^N(-1)^N (N!)\frac{1}{\pi}\int_{-\infty}^{\infty}\exp(-t^2)\{\frac{\sin\{(N+1)(\tan^{-1}[\frac{y}{-t}])\}}{\{t^2+y^2\}^{(N+1)/2}}\}dt \qquad \text{(B-29)}$$

Here, $K = \frac{\sqrt{\log 2}}{\delta v_D}$.

The ratio of the subsequent derivatives at the linecenter can now be written as,

$$\frac{u^{2(V+1)+N}}{u^{2V+N}} = \frac{K^{2(V+1)+N}(-1)^{2(V+1)+N}(2(V+1)+N)!\frac{1}{\pi}\int_{-\infty}^{\infty}\exp(-t^2)\{\frac{\sin\{(2(V+1)+N+1)(\tan^{-1}[\frac{y}{-t}])\}}{\{t^2+y^2\}^{((2V+1)N+1)/2}}\}dt}{K^{2V+N}(-1)^{2V+N}(2v+N)!\frac{1}{\pi}\int_{-\infty}^{\infty}\exp(-t^2)\{\frac{\sin\{(2V+1+N+1)(\tan^{-1}[\frac{y}{-t}])\}}{\{t^2+y^2\}^{(2V+N+1)/2}}\}dt}$$

From Eqn. (B-2) the ratio of subsequent V terms of series expansion of WMS signal,

$$\frac{T_{V+1}}{T_V} = \left(\frac{\beta}{2}\right)^2 \frac{1}{(V+1)(V+1+N)}\frac{u^{2(V+1)+N}}{u^{2V+N}}$$

Let the,integral,

$$\frac{\int_{-\infty}^{\infty} \exp(-t^2)\{\frac{\sin\{(2(V+1)+N+1)(\tan^{-1}[\frac{y}{-t}])\}}{\{t^2+y^2\}^{((2V+1)N+1)/2}}\}dt}{\int_{-\infty}^{\infty} \exp(-t^2)\{\frac{\sin\{(2V+1+N+1)(\tan^{-1}[\frac{y}{-t}])\}}{\{t^2+y^2\}^{(2V+N+1)/2}}\}dt} = I_N$$

$$\frac{T_{V+1}}{T_V} = \left(\frac{\beta}{2}\right)^2 \frac{K^2(2V+N+2)(2V+N+1)}{(V+1)(V+1+N)} I_N$$

$$\frac{T_{V+1}}{T_V} = \left(\frac{\beta}{2}\right)^2 \frac{4\ln 2}{(\Delta\nu_D)^2} \frac{(2V+N+2)(2V+N+1)}{(V+1)(V+1+N)} I_N \qquad \text{(B-30)}$$

$\Delta\nu_D$ is Doppler Full-width.

$$\frac{T_{V+1}}{T_V} = \left(\frac{\beta}{2}\right)^2 \frac{1}{(\overline{\Delta\nu_D})^2} \frac{(2V+N+2)(2V+N+1)}{(V+1)(V+1+N)} I_N \quad , \qquad \overline{\Delta\nu_D} = \Delta\nu_D / \sqrt{4\log(2)}$$

or, $$\frac{T_{V+1}}{T_V} = \left(\frac{\beta}{2\Delta\nu_L}\right)^2 \frac{(\Delta\nu_L)^2}{(\overline{\Delta\nu_D})^2} \frac{(2V+N+2)(2V+N+1)}{(V+1)(V+1+N)} I_N$$

In the limit V→∞

$$\frac{T_{V+1}}{T_V} = \left(\frac{\beta}{2\Delta\nu_L}\right)^2 \left(\frac{\Delta\nu_L}{\Delta\nu_D}\right)^2 4I_N = m^2 b^2 I_N$$

The b parameter of Voigt is given $b = \frac{\Delta\nu_L}{\overline{\Delta\nu_D}}$

From the above ratio two points should be noted here that,

1. For a Gaussian, b→0 $\frac{T_{V+1}}{T_V} \to 0$

2. For a Lorentzian, b→∞ $\frac{T_{V+1}}{T_V} \to \infty$

This again shows that, the number of terms required in a Gaussian (for convergence) is larger than that for a Lorentzian.

In a typical WMS experiment for RR (13, 13) oxygen spectrum, the standard magnitudes of lineshape parameters are b ~ 1.

$$\frac{T_{V+1}}{T_V} = m^2 I_N .$$

For the series to converge $\frac{T_{V+1}}{T_V} < 1$ or $m < \frac{1}{\sqrt{I_N}}$

The plot below shows values of I_N for different detection orders. For example, N=2, I_N = 0.1. Therefore, m<3 for the series to converge.

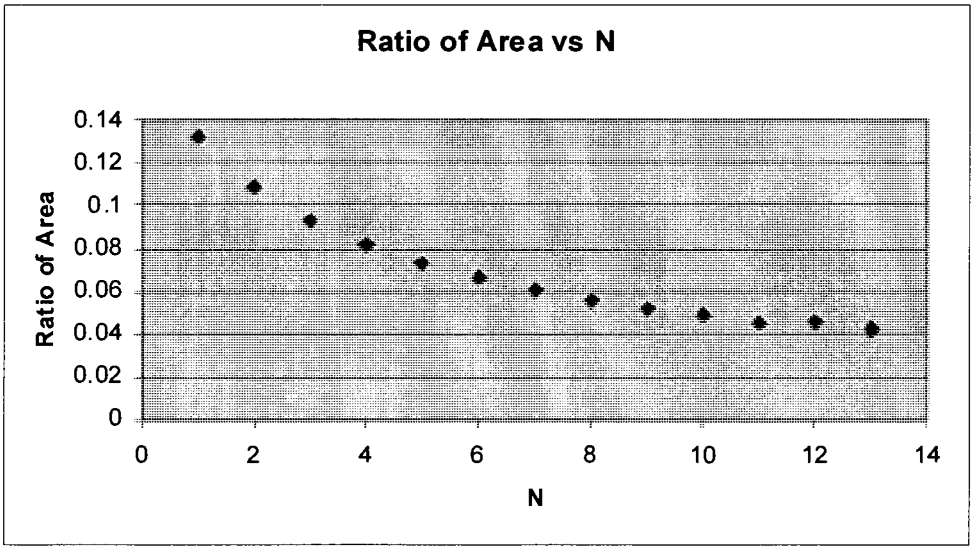

Fig. B-4. Ratio of the integral I_N the detection order. The magnitude of the ratio at a detection order determines the range of convergence for that particular detection order.

Analytical attempts to solve Voigt and its derivatives using Myers and Putzers method have been cumbersome and quite lengthy. Wilsons direct numerical method works reasonably well for WMS analysis.

Numerical Evaluation of Voigt Function

Comparison between Voigt Humlicek Algorithm and Matlab Dblquad: There are several numerical algorithms in literature to compute the complex error function, whose real part is a Voigt function. Humlicek algorithm is most commonly used algorithm to compute Voigt function. Humlicek gave two versions of this algorithm in his 1976 and 1982 papers. The plots below shows computation of Voigt function (both 1976 and 1982 papers) using Humlicek algorithm (with Simpsons integral step size of 10^4) and inbuilt MATLAB dblquad function.

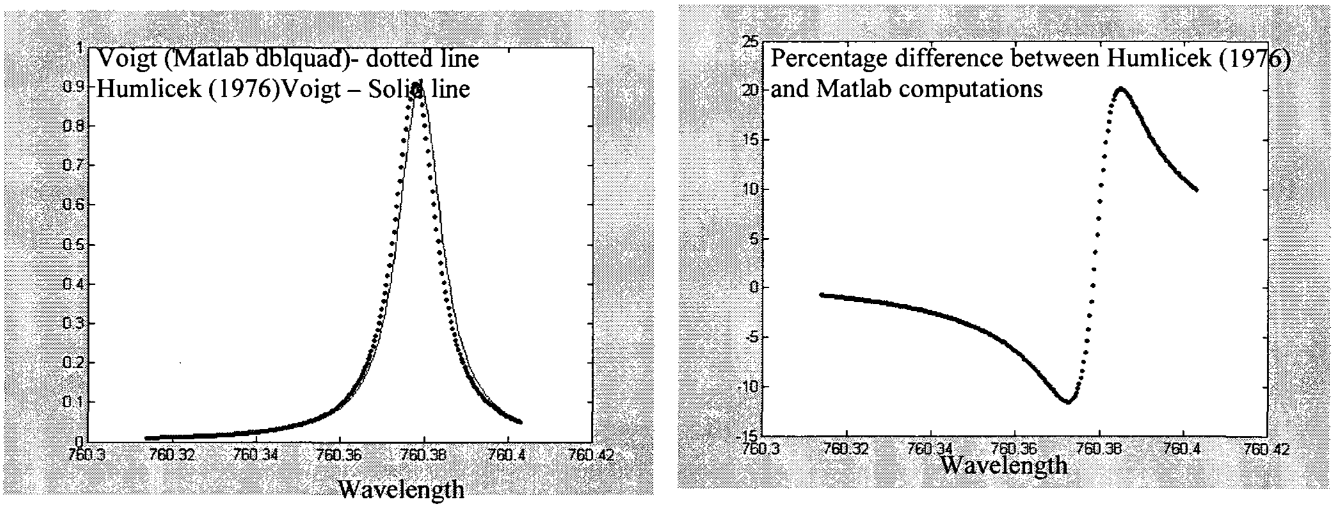

Fig. B-5. Comparison between Voigt profile computed from Humlicek (1976) algorithm and MATLAB dblquad function.

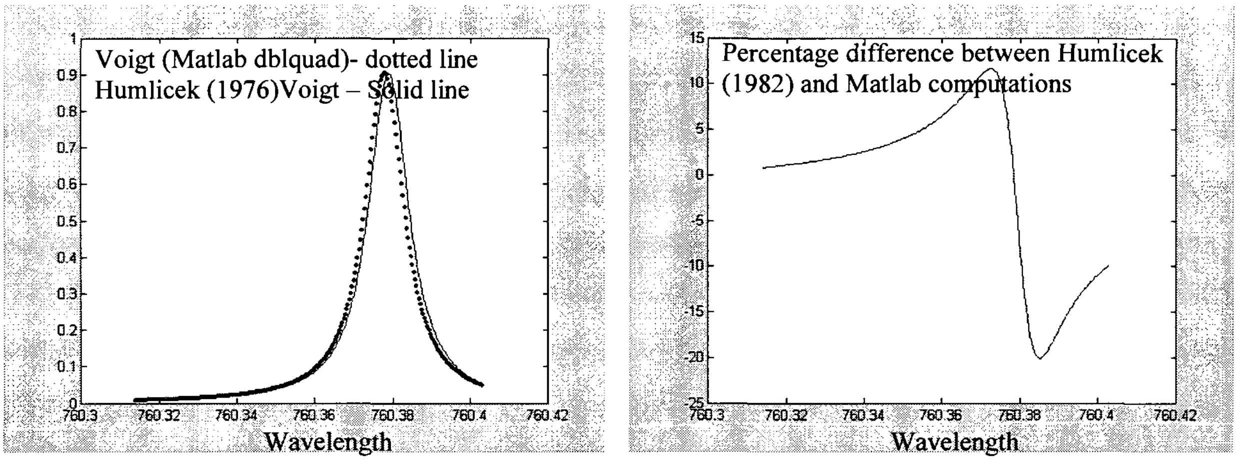

Fig. B-6. Comparison between Voigt profile computed from Humlicek (1982) algorithm and MATLAB dblquad function.

Higher derivatives using Humlicek algorithm and MATLAB dblquad. Higher order plots of Voigt algorithms show greater discrepancies in Humlicek and MATLAB methods, as shown in N=2 plot below.

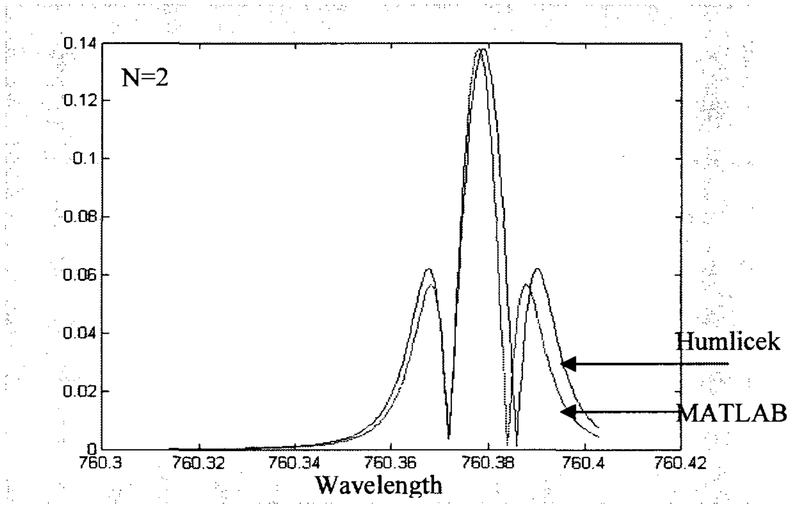

Fig. B-7. Comparison between N=2 Voigt signal computed from Humlicek algorithm and MATLAB dblquad function.

Problems with Humlicek Algorithm: The Humlicek expression is based on complex analysis of the function, whose real term is a Voigt function. The derivatives of this complex probability function ($w(z)=\exp(-z^2)(1+\frac{2i}{\pi^{1/2}}\int_0^z \exp(t^2)dt$) also give derivatives of the Voigt. The derivatives are expresses as a recursion relation ($w^n(z)=-(-2n+2)w^{n-2}(z)-2zw^{n-1}(z); n\geq 3$). Each higher order derivative is expressed as combination of lower order derivatives. The Humlicek expression is an approximation with finite errors. These errors grow very rapidly with the order of the derivatives.

C. MAXIMUM ENTROPY

The entropy of a continuous random variable is given by $H(x)=-\int_{-\infty}^{\infty} f(x)\log f(x)dx$. If there are no constraints on the random variable, x, then the maximum entropy, occurs when f(x) is a uniform distribution, i.e. $f(x)=\frac{1}{a}$. A more practical and versatile distribution occurs when there are constraints on x. This result can also be shown mathematically, for example by maximizing H, under the constraint that $\int_{-\infty}^{\infty} f(x)dx=1$ and using Lagrange's method of multipliers.

Consider, f(x) is a one-dimensional distribution. The form of f(x) giving maximum entropy, subject to the condition that the standard deviation of x is fixed at σ, is a Gaussian. To show this, we maximize, $H(x)=-\int_{-\infty}^{\infty} f(x)\log f(x)dx$

under the constraints,

$$\sigma^2 = \int_{-\infty}^{\infty} x^2 f(x)dx \text{ and, } \int_{-\infty}^{\infty} f(x)dx = 1. \qquad \text{(C-1)}$$

This requires, by calculus of variations, maximizing the integral below,

$$\int -[f(x)\log f(x) + \lambda f(x)x^2 + \mu f(x)]dx. \qquad \text{(C-2)}$$

The relevant condition to find an extremum gives:

$$-1 - \log f(x) + \lambda x^2 + \mu = 0 \qquad \text{(C-3)}$$

Consequently, (adjusting the constants to satisfy the constraints) one gets a Gaussian distribution,

$$f(x) = \frac{1}{\sqrt{2\pi\sigma}} e^{-x^2/\sigma^2} \qquad \text{(C-4)}$$

With this result, the maximum entropy principle can be explained in the following way. Let N_L be the combinatorial arrangements (or sequences) that can be formed from L distinct objects. The frequency of occurrence of each of the (L) objects is their probability. The larger the entropy for a given distribution, the greater is the number of arrangements that can be generated, from independent trials of any probability experiments. Therefore, complexity of any probability distribution can be gauged, from the number of arrangements that can be extracted from it. In other words, the distribution with largest entropy, which therefore contains maximum information, is the one that contains maximum potential disorder.

The Central limit theorem, which seems to be a manifestation of maximum entropy, demonstrates that if there are no random variables whose variance dominates over others, the sum of independent random variables converges towards a Gaussian distribution. Therefore, the theorem allows us to say that, amongst all probability distributions with fixed mean and variance, it is to Gaussian distribution, that the probability density function of the sum must finally converge.

For example, in a coin tossing experiment with N fair coins, the event of appearance of heads, probability of getting k heads is, $h_k = {}^nC_k p^k q^{n-k}$. Since each outcome is independent of the other for a large n, h_k tends to a Gaussian distribution.

In another interpretation of this result, which is analogous to the maximum entropy argument, for a given mean and variance of a coin tossing experiment, the Gaussian distribution is the one which generates the largest number of arrangements or sequences.

A practical application of the concept of maximum entropy or central limit theorem appears in engineering problems. For a given power, the fluctuations from noise, in a physical quantity is considered to be a Gaussian. This can be understood as a hypothesis of maximum disorder, or a priori minimal knowledge. The entropy is the information content that the source of random events can supply during independent realizations. In the case of a source, with a high entropy, each experiment will tend to bring a lot of information. This is compatible with the interpretation, whereby, the information, available to us a priori, i.e. before the trials, is itself minimal.

D. THERMAL NOISE- PHYSICS OF IMPEDANCE MATCHING IN CIRCUITS

Thermal noise occurs due to collisions (which are random in nature) of electrons with atoms or molecules. Thermal noise is due to finite temperature of the elements of the detector (or receiver) system. Therefore, it can partially be alleviated by cooling these elements.

The noise goes by several different names: (1) in engineering it is referred to as "white" noise, because its spectral distribution is uniform or "flat" at video frequencies at room temperatures; (2) it is also referred to as "Johnson's" or Nyquist noise, after early pioneers in the field; and (3) it is also called "blackbody" noise, because its origin lies in the concept of blackbody physics (Planck's formulation of entropy of a blackbody spectrum).

In the treatment of blackbody formulation the underlying assumption is that the size of the cavity (in which the blackbody radiation or photons reside and interact with atoms of the walls of cavity) is huge compared to a wavelength, the same considerations apply at video frequencies for elements that are small compared to a wavelength. The maximum power that can be transferred from a blackbody at a temperature T in a bandwidth Δv (or W in previous section) is the product of the following factors: (1) the number of modes in that bandwidth, Δv, (2) the energy per photon , hv, (3) the photons per mode, $1/\{e^{hv/kT}-1\}$ and (4) the bandwidth Δv.

At video frequencies, there is usually only one mode-the TEM mode extending down to zero frequency, with one direction of polarization of field. Thus, we obtain the low frequency limit pertinent to the detector (or receiver) problem

$$p = 1.\left\{hv/e^{hv/kT}-1\right\}.\Delta v \text{ Watts}$$

At room temperatures and reasonable frequencies (e.g., less than 1 Ghz), the photon energy is much less that the kT (thermal energy) i.e. $hv << kT$ (at room temperature hv / kT is approximately 1/40 eV) and the approximate form of p which is often used is, $p = kT\Delta v$. It is this form, which is referred as Johnson's noise, or also white noise and is an approximation.

$p = kT\Delta v$ is the maximum power that can be transferred from one blackbody circuit element to another blackbody circuit element in the form of thermal noise.

Fig. D-1 below illustrates the restrictions involved in applying $p = 1\{hv/e^{hv/kT} - 1\}\Delta v$. Resistor R_A at a temperature T_A emits noise power according to 'p', to be absorbed by R_B, which in turn, radiates power back to R_A. Only if $R_A = R_B$ will the two systems be "black" to each other's radiation, thereby absorbing all of the incident power.

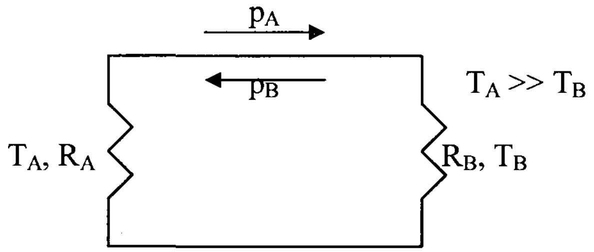

Fig D-1. Exchange of thermal power between two resistors

Therefore, the characterization of an element being "black" is identical to the specification of a system being matched for maximum power transfer. To account for the fact that many systems are not matched, we construct an equivalent circuit with appropriate generators and noiseless resistors, which yields the correct answer for the power transfer when matched and also properly allows for a mismatch. In other words, one of the common practices in designing an electronics circuit is impedance matching. In this, the resistance of various components of a circuit is matched for maximum power transfer. This essentially means that designers wish to construct components that see each other equally "black". Such a model is in Fig. D-2 below.

Further, we define a voltage (or current) generator of such a magnitude as to yield the proper power transfer according to the laws of transmission-line theory, and so that it agrees with the maximum power specified by Planck's formulation. Hence, the mean of the squared rms voltage is

$$\overline{V^2} = 4R\left\{h\nu / e^{h\nu/kT} - 1\right\}\Delta\nu \approx 4RkT\Delta\nu$$

The corresponding current generator is

$$\overline{I^2} = \frac{4}{R}\left\{h\nu / e^{h\nu/kT} - 1\right\}\Delta\nu \approx \frac{4kT}{R}\Delta\nu$$

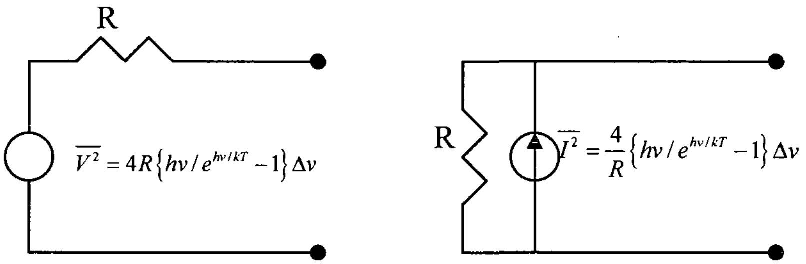

Fig D-2. Equivalent circuits for thermal noise

It is only the resistive part of the circuit that can accept power and, for the same reason, can generate this noise power. A reactive element such as a capacitance affects the bandwidth $\Delta\nu$ under consideration but does not contribute to or accept the noise power.

E. POWER DISTRIBUTION AND ENTROPY

In this analysis we show the connection between distribution of a signal and its power. We further quantify this in bits. Subsequently expressing the harmonics of the signal and using energy conservation one can estimate power in each harmonic, which is magnitude square of its Fourier co-efficient. Therefore, one can quantify the information in each harmonic. The particular example treated below is a source with fixed frequency and phase but varying amplitude (distribution). In the latter part we discuss, a source with frequency and amplitude distribution.

1. Source with fixed frequency and phase

Consider a source emitting Electric fields (photons) of varying amplitudes and phase. The field is given by;

$$f_i(t) = A_i \cos(\omega_0 t + \phi_0) \qquad \text{(E-1)}$$

The energy of the E-field is given by $|A_i|^2$

Now we calculate the distribution of E-field amplitudes assuming that each A_i is independent of the other and the source is thermally excited. In this case one would have a situation where amplitude distribution is such that the entropy is maximized for a fixed average value of the E - field energy.

Let p_i be the probability of the amplitude A_i.

Therefore;

$$\sum_i p_i = 1 \qquad \text{(E-2)}$$

$$\sum_i p_i |A_i|^2 = \langle E \rangle \qquad \text{(E-3)}$$

$$H = -\sum_i p_i \log p_i$$

Maximizing H using Eqns. E-2 and E-3 as constraints;

$$\frac{\partial}{\partial p_i}\left\{\sum_i p_i \log p_i + \lambda_1\left(\sum_i p_i - 1\right) + \lambda_2\left(\sum_i p_i |A_i|^2 - \langle E \rangle\right)\right\} = 0 \qquad \text{(E-4)}$$

$$\left\{1+logp_i+\lambda_1+\lambda_2|A_i|^2\right\}=0$$

$$logp_i=-\left(\lambda_1+1+\lambda_2|A_i|^2\right)$$

$$p_i=Ce^{-\lambda_2|A_i|^2} \tag{E-5}$$

$$p(A)dA=Ce^{-\lambda A^2}dA \tag{E-6}$$

using Eqns. E-2 and E-3 $\int_{-\infty}^{\infty}p(A)dA=1$ and $\int_{-\infty}^{\infty}A^2p(A)dA=\langle E\rangle$

gives, $C=\sqrt{2\pi\sigma}$

$$p(A)dA=\frac{1}{\sqrt{2\pi\sigma}}e^{-\frac{A^2}{2\sigma^2}}dA \quad \textbf{\textit{: Amplitude distribution}} \tag{E-7}$$

Where, $\sigma^2=\langle E\rangle$ (E-8)

writing Eqn. E-7 as energy distribution; $E=A^2$

$$p(E)dE=\frac{1}{w}e^{-\frac{E}{w}}dE \qquad \textbf{\textit{: Energy distribution}} \tag{E-9}$$

Where $w=2\sigma^2=2\langle E\rangle$

Probability distribution of the energy is an exponential with the average value w.

Variance of the energy distribution = w.

Signal energy and Power

If f(t) represents a voltage or electrical signal then its energy is given by

$\int |f(t)|^2\, dt$ Therefore, if $f(t) = A_i \cos(\omega_0 t + \phi_0)$

$$\int |f(t)|^2\, dt = \int |E_i(t)|^2\, dt = |A_i|^2 \qquad \text{(E-10)}$$

Average energy over *p(E$_i$)*; gives the variance of the independent E-filed intensities.

Therefore,

$$\sigma = \left\langle \int |E_i(t)|^2\, dt \right\rangle = \left\langle |A_i|^2 \right\rangle \qquad \text{(E-11)}$$

(Units needs to be adjusted depending on whether A_i is in volts or volts per meter)

Also, time average power of E-field, f_i

$$P_i = \frac{1}{T} \int_0^T |f_i(t)|^2\, dt = \frac{|A_i|^2}{T} \int_0^T \cos^2(\omega_0 t + \phi_0) dt = \frac{|A_i|^2}{T} \qquad \text{(E-12)}$$

Average power over *p(E$_i$)*;

$$\langle P_i \rangle = \left\langle \frac{1}{T} \int_0^T |f_i(t)|^2\, dt \right\rangle = \frac{\left\langle |A_i|^2 \right\rangle}{T} \qquad \text{(E-13)}$$

The above is also equal to the ensemble average (ergodicity)

Signal energy and magnitude of Fourier coefficients: Distribution of the harmonics

Fourier series expansion of a function *f(x)* is expressed as;

$$f(x) = a_0 + \sum_k a_k \cos kx + \sum_k b_k \sin kx \qquad \text{(E-14)}$$

where;

$$a_0 = \int_{-\pi}^{\pi} f(x)dx, \quad a_k = \frac{1}{\pi}\int_{-\pi}^{\pi} f(x)\cos(kx)dx \text{ and } b_k = \int_{-\pi}^{\pi} f(x)\sin(kx)dx$$

Also, from E-14

$$\int_0^T |f(t)|^2\, dt = \int_0^T \left(a_0 + \sum_k a_k \cos(k\omega t) + \sum_k b_k \sin(k\omega t)\right)^2 dt$$

$$\int_0^T |f(t)|^2\, dt = T\{a^2{}_0 + \frac{1}{2}\sum_k (a^2{}_k + b^2{}_k)\} \text{ : \textit{Energy conservation}} \qquad \text{(E-15)}$$

The probability average over *p(E)*; $\int p(E)EdE$ gives the variance of the distribution

$$\left\langle \int_0^T |f_i(t)|^2\, dt \right\rangle = \left\langle T\{a^2{}_{i,0} + \frac{1}{2}\sum_k (a^2{}_{i,k} + b^2{}_{i,k})\} \right\rangle \qquad \text{(E-16)}$$

Probability average of a_0 is zero $\langle a^2{}_{i,0} \rangle = 0$ since it is a constant

$$\langle |E_i|^2 \rangle = T\{\frac{1}{2}\sum_k (\langle a^2{}_{i,k} \rangle + \langle b^2{}_{i,k} \rangle)\} \qquad \text{(E-17)}$$

('k' is the index for harmonic order and averaging is over index 'i')

Therefore, if $f_i(t) = A_i \cos(\omega_0 t + \phi_0)$

$$a_{i,k} = \frac{\omega}{\pi}\int_{-\pi/\omega}^{\pi/\omega} f_i(t)\cos(k\omega t)dt$$

$$a_{i,k} = \frac{\omega A_i}{\pi}\int_{-\pi/\omega}^{\pi/\omega}\cos(\omega_0 t+\phi_0)\cos(k\omega t)dt$$

$$a_{i,k} = \frac{\omega A_i}{2\pi}\int_{-\pi/\omega}^{\pi/\omega}\cos([k\omega+\omega_0]t+\phi_0)dt + \frac{\omega A_i}{2\pi}\int_{-\pi/\omega}^{\pi/\omega}\cos([k\omega-\omega_0]t+\phi_0)dt$$

$$a_{i,k} = \frac{\omega A_i}{\pi}\int_{0}^{\pi/\omega}\cos([k\omega+\omega_0]t+\phi_0)dt + \frac{\omega A_i}{\pi}\int_{0}^{\pi/\omega}\cos([k\omega-\omega_0]t+\phi_0)dt$$

$$a_{i,k} = \frac{\omega A_i}{\pi(k\omega+\omega_0)}\int_{\phi_0}^{c}\cos u\,du + \frac{\omega A_i}{\pi(k\omega-\omega_0)}\int_{\phi_0}^{d}\cos v\,dv$$

$$c = (k+\frac{\omega}{\omega_0})\pi+\phi_0 \qquad\qquad d = (k-\frac{\omega}{\omega_0})\pi+\phi_0$$

$$a_{i,k} = \frac{A_i}{\pi}\left\{\sin(\phi_0)\left(\frac{1}{(k+\omega_0/\omega)}+\frac{1}{(k-\omega_0/\omega)}\right)-\left(\frac{\sin(c)}{(k+\omega_0/\omega)}+\frac{\sin(d)}{(k-\omega_0/\omega)}\right)\right\}$$

Therefore,

$$a_{i,1} = \frac{A_i}{\pi}\left\{\delta(\omega-\frac{\omega_0}{k})+\delta(\omega+\frac{\omega_0}{k})\right\} \tag{E-18}$$

From the above, signal energy $|A_i|^2 = |a_{i,1}|^2$. Therefore, one can express the signal energy in terms of Fourier co-efficient of its expansion. The average energy over *p(E)* is

$$\langle |A_i|^2\rangle = \langle |a_{i,1}|^2\rangle$$

In a more complicated function, *f(t)*, with higher Fourier co-efficient the total signal energy can be shown as a sum magnitude square of the individual Fourier co-efficients, $|a_{i,k}|^2$.

Following, from the above one can write the average power in each harmonic given by,

$$\int p(c_k)c_k dc_k \text{ , with } p(c_k) = \frac{1}{\langle c_{i,k}\rangle} e^{c_k/\langle c_{i,k}\rangle} \; ; c_k = |a_k|^2 \qquad \text{(E-19)}$$

Where, in each harmonics as $|a_k|^2$ *and if these are from a thermally excited source then one can write the amplitude distribution of each harmonic for various* A_i *i.e.* $|a_k|_i^2$

Signal Power

$$\frac{1}{T}\int_0^T |f_i(t)|^2 \, dt = \{a^2_{i,0} + \frac{1}{2}\sum_k (a^2_{i,k} + b^2_{i,k})\}; \text{ 1/ T is the bandwidth}$$

It should be noted that in an absorption or emission experiments, the emitted photons (or the photons on the photodetector) are not the thermal photons i.e. these photons are not part of, or aid in establishing thermal equilibrium of the system (gas in a box) that resulted in emission (or absorption) of these photons. In addition, there is no temperature associated with these photons. Temperature can only be brought in this analysis when these photons interact with the detector and establish equilibrium with the lattice as a result of energy conservation. This is contrary to blackbody photons, i.e. the photons that are collected from a pinhole of (blackbody) cavity: these photons are thermal I nature and has a notion of temperature directly associated with them.

2. Source with fixed amplitude and phase

In this section we will estimate average Intensity of a source (emitting E-fields) with a spectral distribution. We will also estimate the intensity distribution of thermal source and distributions of the Fourier harmonics of the intensity. Consider, a source consisting of large number of atoms or molecules in thermal equilibrium. The source constantly emits Electric fields (photons) a range of frequencies. The field is given by;

$$f(t) = \exp(i\frac{\omega_0}{c}x(t)) \quad \text{where,} \quad x(t) = \int_{-\infty} v(t')dt'$$

Let *f(t)* be in units of Volts/meter

The average power of the E-field is given by;

$$I(\omega) = \lim_{T\to\infty}\left|\frac{1}{\sqrt{2\pi T}}\int_{-T/2}^{T/2} f(t)e^{-i\omega t}dt\right|^2 \qquad \text{(E-20)}$$

$$I(\omega) = \frac{1}{\pi}\int_0^{\infty}\varphi(\tau)e^{-i\omega\tau}d\tau \qquad \textbf{- Einstein - Weiner- Khinchin Theorem} \qquad \text{(E-21)}$$

{where, I is in Joules/sec.m^2 }

Where, $\varphi(\tau) = \lim_{T\to\infty}\frac{1}{T}\int_{-T}^{T} f^*(t)f(t+\tau)dt$ (E-22)

{See Appendix}

Eqn. E-22is also equal to $\varphi(\tau)=\left\langle f^{*}(t)f(t+\tau)\right\rangle$ [1]

$$\varphi(\tau)=\left\langle \exp[i\frac{\omega_0}{c}x(\tau)]\right\rangle \qquad \text{(E-23)}$$

Expressing the above in the form;

$$\varphi(\tau)=\langle \exp[ik.r(\tau)]\rangle,\ \ r(\tau)=\int_0^{\tau} v(t)dt$$

Introducing distribution function $f(r,v,t)$ for the oscillator coordinate, r and velocity, v. This distribution function satisfied Boltzmann equation.

$$\frac{\partial f}{\partial t}+v.\nabla f=\left(\frac{\partial f}{\partial t}\right)_{collision}$$ and the initial condition, $f(r,v,0)=W(v)\delta(r)$

Therefore,

$$\varphi(\tau)=\int dv\int f(r,v,\tau)\exp[ik.r]dr \qquad \text{(E-24)}$$

And

$$I(\omega)=\frac{1}{\pi}\int dv\int f(r,v,\tau)\exp[i(\omega\tau-k.r)]drd\tau \qquad \text{(E-25)}$$

In order to determine the average intensity of the photons, we need to calculate its energy distribution using maximum entropy concepts.

---

[1] This is also known as correlation function. The function is used when phase varies with time (i.e. frequency or phase) is a distribution (one cannot have a constant phase of E-field if the frequency is a random variable). In situations where frequency is constant, e.g. in Lorentzian lineshape one can write intensity as, I = ∫|E(t)E*(t)|dt. In case where frequency is a distribution, intensity is a convolution I = ∫|E(t)E*(t+τ)|dτ.

Correlation function and Spectral density

The correlation function is defined as:

$$\varphi(\tau) = \lim_{T\to\infty} \frac{1}{T} \int_{-T}^{T} f^*(t) f(t+\tau) dt \qquad \text{(E-26)}$$

The Fourier Transform of the function *f(t)* is,

$$f(t) = \int_{-\infty}^{\infty} f(\omega) e^{-i\omega t} d\omega \qquad \text{(E-27)}$$

And the complex conjugate is given by,

$$f^*(t) = \int_{-\infty}^{\infty} f^*(\omega) e^{i\omega t} d\omega \qquad \text{(E-28)}$$

Therefore, substituting Eqns. E-27 and E-28 in E-26,

$$\varphi(\tau) = \lim_{T\to\infty} \frac{1}{T} \int_{-T}^{T} \int_{-\infty}^{\infty} \int_{-\infty}^{\infty} f^*(\omega') e^{i\omega' t} f(\omega) e^{-i\omega(t+\tau)} d\omega' d\omega dt \qquad \text{(E-29)}$$

$$\varphi(\tau) = \lim_{T\to\infty} \frac{1}{T} \int_{-T}^{T} \left\{ e^{i(\omega'-\omega)t} dt \right\} \int_{-\infty}^{\infty} \int_{-\infty}^{\infty} f^*(\omega') f(\omega) e^{-i\omega\tau} d\omega' d\omega$$

$$\varphi(\tau) = \int_{-\infty}^{\infty} \int_{-\infty}^{\infty} \delta(\omega' - \omega) f^*(\omega') f(\omega) e^{-i\omega\tau} d\omega' d\omega \qquad \text{(E-30)}$$

$$\varphi(\tau) = \int_{-\infty}^{\infty} f^*(\omega) f(\omega) e^{-i\omega\tau} d\omega \qquad \text{(E-31)}$$

If *f (t)* describes an E – field (with proper units), φ(τ) represents the Fourier transform of the spectral density *f(ω)f*(ω)*

Special Case: Note that if τ = 0

From Eqn. E-26

$\varphi(0)=\lim_{T\to\infty}\frac{1}{T}\int_{-T}^{T}f^{*}(t)f(t)dt$, φ(0) is the E – field intensity or the Poynting vector.

Also, from Eqn. E-31 if τ = 0

$\varphi(0)=\int_{-\infty}^{\infty}f^{*}(\omega)f(\omega)d\omega$, φ(0) is the spectral density.

F. DISTRIBUTION OF TURNING POINTS OF OVERLAPPING TRANSITIONS

This appendix shows calculations of the probability distribution of turning points of two overlapping lines in WMS signal. Since, the two transitions are statistically independent; WMS signal magnitude at any frequency in spectrum can be expressed as the sum of the signal due to individual transitions i.e.

$V \rightarrow V_{LINE1} \pm V_{LINE2}$

The total signal magnitude depends on the modulation index, m, absorption cross-section, σ_{abs} and line separation.

The distribution of the signal due to overlap can be expressed as,

$$p(V)dV=\frac{1}{\sqrt{2\pi}\sigma}e^{-(V-\{V_{LINE1}\pm V_{LINE2}\})^{2}/2\sigma^{2}}dV \tag{F-1}$$

The total entropy of 2(N+1) turning points of the two overlapping transitions is,

$$H_{N}=\sum_{T=1}^{2(N+1)}\log\{\sigma(V_{T})\} \tag{F-2}$$

Here, $\sigma_n(V_T)$, is the variance of one of the turning point of Nth order harmonic. Therefore, information extracted from a change in modulation indices from m_1 to m_2 is given by;

$$\delta H_N = \sum_T \log\left\{\{\sigma_n(V_T)\}_{m_2} / \{\sigma_n(V_T)\}_{m_1}\right\} \tag{F-3}$$

G. MATLAB CODE

Various algorithms were used while programming WMS signals for modeling the experimental data. A sample Matlab code that computes *k*th order WMS signal is given below. The routine uses different call functions to compute four different oxygen transitions. The lineshape used here is a Voigt profile which can be changed to a Doppler or a Lorentzian from the call function file.

```
%% This code computes WMS signals. The detection order can be changed from
%% k values. The code implements Wilsons method (dblquad integration). The
code has 4 oxygen lines each of them has its own call function. The input
parameters are % taken from HITRAN data file.%%

format long
c1=3*10^10;% speed of light in cm/sec
c=3*10^8 ;
k=6; % Harmonic order
beta=(1.4)*10^9;% modulation frequency in Hz
A= xlsread('wavelengthdata','ExpJune07_09N6','11:13200');% wavelength in nm
from Aug 15 exp
stepsize=1;  % the data is large truncate accordingly to save computation
time.
n1=length(A)/stepsize; % no. of data points
%linecenters in cm-1
linecenterR1313= 13151.340150; % linecenter of R1313 in cm-1
linecenterR1313weak= 13151.72491 % linecenter of R1313weaker line in cm-1
linecenterR4343= 13151.81436 % linecenter of R4343 in cm-1
linecenterR1213= 13152.3203 % linecenter of R1213 in cm-1
%Linecenters in Hz
g0R1313= c1*(linecenterR1313); %linecenter in Hz of R1313 in bracket
linecenter in cm-1 line center =1.3*10^14
g0R1313weak=c1*(linecenterR1313weak);
g0R4343=c1*(linecenterR4343);
g0R1213=c1*(linecenterR1213);

%doppler linewidths calculations %%in some cases directly taken from HITRAN
M1=2*16*10^-27 ;% mass of oxygen in Kilograms of O2 (atomic mass =16); 1 amu
= 1.66054 x 10-24 grams
M2=2*18*10^-27 ;% mass of Nitrogen (as second major molecule in air) in
Kilograms of O2 (atomic mass =16); 1 amu = 1.66054 x 10-24 grams
k1=1.38062*10^-23 ;% Boltzman constant J/K
T=300; % temp in K
linewidthdopR1313=3.1*10^9;%(1/sqrt(4*log(2)))*sqrt(8*k1*T*log(2)/(M1*c^2))*l
inecenter*c1; % normalized linewidth in hz
linewidthdopR1313weak=2.5*10^9;;%(1/sqrt(4*log(2)))*sqrt(8*k1*T*log(2)/(M1*c^
2))*linecenterR1313weak*c1; %  normalized linewidth in hz
linewidthdopR4343=2.3384*10^9;%%(1/sqrt(4*log(2)))*sqrt(8*k1*T*log(2)/(M1*c^2
))*linecenterR4343*c1; %  normalized linewidth in hz
```

```
linewidthdopR1213=2.5*10^9%(1/sqrt(4*log(2)))*sqrt(8*k1*T*log(2)/(M1*c^2))*li
necenterR1213*c1; %  normalized linewidth in hz

%collisional linewidths
linewidthlorR1313=2.4192*10^9;% linewidth in hz
linewidthlorR1313weak=2.0192*10^9;
linewidthlorR4343=2.38641*10^9;
linewidthlorR1213=2.0192*10^9;

% calculation of Voigt function
yR1313=sqrt(4*log(2))*linewidthlorR1313/(2*linewidthdopR1313);% imaginary
part of complex plane NOTE y is inbuilt in the rational approximation in the
code do no need
yR1313weak=sqrt(4*log(2))*linewidthlorR1313weak/(2*linewidthdopR1313weak);
yR4343=sqrt(4*log(2))*linewidthlorR4343/(2*linewidthdopR4343);
yR1213=sqrt(4*log(2))*linewidthlorR1213/(2*linewidthdopR1213);

mR1313=beta/linewidthlorR1313; % modulation index
mR1313weak=beta/linewidthlorR1313weak;
mR1213=beta/linewidthlorR1213;
mR4343=beta/linewidthlorR1313;
%%saturation parameter
n=5.21197e+18;%density cm-3
abscrossR1313= c1*(5.67E-24);% %absorption cross-section(line strength) from
Hitran line, factor of c1 is to convert in proper unit i.e. from cm2-hz to
cm-1 cm2 mol-1
abscrossR1313weak=c1*(1.15E-26); % %absorption cross-section cm-1 cm2 mol-1
of R1313 weak line
abscrossR4343=c1*(1.32E-28);
abscrossR1213=c1*(1.41E-26);
L=20790;% length in centimeters

sigmacollR1313=1;%2.4265E-15 ;
sigmacollR1213=1;%2.4265E-15;
sigmacollR1313weak=1;%2.4265E-15;%
sigmacollR4343=1;%1.8607E-15
gasparamR1313=n*abscrossR1313*L;
gasparamR1313weak=n*abscrossR1313weak*L;
gasparamR1213=n*abscrossR1213*L;
gasparamR4343=n*abscrossR4343*L;
coeffR1313=(2/pi^(3/2))*gasparamR1313/(linewidthlorR1313);
coeffR1313weak=(2/pi^(3/2))*gasparamR1313weak/(linewidthlorR1313weak);
coeffR1213=(2/pi^(3/2))*gasparamR1213/(linewidthlorR1213);
coeffR4343=(2/pi^(3/2))*gasparamR4343/(linewidthlorR4343);
saturationparameterR1313 = coeffR1313*pi*yR1313*exp(yR1313^2)*erfc(yR1313);
freq=0;
d=0;
A2=c1./(A.*10^-7);% conversion of wavelength to frequency in Hz
for A9 = 0:01:n1-4% the loop runs total number of wavelength data points
    freq=freq+stepsize;
    vL=A2(freq) ;
    d=d+1
    A22(d)=A(freq);
```

```
%%NORMALISED FREQUENCIES
xR1313=(A2(freq)-g0R1313)/linewidthlorR1313;
xR1313weak=(A2(freq)-g0R1313weak)/linewidthlorR1313;
xR4343=(A2(freq)-g0R4343)/linewidthlorR1313;
xR1213=(A2(freq)-g0R1213)/linewidthlorR1313;

%%%% R1313 STRONG line
intvoigtterm41(d)=dblquad(@voigtlineshape,-10^1,+10^1,-pi,+pi,10^-
11,@quad,coeffR1313,yR1313,xR1313,mR1313,k);%% % term 4
intvoigtterm51(d)=dblquad(@voigtlineshape,-10^1,+10^1,-pi,+pi,10^-
11,@quad,coeffR1313,yR1313,xR1313,mR1313,k-1);%%
intvoigtterm52(d)=dblquad(@voigtlineshape,-10^1,+10^1,-pi,+pi,10^-
11,@quad,coeffR1313,yR1313,xR1313,mR1313,k+1);%%
intvoigtterm71(d)=dblquad(@voigtlineshape,-10^1,+10^1,-pi,+pi,10^-
11,@quad,coeffR1313,yR1313,xR1313,mR1313,k-2);%%
intvoigtterm72(d)=dblquad(@voigtlineshape,-10^1,+10^1,-pi,+pi,10^-
11,@quad,coeffR1313,yR1313,xR1313,mR1313,k+2);%%
%%%% R1313 weak line
intvoigtterm41R1313weak(d)=dblquad(@voigtlineshapeR1313weak,-10^1,+10^1,-
pi,+pi,10^-9,@quad,coeffR1313weak,yR1313weak,xR1313weak,mR1313weak,k);%%
intvoigtterm51R1313weak(d)=dblquad(@voigtlineshapeR1313weak,-10^1,+10^1,-
pi,+pi,10^-9,@quad,coeffR1313weak,yR1313weak,xR1313weak,mR1313weak,k-1);%%
intvoigtterm52R1313weak(d)=dblquad(@voigtlineshapeR1313weak,-10^1,+10^1,-
pi,+pi,10^-9,@quad,coeffR1313weak,yR1313weak,xR1313weak,mR1313weak,k+1);%%
intvoigtterm71R1313weak(d)=dblquad(@voigtlineshapeR1313weak,-10^1,+10^1,-
pi,+pi,10^-9,@quad,coeffR1313weak,yR1313weak,xR1313weak,mR1313weak,k-2);
intvoigtterm72R1313weak(d)=dblquad(@voigtlineshapeR1313weak,-10^1,+10^1,-
pi,+pi,10^-9,@quad,coeffR1313weak,yR1313weak,xR1313weak,mR1313weak,k+2);%%
% %%%% R4343 weak line
intvoigtterm41R4343(d)=dblquad(@voigtlineshapeR4343,-10^1,+10^1,-pi,+pi,10^-
9,@quad,yR4343,coeffR4343,xR4343,mR4343,k);%%
intvoigtterm51R4343(d)=dblquad(@voigtlineshapeR4343,-10^1,+10^1,-pi,+pi,10^-
9,@quad,yR4343,coeffR4343,xR4343,mR4343,k-1);
intvoigtterm52R4343(d)=dblquad(@voigtlineshapeR4343,-10^1,+10^1,-pi,+pi,10^-
9,@quad,yR4343,coeffR4343,xR4343,mR4343,k+1);%%
intvoigtterm71R4343(d)=dblquad(@voigtlineshapeR4343,-10^1,+10^1,-pi,+pi,10^-
9,@quad,yR4343,coeffR4343,xR4343,mR4343,k-2);
intvoigtterm72R4343(d)=dblquad(@voigtlineshapeR4343,-10^1,+10^1,-pi,+pi,10^-
9,@quad,yR4343,coeffR4343,xR4343,mR4343,k+2);%%
% %%%% R1213 weak line
intvoigtterm41R1213(d)=dblquad(@voigtlineshapeR1213,-10^1,+10^1,-pi,+pi,10^-
9,@quad,yR1213,coeffR1213,xR1213,mR1213,k);
intvoigtterm51R1213(d)=dblquad(@voigtlineshapeR1213,-10^1,+10^1,-pi,+pi,10^-
9,@quad,yR1213,coeffR1213,xR1213,mR1213,k-1);
intvoigtterm52R1213(d)=dblquad(@voigtlineshapeR1213,-10^1,+10^1,-pi,+pi,10^-
9,@quad,yR1213,coeffR1213,xR1213,mR1213,k+1);
intvoigtterm71R1213(d)=dblquad(@voigtlineshapeR1213,-10^1,+10^1,-pi,+pi,10^-
9,@quad,yR1213,coeffR1213,xR1213,mR1213,k-2);%%
intvoigtterm72R1213(d)=dblquad(@voigtlineshapeR1213,-10^1,+10^1,-pi,+pi,10^-
9,@quad,yR1213,coeffR1213,xR1213,mR1213,k+2);%%
end

%%AMPLITUDE MODULATION
%WMS higher order terms due to amplitude modulation, r
k1=k-1;% k-1 if k is odd and k i k is even
```

```
k2=k+1;%k+1 if k is odd and k if k is even
psi=0;%pi;
r=0.08;% amplitude modulation

q4=1;%((factorial(k)/(pi*(2^(1-k))*(beta^k))));
intvoigtterm4=-(1+(r^2)/8)*(-1^(k1/2))*q4*intvoigtterm41;%%
intvoigtterm4R1313weak=-(1+(r^2)/8)*(-1^(k1/2))*q4*intvoigtterm41R1313weak;%%
intvoigtterm4R4343=-(1+(r^2)/8)*(-1^(k1/2))*q4*intvoigtterm41R4343;%%
intvoigtterm4R1213=-(1+(r^2)/8)*(-1^(k1/2))*q4*intvoigtterm41R1213;
q51=1;%(factorial((k-1))./(pi*(2.^(1-(k-1)))*(beta.^(k-1))));
q52=1;%(factorial((k+1))./(pi*(2.^(1-(k+1)))*(beta.^(k+1))));
intvoigtterm5=-r*sin(psi)*(((-1).^(k2/2 +1))/2)*(q51*intvoigtterm51-
q52*intvoigtterm52);
intvoigtterm5R1313weak=-r*sin(psi)*(((-1).^(k2/2
+1))/2)*(q51*intvoigtterm51R1313weak-q52*intvoigtterm52R1313weak);
intvoigtterm5R4343=-r*sin(psi)*(((-1).^(k2/2
+1))/2)*(q51*intvoigtterm51R4343-q52*intvoigtterm52R4343);%%
intvoigtterm5R1213=-r*sin(psi)*(((-1).^(k2/2
+1))/2)*(q51*intvoigtterm51R1213-q52*intvoigtterm52R1213);

q6=1;%(factorial((k-1))/(pi*(2^(1-(k-1)))*(beta^(k-1))));
intvoigtterm6=-r*cos(psi)*(((-1)^(k2/2))/2)*q6*intvoigtterm51;
intvoigtterm6R1313weak=-r*cos(psi)*(((-
1)^(k2/2))/2)*q6*intvoigtterm51R1313weak;
intvoigtterm6R4343=-r*cos(psi)*(((-1)^(k2/2))/2)*q6*intvoigtterm51R4343;
intvoigtterm6R1213=-r*cos(psi)*(((-1)^(k2/2))/2)*q6*intvoigtterm51R1213;
q71=1;%(factorial((k-2))/(pi*(2^(1-(k-2)))*(beta^(k-2))));
q72=1;%(factorial((k+2))/(pi*(2^(1-(k+2)))*(beta^(k+2))));
intvoigtterm7=-((r^2)/8)*sin(2*psi)*((-1^(k2/2))/2)*(-q71*intvoigtterm71+
q72*intvoigtterm72);
intvoigtterm7R1313weak=-((r^2)/8)*sin(2*psi)*((-1^(k2/2))/2)*(-
q71*intvoigtterm71R1313weak+ q72*intvoigtterm72R1313weak);
intvoigtterm7R4343=-((r^2)/8)*sin(2*psi)*((-1^(k2/2))/2)*(-
q71*intvoigtterm71R4343+ q72*intvoigtterm72R4343);
intvoigtterm7R1213=-((r^2)/8)*sin(2*psi)*((-1^(k2/2))/2)*(-
q71*intvoigtterm71R1213+ q72*intvoigtterm72R1213);
q81=1;%=(factorial((k-2))/(pi*(2^(1-(k-2)))*(beta^(k-2))));
q82=1;%(factorial((k+2))/(pi*(2^(1-(k+2)))*(beta^(k+2))));
intvoigtterm8=-((r^2)/8)*cos(2*psi)*((-
1^(k1/2+1))/2)*(q81*intvoigtterm71+q82*intvoigtterm72);
intvoigtterm8R1313weak=-((r^2)/8)*cos(2*psi)*((-
1^(k1/2+1))/2)*(q81*intvoigtterm71R1313weak+q82*intvoigtterm72R1313weak);
intvoigtterm8R4343=-((r^2)/8)*cos(2*psi)*((-
1^(k1/2+1))/2)*(q81*intvoigtterm71R4343+q82*intvoigtterm72R4343);
intvoigtterm8R1213=-((r^2)/8)*cos(2*psi)*((-
1^(k1/2+1))/2)*(q81*intvoigtterm71R1213+q82*intvoigtterm72R1213);

FullvoigtR1313=(intvoigtterm4+intvoigtterm5+intvoigtterm6+intvoigtterm7+intvo
igtterm8);
FullvoigtR1313weak=(intvoigtterm4R1313weak+intvoigtterm5R1313weak+intvoigtter
m6R1313weak+intvoigtterm7R1313weak+intvoigtterm8R1313weak);
FullvoigtR4343=(intvoigtterm4R4343+intvoigtterm5R4343+intvoigtterm6R4343+intv
oigtterm7R4343+intvoigtterm8R4343);
FullvoigtR1213=(intvoigtterm4R1213+intvoigtterm5R1213+intvoigtterm6R1213+intv
oigtterm7R1213+intvoigtterm8R1213);
```

```
%%SUM OF ALL INTERFERING LINES
Alllines=FullvoigtR1313+FullvoigtR1313weak+FullvoigtR4343+FullvoigtR1213;
%ALL MODELED LINES

%%LINECENTR MATCHING OF MODEL AND EXPERIMENT. EXPERIMENT DATA IMPORTED FROM
%%EXCEL FILE
Expsignalfulldata=
transpose(xlsread('Experimentdata','ExpJuly10_09N6','a1:a2200'));% wavelength
in nm from Aug 15 exp
Expsignal=Expsignalfulldata(1,1:stepsize:length(Expsignalfulldata)-30);
nexp=length(Expsignal);
nmodel=length(Alllines);
wavlinecenter = 1200;%input('linecenter index of wavelength data')
Explinecenter = 1700;%input('linecenter index of Exp data')
diffindex = abs(wavlinecenter-Explinecenter);

if wavlinecenter < Explinecenter
Alllines_new(1,1:diffindex)= zeros(1,diffindex);
Alllines_new(1,1+diffindex:diffindex+nmodel)=Alllines(1,1:nmodel);
%n1+diffindex-10
Expsignal_new(1,1:nexp)= Expsignal(1:nexp);
Expsignal_new(1,nexp+1:nexp+diffindex)=zeros(1,diffindex);

else
%if wavlinecenter >Explinecenter
Expsignal_new(1,1:diffindex)= zeros(1,diffindex);
Expsignal_new(1,1+diffindex:diffindex+nexp)=Expsignal(1,1:nexp);
Alllines_new(1,1:nmodel)= Alllines(1:nmodel);
Alllines_new(1,nmodel+1:nmodel+diffindex)=zeros(1,diffindex);
end

t1=(1:length(Expsignal_new));
t2=(1:length(Alllines_new));

plot(t1,Expsignal_new./max(Expsignal_new),t2,abs(Alllines_new)./max(abs(Allli
nes_new)),'r')
pause
frerror = abs(1 - Alllines_new(1:length(t1))./Expsignal_new(1:length(t1)));

for j = 1:length(frerror)

if (100*frerror(j)) > 200 &  (100*frerror(j)) ~= inf % 200 percent mismatch
    frerror1(j)=2;
elseif  frerror(j) == 1 |Expsignal_new(j)==0 |Alllines_new(j)==0
    frerror1(j)=0;
else
    frerror1(j)=frerror(j);
end

end
j2=1:length(frerror1);
varfrerror = var(frerror1)
plot(t1,Expsignal_new,t2,Alllines_new,'r',j2,frerror1,'.')
```

```
pause



%%ESTIMATION OF ZERO CROSSINGS AND TURNING POINTS
d3=0;
d4=0;
for A9=2:length(Expsignal)-2
    x3= (A2(A9)-g0R1313 )/linewidthlorR1313;
    d3=d3+1;
    slope1(d3) = abs(Expsignal(A9)) - abs(Expsignal(A9+1));
    slope2(d3) = abs(Expsignal(A9)) - abs(Expsignal(A9-1));

    if slope1(d3)>0  && slope2(d3)>0 || slope1(d3)< 0 && slope2(d3)< 0
||slope1(d3)==0  && slope2(d3)>0 ||slope1(d3)>0  && slope2(d3)==0
||slope1(d3)==0  && slope2(d3)<0 ||slope1(d3)<0  && slope2(d3)==0
%(10/100)*directwms(g2)
        d4=d4+1;
        TPZC(d4)=abs(Expsignal(A9));%signal magnitude of the turning point or
zero crossing
        wav(d4)= x3; %%spectral location of the turning point or zero
crossing
        ErroravTPZC(d4)= mean(Fracerror(A9-10:A9+10)); % fractional error
around turning points
        PowerTPZC(d4)= sum(abs((Expsignal(A9-10:A9+10)))); %%power around T/Z
        else
    Errorspectrum(d3) = Fracerror(A9);%%fraction error due to spectrum except
turning points and zero crossing w/+-10 points next to them ;see above code
    Powerspectrum(d3) = abs(Expsignal(A9)); %%power in spectrum excluding T/Z
    end
end
   %%The input data can be chnaged from experimental to model to estimate the
   %%turning points of the model data
ErrorTPZC= mean(ErroravTPZC)%cumulative error around turning points
Errorspectrum = mean(Errorspectrum)
AvPowerTPZC=sum(PowerTPZC)
AvPowerspectrum= sum(Powerspectrum)

 TPm = TPZC(1,1:2:length(TPZC)) ;%%turning points
 wavTPm =wav(1, 1:2:length(wav));%spectral location of turning points
 ZCm = TPZC(1, 2:2:length(TPZC)); %%zero crossings
 wavZCm=wav(1, 2:2:length(wav)) ;%%spectral location of zero crossings
 ratioTPm = TPm/max(TPm);

TPZCexceldata=transpose(TPZC)/max(TPZC);
wavTPZCexceldata=transpose(wav);
plot(TPZC,'.-')
TPZCtr=transpose(TPZC)

%%EXAMPLE LINEWIDTH SENSTIVITY AT TURNING POINTS AND ZERO CROSSINGS
 for t = 1:k+1  % k+1 = number  of turning points
       d6=0;
 for linewidthdop=1.8*10^9:0.02*10^9:2.2*10^9
     m1= beta/linewidthdop;
     d6=d6+1;
```

```
 TPintvoigtterm41lw(d6)=coeff*abs(((1/pi))*quadl(@gaussianlineshape2,-
pi,+pi,10^-18,[],linewidthdop,wavTPm(t),m1,k));
 end
 TPintvoigtterm41lwperc(t,1:d6)=100*(TPm(t)-TPintvoigtterm41lw)./TPm(t);  %%
percantage change in the signal with LW
 end

 for t = 1:k  % k = number  of zero crossings
       d7=0;
 for linewidthdop=1.8*10^9:0.02*10^9:2.2*10^9
     m1= beta/linewidthdop;
     d7=d7+1;
  ZCintvoigtterm41lw(d7)=coeff*abs(((1/pi))*quadl(@gaussianlineshape2,-
pi,+pi,10^-18,[],linewidthdop,wavZCm(t),m1,k));
 end
 ZCintvoigtterm41lwperc(t,1:d7)=100*(ZCm(t)-ZCintvoigtterm41lw)./ZCm(t);
end

 linewidthdop=1.8*10^9:0.02*10^9:2.2*10^9;
 pause
 plot(linewidthdop/10^9,abs(TPintvoigtterm41lwperc(1:k+1,1:d6)))
 pause
 plot(linewidthdop/10^9,abs(ZCintvoigtterm41lwperc(1:k,1:d7)))
 spectrallocation = abs(min(abs(wav))-abs(wav));
```

%%CALL FUNCTION FILES

```
function PLVR1313=voigtlineshape(t,theta,coeffR1313,yR1313,xR1313,mR1313,k)
%function V = voigtlineshape(t,theta,y,x,m,k)

%%V= ((y/pi).*exp(-t.^2)./(y^2 +((sqrt(log(2))*((x + m*cos(theta))-
t).^2)))).*(cos(k*theta));  %where m= beta/sigmadop

PLVR1313= (1- exp(-coeffR1313.*exp(-t.^2)./(1+(2*xR1313 + 2*mR1313*
cos(theta)+t./yR1313).^2))).* (cos(k*theta));

function
PLVR1313weak=voigtlineshape(t,theta,coeffR1313weak,yR1313weak,xR1313weak,mR13
13weak,k)
%%V = voigtlineshape(t,theta,y,x,m,k)
%V= ((y/pi).*exp(-t.^2)./(y^2 +((sqrt(log(2))*((x + m*cos(theta))-
t).^2)))).*(cos(k*theta));
%PLVR1313= (1- exp(-coeff*((1/pi).*exp(-t.^2)./(yR1313^2
+((sqrt(log(2))*((xR1313 + m*cos(theta))-t).^2)))))).*(cos(k*theta));
%%voigt with pathlength saturation
PLVR1313weak= (1- exp(-coeffR1313weak.*exp(-t.^2)./(1+((xR1313weak +
mR1313weak*cos(theta))/2-t/yR1313weak).^2))).*(cos(k*theta));


function PLVR1213=voigtlineshape(t,theta,coeffR1213,yR1213,xR1213,mR1213,k)
%%V = voigtlineshape(t,theta,y,x,m,k)
%V= ((y/pi).*exp(-t.^2)./(y^2 +((sqrt(log(2))*((x + m*cos(theta))-
t).^2)))).*(cos(k*theta));  %where m= beta/sigmadop
```

```
%PLVR1313= (1- exp(-coeff*((1/pi).*exp(-t.^2)./(yR1313^2
+((sqrt(log(2))*((xR1313 + m*cos(theta))-t).^2)))))).*(cos(k*theta));
%%voigt with pathlength saturation
PLVR1213= (1- exp(-coeffR1213.*exp(-t.^2)./(1+((xR1213 +
mR1213*cos(theta))/2-t/yR1213).^2))).*(cos(k*theta));
function PLVR4343=voigtlineshape(t,theta,coeffR4343,yR4343,xR4343,mR4343,k)
%%V = voigtlineshape(t,theta,y,x,m,k)
%V= ((y/pi).*exp(-t.^2)./(y^2 +((sqrt(log(2))*((x + m*cos(theta))-
t).^2)))).*(cos(k*theta));  %where m= beta/sigmadop
%PLVR1313= (1- exp(-coeff*((1/pi).*exp(-t.^2)./(yR1313^2
+((sqrt(log(2))*((xR1313 + m*cos(theta))-t).^2)))))).*(cos(k*theta));
%%voigt with pathlength saturation
PLVR4343= (1- exp(-coeffR4343.*exp(-t.^2)./(1+((xR4343 +
mR4343*cos(theta))/2-t/yR4343).^2))).*(cos(k*theta));
```

M. Amir Khan

827 W 48 St. Apt A, Norfolk, VA-23508, Phone: 757 -553- 4069, email: amirkhanodu@gmail.com

EDUCATION

- **2003- 2009: PhD** in Electrical and Computer Engineering from Old Dominion University, Norfolk, VA
- **2001- 2003: Masters of Engineering** in Electrical Engineering from Old Dominion University, Norfolk, VA
- **1998 - 2000: Masters of Science** in Physics from Indian Institute of Technology **(IIT)**, New Delhi, India
- **1995 – 1998: Bachelor of Science** in Physics (Honors) from JMI University, New Delhi, India

EXPERIENCE

Graduate Research Assistant AND Teaching Instructor **May 2001 to Aug 2009**
Laser and Plasma Engineering Institute, OLD DOMINION UNIVERSITY

- Developed ultra-sensitive non-intrusive laser based (VCSEL) sensor utilizing wavelength modulation spectroscopy for precision measurements of trace gas species (molecular oxygen) and materials in optical thick medium.
- Developed automated system for acquisition, signal processing and simulation of modulation spectroscopic signals.
- Developed optimization techniques utilizing concepts of Information theory in spectroscopic measurements.
- Mentored entry level (Masters and PhD) team members in the research group.
- Taught Undergraduate Courses including Laboratory Courses to classes of 30-40 student size class in the subjects of Analog Electronic Circuits, Digital Electronics, Electromagnetic and Introduction to Engineering, Explore Engineering Technology.
- Developed course curriculum, course material, setup of the experimental apparatus and supervision of the laboratory work. Areas of laboratory instruction include Programmable logic devices, Simulink/Workbench Instrumentation and Optical (Photonics) communication projects.
- Taught (100-400 level) courses in Mathematics, Physics, Chemistry and Engineering at Student Support Services (SSS), ODU.

RECENT RESEARCH PROJECTS

- **Laser Based Sensor:** Wavelength modulation spectroscopy (using tunable VCSEL's) is a non-intrusive and ultra-sensitive technique to probe gaseous species (e.g. molecular oxygen A- Band magnetic dipole driven transitions of the order of 10^{-29} cm^2). Signals at higher harmonics (N>2) yield sensitive features e.g. resolution of weak overlapping transitions, higher precision in measurement of collision dynamics and gas parameters.

- **VCSEL's (locking) stabilization and characterization:** Tunable diode lasers can be locked and stabilized using Wavelength modulation spectroscopy signals. Higher harmonic measurements (1f, 3f, 5f ...) provide highly sensitive signals at the location of the linecenter of absorption profile, the feedback signals are used to stabilize the laser from drifts in wavelength and intensity.

COMPUTER (SIMULATION) SKILLS

- **Operating Systems:** MS DOS, WINDOWS, LINUX, UNIX **Computer Languages:** C/C++, FORTRAN
- **Scientific Applications:** MATLAB (Mathworks, Digital Image Processing, Digital Signal Processing, Statistical Analysis Toolbox), SIMULINK, National Instruments (Labview and Electronics Workbench) **OPTICAL DESIGN:** ZEMAX/CODE V
- **Office Applications:** MS Word, MS PowerPoint, MS Excel, MS Publisher, Latex, Photoshop.
- **Internet Development:** Web Page design, HTML **Database:** Microsoft Access

LIST OF RECENT PUBLICATIONS

1. "*Optical pathlength saturation signatures in wavelength modulation spectroscopy signals of atmospheric molecular oxygen*," Applied Physics B: Lasers and Optics, (2009).
2. *"Signal Structure and Sensitive Detection of Molecular Species: Optimal experimental techniques in Modulation Broadened Wavelength Modulation Spectroscopy,"* Proceedings of SPIE, OPTO (2009).
3. *"Information Extraction from Congested Molecular Spectra by Modulation Spectroscopy,"* 75th annual southeastern APS meeting (2008)
4. *"Signal Structure and Precision in Optical Measurements: A new perspective to optimal experimental techniques"*, IEEE Lasers and Electro Optic Society Annual Meeting, Conference Proceedings (2008).
5. *"Information Theory of High-Precision Measurements"* Frontiers in Optics, Laser Science XXIV (2008).
6. "Information Content in Antenna Radiation Patterns"- 75th Annual Meeting of the Southeastern Section of APS meeting (2008).
7. Co-Author- "A quantitative measure for information content in antenna array radiation patterns", SPIE Symposium on Defense and Security, (2009).